The Alliance of Laboratories in Europe for
Education, Research and Technology

ALERT Doctoral School 2017

Discrete Element Modeling

Editors:

Kianoosh Taghizadeh

Gaël Combe

Stefan Luding

Editorial

The ALERT Doctoral School 2017 on “Discrete Element Modeling” will take place as usual in Aussois, from October 5th to 7th, 2017. The School has been organized by Prof. Gaël Combe (3SR Grenoble) and Prof. Stefan Luding (University Twente), who have prepared a very stimulating didactic path, well calibrated both for basic and advanced users, on such a powerful computational approach.

I sincerely thank the organizers, the editors and all the authors of the contributions to this book for their effort: thank you!

Although DEM is a rather well established numerical approach for research purposes since the early Eighties, all its potentialities have not yet been fully investigated, and they are continuously growing with the increase in the available computational capacity and with the introduction of some advanced modelling features (advanced contact laws, fluid/grain coupling, ...). I think that the ALERT community, and especially all the students and researchers who are going to attend the School or read this book, will take great advantage from this school.

Lectures will include topics ranging from basic concepts of DEM simulations (Molecular Dynamics, Event Driven, DEM basics), advanced contact laws for DEM applications, contact dynamics, applications to soil and rock mechanics.

As in 2016, practical sessions will be organized on the last day of the school: I am sure that this will be a very stimulating and efficient way to apply the theoretical concepts learnt in the first two days, and to share the knowledge among the practitioners and the teachers.

As usual, the pdf file of the book can be downloaded for free from the website of ALERT Geomaterials – http://alertgeomaterials.eu/.

On behalf of the ALERT Board of Directors I wish all participants a successful ALERT Doctoral School 2017!

Andrea Galli
Director of ALERT Geomaterials
Politecnico di Milano

Contents

Discrete Element Modeling: Foreword

The chapters in this volume are related to the lectures of the 2017 ALERT Geomaterials Doctoral School devoted to Discrete Element Modeling and its application in geomechanics, geomaterials, and geophysics.

The purpose of this volume is to present the basic concepts of particle simulation methods and their application to classical and modern problems of geomechanics. The volume is organized in 8 chapters.

The first two chapters [Luding et al., and Radjai et al.] concern the basic three different simulation approaches, as there are the soft particle discrete element method (DEM), as well as the event driven (ED), and the contact dynamics (CD) approaches that are starting from rigid particles. On the side of techniques, the third chapter [Delenne et al.] addresses the modeling of partly and/or fully saturated particulate-based porous materials, even though this is not explored in more detail in this course.

Chapters 4 [Martin] and 5 [Combe et al.] address the very important issues of advanced interaction models between the particles, and preparation procedures (best practice and pitfalls), respectively. Both aspects have to be considered before a reliable particle simulation of geomechanical systems can be performed. First, after choosing a contact model, the parameters have to be calibrated. Second, dependent on the experiment and material one plans to simulate, the samples have to be carefully prepared such that the numerical model represents the real system as much as possible. Third, an element or laboratory test has to be carried out and the results should be compared with experiments for validation before, eventually, the simulation results can be interpreted and conclusions can be drawn about the micro-mechanics and its effect on the static, stability and flow behavior of particulate, granular materials like soil.

Chapter 6 [Taghizadeh et al.] is concerned with several experimental procedures like shear- or tri-axial testing as well as mechanical wave propagation in laboratory element tests, and how to simulate such tests. In contrast to small-strain testing there are also large-strain and failure situations described, while the final chapter 7 [Donze et al.] addresses the issues of mechanical stability and the formation of shear-bands in tests of realistically layered materials.

The course will also have practical sessions on particle simulation methods for beginners and for experts as well. The final chapter 8 gives an introduction into the installation and use of an open-source code mercuryDPM [Tunuguntla et al.], and on how to extract continuum scale macroscopic fields from particle simulations, which is addressed already to some extent in almost all other chapters and more worked *out here. Some further material will be made available in electronic form, i.e., all participants should bring their laptop computer for the particle simulation practical sessions.*

We would like to thank all the contributors to this volume, as well as the referees of the papers. We hope that the chapters provide a valuable introduction to basics and advanced issues of particle simulation (like contact models and preparation procedures), theoretical concepts for both particle and continuum modeling, and the application of those in geomechanics laboraty and numerical testing, covering the state of the art of recent developments in the field.

Editors:

K. Taghizadeh
G. Combe
S. Luding

From soft and hard particle simulations to continuum theory for granular flows

S. Luding, N. Rivas, T. Weinhart

Multi-Scale Mechanics, Faculty of Engineering Technology (ET),
MESA+, University of Twente, Enschede, The Netherlands

One challenge of today's research is the realistic simulation of disordered many particle systems in static and dynamic/flow situations. Examples are particulate and granular materials like sand, powders, ceramics or composites, with applications in particle-technology and geo-technical/physical systems. The inhomogeneous micro-structure of such materials makes it very difficult to model them with continuum methods, which typically assume homogeneity on the microscale and scale separation between the constituents and the macroscopic fields. As an alternative, discrete particle methods can be applied, since they intrinsically take the micro-structure into account. The ultimate challenge is to bridge the gap between both approaches by using particle-simulations to obtain appropriate constitutive relations for continuum theories, and work with those on the macro-scale. Here, soft and hard particle simulation methods are introduced as well as the micro-macro transition to obtain the continuum fields from the particle data. Two application examples discussed in detail concern the flow of particle down an incline, as relevant for geo-flows, as well as a vibrated granular system as relevant for highly agitated transport or conveying processes.

1 Introduction

Most general materials have inhomogeneous micro-structures such as powders, sands, and even geo-materials. In such discrete, particulate, granular systems the particles can be complex, non-spherical, and consist of different materials. The idealized constituents we focus on in the following are spherical, polydisperse, elasto-plastic, adhesive, and frictional objects.

One approach towards the microscopic understanding of such macroscopic particulate material behavior [HHL98, Kis01, HW04] is the discrete modeling of particles. Soft and hard particle methods are discussed here, while other particle methods like contact dynamics (CD) are discussed in Ref. [Rad]. The method of particle simulations, and the practical aspects are also addressed in other lectures and practicals [CR, TWT], where more details on contact-models [Mar] are as important as the careful sample preparation [CR], and methods to model and interpret geotechnical experiments [DS, TML].

Even though millions of particles can be simulated, the possible size of such a particle system is in general too small to regard it as macroscopic. Therefore, methods and tools to perform a so-called micro-macro transition [VDE$^+$01, PL01, KBG49] are discussed. “Microscopic” particle simulations can be used to derive macroscopic constitutive relations, as needed to describe the material within the framework of continuum theory, on the scales of large industrial unit-operations and natural/geotechnical phenomena like avalanches or landslides.

In idealized granular materials, when the particle properties and interaction laws are defined, the equations of motion can be integrated in time. The collective behavior of dissipative many-particle systems can be studied in static and dynamic situations as well. For example, from particle simulations one can extract the pressure of the system as a function of density. This “equation of state” can then be used for the macroscopic description of dynamic materials, which can be viewed as a compressible, non-Newtonian complex fluid [LLH01], including fluid-solid phase transitions and energy dissipation terms.

Several techniques have been used to calculate the continuum fields from steady state flow situations, see [LAM11] and references therein. The stress tensor is of particular interest for the momentum balance equations: previous techniques include the Irvin-Kirkwood’s approach [IK50] or the method of planes [TED95]. Here, we use the coarse-graining approach as originally described in Ref. [Bab97, Gol10, WTLB12a, WLT13], and as also presented in the paper by Thornton [TWT]. It has the following advantages as compared to other methods: (*i*) the resulting fields automatically satisfy exactly the equations of continuum mechanics, also near boundaries or in mixtures, if corrected as proposed in [WTLB12a, WLT13], (*ii*) it is not assumed that the particles are spherical (but a single point of contact is required); and, (*iii*) the results are valid even for single particles and at one moment in time, as no ensemble averaging is required to satisfy the mass and momentum balance.

In the following, two particle simulation methods are introduced. The first is the so-called soft sphere Discrete Element Method (DEM), which is also often referred to as Molecular Dynamics (MD), as described in Section 2. It is straightforward to implement a solver for the equations of motion for a system of many interacting particles [AT87, Rap95]. For DEM, both normal and tangential interactions, like friction, are discussed for spherical particles. The second method is the so-called Event-Driven (ED) simulation, discussed in Section 3, which is conceptually different from DEM, since collisions are dealt with via a collision matrix that in one step determines the momentum change on physical grounds. For the sake of brevity, the ED method is only discussed for smooth (that is, frictionless) spherical particles. Furthermore, a method to relate the soft and hard particle methods is provided in Section 4. For more details on ED simulations see Ref. [Lud09] and references therein. To illustrate the micro-macro transition, the density, velocity and stress for a system of soft or hard spheres is defined in Section 5 by means of coarse graining, also referred to as the "micro-macro transition". Two examples are discussed in detail: First, chute flow in Section 6, where the above-described simulation methods can be applied for quasi-static, slow and inertial, dynamic systems. Macroscopic quantities are obtained using the micro-macro transition (or coarse graining) methodology introduced in the earlier chapters and all the resulting tensorial fields are discussed in depth, even though most of them are usually neglected in very many application and research studies. Second, the example of vibrated, collisional systems is presented in Section 7, where the two methods DEM and ED can be directly compared. Situations where he methods lead to the same results are presented together with cases where the results are differing.

2 The Soft-Particle Discrete Element Method

The elementary units of granular materials are mesoscopic grains which deform under stress. Since the realistic modeling of the deformations of the particles is much too complicated, we relate the interaction force to the overlap δ of two particles as a first order approximation, see Fig. 1a. Note that the evaluation of the inter-particle forces based on the overlap may not be sufficient to account for the inhomogeneous stress distribution inside the particles, and related multi-contact effects. Consequently, our results presented below are of the same quality as the simplifying assumptions about the pairwise force-overlap relation.

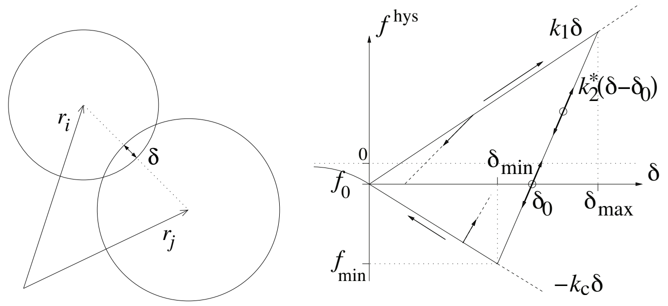

Figure 1: (Left) Two particle contact with overlap δ. (Right) Schematic graph of the piecewise linear, hysteretic, adhesive force-displacement model introduced below in Eq. (6). Note the important non-linearity of contact stiffness with confining stress (previous maximal overlap, $\delta_{\max}$), that manifests in the functional dependence of $k_2^*(\delta_{\max})$, as specified below in Eqs. (7) and (8).

2.1 Equations of Motion

If the total force $\vec{f}_i$ acting on particle i, either due to other particles and boundaries or from external forces, is known, then the problem is reduced to the integration of Newton's equations of motion for the translational and rotational degrees of freedom,

$$m_i \frac{\mathrm{d}^2}{\mathrm{d}t^2} \vec{r}_i = \vec{f}_i + m_i \vec{g}, \quad \text{and} \quad I_i \frac{\mathrm{d}}{\mathrm{d}t} \vec{\omega}_i = \vec{t}_i, \tag{1}$$

with m_i the mass of particle i, $\vec{r}_i$ its position, $\vec{f}_i = \sum_c \vec{f}_i^c$ the total force acting on it due to contacts with other particles or with the walls, $\vec{g}$ the acceleration due to volume forces like gravity, I_i the spherical particle's moment of inertia, $\vec{\omega}_i$ its angular velocity and $\vec{t}_i = \sum_c \left(\vec{l}_i^c \times \vec{f}_i^c + \vec{q}_i^c \right)$ the total torque, where $\vec{q}_i^c$ are torques/couples at contacts other than the torques due to the tangential force, e.g., due to rolling and torsion, and $\vec{l}_i^c$ the vector from the particle's centre of mass to the contact point.

The equations of motion are thus a system of $\mathcal{D} + \mathcal{D}(\mathcal{D}-1)/2$ coupled ordinary differential equations to be solved in $\mathcal{D}$ dimensions. The solution of such equations is straightforward, using numerical integration tools such as the ones nicely described in textbooks [AT87, Rap95]. The typically short-ranged interactions in granular media allow for further optimizations by using linked-cell spatial structures or alternative methods [AT87, Rap95, KOL14] in order to make the search for colliding particles more efficient. In the case of long-range interactions, (e.g. charged particles with Coulomb interaction, or objects in space with self-gravity) this is not possible anymore, so that more advanced methods for optimization have to be applied. Here we restrict ourselves to short-range interactions.

Specifically, two spherical particles i and j, with radii a_i and a_j, respectively, interact only if they are in contact, that is, their overlap

$$\delta = (a_i + a_j) - (\vec{r}_i - \vec{r}_j) \cdot \vec{n} \tag{2}$$

is positive, $\delta > 0$, with the unit vector $\vec{n} = \vec{n}_{ij} = (\vec{r}_i - \vec{r}_j)/|\vec{r}_i - \vec{r}_j|$ pointing from j to i. Note the different sign convention used in the contact dynamics (CD) method, where $\delta > 0$ means a separation and not the contact of particles [Rad]. The force on particle i, from particle j, at contact c, can be decomposed into a normal and a tangential part as $\vec{f}^c := \vec{f}_{ij}^c = f^n \vec{n} + f^t \vec{t}$. In the following, we specify $\vec{f}_{ij}^c$ for different models that take into account increasingly complicated grain interactions, see also Ref. [Mar]. We begin by discussing f^n.

2.2 Normal Contact Force Laws

2.2.1 Linear Normal Contact Model

The simplest normal contact force model, which takes into account excluded volume and dissipation, involves a linear repulsive and a linear dissipative force,

$$f^n = k\delta + \gamma_0 v_n \ , \tag{3}$$

with a spring stiffness k, a viscous damping γ_0, and the relative velocity in normal direction $v_n = -\vec{v}_{ij} \cdot \vec{n} = -(\vec{v}_i - \vec{v}_j) \cdot \vec{n} = \dot{\delta}$. This so-called linear spring dashpot model considers the particle interactions as a damped harmonic oscillator. As such, the half-period of a vibration around an equilibrium position can be computed, obtaining a typical response time on the contact level,

$$t_c = \frac{\pi}{\omega} \ , \quad \text{with} \ \ \omega = \sqrt{(k/m_{ij}) - \eta_0^2} \ , \tag{4}$$

with the eigenfrequency of the contact ω, the rescaled damping coefficient $\eta_0 = \gamma_0/(2m_{ij})$, and the reduced mass $m_{ij} = m_i m_j/(m_i + m_j)$. From the solution of the velocity at the half period of the oscillation, one also obtains the coefficient of restitution,

$$r = -v_n'/v_n = \exp\left(-\pi\eta_0/\omega\right) = \exp\left(-\eta_0 t_c\right) \ , \tag{5}$$

which quantifies the ratio of relative velocities after (primed) and before (unprimed) the collision. For a deeper discussion of the coefficient of restitution and other, more realistic, non-linear contact models, see e.g. [Lud98, SML15, TCC17] and the papers by Martin [Mar] and Radjai [Rad].

The contact duration in Eq. (4) is also of practical technical importance, since the integration of the equations of motion is stable only if the integration time-step Δt_{DEM} is much smaller than t_c. Furthermore, notice that in the extreme case of an overdamped spring, t_c can become very large, and therefore the use of neither too weak nor too strong dissipation is recommended.

2.2.2 Adhesive, Elasto-Plastic Normal Contact Model

Let us now consider a variant of the linear hysteretic spring model [WB86, Lud98, Tom00, Lud08], as an alternative to the frequently used spring-dashpot models. This model is a simple version of some more complicated nonlinear-hysteretic force laws [WB86, ZSS91, STS93], which reflects the fact that plastic deformations take place at the contact point. Overall, the model is meso-scopic [SMSL14], i.e. it describes the collective interactions of a bulk of primary particles that are represented by a meso-particle. The repulsive (hysteretic) force can be written as

$$f^{\mathrm{hys}} = \begin{cases} k_1\delta & \text{for loading,} \qquad \text{if } k_2^*(\delta - \delta_0) \geq k_1\delta \\ k_2^*(\delta - \delta_0) & \text{for un/reloading,} \quad \text{if } k_1\delta > k_2^*(\delta - \delta_0) > -k_c\delta \\ -k_c\delta & \text{for unloading,} \qquad \text{if } -k_c\delta \geq k_2^*(\delta - \delta_0) \end{cases} \ , \tag{6}$$

with $k_2^* \geq k_1 > 0$. The constant k_2^* is determined by the parameter k_2, as explained below. Fig. 1 shows an schematic of the loading and unloading process.

During the initial loading the force increases linearly with the overlap δ, until the maximum overlap $\delta_{\max}$ is reached (which has to be kept in memory as a history parameter). The line with slope k_1 thus defines the maximum force possible for a given δ. During unloading the force drops from its value at $\delta_{\max}$ down to zero at overlap $\delta_0 = (1 - k_1/k_2^*)\delta_{\max}$, on the line with slope k_2^*. Reloading at any instant leads to an increase of the force along this line, until the maximum force is reached; for still increasing δ, the force follows again the line with slope k_1 and $\delta_{\max}$ has to be adjusted accordingly.

Unloading below δ_0 leads to negative, i.e. attractive, forces until the minimum force $-k_c\delta_{\min}$ is reached at the overlap $\delta_{\min} = (k_2^* - k_1)\delta_{\max}/(k_2^* + k_c)$. This minimum force, i.e. the maximum attractive force, is obtained as a function of the model parameters k_1, k_2, k_c, and the history parameter $\delta_{\max}$. Further unloading leads to attractive forces $f^{\text{hys}} = -k_c\delta$ on the adhesive branch with slope $-k_c$. The highest possible attractive force, for given k_1 and k_2, is reached for $k_c \to \infty$, so that $f^{\text{hys}}_{\max} = -(k_2 - k_1)\delta_{\max}$. Since this would lead to a discontinuity at $\delta = 0$, it is avoided by using finite $k_c \geq 0$.

The lines with slope k_1 and $-k_c$ define the range of possible force values and departure from these lines takes place in the case of unloading and reloading, respectively. Between these two extremes, unloading and reloading follow the same line with slope k_2^*. Possible equilibrium states are indicated as circles in Fig. 1, where the upper and lower circle correspond to pre-stressed states with repulsive and attractive forces, respectively. Small overlap perturbations lead to small force deviations along the line with slope k_2^*, as indicated by the arrows.

Even though a non-linear un-/reloading behavior would be more realistic, we use the piecewise linear model as a compromise, mainly due to a lack of detailed experimental information for better calibrating the model. Only recently, due to nano-indenters and their more reliable force-displacement sensors, experimental data for unloading forces on the contact level between small particles become available. One refinement of the older models involves considering an unloading stiffness k_2^* dependent on the maximum overlap, i.e. the contact force and confining stress [LMM05, Lud08, SMSL14, SML15]. Introducing an additional contact-history parameter, the maximal overlap, $\delta^p_{\max}$, one has

$$k_2^*(\delta_{\max}) = \begin{cases} k_2 & \text{if } \delta_{\max} \geq \delta^p_{\max} \\ k_1 + (k_2 - k_1)\delta_{\max}/\delta^*_{\max} & \text{if } \delta_{\max} < \delta^p_{\max} \end{cases} , \qquad (7)$$

increasing from k_1 to k_2 with the maximum overlap, until $\delta^p_{\max}$ is reached, and an elastic branch with maximal stiffness k_2 is established (not shown in Fig. 1, see Ref. [SML15] for details). As a side-remark, the limit-slope k_2 can be introduced for practical reasons. If k_2 is not limited, the contact duration could become very small, i.e. the time step would have to be reduced below values that yield reasonable performance. However, there are also other – physical and mechanical – reasons for an elastic cut-off [SML15]; how to avoid the elastic cut-off was presented in Ref. [SML15].

The linear interpolation in Eq. (7) is arbitrary: one can vary it depending on the material under consideration, using as additional parameter the power ψ, so that the stiffness

$$k_2^*(\delta_{\max}) = \begin{cases} k_2 & \text{if } \delta_{\max} \geq \delta_{\max}^p \\ k_1 + (k_2 - k_1)\left[\delta_{\max}/\delta_{\max}^*\right]^{\psi} & \text{if } \delta_{\max} < \delta_{\max}^p \end{cases} , \qquad (8)$$

is non-linearly interpolated. This includes the linear case, for $\psi = 1$, as originally suggested [Lud08], the invariant stiffness, for $\psi = 0$, or the non-linear interpolation to provide Hertzian-type behavior of the coefficient of restitution, for $\psi = 1/2$, as first suggested in Ref. [SML15] (see Fig. 14), and more recently in Ref. [TCC17]. For different materials, different values of ψ might be more appropriate than those three cases, but the generalized Eq. (8) leaves this as an option to be chosen during parameter calibration.

While in the case of collisions of particles with large deformations, dissipation takes place due to the hysteretic nature of the force-law, stronger dissipation of small amplitude deformations is achieved by adding the viscous, velocity dependent dissipative force from Eq. (3) to the hysteretic force, such that $f^n = f^{\text{hys}} + \gamma_0 v_n$. The hysteretic model contains the linear contact model as the special case when $k_1 = k_2 = k$.

2.2.3 Long Range Normal Forces

Medium range van der Waals forces can be taken into account in addition to the hysteretic force such that $f^n = f^{\text{hys}} + f^{\text{vdW}}$ with, for example, the attractive part of a Lennard-Jones Potential

$$f^{\text{vdW}}(r_{ij}) = -6(\varepsilon/r_0)[(r_0/r_{ij})^7 - (r_0/r_c)^7] \quad \text{for } r_{ij} := |\vec{r}_i - \vec{r}_j| \leq r_c . \qquad (9)$$

The new parameters necessary for this force are an energy scale ε, a typical length scale r_0 and a cut-off length r_c. As long as r_c is not much larger than the particle diameter, the methods for short range interactions can still be applied to such a medium range interaction model – only the linked cells have to be larger than twice the cut-off radius, since no force should be active for $r > r_c$. A piecewise linear non-contact force is proposed in Ref. [SML15] for both reversible and irreversible contact models that mimick van der Waals or Coulomb type interactions and liquid bridges that are hysteretic in nature, respectively.

2.3 Kinematics of Tangential Forces and Torques

For the tangential degrees of freedom, there are three different force- and torque-laws to be implemented: (i) friction, (ii) rolling resistance, and (iii) torsion resistance.

2.3.1 Sliding

For dynamic (sliding) and static *friction*, the relative tangential velocity of the contact points,

$$\vec{v}_t = \vec{v}_{ij} - \vec{n}(\vec{n} \cdot \vec{v}_{ij}) \ , \tag{10}$$

is to be considered for the force computations (or torque computations in subsection 2.4), with the total relative velocity of the particle surfaces at the contact

$$\vec{v}_{ij} = \vec{v}_i - \vec{v}_j + a_i'\vec{n} \times \vec{\omega}_i + a_j'\vec{n} \times \vec{\omega}_j \ , \tag{11}$$

with the corrected radius relative to the contact point $a_\alpha' = a_\alpha - \delta/2$, for $\alpha = i, j$. For strongly different particle sizes and large overlaps, this has to be considered in more detail [TWT]. Tangential forces and torques acting on the contacting particles are computed from the accumulated sliding and rolling/torsion of the contact points relative to each other, as described in detail in subsec. 2.4.1.

2.3.2 Objectivity

Objectivity is about the invariance of contact models in moving or rotating reference frames. In general, two particles can rotate together, due to either a global rotation of the reference frame or a non-central "collision". Either way, the angular velocity $\vec{\omega}_0 = \vec{\omega}_0^n + \vec{\omega}_0^t$, of the rotating reference has the tangential-plane component

$$\vec{\omega}_0^t = \frac{\vec{n} \times (\vec{v}_i - \vec{v}_j)}{a_i' + a_j'} \ , \tag{12}$$

which is related to the relative velocity, while the normal component, $\vec{\omega}_0^n$, is not. Inserting $\vec{\omega}_i = \vec{\omega}_j = \vec{\omega}_0^t$, from Eq. (12), into Eq. (11) leads to zero sliding velocity, proving that the above relations are objective. Tangential forces and torques due to sliding can become active only when the particles are rotating in the same direction with respect to the common rotating reference frame. For rolling and torsion, there is no similar relation between rotational and tangential degrees of freedom: for any rotating reference frame, torques due to rolling and torsion can become active only due to rotation of two particles relative to each other, in opposite direction, in the common reference frame.

Since action should be equal to reaction, the tangential forces are equally strong, but opposite, i.e., $\vec{f}_j^t = -\vec{f}_i^t$, while the corresponding torques are parallel but not necessarily equal in magnitude: $\vec{q}_i^{\text{friction}} = -a_i'\vec{n} \times \vec{f}_i$, and $\vec{q}_j^{\text{friction}} = (a_j'/a_i')\vec{q}_i^{\text{friction}}$. Note that tangential forces and torques *together* conserve the total angular momentum about the pair center of mass

$$\vec{L}_{ij} = \vec{L}_i + \vec{L}_j + m_i r_{i\text{cm}}^2 \vec{\omega}_0^t + m_j r_{j\text{cm}}^2 \vec{\omega}_0^t \ , \tag{13}$$

with the rotational contributions $\vec{L}_\alpha = I_\alpha \vec{\omega}_\alpha$, for $\alpha = i, j$, and the distances $r_{\alpha\text{cm}} = |\vec{r}_\alpha - r_{\text{cm}}|$ from the particle centers to the center of mass $\vec{r}_{\text{cm}} = (m_i\vec{r}_i + m_j\vec{r}_j)/(m_i +$

m_j), see Ref. [Lud98]. The change of angular momentum consists of the change of particle spins (first term) and of the change of the angular momentum of the two masses rotating about their common center of mass (second term):

$$\frac{d\vec{L}_{ij}}{dt} = \vec{q}_i^{\,\text{friction}} \left(1 + \frac{a'_j}{a'_i}\right) + \left(m_i r_{i\text{cm}}^2 + m_j r_{j\text{cm}}^2\right) \frac{d\vec{\omega}_0^t}{dt} \, , \tag{14}$$

which both contribute, but exactly cancel each other, since

$$\begin{aligned} \vec{q}_i^{\,\text{friction}} \left(1 + \frac{a'_j}{a'_i}\right) &= -(a'_i + a'_j)\, \vec{n} \times \vec{f}_i \qquad (15) \\ &= -\left(m_i r_{i\text{cm}}^2 + m_j r_{j\text{cm}}^2\right) \frac{d\vec{\omega}_0^t}{dt} \, , \end{aligned}$$

see [Lud06] for more details.

2.3.3 Rolling

A *rolling* velocity $\vec{v}_r^{\,0} = -a'_i \vec{n} \times \vec{\omega}_i + a'_j \vec{n} \times \vec{\omega}_j$, defined in analogy to the sliding velocity, is not objective in general [Els06, Lud06] – only in the special cases of (i) equal-sized particles or (ii) for a particle rolling on a fixed flat surface.

The rolling velocity should quantify the distance the two surfaces roll over each other (without sliding). Therefore, it is equal for both particles by definition. An *objective rolling velocity* is obtained by using the reduced radius, $a'_{ij} = a'_i a'_j / (a'_i + a'_j)$, so that

$$\vec{v}_r = -a'_{ij} \left(\vec{n} \times \vec{\omega}_i - \vec{n} \times \vec{\omega}_j\right) \; . \tag{16}$$

This definition is objective since any common rotation of the two particles vanishes due to the difference. A more detailed discussion of the issue of rolling is beyond the scope of this paper.

A rolling velocity will activate torques, acting against the rolling motion, e.g., when two particles are rotating anti-parallel with spins in the tangential plane. These torques are then equal in magnitude and opposite in direction, i.e., $\vec{q}_i^{\,\text{rolling}} = -\vec{q}_j^{\,\text{rolling}} = a_{ij}\, \vec{n} \times \vec{f}_r$, with the quasi-force $\vec{f}_r$, computed in analogy to the friction force, as function of the rolling velocity $\vec{v}_r$ in Eq. 16. The quasi-forces for both particles are opposite and equal but do not act on the centers of mass, so that the total momenta (translational and angular) are conserved.

2.3.4 Torsion

For *torsion resistance*, the relative spin along the normal direction

$$\vec{v}_o = a_{ij} \left(\vec{n} \cdot \vec{\omega}_i - \vec{n} \cdot \vec{\omega}_j\right) \vec{n} \, , \tag{17}$$

is to be considered, which activates torques when two particles are rotating anti-parallel with spins parallel to the normal direction. Torsion is not activated by a common rotation of the particles around the normal direction $\vec{n} \cdot \vec{\omega}_0 = \vec{n} \cdot (\vec{\omega}_i + \vec{\omega}_j)/2$, which makes the torsion resistance objective.

The torsion torques are equal in magnitude and directed in opposite directions, i.e., $\vec{q}_i^{\,\mathrm{torsion}} = -\vec{q}_j^{\,\mathrm{torsion}} = a_{ij}\,\vec{f}_o$, with the quasi-force $\vec{f}_o$, computed from the torsion velocity in Eq. 17, and also not changing the translational momentum. Like for rolling, the torsion torques conserve the total angular momentum.

2.3.5 Summary

The implementation of the tangential force computations for $\vec{f}_t$, $\vec{f}_r$, and $\vec{f}_o$ as based on $\vec{v}_t$, $\vec{v}_r$, and $\vec{v}_o$, respectively, is assumed to be identical, i.e., even the same subroutine is used, but with different parameters as specified below. The difference is that friction leads to a force in the tangential plane (changing both translational and angular momentum), while rolling- and torsion-resistance lead to quasi-forces in the tangential plane and the normal direction, respectively, changing the particles' angular momentum only. For more details on tangential contact models, friction, rolling and torsion, see Refs. [BUK$^+$05, DvZTR05, Lud07, Lud06, Els06]. The contact laws are implemented in MercuryDPM [WTLB12b, TWLB12b, TWT].

2.4 Tangential Force and Torque Laws

The tangential contact model presented now is a single procedure (subroutine) that can be used to compute either sliding, rolling, or torsion resistance. The subroutine needs a relative velocity as input and returns the respective force or quasi-force as function of the accumulated deformation. The sliding/sticking friction model will be introduced in detail, while rolling and torsion resistance are discussed only where different.

2.4.1 Sliding/Sticking Friction Model

The tangential force is coupled to the normal force via Coulomb's law, i.e. an inequality: $f^t \leq f_C^s := \mu^s f^n$, see also Ref. [Rad]. For the sliding case one has dynamic friction as equality: $f^t = f_C^t := \mu^d f^n$. The dynamic and the static friction coefficients follow, in general, the relation $\mu^d \leq \mu^s$. The static situation requires an elastic spring in order to allow for a restoring force, i.e., a non-zero remaining tangential force in static equilibrium due to activated Coulomb friction.

If a purely repulsive contact is established, $f^n > 0$, and the tangential force is active. For an adhesive contact, Coulombs law has to be modified in so far that f^n is replaced by $f^n + k_c\delta$. In this model, the reference for a contact is no longer the zero force level, but it is the adhesive, attractive force level along $-k_c\delta$.

If a contact is active, one has to project (or better rotate) the tangential spring into the actual tangential plane, since the frame of reference of the contact may have rotated since the last time-step. The tangential spring

$$\vec{\xi} = \vec{\xi}' - \vec{n}(\vec{n} \cdot \vec{\xi}') \; , \tag{18}$$

is used for the actual computation, where $\vec{\xi}'$ is the old spring from the last iteration, with $|\vec{\xi}| = |\vec{\xi}'|$ enforced by appropriate scaling/rotation. If the spring is new, the tangential spring-length is zero, but its change is well defined after this first initiation step. In order to compute the changes of the tangential spring, a tangential test-force is first computed as the sum of the tangential spring force and a tangential viscous force (in analogy to the normal viscous force)

$$\vec{f_0^t} = -k_t \, \vec{\xi} - \gamma_t \vec{v}_t \; , \tag{19}$$

with the tangential spring stiffness k_t, the tangential dissipation parameter γ_t, and $\vec{v}_t$ from Eq. (10). As long as $|\vec{f_0^t}| \leq f_C^s$, with $f_C^s = \mu^s(f^n + k_c\delta)$, one has static friction and, on the other hand, for $|\vec{f_0^t}| > f_C^s$, sliding friction becomes active. As soon as $|\vec{f_0^t}|$ gets smaller than f_C^d, static friction becomes active again.

In the *static friction* case, below the Coulomb limit, the tangential spring is incremented

$$\vec{\xi}' = \vec{\xi} + \vec{v}_t \, \Delta t_{\mathrm{DEM}} \; , \tag{20}$$

to be used in the next iteration in Eq. (18), and the tangential force $\vec{f^t} = \vec{f_0^t}$ from Eq. (19) is used. In the *sliding friction* case, the tangential spring is adjusted to a length consistent with Coulombs condition, so that

$$\vec{\xi}' = -\frac{1}{k_t} \left(f_C^d \, \vec{t} + \gamma_t \vec{v}_t \right) \; , \tag{21}$$

with the tangential unit vector, $\vec{t} = \vec{f_0^t}/|\vec{f_0^t}|$, defined by Eq. (19), and thus the magnitude of the Coulomb force is used. Inserting $\vec{\xi}'$ from Eq. (21) into Eq. (19) during the next iteration will lead to $\vec{f_0^t} \approx f_C^d \vec{t}$. Note that $\vec{f_0^t}$ and $\vec{v}_t$ are not necessarily parallel in three dimensions. However, the mapping in Eq. (21) always works, rotating the new spring such that the direction of the frictional force is unchanged and, at the same time, limiting the spring in length according to Coulombs law. In short notation the tangential contact law reads

$$\vec{f^t} = f^t \vec{t} = \min\left(f_C, |\vec{f_0^t}| \right) \vec{t}, \tag{22}$$

where f_C follows the static/dynamic selection rules described above. The torque on a particle due to frictional forces at this contact is $\vec{q}^{\,\mathrm{friction}} = \vec{l_i^c} \times \vec{f_i^c}$, where $\vec{l_i^c}$ is the branch vector, connecting the center of the particle with the contact point. Note that the torque on the contact partner is generally different in magnitude, since $\vec{l_i^c}$ can be different, but is directed in the same direction; see subsection 2.3.2 for details.

The four parameters for the friction law are k_t, μ_s, $\phi_d = \mu_d/\mu_s$, and γ_t, accounting for tangential stiffness, the static friction coefficient, the dynamic friction ratio, and the tangential viscosity, respectively. Note that the tangential force described above is identical to the classical Cundall-Strack spring only in the limits $\mu = \mu^s = \mu^d$, i.e., $\phi_d = 1$, and $\gamma_t = 0$. The sequence of computations and the definitions and mappings into the tangential direction can be used in 3D as well as in 2D.

2.4.2 Rolling Resistance Model

The four new parameters for rolling resistance are k_r, μ_r, ϕ_r and γ_r. The new parameters account for rolling stiffness, a static and dynamic rolling "friction" coefficient, and rolling viscosity, respectively. In the subroutine called, the rolling velocity $\vec{v}_r$ is used instead of $\vec{v}_t$ and the computed quasi-force $\vec{f}_r$ is used to compute the torques, $\vec{q}^{\text{rolling}}$, on the particles.

2.4.3 Torsion Resistance Model

The four new parameters for rolling resistance are k_o, μ_o, ϕ_0 and γ_o. The new parameters account for torsion stiffness, a static and dynamic torsion "friction" coefficient, and torsion viscosity, respectively. In the subroutine, the torsion velocity $\vec{v}_o$ is used instead of $\vec{v}_t$ and the projection is a projection along the normal unit-vector, not into the tangential plane as for the other two models. The computed quasi-force $\vec{f}_o$ is then used to compute the torques, $\vec{q}^{\text{torsion}}$, on the particles.

2.5 Background Friction

Note that the viscous dissipation takes place in a two-particle contact. In the bulk material, where many particles are in contact with each other, this dissipation mode is very inefficient for long-wavelength cooperative modes of motion [LCB$^+$94b, LCB$^+$94a]. Therefore, an additional damping with the background can be introduced, so that the total force on particle i is

$$\vec{f}_i = \sum_j \left(f^n \vec{n} + f^t \vec{t} \right) - \gamma_b \vec{v}_i \, , \tag{23}$$

and the total torque

$$\vec{q}_i = \sum_j \left(\vec{q}^{\text{friction}} + \vec{q}^{\text{rolling}} + \vec{q}^{\text{torsion}} \right) - \gamma_{br} a_i^2 \vec{\omega}_i \, , \tag{24}$$

with the damping artificially enhanced in the spirit of a rapid relaxation and equilibration. The sum in Eqs. (23) and (24) takes into account all contact partners j of particle i, but the background dissipation can be attributed to the medium between the particles. Note that the effect of γ_b and γ_{br} should be checked for each flow situation and new set of parameters: it should be small in order to exclude artificial over-damping.

The full set of parameters is summarized in table 1. Note that only a few parameters are specified with dimensions, while most parameters are expressed as dimensionless numbers.

Property	Symbol
Time unit	t_u
Length unit	x_u
Mass unit	m_u
Particle radius	a
Material density	ρ_p
Elastic stiffness (variable)	k_2
Maximal elastic stiffness	$k = k_2$
Plastic stiffness	k_1/k
Adhesion "stiffness"	k_c/k
Friction stiffness	k_t/k
Rolling stiffness	k_r/k
Torsion stiffness	k_o/k
Plasticity depth	ϕ_f
Coulomb friction coefficient	$\mu = \mu_d = \mu_s$
Dynamic to static friction ratio	$\phi_d = \mu_d/\mu_s$
Rolling "friction" coefficient	μ_r
Torsion "friction" coefficient	μ_o
Normal viscosity	$\gamma = \gamma_n$
Friction viscosity	γ_t/γ
Rolling viscosity	γ_r/γ
Torsion viscosity	γ_o/γ
Background viscosity	γ_b/γ
Background viscous torque	γ_{br}/γ

Table 1: Summary of the microscopic contact model parameters. The longer ranged forces and their parameters, ϵ, r_0, and r_c are not included here.

As computer algorithms work by definition with non-dimensional numbers, we also include into the table the mass, length, and time units used in the simulation. These can be the standard SI-units (1 kg, 1 m, and 1 s). However, mass, length and time are often scaled such that all other parameters are non-dimensional. For example, the units $m_u = (4/3)\pi\rho_p a^3$, $x_u = 2a$ and $t_u = \sqrt{2a/g}$ are used in section 6.

3 Hard-Particle Event-Driven Simulations

In this section, the hard-sphere Event-Driven (ED) model is introduced. Hard spheres can be considered as the limit of infinite stiffness or, equivalently, zero contact time t_c, of the previously presented soft spheres contact models. In many situations hard spheres are a good approximation of the real contact dynamics, even though details of the contact- or collision behavior of the particles are ignored. This is especially true when multi-particle contacts are irrelevant, as in highly agitated or low density states. Nevertheless, a generalized model is also introduced that takes into account the finite contact duration of real particle collisions which, besides providing a physical parameter, considerably saves computing time, as it avoids the so called “inelastic collapse”.

In the framework of the hard sphere model, particles are assumed to be perfectly rigid and follow an undisturbed motion until a collision occurs, as detailed below. Together with the fact that collisions occur instantaneously, it becomes possible to implement an event-driven simulation method [Lub91, LM98, ML04b, ML04a, Mil04]. ED simulations are usually orders of magnitude faster than their DEM soft particle equivalents. Nonetheless, it is important to remark that the ED algorithm was only recently implemented in parallel [Lub92, ML04b], a relevant aspect for today’s overall computing efficiency; here we avoid to discuss this issue in detail, and only remark that, to our knowledge, event-driven parallel algorithms scale sub-optimal with the number of processors p, i.e. the speed-up reached was $p^{1/2}$ instead of p, the standard for DEM simulations.

The lack of physical information in the model allows a much simpler treatment of collisions than described in Section 2, by just using a collision matrix based on momentum conservation and energy loss rules. For the sake of simplicity, here we restrict ourselves to smooth hard spheres. Collision rules for rough spheres, that include friction coefficients, are extensively discussed elsewhere, see e.g. [LHMZ98, Lud09] and references therein.

3.1 Smooth Hard Sphere Collision Model

The standard interaction model for instantaneous collisions of identical particles with radius a, and mass m, is discussed in the following. The post-collisional velocities $\vec{v}'$ of two collision partners in their center of mass reference frame are given, in terms of the pre-collisional velocities $\vec{v}$, by

$$\vec{v}'_{1,2} = \vec{v}_{1,2} \mp (1+r)\vec{v}_n /2 \ , \tag{25}$$

with $\vec{v}_n \equiv [(\vec{v}_1 - \vec{v}_2) \cdot \vec{n}]\, \vec{n}$, the normal component of the relative velocity $\vec{v}_1 - \vec{v}_2$, parallel to $\vec{n}$, the unit vector pointing along the line connecting the centers of the colliding particles. The restitution coefficient $r \in [0,1]$ is a measure of the level of inelasticity in every collision, with $r = 1$ corresponding to the elastic case. If two particles collide, their velocities are changed according to Eq. (25), with the corresponding change of the translational energy at a collision

$$\Delta E = -m_{12}(1-r^2)v_n^2/2 \ , \tag{26}$$

with the reduced mass $m_{12} = m_1 m_2/(m_1 + m_2)$.

3.2 Event-Driven Algorithm

The fundamental difference between an event-driven (ED) algorithm and a DEM soft-particle simulation lies in the handling of the time evolution. ED simulations do not possess a fixed time step, as DEM simulations, but a variable one, given always by the immediately next event. An event is either the collision of two particles, or the collision of one particle with a boundary, either physical or virtual. In the following, the conditions needed to use this approach are detailed, as also several optimization techniques for the definition of the next event.

The algorithm essentially consists of a cycle where the minimum of all future collision times is determined, and then the proper collision rule is selected and executed. ED simulations are thus extremely efficient when the time of the upcoming events can be analytically computed. This is the case for a constant and homogeneous external field (usually gravity) and infinitely hard spheres, as the solution for the time of collision between two particles is actually given just by the intersection of their relative linear trajectories. Walls, on the other hand, involve the solution of a quadratic equation. Nevertheless, let us remark that although analytic determination of the collision times highly simplifies the algorithm, the possibility of numerically solving the intersections of the equations of motion is also possible, and has been recently successfully implemented [BSL11].

The critical optimization point for serial ED algorithms is in the determination of the forthcoming collision times. The introduction of cells with virtual boundaries greatly increases the efficiency of this process. Virtual boundaries collisions have no effect on the particles motion, but are only introduced to keep track of which particles belong to which cell. If all the particles with centers in a given cell and its neighboring cells are known, then the search for possible collision partners for a particle in the cell can be done locally. That is, instead of having to check all pairs of particles for possible collisions, only local neighbors are considered, greatly reducing the time for the determination of the next collision.

Another source of optimization involves the treatment of collisions. Simple ED algorithms update the whole system after each event, a method which is straightforward but inefficient for large numbers of particles. In Ref. [Lub91] an ED algorithm was introduced which updates only those two particles involved in the last collision. The fact that the algorithm is “asynchronous”, in so far that an event, i.e. the *next* event, can occur anywhere in the system, makes parallelization a big challenge [ML04b]. For the serial algorithm, a double buffering data structure is implemented, which contains the ‘old’ status and the ‘new’ status, each consisting of: time of event, positions, velocities, and event partners. When a collision occurs, the ‘old’ and ‘new’ status of the participating particles are exchanged. Thus, the former ‘new’ status becomes the actual ‘old’ one, while the former ‘old’ status becomes the ‘new’ one and is then free for the calculation and storage of possible future events. This seemingly complicated exchange of information is carried out extremely simply and fast by only exchanging the pointers to the ‘new’ and ‘old’ status respectively. Note that the ‘old’ status of particle i has to be kept in memory, in order to update the time of the next contact, t_{ij}, of particle i with any other object j if the latter, independently, changed its status due to a collision with yet another particle. During the simulation such updates may be necessary several times so that the predicted 'new' status has to be modified.

The minimum of all t_{ij} is stored in the 'new' status of particle i, together with the corresponding partner j. Depending on the implementation, positions and velocities after the collision can also be calculated. This would be a waste of computer time, since before the time t_{ij}, the predicted partners i and j might be involved in several collisions with other particles, so that we apply a delayed update scheme [Lub91]. The minimum times of event, i.e. the times which indicate the next event for a certain particle, are stored in an ordered heap tree, such that the next event is found at the top of the heap with a computational effort of $O(1)$; changing the position of one particle in the tree from the top to a new position needs $O(\log N)$ operations. The search for possible collision partners is accelerated by the use of a standard linked-cell data structure and consumes $O(1)$ of numerical resources per particle. In total, this results in a numerical effort of $O(N \log N)$ for N particles. For a detailed description of the algorithm see Ref. [Lub91].

Using all these optimizations, we are able to simulate about 10^6 particles within reasonable time on a low-end PC [LH99], where the particle number is more limited by memory than by CPU power. Parallelization, however, is a means to overcome the limits of one processor [ML04b]. Since we could be interested in the behavior of granular particles possibly evolving over several decades in time, the fastness of the event-driven method becomes a crucial feature even for systems with low number of particles.

As a final remark concerning ED, one should note that the disadvantages connected to the assumptions made that allow to use an event driven algorithm limit the applicability of this method. Within their range of applicability, ED simulations are typically much faster than DEM simulations, since the former accounts for a collision in one basic operation (collision matrix), whereas the latter requires order of 40 basic steps (integration time steps). Note that this statement is also true in the dense regime. In the dilute regime, both methods give equivalent results, because collisions are mostly binary [LCB$^+$94a]. When the system becomes denser, multi-particle collisions can occur and the rigidity assumption within the ED hard sphere approach becomes invalid. For a recent study on soft, hard and rigid particles at moderate to high densities above the fluid-solid transition, see Ref. [VL16] and references therein, where it is shown that rigid particles have a strictly limit in density where the confining stress diverges, whereas soft particle systems can be compressed further given the confining stress is large enough. For the densities that can be reached using hard spheres, see Ref. [OL13], where it is shown that the limit density can be approached up to the numerical accuracy, and how this limit density depends on the polydispersity of the particles (their size distribution and its moments).

While softness can not be easily introduced into an ED algorithm, another effect can be elegantly considered: The most striking difference between hard and soft spheres is the fact that soft particles dissipate less energy when they are in contact with many others of their kind. With other words, dissipation takes a finite time during, t_c, the Time of Contact (TC), which decreases with increasing stiffness of the particles. So while ED still builds upon binary collisions, at very high densities, permanent multiple contacts are taken mimicked by multiple collisions within the contact duration t_c. In the following chapter, the so called TC model is discussed as a means to account for the stiffness dependent contact duration in the hard sphere model.

4 Linking ED and DEM via the TC Model

In the hard-sphere ED method the contact duration is implicitly zero, matching well the corresponding assumption of instantaneous contacts used in kinetic theory [Haf83, JR85]. Due to this artificial simplification (which disregards the fact that a real contact takes always finite time) ED algorithms run into problems when the time between events t_n gets too small: in very dense systems with strong dissipation, t_n may even tend towards zero, which leads to a diverging dissipation rate; see Eq. (26). As a consequence the so-called "inelastic collapse" can occur, i.e. the divergence of the number of events per unit time. The problem of the inelastic collapse [MY94] can be avoided using restitution coefficients dependent on the time elapsed since the last event [LM98, LG03]. For the contact that occurs at time t_{ij} between particles i and j, one uses $r = 1$ if at least one of the partners involved had a collision with another particle later than $t_{ij} - t_\mathrm{c}^e$. The time t_c^e can be seen as a typical Time of Contat (TC), or contact duration, and allows for the definition of the dimensionless ratio

$$\tau_c = t_c^e / t_n \ . \tag{27}$$

The effect of t_c^e on the simulation results is negligible for large r and small t_c^e; for a more detailed discussion see [LM98, LH99, LG03].

In assemblies of soft particles, multi-particle contacts are possible and the inelastic collapse is naturally avoided, since the dissipation rate is always finite (less than $\Delta E/t_c^e$). The TC model can be seen as a means to approximate multi-particle collisions for hard spheres in dense systems [LCRD96, Lud97, LM98]. Let us consider the homogeneous cooling system (HCS) to evaluate the influence of the TC model in the cooling dynamics. One can explicitly compute the corrected cooling rate (r.h.s.) in the energy balance equation

$$\frac{d}{d\tau} E = -2 I(E, t_c^e) \ , \tag{28}$$

with the dimensionless time $\tau = (2/3) A t / t_E(0)$ for 3D systems, scaled by $A = (1-r^2)/4$, and the collision rate $t_E^{-1} = (12/a)\nu g(\nu)\sqrt{T/(\pi m)}$, with $T = 2K/(3N)$. In these units, the energy dissipation rate I is a function of the dimensionless energy $E = K/K(0)$ and the cut-off time t_c^e, with K the kinetic energy. In this representation, the restitution coefficient is hidden in the rescaled time via $A = A(r)$,

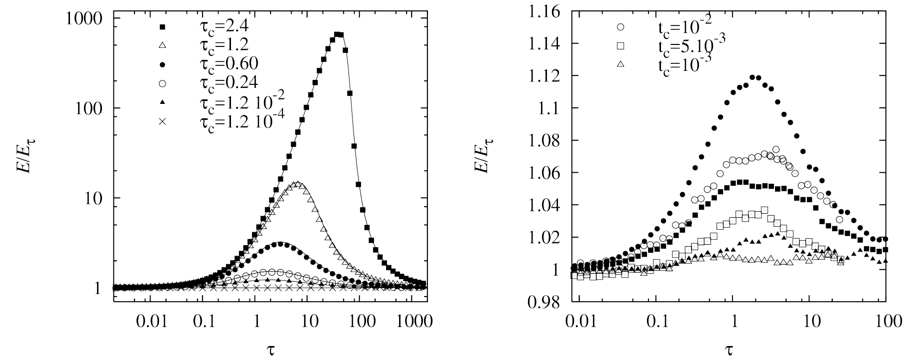

Figure 2: (Left) Deviation from the HCS, i.e. rescaled energy E/E_τ, where E_τ is the classical solution $E_\tau = (1+\tau)^{-2}$. The data are plotted against τ for simulations with different $\tau_c(0) = t_c^e/t_E(0)$ as given in the key/inset, with $r = 0.99$, and $N = 8000$. Symbols are ED simulation results, the solid line results from the third order correction. (Right) E/E_τ plotted against τ for simulations with $r = 0.99$, and $N = 2197$. Solid symbols are ED simulations, open symbols are DEM (soft particle simulations) with three different t_c^e as given in the inset.

so that inelastic hard sphere simulations with different r scale on the same master-curve. When the classical dissipation rate $E^{3/2}$ [Haf83] is extracted from I, so that $I(E, t_c^e) = J(E, t_c^e)E^{3/2}$, one has the correction-function $J \to 1$ for $t_c \to 0$. The deviation from the classical HCS is [LG03]:

$$J(E, t_c^e) = \exp\left(\Psi(x)\right) \,, \tag{29}$$

with the series expansion $\Psi(x) = -1.268x + 0.01682x^2 - 0.0005783x^3 + \mathcal{O}(x^4)$ in the collision integral, with $x = \sqrt{\pi} t_c^e t_E^{-1}(0)\sqrt{E} = \sqrt{\pi}\tau_c(0)\sqrt{E} = \sqrt{\pi}\tau_c$ [LG03]. This is close to the result $\Psi_{\mathrm{LM}} = -2x/\sqrt{\pi}$, proposed by Luding and McNamara, based on probabilistic mean-field arguments [LM98], where Ψ_{LM} thus neglects non-linear terms and underestimates the linear part.

Given the differential equation (28) and the correction due to multi-particle contacts from Eq. (29), it is possible to obtain the solution numerically, and to compare it to the classical $E_\tau = (1+\tau)^{-2}$ solution. Simulation results are compared to the theoretical solution in Fig. 2 (left). The agreement between simulations and theory is almost perfect in the examined range of t_c^e values; only when deviations from homogeneity are evidenced one expects disagreement between simulation and theory. The fixed cut-off time t_c^e has no effect when the time between collisions is very large $t_E \gg t_c^e$, but strongly reduces dissipation when the collisions occur with high frequency $t_E^{-1} \gtrsim (t_c^e)^{-1}$. Thus, in the homogeneous cooling state, there is a strong effect initially when t_c is large, but the long time behavior tends towards the classical decay $E \to E_\tau \propto \tau^{-2}$.

The next verification of the ED results obtained using the TC model involves comparing them to DEM simulations, see Fig. 2 (right). Open and solid symbols correspond to soft and hard sphere simulations, respectively, where the qualitative behavior (the deviation from the classical HCS solution) is identical. The energy decay is delayed due to multi-particle collisions, but later the classical solution is recovered. A quantitative comparison shows that the deviation of E from E_τ is larger for ED than for DEM, given that the same t_c^e is used. This weaker dissipation can be understood from the strict rule used for ED: dissipation is inactive if any particle had a contact already. The disagreement between ED and DEM is systematic and should disappear if an about 30 per-cent smaller t_c value is used for ED. The disagreement is also plausible, since the TC model disregards all dissipation for multi-particle contacts, while the soft particles still dissipate energy — even though much less — in the case of multi-particle contacts.

The above results show that the TC model is in fact a good method to approximate soft particles behaviour with hard particles. The only modification made to straightforward ED involves a reduced dissipation for (rapid) multi-particle collisions. More general corrections and adaptations are the subject of ongoing work.

5 Micro-macro Transition for Particle Simulations

To analyse the static or dynamic behaviour of granular assemblies, bulk properties such as the continuum (macro) fields of mass density ρ, velocity $\vec{V}$, velocity gradient $\nabla\vec{V}$ and stress $\underline{\underline{\sigma}}$ can be extracted from the discrete (micro) particle data. These fields are related to each other via the equations of mass and momentum conservation,

$$\frac{\partial\rho}{\partial t} + \nabla\cdot(\rho\vec{V}) = 0, \tag{30a}$$

$$\frac{\partial(\rho\vec{V})}{\partial t} + \nabla\cdot(\rho\vec{V}\otimes\vec{V}) = -\nabla\cdot\underline{\underline{\sigma}} + \rho\vec{g} + \vec{t}, \tag{30b}$$

and thus the definitions of these fields should satisfy above equations. Here, we use the compressive stress definition such that the pressure, $p = \mathrm{tr}(\underline{\underline{\sigma}})/3$, is positive under compression. The body force density, $\rho\vec{g}$, accounts in this case for gravity, while the external interaction force density, $\vec{t}$, accounts for interactions of the bulk with external objects, such as boundaries [WTLB12b] or drag relations with other constituents in a mixed flow [WLT13].

While it is relatively straightforward to define these fields for homogeneous mixtures, defining locally and temporally varying fields requires some care. Here, we present the coarse-graining formulation [Bab97, Gol10, WTLB12b], where the field definitions are constructed directly from equations (30) and thus satisfy them exactly.

First, the macroscopic density is defined by

$$\rho(\vec{r},t) = \sum_{i=1}^{N} m_i \mathcal{W}\left(\vec{r} - \vec{r}_i(t)\right), \tag{31}$$

where we have replaced the Dirac delta function of the micromechanical density definition, $\rho^{\text{mic}} = \sum_{i=1}^{N} m_i \delta\left(\vec{r} - \vec{r}_i\right)$, by an integrable 'coarse-graining' function $\mathcal{W}$ whose integral over the domain is unity and has a predetermined (non-dimensional) width (or coarse-graining scale) $w = w'/d$, with the dimensional width w', relative to the particle diameter. The resolution and shape of the coarse-graining function used in the formulation can be chosen freely, such that both microscopic and macroscopic effects can be studied. Many shape functions are possible, such as Gaussian distributions or Lucy functions. While the shape of the coarse-graining function has little effect on the macroscopic fields, they depend on the coarse-graining width, see [WLT13] and section 6.3.

Next, the coarse-grained (CG) macroscopic momentum density is defined by

$$\vec{p}(\vec{r},t) = \sum_{i=1}^{N} m_i \vec{v}_i \mathcal{W}(\vec{r} - \vec{r}_i), \tag{32}$$

so that the macroscopic velocity field is defined as the ratio of momentum and density fields,

$$\vec{V}(\vec{r},t) = \vec{p}(\vec{r},t)/\rho(\vec{r},t). \tag{33}$$

Substituting (31) and (33) into (30a) and simplifying shows that the continuity equation is indeed satisfied, as shown in [Gol10, Bab97].

Finally, we consider the momentum conservation equation with the aim of establishing the macroscopic stress field, $\underline{\underline{\sigma}}$. We split the stress

$$\underline{\underline{\sigma}} = \underline{\underline{\sigma}}^k + \underline{\underline{\sigma}}^c, \tag{34a}$$

into its kinetic and contact contributions,

$$\underline{\underline{\sigma}}^k = \sum_{i=1}^{N} m_i \vec{v}_i' \otimes \vec{v}_i' \mathcal{W}(\vec{r} - \vec{r}_i), \tag{34b}$$

$$\underline{\underline{\sigma}}^c = -\sum_{i=1}^{N} \sum_{j=1}^{N+N_w} \vec{f}_{ij} \otimes \vec{l}_{ij} \int_0^1 \mathcal{W}(\vec{r} - \vec{r}_i + s\vec{l}_{ij})\,\mathrm{d}s, \tag{34c}$$

with interaction forces $\vec{f}_{ij} = -\vec{f}_{ji}$ and center-contact vectors $\vec{l}_{ij} = \vec{r}_i - \vec{c}_{ij}$, where $\vec{c}_{ij}$ denotes the contact point between the particle i and particle/wall j and where the indices $N+1$ to $N+N_w$ denote contacts with external objects. Further, the fluctuation velocity of particle i is defined by

$$\vec{v}_i'(\vec{r},t) = \vec{v}_i(t) - \vec{V}(\vec{r},t), \tag{35}$$

and the external interaction force density (IFD) is defined as

$$\vec{t} = \sum_{i=1}^{N} \sum_{k=N+1}^{N+N_e} \vec{f}_{ij} \mathcal{W}(\vec{r} - \vec{c}_{ij}). \tag{36}$$

Substituting (34-36) into (30b) shows that momentum conservation is exactly satisfied. Thus, the results are valid even for single particles and at one moment in time, as no ensemble averaging is required to satisfy the mass and momentum balance. This was first shown in [Gol10] without considering body forces and external forces, and in [WTLB12b] for the full system. One can continue to define other fields in this fashion, such as heat flux and internal energy from the energy equation [Bab97], and the couple stress from the conservation of local angular momentum [Gol10].

The definition of the stress tensor (34c) was shown to be unique under additional symmetry requirements [WAD95]. Note that one can perform the integration in (34c) analytically and obtain an explicit expression, hence the computational cost of this formula is not more expensive than other expressions. Further note that the integral of (34) over the whole volume V satisfies the virial definition of mechanical stress in a volume V,

$$\underline{\underline{\sigma}} = \frac{1}{V} \left(\sum_{i=1}^{N} m_i \vec{v}_i' \otimes \vec{v}_i' - \sum_{i=1}^{N} \sum_{j=1}^{N+N_w} \vec{f}_{ij} \otimes \vec{l}_{ij} \right). \tag{37}$$

Averaging over a time interval Δt and replacing the temporal average over the force vector $\vec{f}_{ij}$ by the change of momentum $\Delta \vec{p}_{ij}$ for each collision of particle i with particle/wall j in the time interval Δt, one obtains for hard spheres [LM98, Lud98]

$$\bar{\underline{\underline{\sigma}}} = \frac{1}{V \Delta t} \left(\int_{t}^{t+\Delta t} \sum_{i=1}^{N} m_i \vec{v}_i' \otimes \vec{v}_i' \, \mathrm{d}t - \sum_{i=1}^{N} \sum_{j=1}^{N+N_e} \Delta \vec{p}_{ij} \otimes \vec{l}_{ij} \right), \tag{38}$$

which connects the soft DEM models with the rigid ED models also on the macroscopic level.

6 Granular chute flow

Granular chute flows are investigated as first exemplary case, in the steady, continuous inertial flow regime. The system, its flow-states and a closure for a shallow-layer continuum model were described in more detail in [WTLB12a, WHTL13, TWLB12a, TWOL13].

The following is a brief review of the more detailed results presented in [WHTL13]. Here, we describe the system setup and parameters in subsections 6.1 and 6.2. In subsection 6.3, we investigate the sensitivity of the macroscopic fields on the width w. Finally we discuss the resulting rheology in subsections 6.4 and 6.5.

6.1 Model system

A Cartesian coordinate system is used where x denotes the flow direction, y the in-plane vorticity direction, and z the height direction normal to the base. The parameters of the system are non-dimensionalized such that the particles' diameter is $\tilde{d} = 1$, their mass is $\tilde{m} = 1$, and the magnitude of gravity is $\tilde{g} = 1$, so that the unit of time becomes $t_u = \sqrt{d/g}$. For the sake of simplicity, the tilde indicating dimensionless quantities is now dropped. The chute is inclined at an angle θ such that gravity acts in the direction $\vec{g} = (\sin\theta, 0, -\cos\theta)^T$. The simulation cell has dimensions 20×10 in the x- and y-directions and is periodic in these directions. The base of the system is a rough surface consisting of N_e fixed particles, see Figure 3 and Ref. [WTLB12a] for details. N monodispersed flowing particles are introduced to the system at random non-overlapping positions well above the base. Due to gravity they fall and accelerate down the slope until they reach a steady state (before $t = 2000$). Macroscopic fields are then extracted and analysed from the steady state data from $t = 2000$ to $t = 2500$.

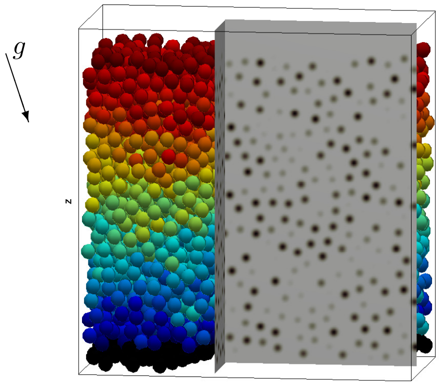

Figure 3: Snapshot of steady-state inertial granular chute flow of $N = 6000$ flowing particles over a rough surface inclined at $\theta = 28°$, with colour indicating speed. The vertical slices show the density $\rho(t, x, y, z)$ using a Lucy function of width $w = 1/2$.

6.2 Material and system parameters

We use a linear viscoelastic normal force model with sliding friction in tangential direction. The dimensionless normal spring and damping constants are $\tilde{k} = 2 \cdot 10^5$ and $\tilde{\gamma} = 50$, respectively; thus, the contact duration for pair collisions is $\tilde{t}_c = 0.005$ and the coefficient of restitution is $r = 0.88$. The tangential spring and damping constants are $k^t/k = 2/7$ and $\gamma^t = \gamma$, such that the frequency of normal and tangential contact oscillation are similar, and the normal and tangential dissipation are comparable. The microscopic friction coefficient is set to $\mu_d = \mu_s = 0.5$. Contacts between two flowing particles and between flowing and fixed base particles are treated equally. The system is integrated using the Velocity-Verlet algorithm with a time step of $dt = t_c/50$. The simulations are implemented in MercuryDPM [TKdV$^+$13, TKF$^+$13, TWT].

6.3 Scale dependence of the macroscopic fields

Depth profiles for steady uniform flow are obtained using a Lucy coarse-graining function of width w, and averaging over $x \in [0, 20]$, $y \in [0, 10]$, and $t \in [2000, 2500]$. The spatial averaging is done analytically, while we average in time with snapshots taken every $t_c/2$.

The macroscopic fields can vary strongly with w, which therefore has to be carefully selected. According to Goldenberg *et al.* [GAC$^+$06], each well-defined macroscopic field should yield a plateau for a range of w-values, where the field (ideally) does not depend on the coarse-graining scale w. For smaller w-values, statistical fluctuations are strong and longer time-averaging or ensemble-averaging is required to obtain useful data. For larger w, the coarse-graining is expected to cause an unphysical smoothing of the field gradients.

Figure 4 shows the volume fraction profile, $\nu(z) = \rho(z)/\rho_p$, for different w. A plateau, as described above, exists for all heights in the range $0.0025 \le w \le 0.1$. On this length scale, the volume fraction is nearly independent of z, while oscillations due to layering of the flow can be observed when approaching the base boundary. All other macroscopic fields show a similar plateau.

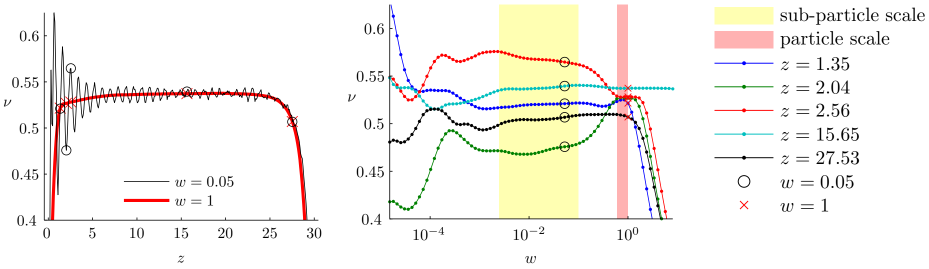

Figure 4: (Left) Density as a function of height, for $w = 0.05$ and $w = 1$. (Right) Density at selected heights as a function of the coarse-graining width w. Circles and crosses in both figures denote the density at the selected heights for $w = 0.05$ and $w = 1$, respectively. Data is taken for $N = 6000$, $\theta = 28°$, as in Ref. [WHTL13].

Further, a second, wider plateau can be observed for $0.6 \le w \le 1$ in the bulk of the flow, further than $2w$ away from the wall. On this scale, the oscillations due to layering are unresolved, which leads to smooth density, velocity and contact stress fields. Only the kinetic stress is scale-dependent, as first shown in [GG01]; however, this scale-dependence can be quantified and removed [WHTL13].

6.4 Stress and boundary conditions

Assuming that the flow is steady and uniform, Eq. (30b) reduces to

$$\frac{\partial}{\partial z}\sigma_{\alpha z} = -\rho g_\alpha - t_\alpha, \quad \alpha = x, y, z, \tag{39}$$

which is in excellent agreement with the stress and external force density profiles [58].

Eq. (39) is called the lithostatic stress relation, since it determines (three) stress components in terms of the density ρ. Since the external interaction force density, $\vec{t}$, is zero everywhere except within an coarse-graining length distance from the basal surface, the slope of $\sigma_{\alpha z}$ equals $-\rho g_\alpha$ everywhere except near the base boundary. Due to the momentum balance (39), both the bulk friction, $\mu = -\sigma_{xz}/\sigma_{zz}$, and the friction due to the interactions with the base, $-t_x/t_z$, are equal to $\tan\theta$ and thus constant for all heights. Further, in all simulations, the stress tensor was found to be nearly symmetric, with the asymmetric part contributing less than 0.1% to the deviatoric stress components.

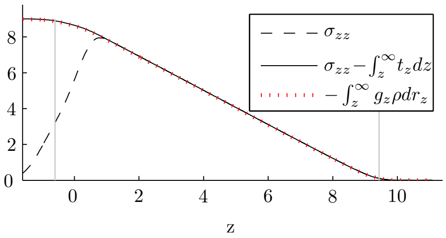

Figure 5: Downward normal stress, see inset, without (dashed) and with (solid) correction by the external IFD for $w = 1/4$. The extended stress, $\sigma'_{zz} = \sigma_{zz} - \int_z^\infty t_z \, dz$, defined in (40) exactly matches the weight of the flow above height z (red dotted line), as expected for steady flows. Grey vertical lines indicate bed and surface location, calculated using the points where the extended stress definition vanishes and reaches its maximum value (to within 2%), as in Ref. [WTLB12a].

Since the external interaction force density, $\vec{t}$, is zero everywhere except close to the basal surface, the gradients of $\vec{t}$ and $\underline{\underline{\sigma}}$ are very steep at the base. Thus, $\vec{t}$ should be incorporated into the continuum equation as a boundary condition rather than a continuous field [WHTL13]. To accomplish this, we introduce the *extended stress*,

$$\sigma_{\alpha z}^{\text{ext}} = \sigma_{\alpha z} + \int_z^\infty t_{\alpha z} \mathrm{d}z \;, \tag{40}$$

which yields the boundary condition,

$$\lim_{z \to -\infty} \sigma_{\alpha z}^{\text{ext}} = \int_{-\infty}^{\infty} t_{\alpha z} \mathrm{d}z \; . \tag{41}$$

Substituting (39) into (40) thus yields a simple relation between stress and density,

$$\sigma_{\alpha z}^{\text{ext}} = \int_{z}^{\infty} \rho g_{\alpha} \mathrm{d}z, \quad \lim_{z \to -\infty} \sigma_{\alpha z}^{\text{ext}} = \int_{-\infty}^{\infty} \rho g_{\alpha} \mathrm{d}z = N m g_{\alpha}, \tag{42}$$

which produces a smooth extended stress field, as shown in Figure 5.

6.5 Inertial number

A widely accepted basic rheological model for granular flows – in the dense, quasi-static and inertial regimes – is the so-called $\mu(I)$-rheology [dCEP$^+$05, IK04, MiD04, JFP06]. Many experimental and numerical studies suggest that the mass density ρ and the macroscopic (bulk) friction μ are functions of the inertial number,

$$I = \dot{\gamma} d \sqrt{\rho_p / p}, \tag{43}$$

where $\dot{\gamma} = \frac{\partial V_x}{\partial z}$ is the shear rate, d the particle diameter, p the (compressive) pressure and ρ_p the particle density, which is assumed constant for all heights.

Deriving the shear rate profile from the velocity field, we plot the inertial number as a function of height in Figure 6. It shows that the inertial number is indeed constant in the bulk, but varies significantly near both base and surface. Thus, we define the bulk of the flow to be the region where I is within 10% of the median value.

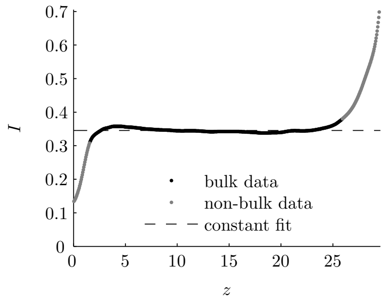

Figure 6: Inertial number plotted as a function of height, for $w = 1$, $\theta = 28°$ and $N = 6000$, The dashed line shows the constant inertial number as predicted by the $\mu(I)$ rheology.

6.6 An objective description of the stress tensor

Next, we generalise the $\mu(I)$ rheology from a Cartesian frame to a rheological model for general flow situations by using (objective) invariants of the tensors, and quantify all non-Newtonian mechanisms that the chute flow features.

For a symmetric stress, when the σ_{xy}, σ_{yz} components are close to zero in steady state, the orientation of the deviatoric stress tensor is determined solely by measuring the orientation ϕ_σ of the largest principal stress in the xz-plane. Then the stress takes the form [WHTL13, HGWL12]

$$\underline{\underline{\sigma}} = p\underline{\underline{I}} + \underline{\underline{R}} \cdot \begin{pmatrix} \lambda_1 & 0 & 0 \\ 0 & \lambda_2 & 0 \\ 0 & 0 & \lambda_3 \end{pmatrix} \cdot \underline{\underline{R}}^T, \tag{44}$$

with the transformation matrix

$$\underline{\underline{R}} = \begin{pmatrix} \cos\phi_\sigma & 0 & \sin\phi_\sigma \\ 0 & 1 & 0 \\ -\sin\phi_\sigma & 0 & \cos\phi_\sigma \end{pmatrix} \tag{45}$$

where the second term is the deviatoric stress, with $\lambda_1 + \lambda_2 + \lambda_3 = 0$. To quantify the anisotropy of the stress tensor, we further decompose the deviatoric stress into: (*i.*) the "anisotropy" of the deviatoric stress, i.e. the ratio of deviatoric stress (norm) and pressure,

$$s_D^\star := \frac{1}{\sqrt{6}p}\sqrt{(\lambda_1-\lambda_2)^2 + (\lambda_2-\lambda_3)^2 + (\lambda_3-\lambda_1)^2}\,, \tag{46a}$$

see Ref. [TML]. (*ii.*) the anisotropic stress distribution between the principal directions,

$$\Lambda_{12} := -\lambda_2/\lambda_1, \tag{46b}$$

and (*iii.*) the orientation of its eigensystem,

$$\Delta\phi := \phi_\sigma - \phi_\epsilon, \tag{46c}$$

where $\phi_\epsilon = 45^\circ$ denotes the orientation angle of the strain rate tensor.

Thus, three objective variables are obtained that fully describe the deviatoric stress tensor and thus determine the flow behaviour. For isotropic flows, we recover the original $\mu(I)$ rheology where $\Delta\phi_\sigma = 0$, $\Lambda_{12} = 0$, $\sigma_{zz}/p = 1$ and $s_D^\star = \mu(I)$.

Simulation results show that the flow rheology is indeed well-described by the inertial number, as shown in figure 7. The anisotropy $s_D^\star$, follows a similar curve as the Cartesian bulk friction μ and is therefore fitted by the curve described in [MiD04]. However, the results show clearly, that non of the Newtonian flow assumptions is satisfied. Λ_{12} deviates from their respective Newtonian values even for small inertial numbers, while $\Delta\phi_\sigma$ deviates from zero with increasing inertial number. Remarkably, the simple $\mu(I)$-rheology represents the dominant mechanism, while the others are relatively small. A generalization for other flow situations is in progress [KLM14, KIML13].

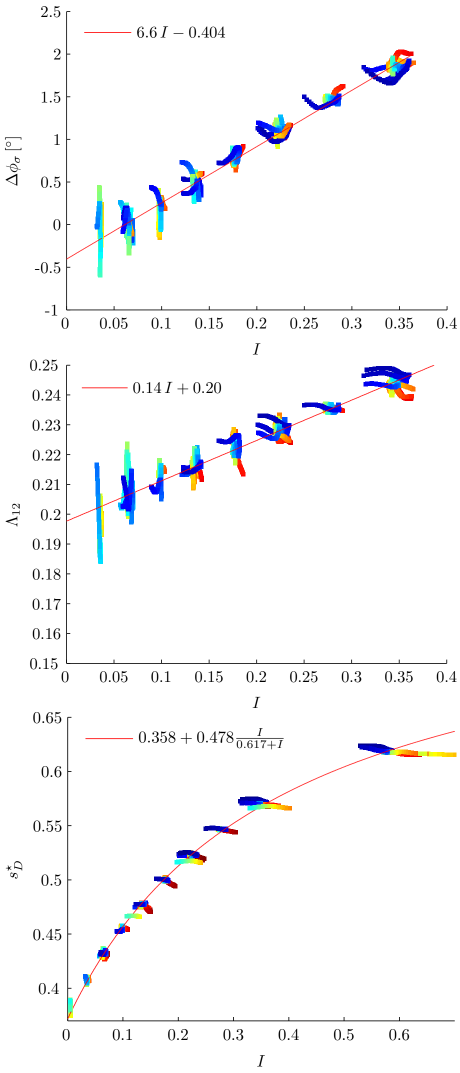

Figure 7: Three objective variables that describe the deviatoric stress tensor, are plotted against the inertial number I. Shade/color indicates relative height z from bottom (blue) to top (red). Lines indicate fits to the bulk data as specified in the insets/keys. *Top:* Angular deviation of the deviatoric stress from collinearity with the strain rate tensor, $\Delta\phi_\sigma$, with linear fit. *Middle:* Ratio of eigenvalues Λ_{12} with linear fit. *Bottom:* Magnitude of the deviatoric stress ratio, $s_D^\star$, with the line a fit to the bulk data. Data are bulk values from steady simulations in the parameter range $4000 \leq N \leq 8000$, $20^\circ \leq \theta \leq 28^\circ$, with coarse graining width $w = 1$, using the reduced kinetic stress [WHTL13].

6.7 Summary

In summary, the micro-macro transition has been successfully applied to steady, inertial granular flows down an inclined plane. The fields are well defined (almost independent of w) if the coarse-graining length-scale w is chosen carefully, either on the particle scale $w \sim 1$ or on the sub-particle resolution scale $w \sim 0.05$. We discussed the macroscopic fields and showed how to interpret the external interaction force density $\vec{t}$ as a boundary condition. The simulation results were then analysed to obtain an objective and complete tensorial rheological model for steady, planar non-Newtonian granular flows, involving all further non-Newtonian mechanisms (as possible in this situation) on top of the classical $\mu(I)$-rheology.

7 Vibrated granular bed

Our second example consists of a vertically vibrated bed of grains. In this case we take the limit of hard-spheres and compare the macroscopic states obtained by ED simulations with both previous experimental realizations and DEM simulations. We compute the macroscopic fields of packing fraction, pressure and temperature from both ED and DEM simulations using different coarse-graining methods. We then study their agreement as a function of the DEM collision time parameter t_c. Even though the system presents highly packed regions, it is expected that the hard particle approximation does not have a big influence on the observed dynamics, as the system is constantly fluidized, thus minimizing the influence of multi-particle contacts. Indeed, a very good agreement between simulations and experiments is found, as also between the macroscopic fields of both simulation approaches, given that a low enough collision time (high enough stiffness) is used in the DEM simulations.

7.1 Model system

The system consists of a quasi-two-dimensional vibrated box with a base of variable width l_x, depth $l_y = 5d$ and infinite height, with d the diameter of the particles. The container is vibrated sinusoidally such that the position of the base is given by $b(t) = A\sin(\omega t)$, with A and ω our parameters of energy injection. Previous experimental and numerical studies have revealed a variety of non-equilibrium stable states, dependent mainly on the amount of energy injection [TMLS89, EvdWvdM$^+$07, RLT13]. Here we focus on the high energy injection limit, where a density inverted and horizontally homogeneous state is present, usually referred to as granular Leidenfrost state [EvdWvdML05]. We restrict our study to this state as it combines a high temperature gaseous state with a low temperature dense state, two adequate limits to test the micro-macro transition approaches and to compare the soft and hard MD models. Previous studies have revealed that the phase-space in this high energy limit is better represented by the dimensionless shaking strength $S \equiv A^2\omega^2/gd$, and the number of filling layers $F \equiv Nd^2/l_x l_y$.

Collisions between particles are determined by a normal coefficient of restitution in ED simulations, $r_{ED} = 0.9$. In the DEM case we use the linear spring-dashpot model (see Eq. (3)), and set the stiffness k and viscous damping γ_0 by choosing t_c, the typical collision time, and r, the coefficient of restitution, as given by Eqs. (4) and (5). Naturally, we set $r = r_{ED}$, and t_c is left as a free parameter. Lateral walls are considered rigid and having the same collision parameters than between particles in both types of simulations.

7.2 Experimental comparison

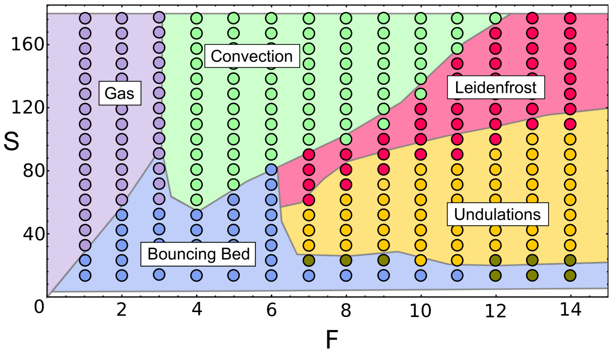

Figure 8: Phase space of the wide $l_x = 100d$ box geometry, for $A = 4.0d$ and variable ω. Circles correspond to ED simulations, while background is taken from experiments presented in [EvdWvdM$^+$07], where also the different states are carefully described.

As a first step of validation, ED simulation results are compared with previous experimental work done in a wide container [EvdWvdM$^+$07], $l_x = 100d$. In this case we account for friction with a fixed coefficient $\mu = 0.1$. The wide system presents many distinct non-homogeneous stable states in the S-F space. For a detail analysis of all states see Ref. [EvdWvdM$^+$07]. Here we remark that ED simulations are able to capture all observed behaviours, as shown in Fig. 8. Quantitatively, the phase space obtained from ED simulations shows a remarkable agreement with the experimental one, although there is a noticeable disagreement for some regions of transition. The source of these disagreements can come from many factors: different effective restitution and friction coefficients, the method for defining the different regions, as also physical relevance of effects ignored in simulations, such as interstitial air or grain-grain attractive forces.

7.3 Leidenfrost state

Having verified that ED simulations are in good agreement with physical experiments, we now turn our attention to the relation of both simulational methods, ED and DEM. The macroscopic states are compared by computing the packing fraction ϕ; the kinetic pressure $p = \mathrm{tr}(\underline{\underline{\sigma}}^k)/3$, with the kinetic stress tensor defined in (34b); and the granular temperature $T = \frac{1}{3}(\langle \vec{v}^2 \rangle - \langle \vec{v} \rangle^2)$. The system is further constrained by setting $l_x = 5.0d$, as we are only interested in studying the horizontally homogeneous Leidenfrost state. In this limit all horizontally inhomogeneous states are suppressed, including the buoyancy-driven convective states expected for higher S [RLT13]. Furthermore, we set $F = 12$ (which implies a total number of particles $N = 300$) and $A = 1.0d$.

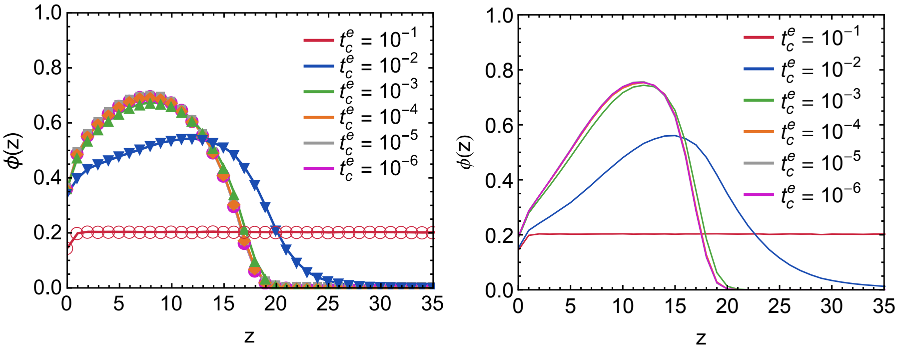

Figure 9: Time averaged packing fraction profiles $\phi(z)$ for different t_c^e, as specified in the labels, with $A = 1.0d$ and $\omega = 2.0\sqrt{g/d}$ (left), and $\omega = 5.0\sqrt{g/d}$ (right). For values of $t_c^e \leq 10^{-4}$ curves are seen to converge and are superimposed.

In ED simulations the TC model is used, both to prevent inelastic collapse and compare with the finite collision time of DEM simulations, as elaborated in Section 4. As t_c^e is reduced, the macroscopic fields converge, as shown in Figure 9 for the averaged packing fraction vertical profile, $\phi(z)$. There is no significant difference between the low and high energy injection limits, both converging for $\tau_c \sim 10^{-5}$, the value taken for the following simulations.

It is important to remark that macroscopic fields are not computed using the same procedure; it is also the purpose of the following work to see how both approaches compare. In the ED case, instantaneous macroscopic fields are obtained by coarse graining space in rectangular bins and computing the relevant quantities by averaging over the bins; after that, time-average is done for at least 10000 oscillation cycles. On the other hand, in DEM simulations the fields are obtained using the homogenization procedure described in Section 5, and with more detail in [WTLB12a]. The homogenization is done for the relevant quantities of density and momentum, from which the other fields can be directly obtained. Then, time-averaged totals can be obtained either as an average of each instantaneous field, or from the time-averaged fields of velocity and density; in our case, we choose the latter method, except with the temperature field where both approaches are compared, as they present significant differences. In both cases, care is taken to acquire data with a sub-period resolution of $0.05T$, in order to prevent aliasing errors.

Figure 10 shows the time averaged vertical profiles $\langle\phi(z)\rangle_t$, $\langle P(z)\rangle_t$ and $\langle T(z)\rangle_t$ for both ED and DEM simulations with $S = 100$. The collision time t_c is modified in order to see how macroscopic fields depend on it. They correspond to 5, 10, to 50 times the collision time, for $t_c = 0.1$, $t_c = 0.05$ and $t_c = 0.01$, respectively.

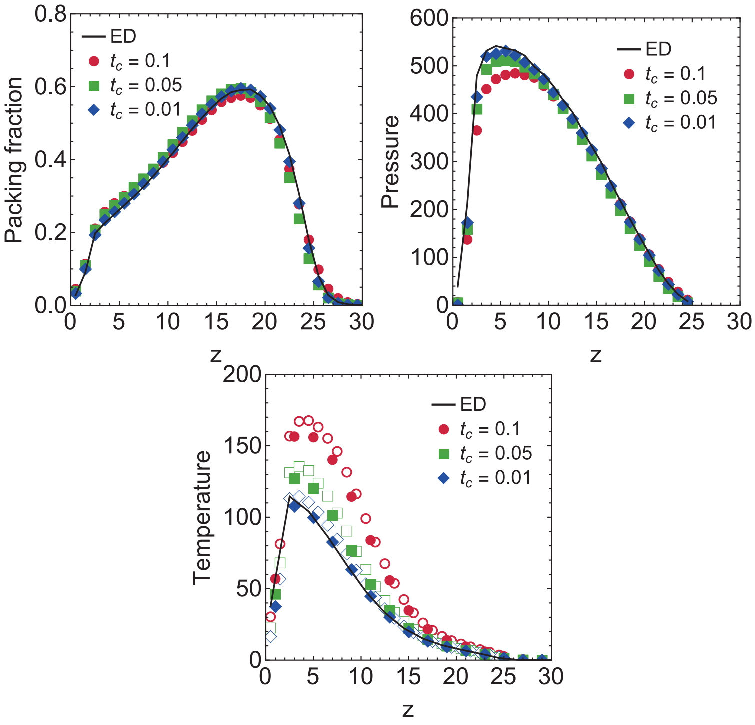

Figure 10: (a) Time averaged packing fraction vertical profiles for ED simulations (black) and soft-particle simulations with $t_c = 0.1$ (red circles), $t_c = 0.05$ (green squares) and $t_c = 0.01$ (blue diamonds). (b) Time averaged pressure vertical profiles, with the same color code. (c) Time averaged granular temperature vertical profiles, with the same color code. Open symbols corresponds to the fluctuating time-averaged velocities, while filled ones show the time-averaged fluctuating velocity, as detailed in the main text.

Remarkably, the packing fraction fields coincide to within 0.1% already for $t_c = 0.05$. The profiles are remarkably similar even for high t_c, although the effect of decreasing the collision time is considerable, specially in highly packed regions, as also near the bottom of the container, that is, in the highly agitated region. At the bottom of the container, softer particles would over predict the time of collision with the fast moving bottom plate, and thus a low t_c is needed to approach the hard sphere limit.

The total pressure, on the other hand, presents a more pronounced difference for higher values of t_c, although there is already only a 3% disagreement between both schemes for $t_c = 0.05$. Reducing t_c further leads to a better overall agreement, although the pressure in the gaseous zone is still considerably lower than in the hard-sphere limit.

The temperature field presents a considerably higher disagreement between ED and MD simulations for higher values of t_c. This could be due to many factors. Mainly, the time-averaging of the fields in the SP case may have a big influence on a highly fluctuating quantity such as temperature. The fluctuations come mainly from the dependency on the inverse of density, which can have very low values instantly, but not in the long time average. The difference between the different time average schemes is shown in dashed and solid lines, respectively: it is clear that computing the temperature at each frame from the density and velocity fields, and then averaging over the whole simulation, leads to a better agreement for all t_c (Figure 10c). Nevertheless, both profiles always present the same overall behaviour, and the agreement is again good for $t_c = 0.001$.

7.4 Summary

In the case of collisional systems, with rather high packing fractions, ED simulations present a surprisingly good agreement with previous experiments of a highly agitated granular bed, and also agree very well with DEM simulations with rather hard particles. A low enough t_c is needed to accurately match the conserved hydrodynamic fields, especially when different time-averaging schemes play a role, such as with the granular temperature. It is important to remark that even though the density and pressure can present remarkably similar profiles for a given t_c, the corresponding temperature field can be considerably over-predicted in DEM simulations. Overall, we see that the hard-particle limit and event-driven simulations present an excellent alternative for the simulation of fluidized, yet quite dense, granular systems, usually being orders of magnitude faster than DEM simulations.

8 Discussion and Conclusion

A summary of soft particle molecular dynamics (referred to as discrete element methods (DEM) in some fields of engineering), and hard particle event-driven (ED) simulations was given. The two approaches were compared in various situations, from dilute/collisional to dense, inertial chute flows. The less dynamic, quasi-static regimes are addressed in Refs. [TML, DS]. In the dilute regime both methods are identical while in denser situations, the finite contact duration time and multi-particle contacts become relevant. Those contacts are readily modeled in DEM, see also Ref. [Mar], but not in ED. An extension of ED involves a new time-scale over which collisions between particles are considered elastic, both to avoid the divergence of the number of collisions per unit time and to model the natural fact of finite collision times, an approach referred to as the TC (time/duration of contacts) model. An alternative simulation method is contact dynamics (CD), which was addressed in Ref. [Rad]. Furthermore, a methodology for relating the particle properties from particle simulations to the state variables and fields in continuum models has been presented, with more details and practical exercises presented in Ref. [TWT]. This micro-macro transition was defined for the density, velocity, velocity gradient, stress and temperature fields via the coarse graining approach, which ensures that mass, momentum and energy balance are exactly preserved. Additional fields like the structure tensor (fabric), couple-stress, rotations, and curvature were not considered here but are subject of ongoing research.

Given any type of particle simulation method, DEM, ED, CD or others, but also given experimental data, the coarse-graining procedure to obtain conserved fields from particle simulations depends on a critical parameter w, the length-scale of the kernel (smoothing) function. Using granular flows down an inclined plane as reference system, we have observed that the choice of w for a particular system can be justified by determining its scale-dependence, and identifying scales that are insensitive to the choice of w. Similarly, coarse-graining in time requires a similar approach with a time-scale t_w. Furthermore, an interaction force density has been introduced, that can capture the boundary conditions of the bulk flow, as well as drag relations with other constituents in a mixed flow (not shown, data to be presented elsewhere). Situations where the w- or t_w-dependence persists (in either space or time, or both) can relate to either flows with micro-structure or transients and are subject to ongoing studies. Note that the micro-macro methodology is valid, but such cases will display strong fluctuations and require further research.

Given one has a steady state situation with a w-independent plateau, one can proceed further and accumulate continuum fields with good statistics and quality from a single simulation. The methodology permits the definition of a complete (tensorial) rheological model for steady, planar non-Newtonian granular flows from particle simulations. The stress is decomposed as: *(i)* the isotropic pressure, *(ii)* the *anisotropy*, i.e., the ratio of deviatoric stress and pressure, *(iii)* the anisotropic stress distribution between the principal directions, and *(iv)* the difference in orientation of tensor eigen-systems. Using the coarse graining methodology in a chute-flow system, we have seen that the rheology deviates from a Newtonian fluid behaviour not only due to its pressure- and strain-rate-dependent viscosity (the well-known macroscopic friction referred to as the $\mu(I)$-rheology), but also has a non-trivial anisotropic stress distribution and a slight lag between the orientation of the stress and the strain rate tensor. These effects need to be taken into account for any truly quantitative prediction of granular flow behaviour; even though being small for chute flows, we expect them to be more important in other situations as, e.g., situations with strain reversal and transient regimes.

Hard-sphere, event-driven (ED) simulations were compared with both previous experimental realizations and soft-particle simulations of a highly agitated granular bed. ED simulations are able to capture the whole spectrum of behaviors observed in the quasi-two-dimensional vibrated system as the energy is increased, from low to very high energy inputs, the phase-space even presenting good quantitative agreement. The TC model, an approach to solve the inelastic collapse problem and model the softness, i.e. the finite collision times, with perfectly hard spheres, was studied in this highly agitated limit, and the parameters needed to obtain convergence were determined. In such situations, ED and DEM simulation approaches coincide remarkably well in their macroscopic fields, given that a low enough collision time is set in DEM simulations, especially for the computation of the most sensitive field: the granular temperature.

In conclusion, discrete element methods (soft or hard) are a helpful tool to understanding many granular, particulate, powder or geo-materials. The same ideas and methods can also be applied to atomistic systems [HGWL12, HTL13]. The micro-macro methods presented in this paper can be applied to both DEM and ED simulation results, but also to CD or experimental data. The overall goal to obtain micro- and particle-based constitutive relations for continuum theory has seen many success-stories but not all challenges have been addressed so far and many open questions remain. The qualitative approach of using DEM in the early years has now developed into the attempt of a quantitative predictive modelling tool for the diverse modes of complex momentum and energy transport in granular media, industrial and natural, environmental processes and phenomena. To achieve the goal of a micro-based macro-theory will remain a research challenge for the next decade, involving enhanced kinetic theories for dense collisional flows and elaborate constitutive models for quasi-static, dense systems with, e.g., shear band localisation. In the future this will allow to better understand, to better design/optimize and to impose the desired behavior, with particular applications in mind as, e.g., modern sintered materials, reactors involving catalysts, tabletting, selective laser-sintering, and many others. This concerns not only man-made processes and flows but also natural phenomena like avalanches, land-slides or civil engineering issues like slow creep or instabilities of foundations.

Acknowledgements
Special thanks to V. Richefeu for proofreading and K. Taghizadeh with helping to assemble, format, edit this and the other papers for this ALERT course. Financial support is acknowledged from NWO, STW, FOM (the Netherlands), and DFG (Germany).

References

[AT87] M. P. Allen and D. J. Tildesley. *Computer Simulation of Liquids*. Oxford University Press, Oxford, 1987.

[Bab97] M. Babic. Average balance equations for granular materials. *International Journal of Engineering Science*, 35(5):523–548, 1997.

[BSL11] M. N. Bannerman, R. Sargant, and L. Lue. DynamO: a free $o(n)$ general event-driven molecular dynamics simulator. *Journal of Computational Chemistry*, 32(15):3329–3338, November 2011.

[BUK$^+$05] G. Bartels, T. Unger, D. Kadau, D. E. Wolf, and J. Kertesz. The effect of contact torques on porosity of cohesive powders. *Granular Matter*, 7:139, 2005.

[CR] G. Combe and J.-N. Roux. Good practice and sample preparation - construction of granular packings. *ALERT geomaterials Doctoral School 2017, Aussois, France*.

[dCEP$^+$05] Frdric da Cruz, Sacha Emam, Michal Prochnow, Jean-Nol Roux, and Franois Chevoir. Rheophysics of dense granular materials: Discrete simulation of plane shear flows. *Physical Review E*, 72(2):021309, 2005.

[DS] F.-V. Donzé and L. Scholtés. Predicting the strength of anisotropic shale rock: empirical nonlinear failure criterion vs. Discrete Element Method. *ALERT geomaterials Doctoral School 2017, Aussois, France*.

[DvZTR05] E. Dintwa, M. van Zeebroeck, E. Tijskens, and H. Ramon. Torsion of viscoelastic spheres in contact. *Granular Matter*, 7:169, 2005.

[Els06] Danie Els. Definition of roll velocity for spherical particles. submitted, 2006.

[EvdWvdM$^+$07] P. Eshuis, K. van der Weele, D. van der Meer, R. Bos, and D. Lohse. Phase diagram of vertically shaken granular matter. *Physics of Fluids*, 19(12):123301, 2007.

[EvdWvdML05] P. Eshuis, K. van der Weele, D. van der Meer, and D. Lohse. Granular leidenfrost effect: Experiment and theory of floating particle clusters. *Physical Review Letters*, 95(25), December 2005.

[GAC$^+$06] C. Goldenberg, A. P. F. Atman, P. Claudin, G. Combe, and I. Goldhirsch. Scale separation in granular packings: Stress plateaus and fluctuations. *Physical Review Letters*, 96(16), 2006.

[GG01] B. J. Glasser and I. Goldhirsch. Scale dependence, correlations, and fluctuations of stresses in rapid granular flows. *Physics of Fluids*, 13(2):407–420, 2001.

[Gol10] I. Goldhirsch. Stress, stress asymmetry and couple stress: from discrete particles to continuous fields. *Granular Matter*, 12(3):239–252, 2010.

[Haf83] P. K. Haff. Grain flow as a fluid-mechanical phenomenon. *J. Fluid Mech.*, 134:401–430, 1983.

[HGWL12] Remco Hartkamp, A. Ghosh, Thomas Weinhart, and Stefan Luding. A study of the anisotropy of stress in a fluid confined in a nanochannel. *Journal of Chemical Physics*, 137(4), 2012.

[HHL98] H. J. Herrmann, J.-P. Hovi, and S. Luding, editors. *Physics of dry granular media - NATO ASI Series E 350*, Dordrecht, 1998. Kluwer Academic Publishers.

[HTL13] R. Hartkamp, B. D. Todd, and S. Luding. A constitutive framework for the non-newtonian pressure tensor of a simple fluid under planar flows. *Journal of Chemical Physics*, 138(24), 2013.

[HW04] H. Hinrichsen and D. E. Wolf. *The Physics of Granular Media*. Wiley VCH, Weinheim, Germany, 2004.

[IK50] J. H. Irving and J. G. Kirkwood. The statistical mechanical theory of transport processes .4. the equations of hydrodynamics. *Journal of Chemical Physics*, 18(6):817–829, 1950.

[IK04] I. Iordanoff and M. M. Khonsari. Granular lubrication: Toward an understanding of the transition between kinetic and quasi-fluid regime. *Journal of Tribology*, 126(1):137–145, 2004.

[JFP06] Pierre Jop, Yol Forterre, and Olivier Pouliquen. A constitutive law for dense granular flows. *Nature*, 441(7094):727–730, 2006.

[JR85] J. T. Jenkins and M. W. Richman. Kinetic theory for plane shear flows of a dense gas of identical, rough, inelastic, circular disks. *Phys. of Fluids*, 28:3485–3494, 1985.

[KBG49] J. G. Kirkwood, F. P. Buff, and M. S. Green. The statistical mechanical theory of transport processes. *J. Chem. Phys.*, 17(10):988, 1949.

[KIML13] N. Kumar, O. I. Imole, V. Magnanimo, and S. Luding. Evolution of the effective moduli for anisotropic granular materials during pure shear. In *AIP Conference Proceedings*, volume 1542, pages 1238–1241. AIP Publishing, June 2013.

[Kis01] Y. Kishino, editor. *Powders & Grains 2001*, Rotterdam, 2001. Balkema.

[KLM14] N. Kumar, S. Luding, and V. Magnanimo. Macroscopic model with anisotropy based on micro-macro information. *Acta Mechanica*, 225:2319–2343, 2014.

[KOL14] Dinant Krijgsman, Vitaliy Ogarko, and Stefan Luding. Optimal parameters for a hierarchical grid data structure for contact detection in arbitrarily polydisperse particle systems. *Computational Particle Mechanics*, 1(3):357–372, 2014.

[LAM11] Stefan Luding and Fernando Alonso-Marroquin. The critical-state yield stress (termination locus) of adhesive powders from a single numerical experiment. *Granular Matter*, 13(2):109–119, 2011.

[LCB$^+$94a] S. Luding, E. Clément, A. Blumen, J. Rajchenbach, and J. Duran. Anomalous energy dissipation in molecular dynamics simulations of grains: The “detachment effect”. *Phys. Rev. E*, 50:4113, 1994.

[LCB$^+$94b] S. Luding, E. Clément, A. Blumen, J. Rajchenbach, and J. Duran. The onset of convection in molecular dynamics simulations of grains. *Phys. Rev. E*, 50:R1762, 1994.

[LCRD96] S. Luding, E. Clément, J. Rajchenbach, and J. Duran. Simulations of pattern formation in vibrated granular media. *Europhys. Lett.*, 36(4):247–252, 1996.

[LG03] S. Luding and A. Goldshtein. Collisional cooling with multiparticle interactions. *Granular Matter*, 5(3):159–163, 2003.

[LH99] S. Luding and H. J. Herrmann. Cluster growth in freely cooling granular media. *Chaos*, 9(3):673–681, 1999.

[LHMZ98] S. Luding, M. Huthmann, S. McNamara, and A. Zippelius. Homogeneous cooling of rough dissipative particles: Theory and simulations. *Phys. Rev. E*, 58:3416–3425, 1998.

[LLH01] S. Luding, M. Lätzel, and H. J. Herrmann. From discrete element simulations towards a continuum description of particulate solids. In A. Levy and H. Kalman, editors, *Handbook of Conveying and Handling of Particulate Solids*, pages 39–44, Amsterdam, The Netherlands, 2001. Elsevier.

[LM98] S. Luding and S. McNamara. How to handle the inelastic collapse of a dissipative hard-sphere gas with the TC model. *Granular Matter*, 1(3):113–128, 1998. e-print cond-mat/9810009.

[LMM05] S. Luding, K. Manetsberger, and J. Muellers. A discrete model for long time sintering. *Journal of the Mechanics and Physics of Solids*, 53(2):455–491, 2005.

[Lub91] B. D. Lubachevsky. How to simulate billards and similar systems. *J. Comp. Phys.*, 94(2):255, 1991.

[Lub92] B. D. Lubachevsky. Simulating billiards: Serially and in parallel. *Int.J. in Computer Simulation*, 2:373–411, 1992.

[Lud97] S. Luding. Surface waves and pattern formation in vibrated granular media. In *Powders & Grains 97*, pages 373–376, Amsterdam, 1997. Balkema.

[Lud98] S. Luding. Collisions & contacts between two particles. In H. J. Herrmann, J.-P. Hovi, and S. Luding, editors, *Physics of dry granular media - NATO ASI Series E350*, page 285, Dordrecht, 1998. Kluwer Academic Publishers.

[Lud06] S. Luding. About contact force-laws for cohesive frictional materials in 2d and 3d. In P. Walzel, S. Linz, Ch. Krülle, and R. Grochowski, editors, *Behavior of Granular Media*, pages 137–147. Shaker Verlag, 2006. Band 9, Schriftenreihe Mechanische Verfahrenstechnik, ISBN 3-8322-5524-9.

[Lud07] S. Luding. Contact models for very loose granular materials. In Peter Eberhard, editor, *Symposium on Multiscale Problems in Multibody System Contacts*, pages 135–150. Springer, 2007. ISBN 978-1-4020-5980-3.

[Lud08] S. Luding. Cohesive frictional powders: Contact models for tension. *Granular Matter*, 10:235–246, 2008.

[Lud09] Stefan Luding. Towards dense, realistic granular media in 2d. *Nonlinearity*, 22(12):R101, 2009.

[Mar] C.L. Martin. Advanced contact laws. *ALERT geomaterials Doctoral School 2017, Aussois, France.*

[MiD04] GDR MiDi. On dense granular flows. *The European Physical Journal E*, 14(4):341–365, 2004.

[Mil04] S. Miller. *Clusterbildung in granularen Gasen*. PhD thesis, Universität Stuttgart, 2004.

[ML04a] S. Miller and S. Luding. Cluster growth in two- and three-dimensional granular gases. *Phys. Rev. E*, 69:031305, 2004.

[ML04b] S. Miller and S. Luding. Event driven simulations in parallel. *J. Comp. Phys.*, 193(1):306–316, 2004.

[MY94] S. McNamara and W. R. Young. Inelastic collapse in two dimensions. *Phys. Rev. E*, 50(1):R28–R31, 1994.

[OL13] Vitaliy Ogarko and Stefan Luding. Prediction of polydisperse hard-sphere mixture behavior using tridisperse systems. *Soft Matter*, 9:9530–9534, 2013.

[PL01] T. Pöschel and S. Luding, editors. *Granular Gases*, Berlin, 2001. Springer. Lecture Notes in Physics 564.

[Rad] F. Radjai. The contact dynamics (CD) method. *ALERT geomaterials Doctoral School 2017, Aussois, France.*

[Rap95] D. C. Rapaport. *The Art of Molecular Dynamics Simulation*. Cambridge University Press, Cambridge, 1995.

[RLT13] N. Rivas, S. Luding, and A. R. Thornton. Low-frequency oscillations in narrow vibrated granular systems. *New Journal of Physics*, 15(11):113043, November 2013.

[SML15] A. Singh, V. Magnanimo, and S. Luding. Mesoscale contact models for sticky particles. *arXiv:1503.03720*, 2015.

[SMSL14] Abhinendra Singh, Vanessa Magnanimo, Kuniyasu Saitoh, and Stefan Luding. Effect of cohesion on shear banding in quasistatic granular materials. *Phys. Rev. E*, 90:022202, Aug 2014.

[STS93] M. H. Sadd, Q. M. Tai, and A. Shukla. Contact law effects on wave propagation in particulate materials using distinct element modeling. *Int. J. Non-Linear Mechanics*, 28(2):251, 1993.

[TCC17] Colin Thornton, Sharen J. Cummins, and Paul W. Cleary. On elastic-plastic normal contact force models, with and without adhesion. *Powder Technology*, 315:339 – 346, 2017.

[TED95] B. D. Todd, D. J. Evans, and P. J. Daivis. Pressure tensor for inhomogeneous fluids. *Physical Review E*, 52(2):1627–1638, 1995.

[TKdV$^+$13] A.R. Thornton, D. Krijgsman, A. de Voortwis, O. Orgarko, S. Luding, R. Fransen, S. Gonzalez, O. Bokhove, O. Imole, and T Weinhart. A review of recent work on the discrete particle method at the university of twente: An introduction to the open- source package mercurydpm. In *Discrete Element Methods 6*, 2013.

[TKF$^+$13] Anthony Thornton, Dinant Krijgsman, Rudi Fransen, Sebastian Gonzalez, Deepak Tunuguntla, Ate ten Voortwis, Stefan Luding, Onno Bokhove, and Thomas Weinhart. Mercury-dpm: Fast particle simulations in complex geometries. *EnginSoft Newsletter*, 10(1), 2013.

[TML] K. Taghizadeh, S. Luding, and V. Magnanimo. DEM applied to soil mechanics. *ALERT geomaterials Doctoral School 2017, Aussois, France*.

[TMLS89] B. Thomas, M. O. Mason, Y. A. Liu, and A. M. Squires. Identifying states in shallow vibrated beds. *Powder Technology*, 57(4):267–280, April 1989.

[Tom00] Jürgen Tomas. Particle adhesion fundamentals and bulk powder consolidation. *KONA*, 18:157–169, 2000.

[TWLB12a] A. R. Thornton, T. Weinhart, S. Luding, and O. Bokhove. Frictional dependence of shallow-granular flows from discrete particle simulations. *Eur Phys J E Soft Matter*, 35(12):9804, 2012.

[TWLB12b] Anthony Thornton, Thomas Weinhart, Stefan Luding, and Onno Bokhove. Modeling of particle size segregation: calibration using the discrete particle method. *International Journal of Modern Physics C*, 23(8), 2012.

[TWOL13] Anthony Thornton, Thomas Weinhart, Vitaliy Ogarko, and Stefan Luding. Multiscale modeling of multi-component granular materials. *Computer Methods in Materials Science*, 13:197–212, 2013.

[TWT] D. Tunuguntla, T. Weinhart, and A. Thornton. Discrete particle simulations with MercuryDPM. *ALERT geomaterials Doctoral School 2017, Aussois, France*.

[VDE$^+$01] P. A. Vermeer, S. Diebels, W. Ehlers, H. J. Herrmann, S. Luding, and E. Ramm, editors. *Continuous and Discontinuous Modelling of Cohesive Frictional Materials*, Berlin, 2001. Springer. Lecture Notes in Physics 568.

[VL16] Dalila Vescovi and Stefan Luding. Merging fluid and solid granular behavior. *Soft Matter*, 12:8616–8628, 2016. arXiv:1609.07414.

[WAD95] Eligiusz Wajnryb, Andrzej R. Altenberger, and John S. Dahler. Uniqueness of the microscopic stress tensor. *The Journal of Chemical Physics*, 103(22):9782–9787, 1995.

[WB86] O. R. Walton and R. L. Braun. Viscosity, granular-temperature, and stress calculations for shearing assemblies of inelastic, frictional disks. *J. Rheol.*, 30(5):949–980, 1986.

[WHTL13] Thomas Weinhart, Remco Hartkamp, Anthony R. Thornton, and Stefan Luding. Coarse-grained local and objective continuum description of three-dimensional granular flows down an inclined surface. *Physics of Fluids*, 25(7), 2013.

[WLT13] Thomas Weinhart, Stefan Luding, and Anthony R. Thornton. From discrete particles to continuum fields in mixtures. In *AIP Conference Proceedings*, volume 1542, pages 1202–1205. AIP Publishing, 2013.

[WTLB12a] Thomas Weinhart, Anthony R. Thornton, Stefan Luding, and Onno Bokhove. Closure relations for shallow granular flows from particle simulations. *Granular Matter*, 14(4):531–552, 2012.

[WTLB12b] Thomas Weinhart, Anthony R. Thornton, Stefan Luding, and Onno Bokhove. From discrete particles to continuum fields near a boundary. *Granular Matter*, 14(2):289–294, 2012.

[ZSS91] C. Y. Zhu, A. Shukla, and M. H. Sadd. Prediction of dynamic contact loads in granular assemblies. *J. of Applied Mechanics*, 58:341, 1991.

The contact dynamics (CD) method

F. Radjai

LMGC, UMR 5508, University of Montpellier, CNRS, F-34090
Montpellier, France
$\langle$MSE$\rangle^2$, UMI CNRS-Massachusetts Institute of Technology,
Cambridge, USA

This chapter provides a brief description of the contact dynamics (CD) method as a discrete element approach for the simulation of granular materials. The mathematical formulation of this method involves only particle displacements and velocities, thus neglecting elastic response times and deflections at the contact points. Two main ingredients of the method are detailed: i) the contact laws expressed as complementarity relations between the contact forces and velocities and ii) the nonsmooth motion involving velocity jumps with impulsive unresolved forces as well as smooth motion with resolved static forces. We show that a consistent description of the dynamics at the velocity level leads to an implicit time-stepping scheme together with an explicit treatment of the evolution of the particle configuration.

1 Introduction

Granular materials are of primary importance in a variety of scientific and technological areas such as soil mechanics, geological processes and flows, soft matter physics, powder technology and agronomy. Frictional-contact interactions between particles and physical and/or chemical effects of an interstitial fluid or solid material lead to a nonlinear rheological behavior that has not yet been fully formulated in the framework of a continuum theory. In particular, the state variables in quasi-static and/or inertial granular flows and their evolution with shear strain rate and amplitude reflect the complex evolution of the contact network, and still need to be clearly identified and included in a continuum description of the flow behavior of granular materials, see also Refs. [TLM17, DS17, LRW17, TWT17] by the lecturers of the Alert 2017 school.

The particle-scale modeling of granular materials was considerably reinforced by the application of the Discrete Element Method (DEM) for the simulation of particle dynamics [CS79, TY91, Her93, Tho93, PB95, Tho97, Lud98, MLH99, MH04, aM07, GRC07, RRY07]. The DEM [LRW17] is based on the step-wise integration of the equations of motion for all particles, described as rigid elements, by accounting for contact interactions [LRW17, Mar17] and boundary conditions [CR17, TLM17]. The DEM can also be seen as an application of the Molecular Dynamics (MD) method to rigid particles. The event driven (ED) method for rigid particles, as described in [LRW17], can only deal with dynamic collisions, while the CD described below is able to deal with both dynamic and static situations for rigid particles. Modeling perfectly rigid particles (ED, CD) involves only their rigid-body degrees of freedom, but the application of classical explicit integration methods (MD, DEM) requires a regular (smooth) *force law* at the contact point between two particles with a *contact deflection* defined from their overlap. Generally, the repulsive force is considered to be proportional to the overlap and a viscous damping term is added to account for inelastic collisions.

A new approach to discrete particle modeling emerged from a mathematical formulation of nonsmooth dynamics and algorithmic developments by J. J. Moreau and M. Jean [Mor77, Mor83, Mor88a, Mor88b, Mor93, Mor94, JP85, Jea88, JM92]. This approach, called Contact Dynamics (CD), is based on a nonsmooth formulation of particle dynamics in the sense that the particle velocities and contact forces are simultaneously computed at each time step from the balance of momenta by taking into account the unilateral contact interactions and Coulomb friction law, hence without introducing contact deflection and a repulsive potential. The mathematical concepts and tools for the treatment of nonsmooth dynamics were developed in relation with mechanical problems involving unilateral constraints and in the context of convex analysis; see [Bro99] for a detailed history. The multicontact feature is present in static states and in dense flows of granular materials where spatial correlations occur at large length scales and impulse dynamics is mixed with smooth particle motions at different time scales [PBL02, RR02, SGL02, SVR02, Pou04, MB05, AR07, BDMS07, OT07].

The CD method has been applied to investigate granular materials [Mor97, RJMR96, RWJM98, BRH02, RR02, SVR02, NLCV03, RDA04, MH04, TCRB05, SCG$^+$06, ARPS07, RWU07], as well as masonry and tensegrity structures [AJ98, NAD06]. For static and plastic shear properties, the CD simulations agree well with MD simulations [REBR95, Mor97, RSDW97, Rad99, LJ00, RR04]. The main difference between the two methods in application to granular materials is the resolution of elastic time scales in the MD/DEM method in contrast to the CD/ED methods in which the natural time unit is imposed by particle dynamics and external actions [RSDW97, MH04, MH06].

In this chapter, we present the CD method as a consistent model of nonsmooth and multicontact granular dynamics expressed more specifically in the contact coordinates.

2 Contact laws

Consider two particles i and j touching at a contact point κ inside a granular material. We assume that a unique common line (here in 2D, for 3D see [LRW17]) tangent to the two particle surfaces at κ can be defined. The contact can therefore be endowed with a local reference frame defined by a unit vector $\vec{n}$ normal to the line and a unit vector $\vec{t}$ along the line.

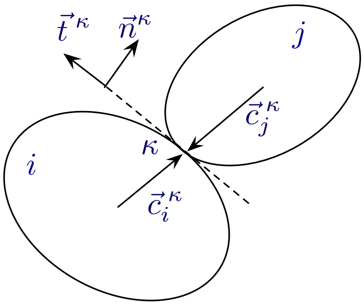

Figure 1: A contact κ between two non-spherical particles i and j with contact vectors $\vec{c}_i^{\kappa}$ and $\vec{c}_j^{\kappa}$, and contact frame $(\vec{n}^{\kappa}, \vec{t}^{\kappa})$.

A potential (or prospective) contact exists if the gap δ_n between two particles (partners) is sufficiently small so that a collision may occur between the two particles within a small time interval δt (time step in numerical simulations). If the contact is effective ($\delta_n = 0$), a repulsive (positive) normal force f_n may appear at κ with a value depending on the particle velocities and forces exerted on the two partners by their neighboring particles; see Fig. 1. But if $\delta_n > 0$ (nonzero gap), the contact is not effective and f_n is identically zero. These conditions can also be represented by the "complementarity relations" $\delta_n \geq 0$, $f_n \geq 0$ and $\delta_n f_n = 0$ or be cast into the so-called Signorini inequalities:

$$\left\{ \begin{array}{lll} \delta_n > 0 & \Rightarrow & f_n = 0 \\ \delta_n = 0 & \Rightarrow & f_n \geq 0\,. \end{array} \right. \tag{1}$$

Note that the positive δ_n here means a separation of the particles, whereas in most literature on DEM and smooth contact laws separation means $\delta_n^{\mathrm{DEM}} < 0$, while mechanical contacts are associated with overlaps $\delta_n^{\mathrm{DEM}} > 0$ [LRW17]. In contrast to simple DEM contact laws like linear or Hertz [LRW17, Mar17], this relation can not be reduced to a (mono-valued) functional dependence between δ_n and f_n.

The above conditions imply that the normal force vanishes when the contact is not effective. However, the normal force may also vanish at an effective contact. This is the case for $u_n = \dot{\delta}_n > 0$, i.e. for incipient opening of a contact. Otherwise, the effective contact is *persistent* and we have $u_n = \dot{\delta}_n = 0$. Hence, Signorini's inequalities can be extended as follows:

$$\begin{cases} \delta_n > 0 & \Rightarrow \quad f_n = 0 \\ \delta_n = 0 & \wedge \quad \begin{cases} u_n > 0 & \Rightarrow \quad f_n = 0 \\ u_n = 0 & \Rightarrow \quad f_n \geq 0 \end{cases} \end{cases} \tag{2}$$

This means that for $\delta_n = 0$, Signorini's inequalities hold between the variables u_n and f_n.

In the same way, the Coulomb friction law at an effective contact can be expressed by a set of inequalities for the friction force f_t and sliding velocity u_t:

$$\begin{cases} u_t > 0 & \Rightarrow \quad f_t = -\mu f_n \\ u_t = 0 & \Rightarrow \quad -\mu f_n \leq f_t \leq \mu f_n \\ u_t < 0 & \Rightarrow \quad f_t = \mu f_n \end{cases} \tag{3}$$

where μ is the friction coefficient. It is assumed that the unit tangent vector $\vec{t}$ points in the direction of sliding velocity such that $\vec{u}_t \cdot \vec{t} = u_t$. Coulomb's friction law can not be reduced to a (mono-valued) functional dependence between u_t and f_t.

Figure 2 displays Signorini's inequalities (2) and Coulomb's friction law (3) for an effective contact. The force laws employed in MD may be considered as regularizations of the above contact laws with their vertical branches replaced by steep linear or nonlinear functions.

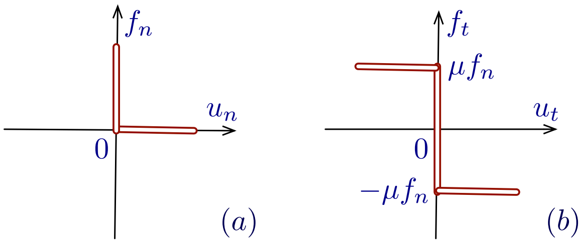

Figure 2: Graphs of (a) Signorini's inequalities and (b) Coulomb's friction law.

The use of 'nonsmooth' contact laws in the CD method is consistent with a discrete model of particle motions involving no sub-particle length scale or inherent force scale. But such a coarse model of particle motion implies *nonsmooth dynamics*, i.e. possible discontinuities in particle velocities and forces due to collisions (like in ED [LRW17]) and variations of the contact network (which does not exist in ED). Hence, the approximation of the contact force f_n during a time step δt is a measure problem in the mathematical sense [Mor94, Mor04]. A resolved force f^s is the density of the measure $f^s \, dt$ with respect to time differential dt. In contrast, a normal impulse p

generated by a collision has no density with respect to dt. In other words, the forces at the origin of the impulse are not resolved at the scale δt. In practice, however, we do not differentiate between these contributions in a coarse (particle-scale) dynamics, and the two contributions sum up to a single measure. The contact force is defined as the average of this measure over δt.

In a similar vein, the left (pre-collision) velocities u_n^- and u_t^- at time t are not always related by a smooth variation (acceleration multiplied by time step δt) with the right (post-collision) velocities u_n^+ and u_t^+ at $t + \delta t$. Hence, the contact laws (2) and (3) are assumed to be satisfied for a weighted mean of the left and right contact velocities:

$$u_n = \frac{u_n^+ + e_n\, u_n^-}{1 + e_n}, \tag{4}$$

$$u_t = \frac{u_t^+ + e_t\, u_t^-}{1 + |e_t|}. \tag{5}$$

For a binary collision, see also [LRW17], the normal force is nonzero, and Signorini's graph implies $u_n = 0$. Therefore, we have $-u_n^+/u_n^- = e_n$. Hence, the coefficient e_n corresponds to the normal restitution coefficient. In the same way, for $u_t = 0$, corresponding to a non-sliding contact we have $-u_t^+/u_t^- = e_t$, that coincides with the tangential restitution coefficient. We see that, when Signorini's and Coulomb's graphs are used with the formal velocities given by equation (5), a contact is persistent ($u_n^+ = 0$) only if $e_n = 0$.

In a dense granular flow, the collisions are not binary, and the generated impulses propagate through the contact network. For this reason, a contact may experience many successive impulses during δt. Such events can be resolved for a sufficiently small time interval δt or tracked by means of an event-driven scheme [LRW17]. However, this strategy is numerically inefficient, and contradicts the spirit of the CD method based on coarse-time dynamics. Hence, the use of intermediate velocities (5) with contact laws is a generalization of restitution coefficients to multiple collisions and contact networks. In this model, the right velocities u_n^+ and u_t^+ (at the end of a time step) are not given by the left velocities multiplied by the coefficients of restitution as in binary collisions but by combining the contact laws with the equations of dynamics.

3 Nonsmooth dynamics

The particle motions are governed by Newton's equations under the action of external bulk or boundary forces $\vec{F}_{ext}$, and the contact forces $\vec{f}^\kappa$ exerted by neighboring particles at the contact points κ. Let unit vectors ($\hat{x}$, $\hat{y}$) represent a reference frame in the plane and $\hat{z} = \hat{x} \times \hat{y}$ be the normal to the plane. Each particle is characterized by its mass m, moment of inertia I, mass center coordinates $\vec{r}$, mass center velocity $\vec{U}$, angular coordinates θ with respect to $\hat{z}$, and angular velocity ω. For a smooth motion (twice differentiable), the equations of motion (2D) of a particle are

$$\begin{array}{rcl} m\,\dot{\vec{U}} & = & \vec{F} + \vec{F}_{ext} \\ I\,\dot{\omega} & = & \mathcal{M} + \mathcal{M}_{ext}\ , \end{array} \tag{6}$$

where $\vec{F} = \sum_\kappa \vec{f}^\kappa$ and $\mathcal{M} = \sum_\kappa \vec{c}^\kappa \times \vec{f}^\kappa$ where $\vec{c}^\kappa$ is the *contact vector* joining the center of mass to the contact κ and $\mathcal{M}_{ext}$ represents the moment of external forces.

For a nonsmooth motion with time resolution δt involving impulses and velocity jumps, an integrated form of the equations of dynamics should be used. Hence, the equations of dynamics should be written as an equality of measures:

$$\begin{array}{rcl} m\,d\vec{U} & = & d\vec{F}' + \vec{F}_{ext}\,dt \\ I\,d\omega & = & d\mathcal{M}' + \mathcal{M}_{ext}\,dt\ , \end{array} \tag{7}$$

where $d\vec{F}' = \sum_\kappa d\vec{f}'^\kappa$ and $d\mathcal{M}' = \sum_\kappa \vec{c}^\kappa \times d\vec{f}'^\kappa$. These measure equations can be integrated over δt with $\vec{F}$ and $\mathcal{M}$ as approximations of the integral of $d\vec{F}'$ and $d\mathcal{M}'$. With these definitions, we have

$$\begin{array}{rcl} m\,(\vec{U}^+ - \vec{U}^-) & = & \delta t\,\vec{F} + \delta t\,\vec{F}_{ext} \\ I\,(\omega^+ - \omega^-) & = & \delta t\,\mathcal{M} + \delta t\,\mathcal{M}_{ext}\ , \end{array} \tag{8}$$

where $(\vec{U}^-, \omega^-)$ and $(\vec{U}^+, \omega^+)$ are the left and right velocities of the particle, respectively, at each time step.

The equations of dynamics can be written in matrix form for a set of N_p particles labeled with integers $i \in [1, N_p]$. The forces and force moments $F_x^i, F_y^i, \mathcal{M}^i$ acting on the particles i are arranged in a column vector represented by a boldface letter $\mathbf{F}$ and belonging to $\mathbb{R}^{3N_p}$. In the same way, the external bulk forces $F_{ext,x}, F_{ext,y}, \mathcal{M}_{ext}$ applied on the particles and the particle velocity components U_x^i, U_y^i, ω^i are represented by column vectors $\mathbf{F}_{ext}$ and $\mathbf{U}$, respectively. The particle masses and moments of inertia define a diagonal $3N_p \times 3N_p$ matrix denoted by $\mathbf{M}$. With these notations, the equations of dynamics (8) are represented by the matrix equation

$$\mathbf{M}(\mathbf{U}^+ - \mathbf{U}^-) = \delta t(\mathbf{F} + \mathbf{F}_{\mathbf{ext}})\ . \tag{9}$$

4 Contact dynamics equations

Since the contact laws involve contact variables (u_n, u_t, f_n and f_t), we need to express the equations (9) in the same terms of the same variables. The contacts are labeled with integers $\kappa \in [1, N_c]$, where N_c is the total number of contacts. Like particle velocities, the contact velocities u_n^κ and u_t^κ can be collected in a column vector $\mathbf{u} \in \mathbb{R}^{2N_c}$. In the same way, the contact forces f_n^κ and f_t^κ are represented by a vector $\mathbf{f} \in \mathbb{R}^{2N_c}$. We would like to express the equations of dynamics in terms of $\mathbf{f}$ and $\mathbf{u}$. Since the contact velocities $\mathbf{u}$ are linear in particle velocities $\mathbf{U}$, the transformation of the velocities is an affine transformation:

$$\mathbf{u} = \mathbf{G}\,\mathbf{U} \tag{10}$$

where $\mathbf{G}$ is a $2N_c \times 3N_p$ matrix carrying the information on the geometry of the contact network. A similar linear transformation relates $\mathbf{f}$ to $\mathbf{F}$:

$$\mathbf{F} = \mathbf{H}\,\mathbf{f} \tag{11}$$

where $\mathbf{H}$ is a $3N_p \times 2N_c$ matrix. We refer to $\mathbf{H}$ as *contact matrix*. It contains the same information as $\mathbf{G}$. It can be shown that $\mathbf{H} = \mathbf{G}^T$ where $\mathbf{G}^T$ is the transpose of $\mathbf{G}$. This property can be inferred from the equivalence between the virtual power $\mathbf{F} \cdot \mathbf{U}$ developed by "generalized" forces $\mathbf{F}$ and the virtual power $\mathbf{f} \cdot \mathbf{u}$ developed by the bond forces $\mathbf{f}$. In general, the matrix $\mathbf{H}$ is singular and, by definition, its null space has a dimension at least equal to $2N_c - 3N_p$.

The matrix $H^{i\kappa}$ can be partitioned into two matrices $H_n^{i\kappa}$ and $H_t^{i\kappa}$ such that

$$\begin{array}{rcl} u_n^\kappa & = & \sum\limits_i H_n^{T,\kappa i}\, U^i \\ u_t^\kappa & = & \sum\limits_i H_t^{T,\kappa i}\, U^i \end{array} \tag{12}$$

and

$$F^i = \sum_\kappa (H_n^{i\kappa}\, f_n^\kappa + H_t^{i\kappa}\, f_t^\kappa) \tag{13}$$

Using these relations, (9) can be transformed into two equations for each contact κ:

$$\begin{array}{rcl} u_n^{\kappa+} - u_n^{\kappa-} & = & \delta t \sum\limits_{i,j} H_n^{T,\kappa i}\, M^{-1,ij} \\ & & \times\{\sum\limits_\lambda (H_n^{j\lambda} f_n^\lambda + H_t^{j\lambda} f_t^\lambda) + F_{ext}^j\} \\ u_t^{\kappa+} - u_t^{\kappa-} & = & \delta t \sum\limits_{i,j} H_t^{T,\kappa i}\, M^{-1,ij} \\ & & \times\{\sum\limits_\lambda (H_n^{j\lambda} f_n^\lambda + H_t^{j\lambda} f_t^\lambda) + F_{ext}^j\} \end{array} \tag{14}$$

We now can write down explicit linear relations between the contact variables from equations (14) and (12). Let us set

$$\mathcal{W}_{k_1 k_2}^{\kappa\lambda} = \sum_{i,j} H_{k_1}^{T,\kappa i} M^{-1,ij} H_{k_2}^{j\lambda}, \tag{15}$$

where k_1 and k_2 stand for n or t. With this notation, (14) can be rewritten as

$$\begin{aligned}
\frac{1+e_n}{\delta t}\left(u_n^\kappa - u_n^{\kappa -}\right) &= \mathcal{W}_{nn}^{\kappa\kappa} f_n^\kappa + \mathcal{W}_{nt}^{\kappa\kappa} f_t^\kappa \\
&+ \sum_{\lambda(\neq\kappa)} \{\mathcal{W}_{nn}^{\kappa\lambda} f_n^\lambda + \mathcal{W}_{nt}^{\kappa\lambda} f_t^\lambda\} \\
&+ \sum_{i,j} H_n^{T,\kappa i} M^{-1,ij} F_{ext}^j \qquad (16) \\
\frac{1+e_t}{\delta t}\left(u_t^\kappa - u_t^{\kappa -}\right) &= \mathcal{W}_{tn}^{\kappa\kappa} f_n^\kappa + \mathcal{W}_{tt}^{\kappa\kappa} f_t^\kappa \\
&+ \sum_{\lambda(\neq\kappa)} \{\mathcal{W}_{tn}^{\kappa\lambda} f_n^\lambda + \mathcal{W}_{nt}^{\kappa\lambda} f_t^\lambda\} \\
&+ \sum_{i,j} H_t^{T,\kappa i} M^{-1,ij} F_{ext}^j \qquad (17)
\end{aligned}$$

The coefficients $\mathcal{W}_{k_1 k_2}^{\kappa\kappa}$ for each contact κ can be calculated from the contact network geometry and inertia parameters of the two partners 1_κ and 2_κ of the contact κ. Let $\vec{c}_i^{\,\kappa}$ be the contact vector joining the center of mass of particle i to the contact κ. We get

$$\begin{aligned}
\mathcal{W}_{nn}^{\kappa\kappa} &= \frac{1}{m_{1_\kappa}} + \frac{1}{m_{2_\kappa}} + \frac{(c_{1t}^\kappa)^2}{I_{1_\kappa}} + \frac{(c_{2t}^\kappa)^2}{I_{2_\kappa}}, \\
\mathcal{W}_{tt}^{\kappa\kappa} &= \frac{1}{m_{1_\kappa}} + \frac{1}{m_{2_\kappa}} + \frac{(c_{1n}^\kappa)^2}{I_{1_\kappa}} + \frac{(c_{2n}^\kappa)^2}{I_{2_\kappa}}, \qquad (18) \\
\mathcal{W}_{nt}^{\kappa\kappa} &= \mathcal{W}_{tn}^{\kappa\kappa} = \frac{c_{1n}^\kappa c_{1t}^\kappa}{I_{1_\kappa}} + \frac{c_{2n}^\kappa c_{2t}^\kappa}{I_{2_\kappa}},
\end{aligned}$$

where $c_{in}^\kappa = \vec{c}_i^{\,\kappa} \cdot \vec{n}^\kappa$ and $c_{it}^\kappa = \vec{c}_i^{\,\kappa} \cdot \vec{t}^\kappa$ are the components of the contact vectors in the contact frame. The coefficients $\mathcal{W}_{k_1 k_2}^{\kappa\kappa}$ are inverse reduced inertia.

An alternative representation of equations (16) and (17) is

$$\mathcal{W}_{nn}^{\kappa\kappa} f_n^\kappa + \mathcal{W}_{nt}^{\kappa\kappa} f_t^\kappa = (1+e_n)\,\frac{1}{\delta t} u_n^\kappa + a_n^\kappa, \qquad (19)$$

$$\mathcal{W}_{tt}^{\kappa\kappa} f_t^\kappa + \mathcal{W}_{tn}^{\kappa\kappa} f_n^\kappa = (1+e_t)\,\frac{1}{\delta t} u_t^\kappa + a_t^\kappa. \qquad (20)$$

The two offsets a_n^κ and a_t^κ can be expressed from equations (16) and (17). We refer to equations (19) and (20) or, equivalently, to equations (16) and (17) as *contact dynamics equations* as they replace the equations of dynamics for the particles; see Fig. 3 [RR09].

The two terms a_n and a_t are given by the following expressions:

$$a_n^\kappa = b_n^\kappa - (1 + e_n)\frac{1}{\delta t}\, u_n^{\kappa -} + \left(\frac{\vec{F}_{ext}^{2_\kappa}}{m_{2_\kappa}} - \frac{\vec{F}_{ext}^{1_\kappa}}{m_{1_\kappa}} \right) \cdot \vec{n}^\kappa. \tag{21}$$

$$a_t^\kappa = b_t^\kappa - (1 + e_t)\frac{1}{\delta t}\, u_t^{\kappa -} + \left(\frac{\vec{F}_{ext}^{2_\kappa}}{m_{2_\kappa}} - \frac{\vec{F}_{ext}^{1_\kappa}}{m_{1_\kappa}} \right) \cdot \vec{t}^\kappa. \tag{22}$$

The contribution of left velocities $(u_n^{\kappa -}, u_t^{\kappa -})$ appears in these equations as an impulse depending on the reduced mass and the restitution coefficient. The contribution of contact forces $\vec{f}_i^\lambda$ acting on the two touching particles are represented by the terms b_n^κ and b_t^κ given by

$$b_n^\kappa = \frac{1}{m_{2_\kappa}} \sum_{\lambda(\neq\kappa)} \vec{f}_{2_\kappa}^\lambda \cdot \vec{n}^\kappa - \frac{1}{m_{1_\kappa}} \sum_{\lambda(\neq\kappa)} \vec{f}_{1_\kappa}^\lambda \cdot \vec{n}^\kappa, \tag{23}$$

$$b_t^\kappa = \frac{1}{m_{2_\kappa}} \sum_{\lambda(\neq\kappa)} \vec{f}_{2_\kappa}^\lambda \cdot \vec{t}^\kappa - \frac{1}{m_{1_\kappa}} \sum_{\lambda(\neq\kappa)} \vec{f}_{1_\kappa}^\lambda \cdot \vec{t}^\kappa. \tag{24}$$

The contact dynamics equations (19) and (20) define a system of two linear equations between the contact variables at each contact point. For given values of a_n and a_t at a contact, the contact laws (2) and (3) should also be satisfied. Hence, the solution is at the intersection between the straight line (19) and Signorini's graph on one hand, and between (20) and Coulomb's graph, on the other hand.

5 Iterative resolution

To solve the system of $2N_c$ contact dynamics equations (in 2D) with the corresponding contact laws, we proceed by an iterative method which converges to the solution simultaneously for all contact forces and velocities. We first consider the single-contact problem that consists in calculating the contact variables f_n^κ, f_t^κ, u_n^κ and u_t^κ at a single contact given the values of the offsets a_n^κ and a_t^κ at the same contact. The solution is given by intersecting the lines representing contact dynamics equations with Signorini's and Coulomb's graphs; see Fig. 3. The intersection occurs at a unique point due to the positivity of the coefficients $\mathcal{W}_{k_1 k_2}^{\kappa\kappa}$ (positive slope).

However, the two intersections can not be established separately when $\mathcal{W}_{nt}^{\kappa\kappa} \neq 0$. To find the solution, one may consider the intersection of contact dynamics equations with the force axis, i.e. by setting $u_n = u_t = 0$. This yields two values g_n^κ and g_t^κ of f_n^κ and f_t^κ, respectively:

$$g_n^\kappa = \frac{\mathcal{W}_{tt}^{\kappa\kappa} a_n^\kappa - \mathcal{W}_{nt}^{\kappa\kappa} a_t^\kappa}{\mathcal{W}_{nn}^{\kappa\kappa}\mathcal{W}_{tt}^{\kappa\kappa} - (\mathcal{W}_{nt}^{\kappa\kappa})^2}, \tag{25}$$

$$g_t^\kappa = \frac{\mathcal{W}_{nn}^{\kappa\kappa} a_n^\kappa - \mathcal{W}_{tn}^{\kappa\kappa} a_t^\kappa}{\mathcal{W}_{tt}^{\kappa\kappa}\mathcal{W}_{nn}^{\kappa\kappa} - (\mathcal{W}_{tn}^{\kappa\kappa})^2}. \tag{26}$$

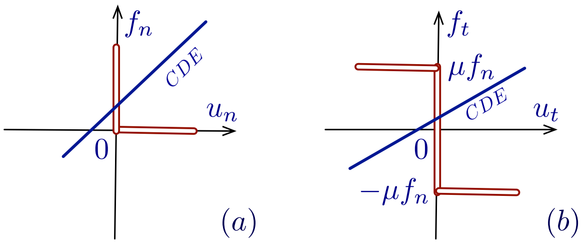

Figure 3: Solution of the local equations of dynamics obtained from the intersection between contact dynamics equations (CDE) and the Signorini and Coulomb contact laws.

It can be shown that the denominator is positive. If $g_n^\kappa < 0$, then the solution is $f_n^\kappa = f_t^\kappa = 0$. This corresponds to a *breaking contact*. Otherwise, i.e. if $g_n^\kappa \geq 0$, we have $f_n^\kappa = g_n^\kappa$. With this value of f_n^κ, we can determine the solution of the Coulomb problem. If $g_t^\kappa > \mu f_n^\kappa$, the solution is $f_t^\kappa = \mu f_n^\kappa$ and in the opposite case, i.e. if $g_t^\kappa < -\mu f_n^\kappa$, the solution is $f_t^\kappa = -\mu f_n^\kappa$ (*sliding contact*). Otherwise, i.e. when $-\mu f_n^\kappa < g_t^\kappa < \mu f_n^\kappa$, the solution is $f_t^\kappa = g_t^\kappa$ (*rolling contact*).

In a multi-contact system, the contributions of b_n^κ and b_t^κ to the offsets a_n^κ and a_t^κ depend on the forces and velocities at contacts $\lambda \neq \kappa$; see equations (21), (22), (23) and (24). Hence, the solution for each contact depends on all other contacts of the system and it must be determined simultaneously for all contacts. A robust method consists in searching the solution as the limit of a sequence $\{f_n^\kappa(k), f_t^\kappa(k), u_n^\kappa(k), u_t^\kappa(k)\}$ with $\kappa \in [1, N_c]$. Let us assume that a temporary set of contact forces $\{f_n^\kappa(k), f_t^\kappa(k)\}$ at iteration step k is given. From this set, the offsets $\{a_n^\kappa(k), a_t^\kappa(k)\}$ for all contacts can be calculated through the relations (21) and (22). The local problem can then be solved for each contact κ with these values of the offsets, yielding an updated set of contact forces $\{f_n^\kappa(k+1), f_t^\kappa(k+1)\}$.

This force update procedure does not require the calculation of contact velocities $u_n^\kappa(k+1), u_t^\kappa(k+1)\}$ since the offsets depend only on the contact forces. The set $\{f_n^\kappa(k), f_t^\kappa(k)\}$ evolves with k by successive corrections and it converges to a solution satisfying the contact dynamics equations and contact laws at all potential contacts of the system. The iteration can be stopped when the set $\{f_n^\kappa(k), f_t^\kappa(k)\}$ is stable with regard to the force update procedure within a prescribed precision criterion ε_f:

$$\frac{\mid f^\kappa(k+1) - f^\kappa(k) \mid}{f^\kappa(k+1)} < \varepsilon_f \quad \forall\kappa. \tag{27}$$

Finally, from the converged contact forces, the particle velocities $\{\vec{U}^i\}$ can be computed by means of the equations of dynamics (8).

This iterative procedure provides a robust method which has proven efficient in application to the dynamics of granular materials. The information is treated locally and no large matrices are manipulated during iterations. The number N_i of necessary iterations for convergence depends on the precision ε_f but not on the time step δt. The number of necessary iterations is substantially reduced when the iteration at each time step is initialized with a good guess of the forces such as those computed in the preceding step. On the other hand, the time step should be small enough to avoid large overlaps although such overlaps are not elastic deflections as in the MD method.

The uniqueness of the solution in a multi-contact system with rigid particles is not guaranteed at each step of evolution. There are $3N_p$ equations of dynamics and $2N_c$ contact relations. The unknown variables are the $3N_p$ particle velocities and $2N_c$ contact forces. The indeterminacy arises from the fact that the $2N_c$ contact relations are *inequations*. Thus, the extent of indeterminacy of the solution reflects all possible combinations of contact forces accommodating the contact inequations. The indeterminacy may be high, but it does not imply significant force variability since the solutions are strongly constrained by contact laws. In practice, as a result of finite numerical precision, the risk of not finding a mechanically admissible solution (satisfying both the contact laws and equations of dynamics) is higher than that of missing the right solution. In other words, the variability of the solution is generally below the precision ε_f when the forces are computed at each time step from the forces at the preceding step.

6 Time-stepping scheme

The time-stepping scheme is based on the fact that Signorini's condition (2) for particle positions is the only condition referring to space coordinates. Both the equations of dynamics and contact laws are formulated at the velocity level, and Signorini's condition for particle positions is accounted for by considering only the *effective contacts* where $\delta_n = 0$. Hence, the contact network is defined explicitly from particle positions and it does not evolve during a time step δt. But the iterative determination of forces and velocities is fully implicit, and the right (new) velocities $\{\vec{U}^{i+}, \omega^{i+}\}$ at the end of a time step should be used to increment particle positions.

Let t and $t+\delta t$ be the considered time interval. The configuration $\{\vec{r}^i(t)\}$ and particle velocities $\{\vec{U}^i(t), \omega^i(t)\}$ are given at time t. These velocities coincide with the left velocities $\{\vec{U}^{i-}, \omega^{i-}\}$. The contact network $\{\kappa, \vec{n}^\kappa, \vec{t}^\kappa\}$ is set up from the particle configuration at time t or from an intermediate configuration $\{\vec{r}^i_m\}$ defined by

$$\vec{r}^i_m \equiv \vec{r}^i(t) + \frac{\delta t}{2}\, \vec{U}^i(t). \tag{28}$$

When this configuration is used for contact detection, other space-dependent quantities such as the inverse mass parameters $\mathcal{W}^{\kappa\kappa}_{k_1 k_2}$ and external forces $\vec{F}^i_{ext}$ should consistently be defined for the same configuration and at the same time $t + \delta t/2$. Then, the forces and velocities are iteratively determined for this configuration, and the new particle velocities $\{\vec{U}^{i+}, \omega^{i+}\}$ are calculated. These are the velocities at the end of the time step $t + \delta t$:

$$\begin{aligned} \vec{U}^i(t+\delta t) &= \vec{U}^{i+}, && (29)\\ \omega^i(t+\delta t) &= \omega^{i+}. && (30) \end{aligned}$$

Finally, the positions are updated by integrating the updated velocities:

$$\begin{aligned} \vec{r}^i(t+\delta t) &= \vec{r}^i_m + \frac{\delta t}{2}\,\vec{U}^i(t+\delta t), && (31)\\ \theta^i(t+\delta t) &= \theta^i_m + \frac{\delta t}{2}\,\omega^i(t+\delta t). && (32) \end{aligned}$$

This scheme is unconditionally stable due to its inherent implicit time integration. Hence, no damping parameters at any level are needed and the time step δt can be large. The real limit on the time step is imposed by the cumulative round-off errors in particle positions, which are updated from the integration of the velocities. Although excessive overlaps have no dynamic effect in the CD method, they can falsify the particle configuration and the long-term evolution of the system. Note that the time step in the CD method is not a precision parameter but a temporal coarse-graining parameter for nonsmooth dynamics. It should be reduced if the impulse dynamics at small time scales is of interest.

7 Concluding remarks

The basics of the CD (contact dynamics) method for the discrete simulation of granular materials were presented, where this paper was adapted from reference [RR09]. This method can be viewed as the algorithmic formulation of nonsmooth granular dynamics at the scale of particle rearrangements, where small elastic response times and displacements are neglected. The CD method has the unique feature of bringing together in the same formalism two limit regimes of granular dynamics: (i) the collisional regime governed by binary shocks and incomplete energy restitution and (ii) the static regime governed by multiple contacts, geometrical disorder, force balance and dynamic rearrangements. Hence, this method provides a suitable framework for the investigation of dense granular flows where smooth evolutions are intermingled with sharp transitions.

The CD method can also be considered as an adequate framework for the numerical treatment of frictional contact problems. Indeed, the Coulomb friction and perfectly rigid contact condition are implemented in an exact form, i.e. without introducing artificial penalization parameters or damping. Given a contact network, all kinematic constraints implied by contact laws are simultaneously taken into account together with the equations of dynamics in order to determine the velocities and contact forces in the system. This global Signorini-Coulomb problem is solved by an iterative process pertaining to the Gauss-Seidel iterative method that consists of solving a single contact problem, and successively and iteratively updating the forces until a convergence criterion is fulfilled. The method is thus capable of dealing properly with the nonlocal character of the momentum transfers resulting from the impenetrability of the particles. It can be employed to study stiff systems for which smooth MD-like methods require small time steps for numerical stability and the stiffness matrix may become ill-conditioned as the contact network evolves.

The CD method is unconditionally stable due to its inherent implicit time integration scheme. The uniqueness of the solution at each time step is not guaranteed for perfectly rigid particles. However, the variability of admissible solutions is generally below the numerical precision. The variability resulting from the numerical precision can be reduced and the calculations significantly accelerated by initializing the iterative procedure at each step with the forces computed in the preceding step.

The basic algorithm presented in this course can be (and has been) extended to deal with richer contact laws, various particle shapes and more efficient resolution of the multicontact problem in 2D and 3D [BRH02, RDA04, RA05, NASR15]. The contact laws can be supplemented with a complementarity relation between a torque and a contact spin variable [BRH02]. Using such a complementarity relation, the rolling friction is easily implemented in this framework. Adhesion forces can be introduced by a simple shift of the complementarity relations:

$$u_n \quad \overset{S}{\longleftrightarrow} \quad f_n - f_n^a, \tag{33}$$

$$u_t \quad \overset{C}{\longleftrightarrow} \quad f_t, \tag{34}$$

where f_n^a is the adhesion threshold. Particle deformability can also be treated in the CD method by associating strain variables to the particles rather than to the contacts. The strains can be defined either from rigid-body degrees of freedom, as in the MD method, or associated with new internal degrees of freedom. Concerning particle shapes, it is a generic feature of the CD method that, in contrast to force laws, the nature of the contact complementarity relations does not depend on the particle shape. Hence, the resolution of the multicontact problem is independent of particle shape. The potential face-face or face-edge contacts are represented by three or two points which are treated as independent point contacts by the solver [SCG$^+$06, ASR09]. The basics of the method are the same in 2D and 3D. The only difference lies in the treatment of the tangential force whose direction in 3D is an unknown variable of the contact problem and is determined in the course of the iterative procedure.

Particular attention should be paid to the origin of the contact forces in the CD method. An example is the uniaxial compression of a dense granular material by imposing a constant velocity on a wall. In MD/DEM simulations of such or similar problems, see Refs. [LRW17, CR17, DS17, TLM17] and refences therein, the displacement of the wall causes mainly the elastic deformation of the particles and the contact forces increase accordingly. In the CD simulation of the same problem, since the contact laws involve no force scale and no static boundary or bulk forces are applied, the force scale is fixed by the imposed velocity through the impulsive terms in Eqs. (21) and (22). Since no rearrangements can occur due to a too high density, the corresponding kinetic energy is not dissipated. This energy increases adiabatically, the contact forces increase proportionally to the displacement and the particles interpenetrate. In contrast, if the uniaxial compression is controlled by an increasing boundary force, the contact forces increase in proportion to the applied force and the contact reaction forces balance exactly the driving force so that the packing remains in static equilibrium. In the MD/DEM approach, for simple (complex) contact force laws [LRW17, Mar17], the static forces are fully encoded in the particle positions (and history) with a scale given by the contact stiffness. In the CD approach, there is no such force/stiffness scale and thus the static force scale should be defined externally. This example shows that the CD method should be applied with special attention to the boundary conditions [CR17].

References

[AJ98] V Acary and M Jean. Numerical simulation of monuments by the contact dynamics method. In DGEMN-LNEC-JRC, editor, *Monument-98, Workshop on Seismic Performance of Monuments*, pages 12–14. LNEC, 1998.

[aM07] Xavier García and Ernesto Medina. Acoustic response of cemented granular sedimentary rocks: molecular dynamics modeling. *Phys Rev E Stat Nonlin Soft Matter Phys*, 75(6 Pt 1):061308, Jun 2007.

[AR07] Ivana Agnolin and Jean-Noël Roux. Internal states of model isotropic granular packings. i. assembling process, geometry, and contact networks. *Phys Rev E Stat Nonlin Soft Matter Phys*, 76(6-1):061302, 2007.

[ARPS07] Emilien Azéma, Farhang Radjai, Robert Peyroux, and Gilles Saussine. Force transmission in a packing of pentagonal particles. *Phys. Rev. E*, 76(1 Pt 1):011301, 2007.

[ASR09] E. Azéma, G. Saussine, and F. Radjai. Quasistatic rheology, force transmission and fabric properties of a packing of irregular polyhedral particles. *Mechanics of Materials*, 41:729–741, 2009.

[BDMS07] R. P. Behringer, Karen E Daniels, Trushant S Majmudar, and Matthias Sperl. Fluctuations, correlations and transitions in granular materials: statistical mechanics for a non-conventional system. *Philos Transact A Math Phys Eng Sci*, 2007.

[BRH02] I. Bratberg, F. Radjai, and A. Hansen. Dynamic rearrangements and packing regimes in randomly deposited two-dimensional granular beds. *Phys. Rev. E*, 66:031303–1, 2002.

[Bro99] B Brogliato. *Nonsmooth mechanics*. Springer, London, 1999.

[CR17] G. Combe and J.-N. Roux. Good practice and sample preparation - construction of granular packings. *ALERT geomaterials Doctoral School 2017, Aussois, France*, 2017.

[CS79] P. A. Cundall and O. D. L. Strack. A discrete numerical model for granular assemblies. *Géotechnique*, 29(1):47–65, 1979.

[DS17] F.V. Donzé and L. Scholtés. Predicting the strength of anisotropic shale rock: empirical nonlinear failure criterion vs. discrete element method. *ALERT geomaterials Doctoral School 2017, Aussois, France*, 2017.

[GRC07] F. A. Gilabert, J-N. Roux, and A. Castellanos. Computer simulation of model cohesive powders: influence of assembling procedure and contact laws on low consolidation states. *Phys. Rev. E*, 75(1 Pt 1):011303, Jan 2007.

[Her93] H. J. Herrmann. Molecular dynamics simulations of dry granular media. In *The first Nisshin Engineering Particle Technology International Seminar: Discrete Particle Simulations in Powder Technology*, page 8, Osaka, Japan, 1993.

[Jea88] M. Jean. Unilateral contact and dry friction: time and space variables discretization. *Arch. of Mech., Warszawa*, 40(1):677–691, 1988.

[JM92] M. Jean and J. J. Moreau. Unilaterality and dry friction in the dynamics of rigid body collections. In *Proceedings of Contact Mechanics International Symposium*, pages 31–48, Lausanne, Switzerland, 1992. Presses Polytechniques et Universitaires Romandes.

[JP85] M. Jean and E. Pratt. A system of rigid bodies with dry friction. *International Journal Eng. Sci.*, pages 497–513, 1985.

[LJ00] J. Lanier and M. Jean. Experiments and numerical simulations with 2d disks assembly. *Powder Technology*, 109:206–221, 2000.

[LRW17] S. Luding, N. Rivas, and T. Weinhart. From soft and hard particle simulations to continuum theory for granular flows. *ALERT geomaterials Doctoral School 2017, Aussois, France*, 2017.

[Lud98] S. Luding. Collisions and contacts between two particles. In H. J. Herrmann, J.-P. Hovi, and S. Luding, editors, *Physics of dry granular media - NATO ASI Series E350*, page 285, Dordrecht, 1998. Kluwer Academic Publishers.

[Mar17] C.L. Martin. Advanced contact laws. *ALERT geomaterials Doctoral School 2017, Aussois, France*, 2017.

[MB05] T. S. Majmudar and R. P. Behringer. Contact force measurements and stress-induced anisotropy in granular materials. *Nature*, 435(7045):1079–1082, Jun 2005.

[MH04] Sean McNamara and Hans Herrmann. Measurement of indeterminacy in packings of perfectly rigid disks. *Phys. Rev. E*, 70(6 Pt 1):061303, Dec 2004.

[MH06] Sean C McNamara and Hans J Herrmann. Quasirigidity: some uniqueness issues. *Phys. Rev. E*, 74(6 Pt 1):061303, Dec 2006.

[MLH99] H.-G. Matuttis, S. Luding, and H. J. Herrmann. Discrete element methods for the simulation of dense packings and heaps made of spherical and non-spherical particles. *Powder Technology*, 1999. in press.

[Mor77] J. J. Moreau. Evolution problem associated with a moving convex set in a hilbert space. *Journal of differential equations*, 26:347–374, 1977.

[Mor83] J. J. Moreau. Liasons unilatérales sans frottement et chocs inélastiques. *Comptes Rendus de l'Académie des Sciences*, 296:1473–1476, 1983.

[Mor88a] J. J. Moreau. Bounded variation in time. In P.D. Panagiotopoulos and G. Strang, editors, *Topics in Nonsmooth Mechanics*, pages 1–74. Bikhäuser, Basel, 1988.

[Mor88b] J.J. Moreau. *Unilateral contact and dry friction in finite freedom dynamics*, volume 302 of *International Centre for Mechanical Sciences, Courses and Lectures*. Springer, Vienna, 1988.

[Mor93] J. J. Moreau. New computation methods in granular dynamics. In *Powders & Grains 93*, page 227, Rotterdam, 1993. A. A. Balkema.

[Mor94] J.J. Moreau. Some numerical methods in multibody dynamics : application to granular. *European J. Mech. A Solids*, 13:93–114, 1994.

[Mor97] J. J. Moreau. Numerical investigation of shear zones in granular materials. In D. E. Wolf and P. Grassberger, editors, *Friction, Arching, Contact Dynamics*, pages 233–247, Singapore, 1997. World Scientific.

[Mor04] J.J. Moreau. An introduction to unilateral dynamics. In M. Frémond and F. Maceri, editors, *Novel approaches in civil engineering*, number 14 in Lecture Notes in Applied and Computational Mechanics, pages 1–46. Springer-Verlag, 2004.

[NAD06] S. Nineb, P. Alart, and D. Dureisseix. Approche multi-échelle des systèmes de tenségrité. *Revue Européenne de Mécanique Numérique*, 15:319–328, 2006.

[NASR15] D.-H. Nguyen, E. Azéma, P. Sornay, and F. Radjai. Bonded-cell model for particle fracture. *Phys. Rev. E*, 91:022203, 2015.

[NLCV03] C. Nouguier-Lehon, B. Cambou, and E. Vincens. Influence of particle shape and angularity on the behavior of granular materials: a numerical analysis. *Int. J. Numer. Anal. Meth. Geomech*, 27:1207–1226, 2003.

[OT07] Peter Olsson and S. Teitel. Critical scaling of shear viscosity at the jamming transition. *Phys Rev Lett*, 99(17):178001, Oct 2007.

[PB95] T. Pöschel and V. Buchholtz. Molecular dynamics of arbitrarily shaped granular particles. *J. Phys. I France*, 5(11):1431–1455, 1995.

[PBL02] A. Puglisi, A. Baldassarri, and V. Loreto. Fluctuation-dissipation relations in driven granular gases. *Phys Rev E Stat Nonlin Soft Matter Phys*, 66(6 Pt 1):061305, Dec 2002.

[Pou04] O. Pouliquen. Velocity correlations in dense granular flows. *Phys. Rev. Lett.*, 93(24):248001–4, December 2004.

[RA05] Mathieu Renouf and Pierre Alart. Conjugate gradient type algorithms for frictional multi-contact problems: applications to granular materials. *Computer Methods in Applied Mechanics and Engineering*, 194(18-20):2019–2041, May 2005.

[Rad99] F. Radjai. Multicontact dynamics of granular systems. *Computer Physics Communications*, 121-122:294–298, 1999.

[RDA04] Mathieu Renouf, Frederic Dubois, and Pierre Alart. A parallel version of the non smooth contact dynamics algorithm applied to the simulation of granular media. *Journal of Computational and Applied Mathematics*, 168(1-2):375–382, July 2004.

[REBR95] Radjai, Evesque, Bideau, and Roux. Stick-slip dynamics of a one-dimensional array of particles. *Phys. Rev. E*, 52(5):5555–5564, Nov 1995.

[RJMR96] Farhang Radjai, Michel Jean, Jean-Jacques Moreau, and Stéphane Roux. Force distributions in dense two-dimensional granular systems. *Phys. Rev. Lett.*, 77(2):274–, July 1996.

[RR02] Farhang Radjai and Stéphane Roux. Turbulentlike fluctuations in quasistatic flow of granular media. *Phys Rev Lett*, 89(6):064302, Aug 2002.

[RR04] F. Radjai and S. Roux. Contact dynamics study of 2d granular media : Critical states and relevant internal variables. In H. Hinrichsen and D. E. Wolf, editors, *The Physics of Granular Media*, pages 165–186, Weinheim, 2004. Wiley-VCH.

[RR09] F. Radjai and V. Richefeu. Contact dynamics as a nonsmooth discrete element method. *Mechanics of Materials*, 41:715–728, 2009.

[RRY07] V. Richefeu, F. Radjai, and M. S. El Youssoufi. Stress transmission in wet granular materials. *Eur. Phys. J. E*, 21:359–369, Feb 2007.

[RSDW97] F. Radjai, J. Schäfer, S. Dippel, and D. Wolf. Collective friction of an array of particles: A crucial test for numerical algorithms. *J. Phys. I France*, 7:1053, 1997.

[RWJM98] F. Radjai, D. E. Wolf, M. Jean, and J.J. Moreau. Bimodal character of stress transmission in granular packings. *Phys. Rev. Letter*, 80:61–64, 1998.

[RWU07] Alexander Ries, Dietrich E Wolf, and Tamás Unger. Shear zones in granular media: three-dimensional contact dynamics simulation. *Phys Rev E Stat Nonlin Soft Matter Phys*, 76(5 Pt 1):051301, Nov 2007.

[SCG$^+$06] G. Saussine, C. Cholet, P.E. Gautier, F. Dubois, C. Bohatier, and J.J. Moreau. Modelling ballast behaviour under dynamic loading. part 1: A 2d polygonal discrete element method approach. *Computer Methods in Applied Mechanics and Engineering*, 195(19-22):2841–2859, April 2006.

[SGL02] Leonardo E Silbert, Gary S Grest, and James W Landry. Statistics of the contact network in frictional and frictionless granular packings. *Phys Rev E Stat Nonlin Soft Matter Phys*, 66(6 Pt 1):061303, Dec 2002.

[SVR02] L. Staron, J.-P. Vilotte, and F. Radjai. Preavalanche instabilities in a granular pile. *Phys. Rev. Lett.*, 89:204302, 2002.

[TCRB05] A. Taboada, K. J. Chang, F. Radjai, and F. Bouchette. Rheology, force transmission, and shear instabilities in frictional granular media from biaxial numerical test using the contact dynamics method. *Journal Of Geophysical Research*, 110:1–24, 2005.

[Tho93] C. Thornton. Computer simulation of impact fracture/fragmentation. In *The first Nisshin Engineering Particle Technology International Seminar: Discrete Particle Simulations in Powder Technology*, page 17, Osaka, Japan, 1993.

[Tho97] C. Thornton. Coefficient of restitution for collinear collisions of elastic-perfectly plastic spheres. *Journal of Applied Mechanics*, 64:383–386, 1997.

[TLM17] K. Taghizadeh, S. Luding, and V. Magnanimo. DEM applied to soil mechanics. *ALERT geomaterials Doctoral School 2017, Aussois, France*, 2017.

[TWT17] D. Tunuguntla, T. Weinhart, and A. Thornton. Discrete particle simulations with MercuryDPM. *ALERT geomaterials Doctoral School 2017, Aussois, France*, 2017.

[TY91] C. Thornton and K. K. Yin. Impact of elastic spheres with and without adhesion. *Powder Technol.*, 65:153, 1991.

Fluid-grain coupling using the Lattice Boltzmann method

J.-Y. Delenne[1], L. Amarsid[2], P. Mutabaruka[3],
V. Richefeu[4], F. Radjai[2,3]

[1]IATE, UMR 1208, Université de Montpellier, INRA, CIRAD, SupAgro, F-34060 Montpellier, France
[2]LMGC, UMR 5508, Université de Montpellier, CNRS, F-34090 Montpellier, France
[3]$\langle$MSE$\rangle^2$, UMI CNRS, Massachusetts Institute of Technology, Cambridge, USA
[4]3SR, UMR 5521, Université Grenoble Alpes, Grenoble-INP, CNRS, F-38000 Grenoble, France

---

The objective of this chapter is to describe the interfacing of the Lattice Boltzmann Method for the simulation of fluids with the Discrete Element Method for the simulation of a collection of rigid particles. For the sake of simplicity, the statistical physics concepts underlying the method are not detailed, and the algorithms are only presented in 2D. The Boltzmann equation is discretized using a standard D2Q9 model in which the fluid pseudo-particles can move on a lattice with 9 possible directions of motion. The classical fluid dynamics quantities are defined as sums of local probability densities of finding particles at a specific time and position, and with a given momentum. The Lattice Boltzmann equation is then resolved in two steps. The first step is the so-called Streaming step that consists in computing the advection of the fluid particles. The second step computes the relaxation of the system as a result of possible collisions between fluid particles. Two models are presented for the collision step: the Single Relaxation Time model and the Multiple Relaxation time model. Different boundary conditions are detailed for the implementation of no-slip conditions for the fluid in contact with solid grains or walls (imposed pressure, imposed flow, open boundary conditions and Bounce Back approaches…). Finally, we detail the momentum exchange method for the fluid-grain coupling, and we conclude with examples of simulated systems using this approach.

1 Introduction

Fluid-grain interactions remain poorly understood despite their very broad range of applications in science and engineering. These interactions control the physical properties of fluid-filled granular media in many industrial processes or environmental systems such as fluid-grain mixtures, fluidized beds, agglomeration processes, suspensions, saturated soils, landslides and etc.

Different methods have been developed for the simulation of an assembly of grains [RD11, PS05]. The Discrete Element Method (DEM) is well documented, and it has become a popular tool for the modeling of granular materials. It has been employed for numerous engineering and environmental applications [SCDV$^+$11, SR05]. The case of the coupling of a fluid with a granular phase is much less developed in the literature, and many technical issues remain unexplored. Several numerical approaches are available to account for fluid-grain interactions:

- The Stokesian Dynamics Method was initiated by Brady and Bossis [BB88]. It is based on a multipole expansion of hydrodynamic interactions into long-range contributions of all the particles and the effect of lubrication between pairwise interactions. The main issue with this type of approach is its low numerical efficiency.
- The Pore-scale fluid network model developed by Chareyre *et al.* [CCCB12] combines the DEM for the solid phase and a finite volume formulation for the fluid phase modeled as flowing in channels connecting the pores between the grains. This method considers an incompressible Stokes flow and assumes only viscous forces.
- Tsuji *et al.* [TKT93] and McNamara *et al.* [McN93] proposed a DEM-CFD coupling in which the fluid is resolved on a meso-scale grid with a mesh-size of a few grain diameters. The fluid-granular material interaction relies on a Darcy law evaluated at the scale of the grid. This type of approach is computationally very efficient but fails to provide information about the fluid dynamics at the scale of contacts.
- The continuum mechanics approaches based on the resolution of the classical Navier-Stokes equation allows one to simulate the motion of Newtonian fluids at a sub-particle scale. Several models were proposed to describe the fluid-grain coupling such as the Distributed Lagrange Multiplier/Fictitious Domain [GPHJ99] for a regular mesh [Wac11] or adaptative mesh [Mau99]. In these methods the main variables are the density, velocity and pressure fields determined at the level of the meshing nodes.
- A popular method for grain-fluid coupling is the Lattice Boltzmann Method (LBM) [CD98]. The advantages of the LBM among other methods are its straightforward implementation of boundary conditions and its good scalability in parallel computing. Another great advantage of the LBM is its ability to sim-

ulate complex physics such as, for example, emulsions [FZB$^+$16], liquid-gas phase change in porous materials [WWPC07], foams [KTH$^+$05], free surfaces [JGK13].

In this chapter, we focus on the LBM and its coupling with the DEM. The LBM evolved from the Lattice-Gas Cellular Automata (LGCA), a statistical model based on the kinetic theory of gases, which simulates the fluids as pseudo-particles at discrete points in space[Suc01]. Contrary to the other numerical methods, in LBM the fluid variables are partial probability functions of finding virtual fluid particles moving from site to site on a lattice. In the most classical methods, the LBM relies on a regular grid of nodes, called lattice nodes, which interact only with their direct neighbors. In the LBM, the "classical" fluid variables mentioned previously are upscaled by averaging the partial distribution functions at each node.

Below, we briefly present the LBM to simulate fluid flows. Then, we consider the coupling of the fluid phase to a particle phase modeled by the DEM. For clarity, in this chapter we only consider the 2D case.

2 Lattice Boltzmann Method

In the LBM, the fluid is described by the time-dependent distribution function $f(\vec{r}, \vec{v}, t)$ of the positions $\vec{r}$ and velocities $\vec{v}$ of fluid particles. The spatio-temporal evolution of f is governed by the Boltzmann equation:

$$\left(\frac{\partial}{\partial t} + \vec{v} \cdot \frac{\partial}{\partial \vec{r}} + \frac{\vec{F}(\vec{r})}{m} \cdot \frac{\partial}{\partial \vec{v}}\right) f(\vec{r}, \vec{v}, t) = \Omega_{coll} \tag{1}$$

where m is the particle mass, $\vec{F}(\vec{r})$ represents the external forces, and Ω_{coll} is the collision operator describing the dynamics of collisions between fluid particles.

A limited number of velocity directions are considered. While different lattice type can be used for velocity directions, we present here more specifically the D2Q9 model (Fig. 1), which assumes 9 directions of motion for the fluid particles $i = \{0, 1, \ldots, 8\}$. A distinct partial distribution function f_i is attributed to each velocity direction $\vec{e}_i$:

$$[\vec{e}_0, \vec{e}_1, \ldots, \vec{e}_8] = c \begin{bmatrix} 0 & 1 & 0 & -1 & 0 & 1 & -1 & -1 & 1 \\ 0 & 0 & 1 & 0 & -1 & 1 & 1 & -1 & -1 \end{bmatrix} \tag{2}$$

where c is the so-called 'lattice velocity' defined by:

$$c = \Delta x / \Delta t \tag{3}$$

with lattice step Δx and time step Δt.

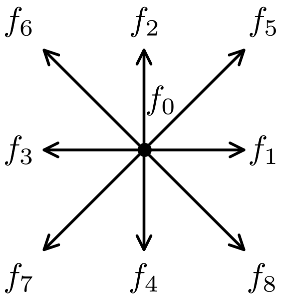

Figure 1: D2Q9 model.

The density and velocity fields $\rho(\vec{r},t)$ and $\vec{u}(\vec{r},t)$, respectively, are defined from partial density functions and lattice directional velocities as

$$\begin{aligned}\rho(\vec{r},t) &= \sum_i f_i(\vec{r},t)\\ \rho(\vec{r},t)\vec{u}(\vec{r},t) &= \sum_i \vec{e}_i f_i(\vec{r},t)\end{aligned} \tag{4}$$

To simplify the equations, we set $\Delta x = 1$, $\Delta t = 1$. In these“lattice units”, the lattice speed is $c = 1$.

2.1 Discrete Boltzmann equation

The evolution of the density distribution functions is given by the discretized Boltzmann equation:

$$f_i(\vec{r} + \Delta t\vec{e}_i, t + \Delta t) - f_i(\vec{r},t) = \Omega_i \tag{5}$$

This equation is computed at each node in two steps:

1. A streaming or advection step, which consists in propagating the values of the density functions $f_i^{out}(\vec{r},t)$ along each direction i (Fig. 2):

$$f_i(\vec{r} + \Delta t\vec{e}_i, t + \Delta t) = f_i^{out}(\vec{r},t) \tag{6}$$

2. A collision step, in which the densities $f_i^{out}(\vec{r},t)$ are updated from the collisions between fluid particles coming from adjacent nodes $f_i^{in}(\vec{r},t)$ (Fig. 3) :

$$f_i^{out}(\vec{r},t) = f_i^{in}(\vec{r},t) + \Omega_i \tag{7}$$

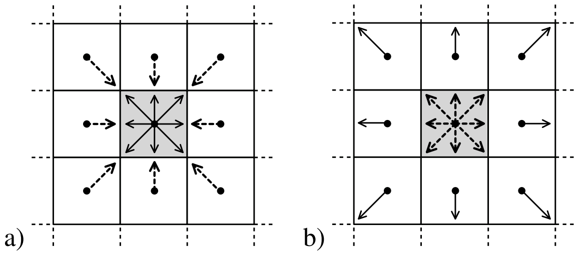

Figure 2: Streaming step : (a) state of the fluid node at time t. (b) At $t + \Delta t$ density functions are propagated toward the neighboring nodes using Eq. 6.

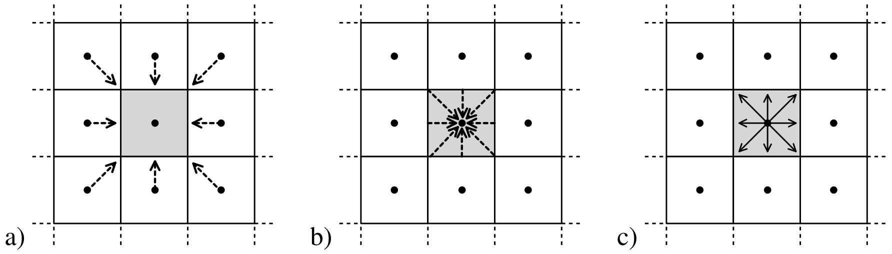

Figure 3: Collision step: (a) density functions f_i^{in} at time t. (b) Collision of nodes with density function f_i^{in}. (c) New density functions f_i^{out} at time $t + \Delta t$.

2.2 Single Relaxation Time collision operator

The collision operator can be approximated in different ways. The most classical approximation is the so-called Single Relaxation Time[1]:

$$\Omega_i = -\frac{1}{\tau}(f_i(\vec{r},t) - {f_i}^{eq}(\vec{r},t)),\ i \in \{0,1,\ldots,8\} \tag{8}$$

In this approximation, for each direction i, the collision process is considered as a linear relaxation of the density function $f_i(\vec{r},t)$ toward an equilibrium function ${f_i}^{eq}(\vec{r},t)$ in a time τ. These equilibrium functions can be obtained using a Taylor expansion of Maxwell's equilibrium function:

$$f_i^{eq} = w_i\rho(1 + 3\vec{e}_i \cdot \vec{u} + \frac{9}{2}(\vec{e}_i \cdot \vec{u})^2 - \frac{3}{2}\vec{u} \cdot \vec{u}) \tag{9}$$

---

[1] SRT is frequently called BGK operator following the work by Bhatnagar, Gross and Krook [BGK54]

where the coefficients w_i are weight coefficients depending on the meshing model. For the D2Q9 model, we have

$$\begin{cases} w_i = 4/9, & \text{for } ||\vec{e}_i|| = 0 \\ w_i = 1/9, & \text{for } ||\vec{e}_i|| = 1 \\ w_i = 1/36, & \text{for } ||\vec{e}_i|| = \sqrt{2} \end{cases} \qquad i \in \{0, 1, \ldots, 8\} \tag{10}$$

The relaxation time is directly related to the kinematic viscosity ν of the fluid:

$$\nu = \frac{2\tau - 1}{6} \tag{11}$$

It is worth noting that the Navier Stokes equations can be recover directly from the Boltzmann equation and SRT [BGL91]. For perfectly quasi-incompressible fluids at low Mach number, we have

$$P = {c_s}^2 \rho \tag{12}$$

where ${c_s}^2 = \frac{1}{3}c$ is the velocity of sound in the fluid.

2.3 Multi-Relaxation-Time operator

In the SRT approach, all physical variables, and thus all moments of the distribution function, are relaxed with a single characteristic time τ. On the contrary, in the Multi-Relaxation-Time (MRT) approach all moments of the distribution can be relaxed with a specific independent characteristic time [D'H94, LL00, Del03, Del06]. In this approach, at each node of the domain one computes 9 moments m_i attributed to the 9 partial distribution functions f_i:

$$\mathbf{m} = \mathbf{M}\mathbf{F} \tag{13}$$

with $\mathbf{m} = (m_0\ m_1\ m_2\ m_3\ m_4\ m_5\ m_6\ m_7\ m_8\ )^T$ & $\mathbf{F} = (f_0\ f_1\ f_2\ f_3\ f_4\ f_5\ f_6\ f_7\ f_8)^T$. The matrix $\mathbf{M}$ is of order 9. It is inversible and each line is orthogonal to other lines:

$$\mathbf{M} = \begin{pmatrix} 1 & 1 & 1 & 1 & 1 & 1 & 1 & 1 & 1 \\ -4 & -1 & 2 & -1 & 2 & -1 & 2 & -1 & 2 \\ 4 & -2 & 1 & -2 & 1 & -2 & 1 & -2 & 1 \\ 0 & 1 & 1 & 0 & -1 & -1 & -1 & 0 & 1 \\ 0 & -2 & 1 & 0 & -1 & 2 & -1 & 0 & 1 \\ 0 & 0 & 1 & 1 & 1 & 0 & -1 & -1 & -1 \\ 0 & 0 & 1 & -2 & 1 & 0 & -1 & 2 & -1 \\ 0 & 1 & 0 & -1 & 0 & 1 & 0 & -1 & 0 \\ 0 & 0 & 1 & 0 & -1 & 0 & 1 & 0 & -1 \end{pmatrix} \tag{14}$$

The details of the full determination of this matrix for D2Q9 can be found in [DGK+02].

The collision step is applied in the moment space, each moment m_i being relaxed to its equilibrium state m_i^{eq} with a relaxation time s_i. The moment vector $\mathbf{m}^{out}$ resulting from collision can be written as follows:

$$\mathbf{m}^{out} = \mathbf{m} - \mathbf{S}(\mathbf{m} - \mathbf{m}^{eq}) \tag{15}$$

where $\mathbf{S} = diag\left(0, s_2, s_3, 0, s_5, 0, s_7, s_8, s_9\right)$ is a diagonal 9×9 matrix. All relaxation times are proportional to τ^{-1} [MAL09]. The equilibrium moment vector $\mathbf{m}^{eq}$ is given by:

$$\mathbf{m}^{\mathrm{eq}} = \begin{bmatrix} \rho \\ -2\rho + 3\left(j_x^2 + j_y^2\right)/\rho \\ \rho - 3\left(j_x^2 + j_y^2\right)/\rho \\ j_x \\ -j_x \\ j_y \\ -j_y \\ \left(j_x^2 - j_y^2\right)/\rho \\ j_x j_y/\rho \end{bmatrix} \tag{16}$$

The distribution functions $f_i^{out}(\vec{r}, t)$ resulting from the collision step are given by $\mathbf{f}^{\mathrm{out}} = \mathbf{M}^{-1}\mathbf{m}^{\mathrm{out}}$ and the streaming step is applied in the velocity space. The values of the relaxation times s_i can be determined from a stability analysis [NSCP06, LL00, MAL09]. Note that the moments corresponding to the density $\rho(\vec{r}, t)$ and the the momenta $(j_x, j_y) = (\rho\vec{u}_x, \rho\vec{u}_y)$ are conserved so that the corresponding relaxation times are equals to 0 (i.e. $s_1 = 0$, $s_4 = 0$ et $s_6 = 0$).

For the simulations reported below we use the values suggested by Mussa *et al.* [MAL09]:

$$s_2 = 1.63, s_5 = s_7 = 1.92, s_8 = s_9 = 1/\tau \tag{17}$$

We note that the SRT approach can be recovered by setting all relaxation times to $1/\tau$ in the MRT approach.

2.4 Algorithm

To simulate the flow of a newtonian fluid using the LBM, we first need to initiate $f_i(\vec{r}, t)$ at $t = 0$ using the average density ρ_0 and the initial velocities $\vec{u}_0$. This can be done thanks to the equilibrium function (Eq. 9):

$$f_i(\vec{r}, t = 0) = f_i^{eq}(\rho_0, \vec{u}_0) \tag{18}$$

A standard LBM algorithm consists in iterating over the steps:

- Computation of the collisions (Eq. 7).
- Streaming of fluid particles (Eq. 6).
- Computation of the missing f_i at the boundaries (Eq. 19).
- Update of the densities $\rho(\vec{r}, t)$ and velocities $\vec{u}(\vec{r}, t)$ using Eq. (4).

The following conditions must be satisfied to ensure the stability of the algorithm [SC96]:

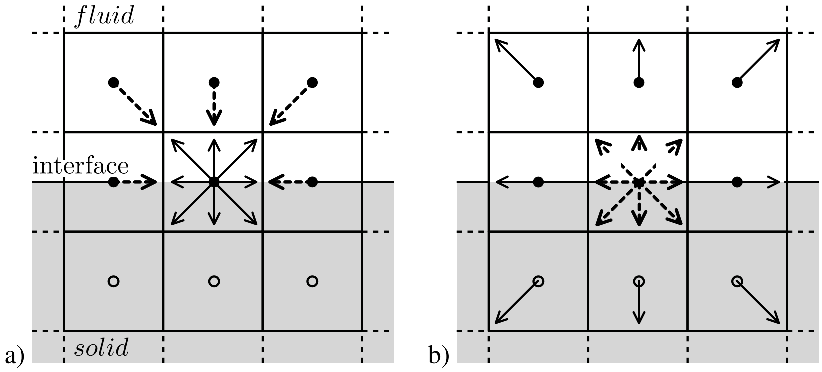

Figure 4: (a) Density functions of a fluid node in contact with a solid wall. (b) The missing f_i values after streaming step.

1. For each node of the fluid domain, $\|\vec{u}(\vec{r},t)\|$ must be lower than the sound velocity on the lattice $c_s = \frac{1}{\sqrt{3}}\frac{\Delta x}{\Delta t}$. This condition corresponds to a Mach number $Ma = \frac{\max \|\vec{u}(\vec{r},t)\|}{c_s} < 1$ and ρ satisfies $\rho = \rho_0 + O(Ma^2)$ [Del03].
2. The relaxation time τ is related to the viscosity ν through Eq. (11). As the viscosity is a positive quantity, the condition $\tau > 1/2$ must be satisfied. This condition may be difficult to fulfill with SRT as this collision operator generates numerical instabilities at values of the viscosity. For this reason, the MRT approach should be preferred [MA05, CZ11].

3 Boundary conditions

One of the main advantages of the LBM is that complex boundary conditions can easily be implemented. To illustrate the way the boundary conditions are implemented, let us consider a fluid domain with a wall at the lower boundary (Fig. 4b). This figure shows that after the streaming step the values of f_i at the fluid nodes in contact with the wall are unknown. In the following we detail how such values can be determined for different boundary conditions.

3.1 Periodic boundaries

The periodic boundaries are simple to program. They are frequently employed to limit the size of the fluid domain, and they are particularly interesting for the investigation of large cumulative shearing in fluid or suspensions. To set a periodicity of the domain along the x axis, we use cylindrical topology as illustrated in Fig. 5. For this specific case, the fluid nodes on both side of the periodic domain become adjacent. Hence, the streaming step can be computed without additional operation and the ${f_i}^{in}$ leaving the domain from the position x_{in} are advected to the nodes located at x_{out}. In the same way, the ${f_i}^{out}$ leave the nodes x_{out} and are advected towards the nodes x_{in}.

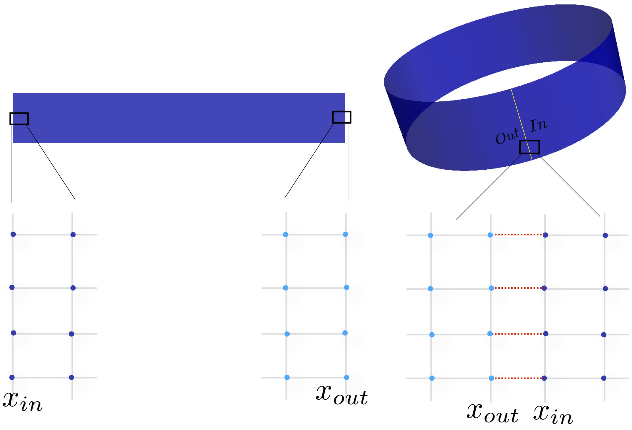

Figure 5: Analogy between periodic domain and a cylindrical domain. The fluid nodes at x_{in} and x_{out} becomes adjacent.

3.2 Bounce-Back condition

In the LBM, the Bounce-Back (BB) technique is widely used to implement the no-slip condition at the boundary of a solid obstacle. In 2D, the BB condition (Fig. 6) consists in setting all unknown values of f_i to those of the opposite values f_{iopp}.

$$f_i^{in}(\vec{r}, t + \Delta t \vec{e}_i) = f_{iopp}^{out}(\vec{r}, t) \tag{19}$$

where f_i^{in} and f_{iopp}^{out} are, respectively, the 'in' and 'out' distribution functions and $iopp$ stands for the direction opposite to i. The precision of this boundary condition is of first order [CdL91] and may be improved by placing the interface at mid-distance between the wall and the fluid node [Zie93, CMM96, GNGB97, KKH$^+$99].

3.3 Bounce-Forward condition

The Bounce-Forward condition (BF) is used allow the slipping of the fluid in contact with a wall. Fig. 7 shows an example of BF which consists in a specular reflection of the f_i at the level of the wall.

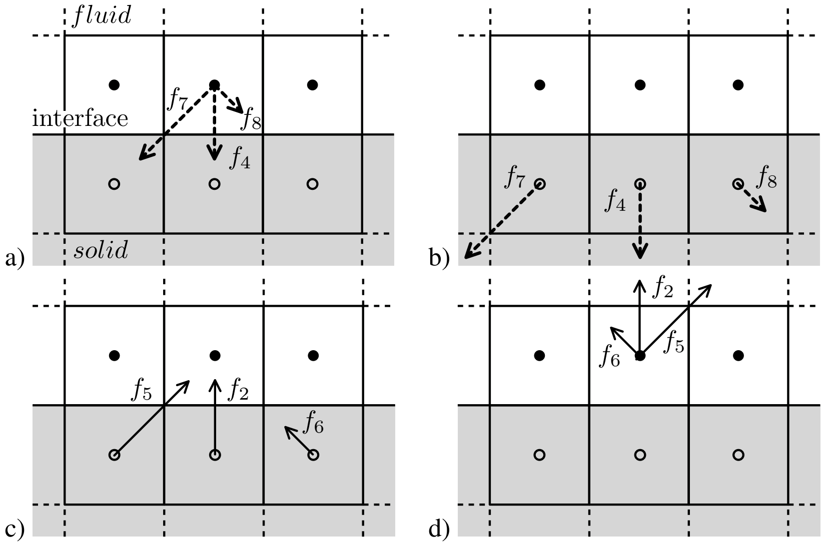

Figure 6: Missing f_i in the Bounce-Back technique, (a) before streaming, (b) streaming, (c) bounce back, (d) after streaming.

.

Note that it is also possible to associate BB and BF in order to control the slipping condition between fluid and solid surfaces[AH09, Suc01, Suc02, ZTPM05, VDR07] :

$$f_i^{in}(\vec{r}, t + \Delta t \vec{e}_i) = Scf_i{}^{BF} + (1 - Sc)f_i{}^{BB} \tag{20}$$

where $f_i{}^{BB}$ and $f_i{}^{BF}$ are respectively the density functions obtained from the BB and the BF, $Sc \in [0, 1]$ controls the slipping magnitude. Fig. 8 shows the effect of the latter for a pipe flow [Suc02].

3.4 Dirichlet Pressure Boundary condition

A Pressure Boundary (PB) condition can be implemented [ZH97] at a boundary of a fluid domain by using equation (12), which links the pressure to the fluid density. Applying a pressure P can thus be done by controlling ρ.

Fig. 9 shows a PB condition in which a pressure P is applied. By assuming zero velocity along the y axis ($u_y = 0$), four unknown variables have to be determined (f_1, f_5, f_8 and the velocity u_x along x) using four equations:

$$\rho = f_1 + f_2 + \cdots + f_8 \tag{21}$$

which is the expression of ρ (Eq. (4)).

$$\rho u_x = f_1 + f_5 + f_8 - (f_3 + f_6 + f_7) \tag{22}$$

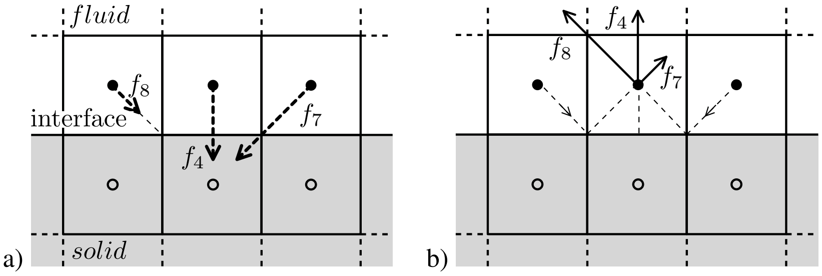

Figure 7: Bounce-Forward, before (a) and after (b) streaming step.

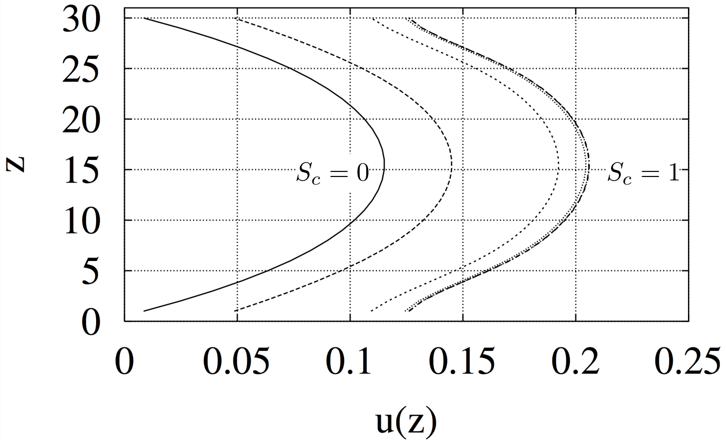

Figure 8: Velocity profile in a pipe showing the velocity u as a function of the height z for $Sc = 0, 10^{-5}, 10^{-4}, 10^{-3}, 10^{-2}, 1$. The curve $S_c = 0$ corresponds to a classical Poiseuille profile [Suc02].

.

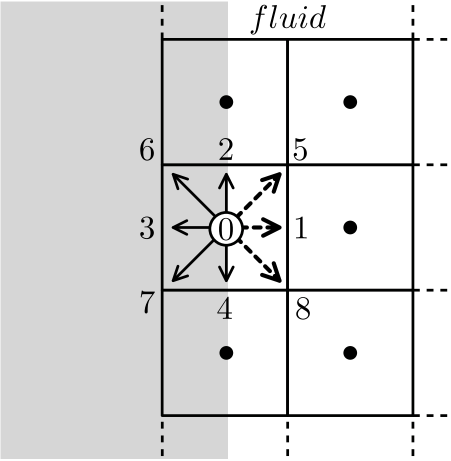

Figure 9: Pressure Boundary condition. The directions in red correspond to the f_i values which should be determined.

and

$$\rho u_y = 0 = f_2 + f_5 + f_6 - (f_4 + f_7 + f_8) \tag{23}$$

which are the projections of $\rho\vec{u}$ (Eq. 4) on x and y axes. The last equation is called the Zou and He [ZH97] assumption. It consists in applying a bounce-back for the non-equilibrated part of both f_i whose velocity directions $\vec{e}_i$ are perpendicular to the boundary surface:

$$f_1 - {f_1}^{eq} = f_3 - {f_3}^{eq} \tag{24}$$

where ${f_1}^{eq}$ and ${f_3}^{eq}$ are given by Eq. (9). The solution of the above system of equations is

$$\begin{array}{c} u_x = -1 + (f_0 + f_2 + f_4 + 2(f_3 + f_7 + f_6))/\rho \\ f_1 = f_3 + \frac{2}{3}\rho u_x \\ f_5 = f_7 - \frac{1}{2}(f_2 - f_4) + \frac{1}{6}\rho u_x \\ f_8 = f_6 + \frac{1}{2}(f_2 - f_4) + \frac{1}{6}\rho u_x \end{array} \tag{25}$$

3.5 Neumann Flux Boundary condition

Flux Boundary Condition (FB) is used to impose a flow rate by setting the velocity $\vec{u} = (u_x, 0)$ at a boundary. The unknown variables are then f_1, f_5, f_8 and the fluid density ρ. Using the above equations we get the same expressions (Eq. 25) for f_1, f_5 and f_8 with

$$\rho = (f_0 + f_2 + f_4 + 2(f_3 + f_7 + f_6))/(1 - u_x) \tag{26}$$

3.6 Open Boundary condition

An Open Boundary Condition (OB) condition is used when it is necessary to absorb pressure waves at the boundaries of the fluid domain. Several authors have worked on the OBC [LGS13, JY08, JY11, IMLF09, OS00] and some methods may be difficult to implement. In this chapter, we only discuss the Extrapolation Boundary Condition (EBC) [JY11] which is a simple linear approach. The unknown density functions f_i at the boundary of the domain are determined using the two first neighboring nodes (Fig. 10). The $f_i(x_n, t)$, which are unknown at the position x_n, are computed using:

$$f_i(x_n, t) = 2f_i(x_{n-1}, t) - f_i(x_{n-2}, t) \tag{27}$$

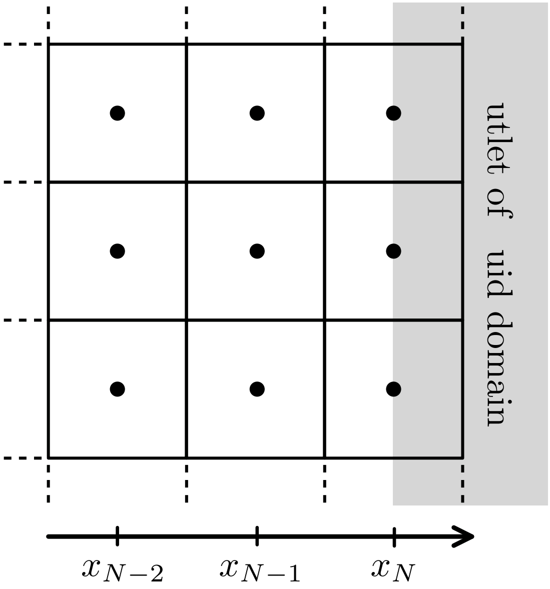

Figure 10: Schematic view of free boundary conditions.

Fig. 11 shows an example in which a pressure wave propagates in a square domain. The wave is obtained by imposing at initial time an overpressure on the circular zone in the middle of the sample. Two simulations were performed with 1) zero pressure using the Pressure Boundary conditions and 2) Open Boundary conditions.

Fig. 12 shows the results for different running times. For the OB conditions the density wave expands out of the domain with very little perturbation at the level of the boundaries. On the contrary, with the PB conditions the wave is partially reflected at the boundary surface. Fig. 13 compares the waves along the x axis before and after reflection for both OB and PB conditions.

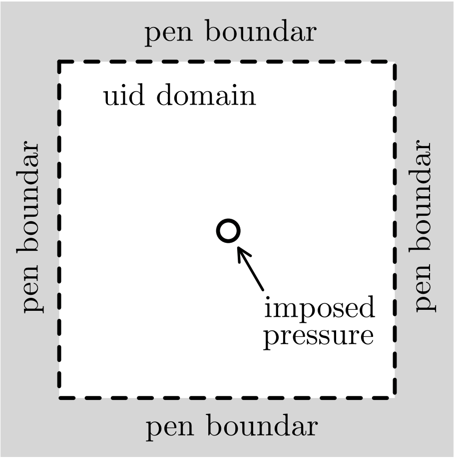

Figure 11: Simulation of the propagation of a density wave in a square domain.

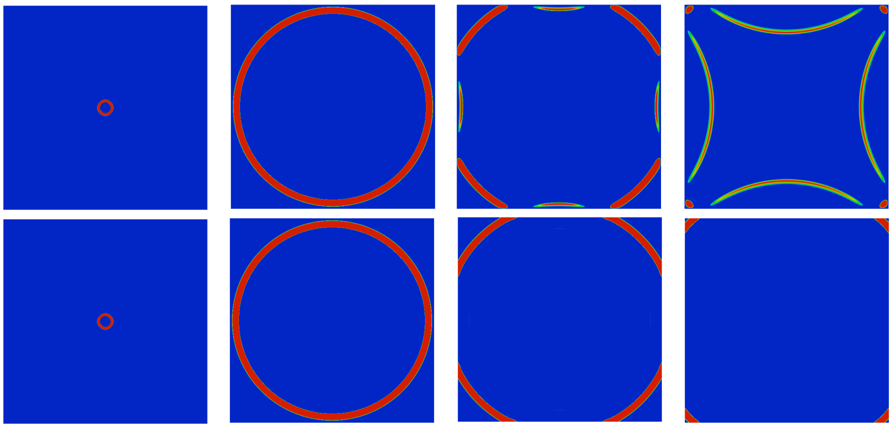

$t = 0$ $t = 0.75s$ $t = 0.9s$ $t = 1.1s$

Figure 12: Comparison of the wave propagation with PB condition (above) and OB condition (below).

4 LBM–DEM coupling

In this section, we discuss the coupling between the Discrete Element Method (DEM) and the Lattice Boltzmann Method. We first recall the basics of the classical DEM [CS79]. The fluid-grain interaction is then described in detail and finally some benchmark tests are presented.

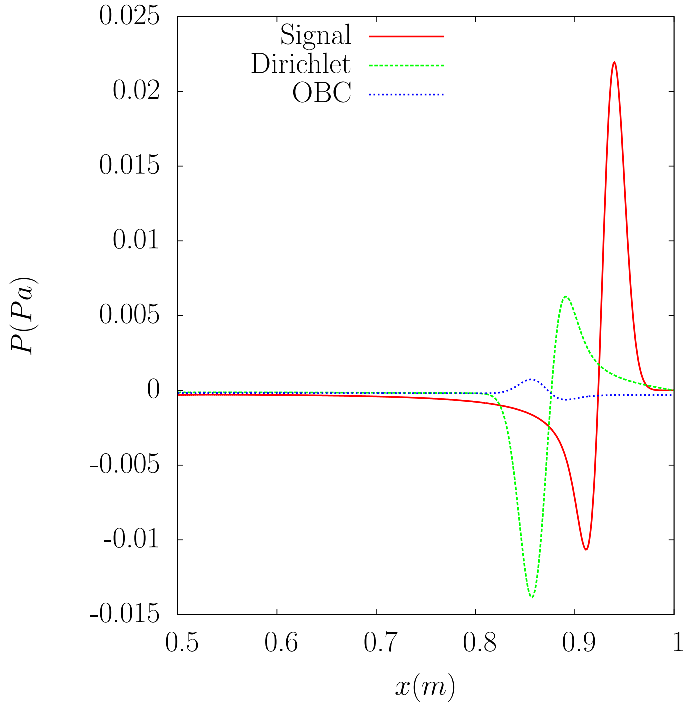

Figure 13: Pressure wave along the x axis. The red curve shows the pressure wave before touching the boundary whereas the two other curves show the reflected waves.

4.1 Discrete Element Method

The DEM is based on the assumption of rigid grains interacting through frictional contacts. Newton's equations of motion are integrated for all rigid-body degrees of freedom with simple force laws expressing the normal and friction forces as explicit functions of the elastic deflexion defined from the relative positions and displacements of the grains at their contact points:

$$m_i \frac{d^2 \vec{r}_i}{dt^2} = \vec{F}_i, \; i = 1 \ldots N \tag{28}$$

where N is the total number of grains and m_i and $\vec{r}_i$ are respectively the mass and the position of the grain i. The resultant force $\vec{F}_i$ applied on i can be decomposed as

$$\vec{F}_i = \sum_{j \neq i} \vec{F}c_{ij} + \vec{F}g_i + \vec{F}h_i \tag{29}$$

where $\sum\limits_{j\neq i} \vec{F}c_{ij}$ represents the contact forces, $\vec{F}g_i$ is the gravity force and $\vec{F}h_i$ is the hydrodynamics force which results from the action of the fluid at the surface of the grain.

Let us consider a local reference frame $(\vec{n}_{ij}, \vec{t}_{ij})$ at the contact between two grains, $\vec{F}_{ij}$ can be projected on these axis (Fig. 14):

$$\vec{F}_{ij} = F_N \vec{n}_{ij} + F_T \vec{t}_{ij} \tag{30}$$

where F_N and F_T are the normal and tangential components of the contact force.

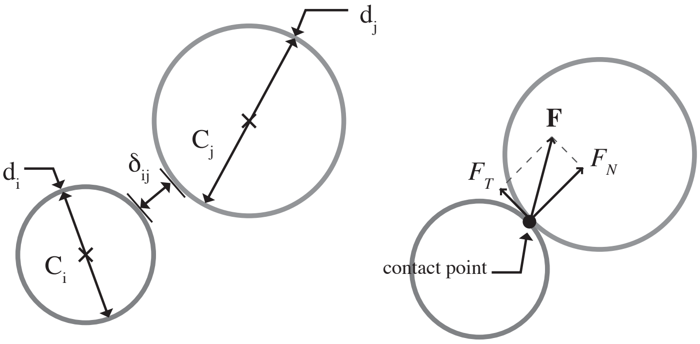

Figure 14: Contact between two grains.

Although more accurate models exist in the literature, we consider here a simple viscoelastic law for the contact force (Fig. 15a):

$$\vec{F}_N = \begin{cases} \left(-k_n \delta_{ij} - \gamma_n v_n\right) \vec{n}_{ij} & \text{if } \delta_{ij} < 0 \\ \vec{0} & \text{else} \end{cases} \tag{31}$$

where k_n is normal contact stiffness, γ_n is a damping coefficient, δ_{ij} (Fig. 14) is the normal distance between particles (or overlap when there is a contact between grains). For disks, we have $\delta_{ij} = \|\vec{r}_i - \vec{r}_j\| - (R_i - R_j)$. F_T can be calculated using a regularized Coulomb's friction law (Fig. 15b) that depends on the tangential relative velocity $\vec{v}_t$:

$$\vec{F}_T = -\min\left\{\gamma_t \|\vec{v}_t\| \,; \mu_f F_N\right\} \vec{t}_{ij} \tag{32}$$

The equations of motion are integrated according to a velocity Verlet scheme :

1. $\vec{v}_i(t + \frac{1}{2}\Delta t) = \vec{v}_i(t) + \frac{1}{2}\vec{a}_i(t)\Delta t$
2. $\vec{r}_i(t + \Delta t) = \vec{r}_i(t) + \vec{v}_i(t + \frac{1}{2}\Delta t)\Delta t$

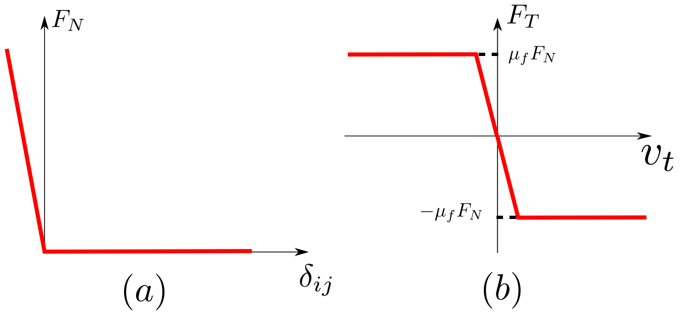

Figure 15: (a) Linear contact law; (b) Regularized friction law.

3. $\vec{a}_i(t+\Delta t) = \frac{1}{m_i}\vec{F}_i$
4. $\vec{v}_i(t+\Delta t) = \vec{v}_i(t+\frac{1}{2}\Delta t) + \frac{1}{2}\vec{a}_i(t+\Delta t)\Delta t$

The conditions of stability of this mass-spring system have been studied in detail in [RD11]. Without entering the details, the numerical stability of the above scheme is ensured for a time step below collision duration, which may be estimated for linear elastic interactions to be $t_c = \sqrt{m/k_n}$, where $k = \max\{k_n, k_t\}$. In order to damp the elastic oscillations, the viscosity parameters can be increased but should remain below $\gamma_n = 2\sqrt{mk_n}$. More information about Discrete Element modeling (DEM) can be found in [LRW17, TWT17].

To compute the fluid-grain interactions, the grains need first to be meshed on the same lattice grid as the fluid. The nodes which belong to the grains are the 'solid nodes'. The coupling of LBM and DEM is thus ensured by calculating the interactions at the interface between the fluid and the solid nodes (Fig. 16). The latter are considered as moving boundaries over which the no-slip condition is imposed [BFL01]. On the other hand, the hydrodynamic forces acting on particles are calculated by the momentum exchange method proposed in [Lad94].

4.2 Effect of the grain on the fluid

For the fluid, the solid nodes at the fluid-grain interface are mobile boundaries where a Bounce-Back technique can be applied to determine the missing values of the partial distribution functions during the streaming step. In order to take accurately into account the positions of these moving boundaries, an interpolation method developed by Bouzidi et Lallemand [BFL01, LL03], can be used.

Let us consider a simple one-dimensional case in which the velocity of the wall is

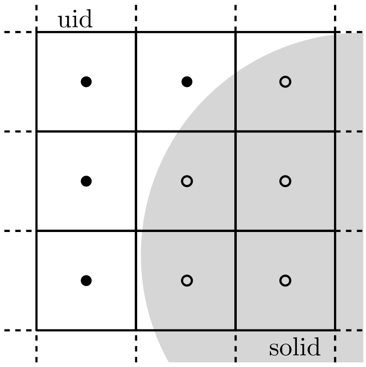

Figure 16: A grain immersed in the lattice fluid domain.

assumed to be zero. The location of the wall can be given by $q = |x_f - x_b|/\Delta x$. where x_f and x_s are the positions of the closest fluid and solid nodes to the interface and x_b is the position of the ”real” solid interface of the grain. A particle leaving x_f and reflected on the wall will not reach a fluid node after moving over a total distance of Δx except if q is equal to 0, 1/2, or 1; see Fig. 17. The algorithm thus depends on q:

- For $q = 1/2$, a fluid particle leaving the position x_f bounces back on the wall and comes back to its initial position x_f (Fig. 17a). The classical Bounce-Back condition can be used without modification and $f_i(x_f, t + \Delta t) = f_{iopp}^{out}(x_f, t)$.
- for $q > 1/2$ the fluid particle leaves the position x_f and bounces on the wall to a position which is between x_f and x_b (Fig. 17b). The partial density function can be determined using linear interpolation: $f_i(x_f, t+\Delta t) = \dfrac{1}{2q} f_{iopp}^{out}(x_f, t) + \dfrac{(2q-1)}{2q} f_i^{out}(x_f, t)$
- for $q < 1/2$, the particle leaves x_f and bounces to a position between x_f and $x_{f'}$ (Fig. 17c). In this last case, a linear interpolation yields $f_i(x_f, t + \Delta t) = 2q f_{iopp}^{out}(x_f, t) + (1 - 2q) f_{iopp}^{out}(x_{f'}, t)$.

In the case of moving boundaries, we need to take into account the motion of the grains in the calculation of the partial density functions $f_i(x_f, t + \Delta t)$ [BFL01]. Thus,

- for $q \geqslant 1/2$

$$f_i(x_f, t + \Delta t) = \frac{1}{2q} f_{iopp}^{out}(x_f, t) + \frac{(2q-1)}{2q} f_i^{out}(x_f, t) + \partial f_i \tag{33}$$

- for $q < 1/2$

$$f_i(x_f, t + \Delta t) = 2q f_{iopp}^{out}(x_f, t) + (1 - 2q) f_{iopp}^{out}(x_{f'}, t) + \partial f_i \tag{34}$$

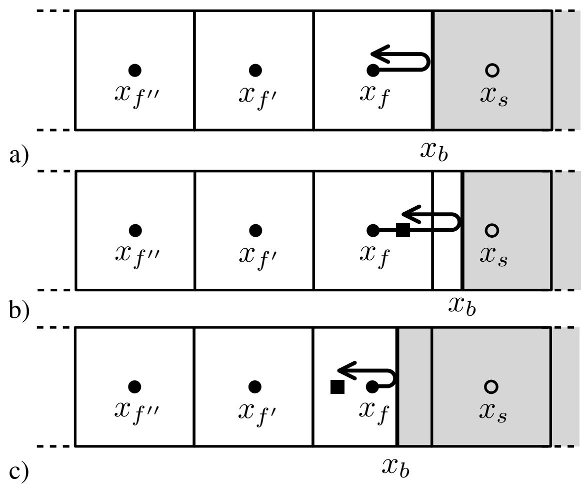

Figure 17: Details of the collision process on a rigid wall.

where ∂f_i is used to impose a velocity of the fluid equal to the velocity $\vec{V_0}$ of the wall, which corresponds to vanishing relative velocity. Thus,

- $q \geqslant 1/2$

$$\partial f_i = \frac{3}{q} w_i \vec{V_0}.\vec{e_i} \tag{35}$$

- $q < 1/2$

$$\partial f_i = 6 w_i \vec{V_0}.\vec{e_i} \tag{36}$$

where the w_i are the density weights defined previously (Eq. (10)) and the $\vec{e_i}$ are the velocities (Eq. (2)).

4.3 Effect of the fluid on the grain

The effect of the fluid on the grain is taken into account through the resulting hydrodynamic force $\vec{F}$. This force is then directly applied to the center of mass of the grain. In order to compute the hydrodynamic force, we use a method proposed by Ladd [Lad94], which relies on the momentum transfer through the fluid-grain interface. During the streaming step, the partial distribution function $f_i(x_f, t)$ at a position x_f at a fluid node attached to the interface rebounds on the wall and becomes $f_{iopp}(x_f, t + \Delta t)$. The resulting hydrodynamic force $\partial\vec{F}$ is thus given by

$$\partial\vec{F} = \left(f_{iopp}(x_f, t + \Delta t) + f_i(x_f, t)\right) \vec{e_i} \tag{37}$$

As the distribution function $f_i(x_f, t)$ is propagated to the position x_s, we get $f_i(x_s, t+\Delta t) = f_i(x_f, t)$. The resultant force can be obtained by adding all $\partial\vec{F}$ values for each solid node x_s of the interface which have at least one neighbor fluid node.

5 Conclusions

In this chapter, a short and functional presentation of the Lattice Element Method (LBM) for the simulation of fluids was given in 2D. We also described the basics of a coupled DEM-LBM approach for the simulation of fluid-grain mixtures. A major advantage of this approach is that it provides a detailed description of fluid dynamics at the scale of the particles. Furthermore, it has a very good scalability for parallel computing. Another important advantage of the DEM-LBM approach is that complex boundary conditions can easily be implemented. It is also important to mention here that the LBM can be used for the simulation of multi-fluid systems such as liquid-vapor systems and their interface by introducing temperature- and pressure- dependent densities.

As a conclusion of this chapter, we show in Fig. 18 recent examples in the case of dense suspensions of granular materials and in Fig. 19 advanced LBM simulations of grain-liquid-gas systems.

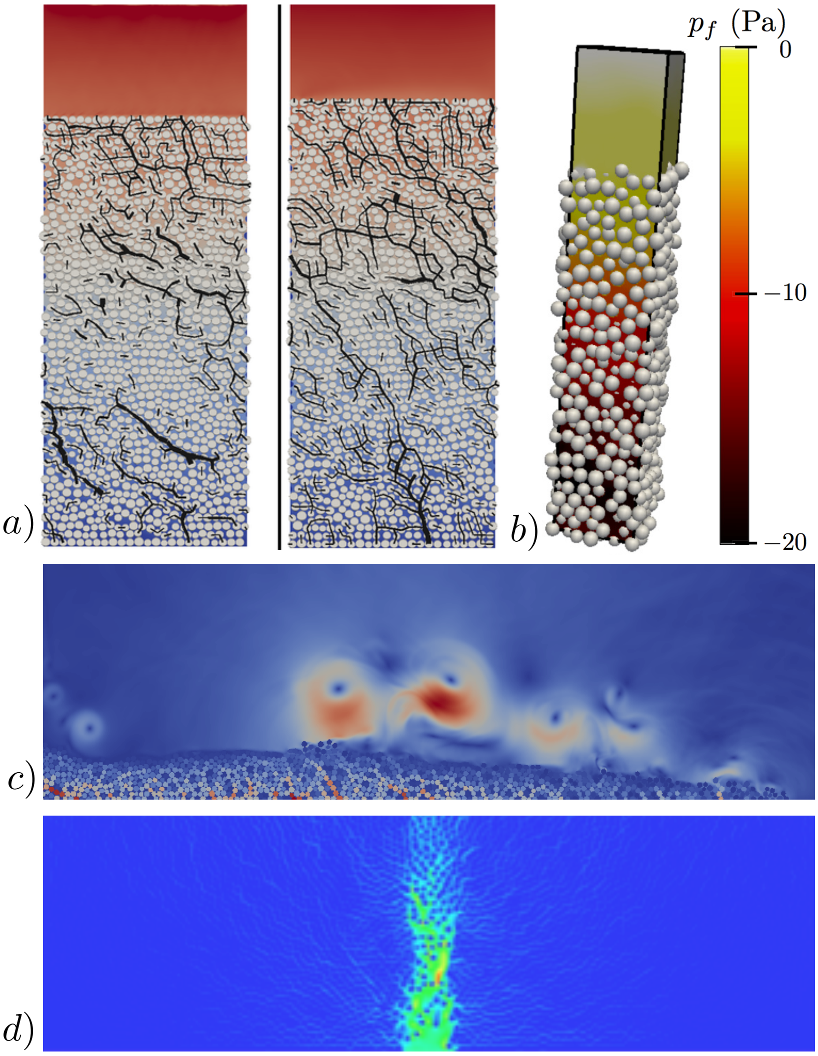

Figure 18: a) A periodic granular sample immersed in water is sheared (left). Increase in volume for a highly viscous fluid (right) [ADM$^+$17]. b) Example of a 3D biperiodic column of grains spreading under its own weight. The colors show the negative pressure during a creeping phase before the onset of the avalanche [MDSR14]. c) Example of deposit due to the underwater spreading of an immersed granular column. d) Simulation of the internal erosion of a sand bed by localized resurgence of water [NPB$^+$15].

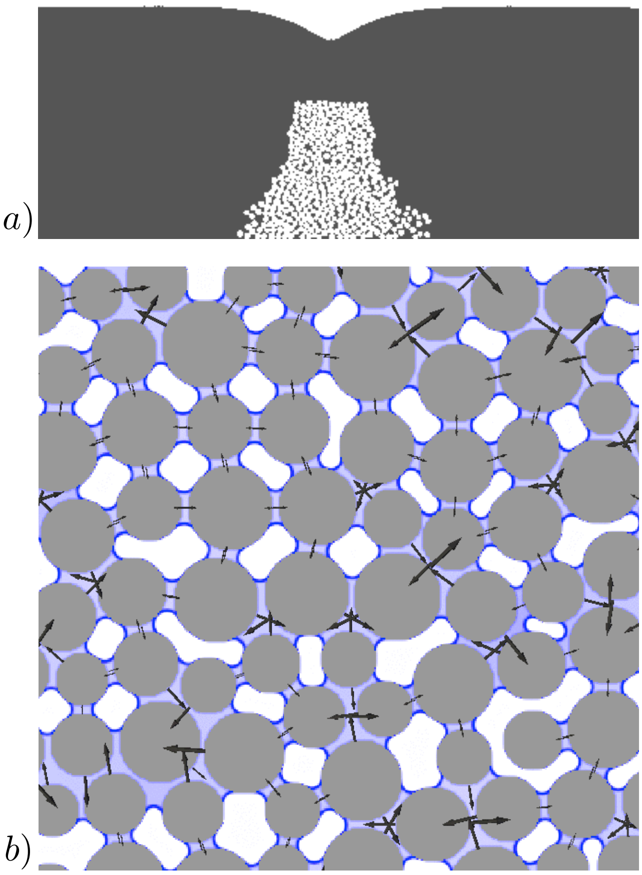

Figure 19: a) Simulation of surface waves generated by the collapse of a rock mass inside water [ADD$^+$12]. Simulation of the capillary wetting of a granular material. The arrows represent the forces applied by the liquid phase on the grains [DRR15].

References

[ADD$^+$12] L. Amarsid, C. Delenne, J.-Y. Delenne, V. Guinot, and F. Radjai. Surface wave generation by seabed collapse simulated by the coupled lattice boltzmann/discrete element method. In *Proceedings of 10th International conference on hydroinformatics*, 14–18 July 2012.

[ADM$^+$17] L. Amarsid, J.-Y. Delenne, P. Mutabaruka, Y. Monerie, F. Perales, and F. Radjai. Visco-inertial regime of immersed granular flows. *Physical Review E (accepted)*, 2017.

[AH09] N. K. Ahmed and M. Hecht. A boundary condition with adjustable slip length for lattice boltzmann simulations. *J. Stat. Mech.*, 2009(09):09017, 2009.

[BB88] J. F. Brady and G. Bossis. Stokesian dynamics. *Annual Review of Fluid Mechanics*, 20:111–157, 1988.

[BFL01] M. Bouzidi, M. Firdaouss, and P. Lallemand. Momentum transfer of a boltzmann-lattice fluid with boundaries. *Physics of Fluids*, 13(11):3452–3459, 2001.

[BGK54] P. L. Bhatnagar, E. P. Gross, and M. Krook. A model for collision processes in gases. i. small amplitude processes in charged and neutral one-component systems. *Physical Review*, 94(511), 1954.

[BGL91] C. Bardos, F. Golse, and D. Levermore. Fluid dynamic limits of kinetic equations. i. formal derivations. *Journal of Statistical Physics*, 63(1-2), 1991.

[CCCB12] B. Chareyre, A. Cortis, E. Catalano, and Eric Barthélemy. Pore-scale modeling of viscous flow and induced forces in dense sphere packings. *Transport in porous media*, 94:595–615, 2012.

[CD98] S. Chen and G. D. Doolen. Lattice Boltzmann Method for Fluid flows. *Annual Review of Fluid Mechanics*, 30:329–364, 1998.

[CdL91] R. Cornubert, D. d'Humères, and D. Levermore. A knudsen layer theory for lattice gases. *Phys. D*, 47(1-2):241–259, 1991.

[CMM96] S. Chen, D. Martinez, and R. Mei. On boundary conditions in lattice boltzmann methods. *Physics of Fluids*, 8(9):2527–2536, 1996.

[CS79] P. A. Cundall and O. D. L. Strack. A discrete numerical model for granular assemblies. *Géotechnique*, 29(1):47–65, 1979.

[CZ11] Y. Cheng and H. Zhang. A viscosity counteracting approach in the lattice boltzmann {BGK} model for low viscosity flow: Preliminary verification. *Computers & Mathematics with Applications*, 61(12):3690 – 3702, 2011.

[Del03] P. J. Dellar. Incompressible limits of lattice boltzmann equations using multiple relaxation times. *J. Comput. Phys*, page 2003, 2003.

[Del06] P. J. Dellar. Non-hydrodynamic modes and general equations of state in lattice Boltzmann equations. *Physica A*, 362:132–138, 2006.

[DGK$^+$02] D. D'Humières, I. Ginzburg, M. Krafczyk, P. Lallemand, and L. Luo. Multiple-relaxation-time lattice boltzmann models in three dimensions. *Philos Trans A Math Phys Eng Sci*, 360(1792):437–51, 2002.

[D'H94] D. D'Humières. Generalized lattice-boltzmann equations. In *Rarefied Gas Dynamics: Theory and Simulations*, pages 450–458. American Institute of Aeronautics and Astronautics (AIAA), 1994.

[DRR15] J.-Y. Delenne, V. Richefeu, and F. Radjai. Liquid clustering and capillary pressure in granular media. *Journal of Fluid Mechanics*, 762(5), 2015.

[FZB$^+$16] Y. Fu, S. Zhao, L. Bai, Y. Jin, and Y. Cheng. Numerical study of double emulsion formation in microchannels by a ternary lattice boltzmann method. *Chemical Engineering Science*, 146:126–134, 2016.

[GNGB97] M. A. Gallivan, D. R. Noble, J. G. Georgiadis, and R. O. Buckius. An evaluation of the bounce-back boundary condition for lattice boltzmann simulations. *International Journal for Numerical Methods in Fluids*, 25(3):249–263, 1997.

[GPHJ99] R. Glowinski, T. W. Pan, T. I. Hesla, and D. D. Joseph. A distributed Lagrange multiplier/fictitious domain method for particulate flows. *International Journal of Multiphase Flow*, 25(5):755–794, 1999.

[IMLF09] S. Izquierdo, P. Martínez-Lera, and N. Fueyo. Analysis of open boundary effects in unsteady lattice boltzmann simulations. *Computers & Mathematics with Applications*, 58(5):914 – 921, 2009.

[JGK13] C. F. Janßen, S. T. Grilli, and M. Krafczyk. On enhanced non-linear free surface flow simulations with a hybrid LBM–VOF model. *Computers & Mathematics with Applications*, 65(2):211–229, 2013.

[JY08] M. Junk and Z. Yang. Outflow boundary conditions for the lattice boltzmann method. *PCFD*, 8(1-4):38, 2008.

[JY11] M. Junk and Z. Yang. Asymptotic analysis of lattice boltzmann outflow treatments. *Communications in Computational Physics*, 2011.

[KKH$^+$99] D. Kandhai, A. Koponen, A. Hoekstra, M. Kataja, J. Timonen, and P. M. A. Sloot. Implementation aspects of 3d lattice-bgk: Boundaries, accuracy, and a new fast relaxation method. *Journal of Computational Physics*, 150(2):482–501, 1999.

[KTH$^+$05] C. Körner, M. Thies, T. Hofmann, N. Thürey, and U. Rüde. Lattice boltzmann model for free surface flow for modeling foaming. *Journal of Statistical Physics*, 121(1/2):179–196, 2005.

[Lad94] A. J. C. Ladd. Numerical simulations of particulate suspensions via a discretized boltzmann equation. part 1. theoretical foundation. *Journal of Fluid Mechanics*, 271:285–309, 1994.

[LGS13] Q. Lou, Z. Guo, and B. Shi. Evaluation of outflow boundary conditions for two-phase lattice boltzmann equation. *Phys. Rev. E*, 87:063301, 2013.

[LL00] P. Lallemand and L. Luo. Theory of the lattice boltzmann method: Dispersion, dissipation, isotropy, galilean invariance, and stability. *Phys. Rev. E*, 61:6546–6562, 2000.

[LL03] P. Lallemand and L. Luo. Lattice boltzmann method for moving boundaries. *Journal of Computational Physics*, 184(2):406 – 421, 2003.

[LRW] S. Luding, N. Rivas, and T. Weinhart. From soft and hard particle simulations to continuum theory for granular flows. *ALERT geomaterials Doctoral School 2017, Aussois, France*.

[MA05] M. E. McCracken and J. Abraham. Multiple-relaxation-time lattice-boltzmann model for multiphase flow. *Phys. Rev. E*, 71:036701, 2005.

[MAL09] A. Mussa, P. Asinari, and L. Luo. Lattice boltzmann simulations of 2d laminar flows past two tandem cylinders. *Journal of Computational Physics*, 228(4):983 – 999, 2009.

[Mau99] B. Maury. Direct Simulations of 2D Fluid-Particle Flows in Biperiodic Domains. *Journal of Computational Physics*, 156:325–351, 1999.

[McN93] S. McNamara. Hydrodynamic modes of a uniform granular medium. *Phys. Fluids A*, 5(12):3056 – 3070, 1993.

[MDSR14] P. Mutabaruka, J.-Y. Delenne, K. Soga, and F. Radjai. Initiation of immersed granular avalanches. *Phys. Rev. E*, 89(052203), 2014.

[NPB$^+$15] J. Ngoma, P. Philippe, S. Bonelli, P. Cuéllar, J.-Y. Delenne, and F. Radjai. Transient regime to fluidized chimney within a granular bed by means of a 2D DEM/LBM modeling. In *IV International Conference on Particle-based Methods – Fundamentals and Applications*, 2015.

[NSCP06] X. D. Niu, C. Shu, Y. T. Chew, and Y. Peng. A momentum exchange-based immersed boundary-lattice boltzmann method for simulating incompressible viscous flows. *Physics Letters A*, 354(3):173–182, 2006.

[OS00] M. A. Ol'shanskii and V. M. Staroverov. On simulation of outflow boundary conditions in finite difference calculations for incompressible fluid. *International Journal for Numerical Methods in Fluids*, 33(4):499–534, 2000.

[PS05] T. Pöschel and T. Schwager. *Computational Granular Dynamics*. Spring, Berlin, Germany, 2005.

[RD11] F. Radjai and F. Dubois. *Discrete-element Modeling of Granular Materials*. Iste-Wiley, London, 2011.

[SC96] J. D. Sterling and S. Chen. Stability analysis of lattice boltzmann methods. *Journal of Computational Physics*, 123(1):196 – 206, 1996.

[SCDV$^+$11] B. Saint-Cyr, J.-Y. Delenne, C. Voivret, F. Radjai, and P. Sornay. Rheology of granular materials composed of nonconvex particles. *Physical Review E*, 84(4), 2011.

[SR05] L. Staron and F. Radjaï. Friction versus texture at the approach of a granular avalanche. *Phys Rev E*, 72(4):041308, 2005.

[Suc01] S. Succi. *The Lattice Boltzmann Equation for Fluid Dynamics and Beyond*. Clarendon Press, Oxford, 2001.

[Suc02] S. Succi. Mesoscopic modeling of slip motion at fluid-solid interfaces with heterogeneous catalysis. *Phys. Rev. Lett.*, 89:064502, 2002.

[TKT93] Y. Tsuji, T. Kawaguchi, and T. Tanaka. Discrete particle simulation of two-dimensional fluidized bed. *Powder Technol.*, 77:79–87, 1993.

[TWT] D. Tunuguntla, T. Weinhart, and A. Thornton. Discrete particle simulations with MercuryDPM. *ALERT geomaterials Doctoral School 2017, Aussois, France*.

[VDR07] F. Varnik, D. Doner, and D. Raabe. Roughness-induced flow instability: a lattice boltzmann study. *Journal of Fluid Mechanics*, 573:191–209, 2007.

[Wac11] A. Wachs. PeliGRIFF, a parallel DEM-DLM/FD direct numerical simulation tool for 3D particulate flows. *Journal of Engineering Mathematics*, 71(1):131–155, 2011.

[WWPC07] M. Wang, J. Wang, N. Pan, and S. Chen. Mesoscopic predictions of the effective thermal conductivity for microscale random porous media. *Physical review. E*, 75:036702, 2007.

[ZH97] Q. Zou and X. He. On pressure and velocity boundary conditions for the lattice boltzmann bgk model. *Physics of Fluids (1994-present)*, 9(6):1591–1598, 1997.

[Zie93] D. Ziegler. Boundary conditions for lattice boltzmann simulations. *Journal of Statistical Physics*, 71(5-6):1171–1177, 1993.

[ZTPM05] L. Zhu, D. Tretheway, L. Petzold, and C. Meinhart. Simulation of fluid slip at 3d hydrophobic microchannel walls by the lattice boltzmann method. *Journal of Computational Physics*, 202(1):181 – 195, 2005.

Advanced contact laws

C.L. Martin

Univ. Grenoble Alpes, CNRS, SIMaP, F-38000 Grenoble, France

This chapter will briefly introduce the basics of contact laws that can be used in Discrete Element Method simulations. The focus will be on contact laws that have been derived analytically from the constitutive equations of the material that constitutes the two particles in contact. This generally restricts the validity of these laws to spherical particles but allows the interested user to obtain directly the material parameters. We treat elasticity, adhesion, plasticity, viscoplasticity, solid bonds and sintering.

1 Introduction

Discrete Element Method (DEM) simulations need contact laws as these represent the first ingredient of a physically-based model. Contact laws define the interaction between particles. Forces are generated when particles form a contact and these forces need to be defined carefully since the physics of the problem to be modeled is very often embedded in these forces. In other words, the local interactions are responsible for the behaviour of the particulate material at the macroscopic scale. The contact law is usually decomposed into a normal and a tangential component. It is generally formulated as a contact force-displacement law that relates the contact force acting between the two particles to their relative displacement and/or to their relative velocity.

In this chapter, we will focus on contact forces that go beyond linear models, which are the most intuitive and simple models. The most common linear model is the linear spring–dashpot model proposed by Cundall and Strack [CS79], where the spring is used for the elastic deformation while the dash-pot accounts for the viscous dissipation [LRW17]. However, we will not be able to give a full review of existing contact laws since the rapid development of DEM in the last decades has been accompanied by a very large number of papers proposing new contact laws. Also, it is worth noting that many papers on contact forces were not primarily intended for DEM users, but still offer very valuable analytical developments that can be of interest to the DEM community. Here we will give only a compact description of contact laws specialized for spherical particles. For a more complete review of available contact laws, we refer to Refs. [Mis03, PC04, KESR$^+$07, ZZYY08, Lud08, RD11, SML15, WSB$^+$15]. Here, we will restrict ourselves to a description of models that do not need a calibration of material parameters. The models discussed here only need parameters that are generally available from the literature. These are typically the elastic constants, the yield stress, and the surface energy. Note also that we will only describe normal interactions and let the interested reader go through the literature for contact laws that define tangential interactions (typically friction).

In this paper, we will show that a simple dimensional analysis on contact laws allows for some insights on particle size effect. In other words, the contact laws described hereafter may (or may not) bring particle size effect at the macroscopic scale. This simple analysis is based on the Love's equation that gives the macroscopic stress tensor σ_{xy} of a packing of discrete particle as a function of its volume V [Dan68, CMNN81]:

$$\sigma_{xy} = \frac{1}{V} \sum_{contacts} F_{,x} l_{,y} \tag{1}$$

where the summation is carried out on all contacts, $F_{,x}$ is the x component of the contact, and $l_{,y}$ is the y component of the branch vector between the two particles.

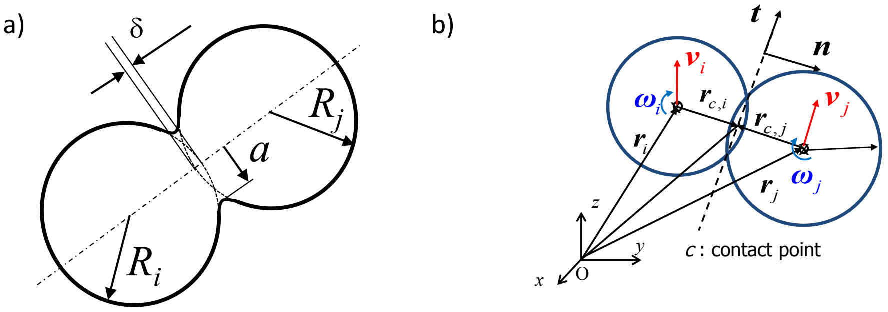

Figure 1: a) Contact geometry and b) contact kinematics

2 Contact geometry and kinematics

We briefly introduce the main contact geometry and kinematics parameters that will be handy in the following sections. Considering two particles of radii R_i and R_j (Fig. 1a), we define the equivalent radius R^* as:

$$R^* = \frac{R_i R_j}{R_i + R_j} \tag{2}$$

The overlap or indentation between the two particles is δ and the two particles form a circular contact with radius a. The unit vectors $\boldsymbol{n}$ and $\boldsymbol{t}$, normal and tangent to the contact are defined from the relative velocities of the particles at the contact (Fig. 1b):

$$\boldsymbol{n} = \frac{\boldsymbol{r_j} - \boldsymbol{r_i}}{\mid \boldsymbol{r_j} - \boldsymbol{r_i} \mid}; \quad \boldsymbol{t} = \frac{\boldsymbol{v_{c,rel}} - (\boldsymbol{v_{c,rel}} \cdot \boldsymbol{n}) \cdot \boldsymbol{n}}{\mid \boldsymbol{v_{c,rel}} - (\boldsymbol{v_{c,rel}} \cdot \boldsymbol{n}) \cdot \boldsymbol{n} \mid} \tag{3}$$

where $\boldsymbol{v_{c,rel}}$ is calculated from the particle translational $(\boldsymbol{v_i}, \boldsymbol{v_j})$ and angular $(\boldsymbol{w_i}, \boldsymbol{w_j})$ velocities.

3 Contact laws

3.1 Elasticity

The normal Hertzian force between two elastic spheres with Young's moduli E_i, E_j and Poisson's ratios ν_i, ν_j is:

$$F_n = \frac{4E^* a^3}{3R^*} = \frac{4}{3} E^* \left(\frac{\delta}{R^*} \right)^{\frac{3}{2}} R^{*2} \tag{4}$$

where E^* is given by:

$$\frac{1}{E^*} = \frac{1-\nu_i^2}{E_i} + \frac{1-\nu_j^2}{E_j} \tag{5}$$

The contact radius a is simply given for elasticity by:

$$a^2 = R^* \delta \tag{6}$$

When adhesion between particles needs to be taken into account, two classical models are available. The DMT (Derjaguin, Muller and Toporov) theory [DMT75] is appropriate for "hard" and "small" particles, while the JKR (Johnson, Kendall, Roberts) model [JKR71] is more appropriate for "soft" and "large" particles [Bar08]. An additional tensile term, accounting for the work of adhesion $w = 2\gamma_s$ (γ_s is the surface energy) is added to Eq. (4). The DMT model force is:

$$F_n = \frac{4E^* a^3}{3R^*} - 2\pi w R^*, \tag{7}$$

while the JKR model force is:

$$F_n = \frac{4E^* a^3}{3R^*} - 2\sqrt{2\pi w E^* a^3}. \tag{8}$$

In both models, the contact radius is still given by Eq. (6). The critical pull-out force at which the two surfaces separate is simply derived from $\left(\frac{\mathrm{d}F_n}{\mathrm{d}a}\right)_c = 0$.

When adhesive effects are neglected ($w \to 0$), no macroscopic size effect emerges from Eq. (1). However, when adhesive forces play a role Eqs. (7) or (8) lead to a size effect: the macroscopic strength of a packing of adhesive spheres is inversely proportional to their size.

3.2 Plasticity and viscoplasticity

When particles are pressed, they might undergo plastic deformation. We will not detail the features of plastic indentation, for which ample literature is available. Here, we only describe the model of Storåkers [SFM99], which is quite handy for a simple implementation in DEM. For two spherical particles made from viscoplastic materials with a uniaxial stress response given by:

$$\sigma = \sigma_i \varepsilon^M \dot{\varepsilon}^N \tag{9}$$

where σ is the uniaxial stress, and ε and $\dot{\varepsilon}$ are the uniaxial strain and strain-rate, and σ_i, M and N are material constants for particle i. The normal force between the two particles is:

$$F_n = \eta \delta^{(1+M/2-N/2)} \dot{\delta}^N \tag{10}$$

where $\dot{\delta}$ is the normal rate of approach of the two particles. F_n opposes the relative motion of the two particles in tension and compression. η is defined as [SFM99]:

$$\eta = 2^{1-\frac{M}{2}-\frac{3N}{2}} 3^{1-M-N} \left(1+2N\right) \pi c^{2+M+N} \sigma_0 \left(R^*\right)^{1-\frac{M}{2}-\frac{N}{2}} \tag{11}$$

where $\sigma_0^{-\frac{1}{M+N}} = \sigma_1^{-\frac{1}{M+N}} + \sigma_2^{-\frac{1}{M+N}} = 2\sigma_1^{-\frac{1}{M+N}}$ in the case of two particles made of the same material ($\sigma_2 = \sigma_1$). The exact expression of c^2 is given by plastic indentation theory [SFM99]. The interest of Eq. (10) is that, as for elasticity, the knowledge of the particle material constitutive behavior leads directly to the writing of the contact law. Note that the model imposes that M and N are identical for particles i and j (although particles i and j may be defined by different values of σ_i in Eq. (9)).

Lets simplify the general constitutive equation in Eq. (9) to a simple perfectly plastic material with yield stress $\sigma_i = \sigma$ ($M \to 0$, $N \to 0$) and to two particles made of the same material. In that case, Eq. (10) simplifies to:

$$F_n = 3\pi\sigma a^2 \tag{12}$$

which is the classic indentation force, with the contact radius given by:

$$a^2 = 3R^*\delta \tag{13}$$

Note that in elasticity, the normal force scales with $\delta^{\frac{3}{2}}$ (Eq. (4)) while it scales linearly with δ for perfect plasticity (Eqs. (12) and (13)). Also, note how the contact size for a given indentation δ, is different in elasticity (Eq. (6)) and in plasticity (Eq. (13)), reflecting plastic flow around the contact.

Often when plasticity is at work, unloading of contacts is of interest. Again, the literature gives tools to resolve analytically the problem of two spheres, whose contact has undergone plasticity and that unload up to full separation with or without adhesion effects [MJ00].

When adhesion plays a role, the unloading (and subsequent failure) of a packing of previously plastified particles leads to an inverse relation between the macroscopic stress and the size of the particles.

3.3 Sintering

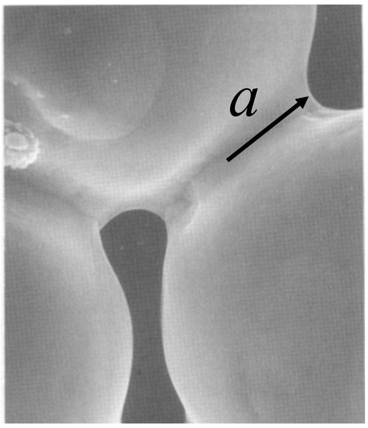

Figure 2: The sintered contact between two metallic particles.

When metallic, ceramic or polymeric particles (typical powders for engineering applications) are submitted to high enough temperatures (above half the melting temperature), they may sinter. Sintering of particles induces the growing of interparticle necks by solid diffusion mechanisms, the driving force being the reduction of the free surface energy of the system (Fig. 2). It usually results in overall shrinkage of the powder compact. Solid diffusion mechanisms are thermally activated processes and thus viscous effects are expected. Different models for two sintering spheres exist in the literature. We focus on one of the simplest [BM96, PLKY98, MB09], which leads to the following contact law:

$$F_n = \frac{\pi a^4}{8\Delta_b}\dot{\delta} - \frac{9}{4}\pi R^* \gamma_s \tag{14}$$

that considers grain boundary and surface diffusion to be the major mechanisms of mass transport. γ_s is the surface energy and

$$\Delta_b = \frac{\Omega}{kT}\delta_b D_b \tag{15}$$

with $D_b = D_{0b}\exp(-Q_b/RT)$ the diffusion coefficient for vacancy transport in the grain boundary with thickness δ_b and activation energy Q_b, Ω is the atomic volume. The first term on the rhs of equation (14) may be considered as a normal viscosity, which scales with a^4, whereas the second term relates to a tensile force due to surface energy. The sintering contact radius a (Fig. 2) is related to the indentation δ by:

$$a^2 = 4R^*\delta \tag{16}$$

The nature of Eq. (14) leads to size effects that are commonly observed by practitioners: small particles sinter faster than large ones. More precisely, the time necessary to attain a given density for a packing of particles of radius R is proportional to $\frac{R^4}{\Delta\gamma_s}$. In other words, the kinetics of sintering is favored by small particles (that should not coalesce too much) and large diffusion coefficients (or high temperature).

3.4 Solid bonds

When two particles form a solid bond through some physical mechanism (sintering, cementation, calcination, precipitation, ...), the tensile or compressive forces arising from their relative displacement can be derived analytically from the bond geometry [JHM02, ODVE13]. In that case, elasticity and eventually fracture, need to be modeled starting from the geometry of a bonded contact of bond radius a as shown in Fig. 3. For two such particles which have accumulated a normal displacement u_n the normal contact force is given by:

$$F_n = E^* \phi_n a u_n \tag{17}$$

where ϕ_n is a function that describes the interaction between neighboring bonds:

$$\phi_n = \frac{1 + a^*[\frac{\pi}{6}(1-\nu^2)(1+2a^*) - a^*]}{\sqrt{1-a^{*2}} - \bar{\psi}(a^* + a^{*2}[\frac{\pi}{6}(1-\nu^2)(1+2a^*) - a^*])} \tag{18}$$

where $a^* = a/2R^*$ is the bond normalized radius, and $\bar{\psi}$ is a material independent factor that allows bond interaction to be taken into account in a simplified manner [JHM02]. When bond size increases to such an extent that the constitutive law (Eq. (17)) is not any more valid due to the influence of neighboring bonds, it is possible to use the principle of superposition of linear elastic fields to propose an alternative formulation [JMLB12]. In that case, the expression of the accumulated normal displacement u_n is replaced in Eq. (17) by:

$$u'_n = u_n - \sum_{contacts} u_n^i\,(\theta_i, Fn) \tag{19}$$

where the term $\sum_a u_n^i\,(\theta_i, Fn)$ is a correction accounting for bond interactions that depends on the angles θ_i that neighboring bonds make with the considered bond (Fig. 3). The analytical expression of $u_n^i\,(\theta_i, Fn)$ is deduced from FEM analysis of a truncated sphere under body loading [JHM02, JMLB12].

The term $\sum_{contacts} u_n^i\,(\theta_i, Fn)$ is generally small compared to u_n but is still necessary to fully reproduce Poisson's effect of a bonded packing. Similarly a tangential force complements the model, together with resisting normal and tangential moments [PC04].

Note that in Eq. (17), the bond radius a is considered constant (it does not depend on the accumulated relative displacement u_n). Eq. (17) shows that the force is proportional to the bond radius. The bond radius, depending on the bond formation mechanism may be given by Eq. (16) or simply by the geometric intersection of the two spheres:

$$a^2 = 2R^*\delta \tag{20}$$

When particles are bonded together, it is generally interesting to equip the model with a fracture criterion which is physically based. Considering the elastic stress intensity factor associated with the singular stress field along the edge of the bond, it writes [FJMZ04, FC01]:

$$\sigma_c = \sqrt{E^* \frac{\Gamma}{\pi a}} \tag{21}$$

where Γ is the bond toughness. Γ is generally approximated by the surface energy contribution of the two particles i and j that make the bond ($\Gamma = 2\gamma_s$). This is a reasonable assumption if energy dissipating processes are very limited in the small process zone of the bond (typically correct for elastic brittle materials like ceramic). Note the similarity with the elastic case, which simplifies also the fracture energy to the work necessary to separate the contact surfaces (section 3.1).

Importantly, Eq. (21) introduces a length dependence as it relates the bond fracture stress to the inverse of the bond size square root. Consequently, the macroscopic stress necessary to fracture an aggregate of bonded particles for a given $a^* = \frac{a}{2R^*}$ value is inversely proportional to the square root of their size (Eq. (1)).

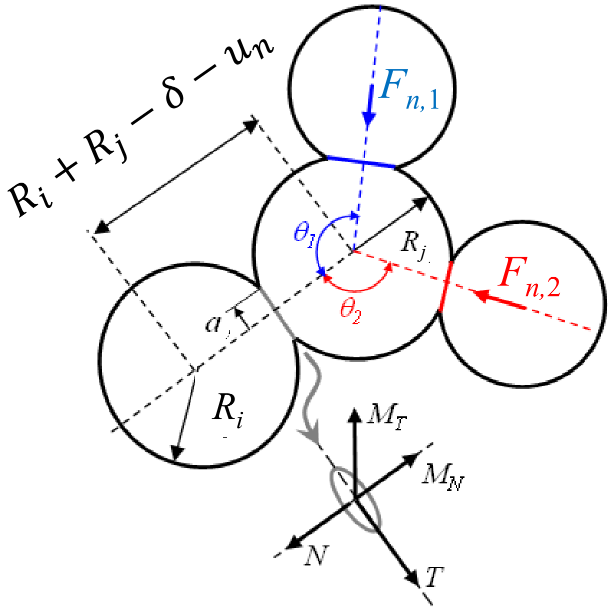

Figure 3: Four bonded particles. Particles 1 and 2 make angles θ_i and θ_j with particle j. The contact law between particles i and j is modified by the bonds with particles 1 and 2.

4 Concluding remarks

The contact laws briefly described above encompass a large panel of deformation mechanisms at the contact length scale, elasticity, plasticity, high temperature sintering, and solid bonds. An interesting signature of the contact deformation mechanism is the contact size. For a given indentation δ, and simplifying the problem to the contact of two identical particles ($R_i = R_j$), inspection of Table 1 indicates that the elastic contact is actually smaller than the contact defined by the simple intersection of the two spherical particles. When material flows (plasticity or sintering), Table 1 shows that the deformation mechanism dictates the manner in which volume conservation operates at the contact length scale (except for elasticity which does not imply volume conservation). The contact size has significant implications at the macroscopic scale, beyond the mere mechanical response of the packing. Conduction, gas diffusion, liquid interaction are important phenomena which all depend on the contact geometry.

Table 1: Contact radius a for various deformation mechanisms (Eqs. (6), (13), (16), (20))

elasticity	geometric contact	perfect plasticity	sintering
$\sqrt{\frac{1}{2}R\delta}$	$\sim \sqrt{R\delta}$	$\sqrt{\frac{3}{2}R\delta}$	$\sqrt{2R\delta}$

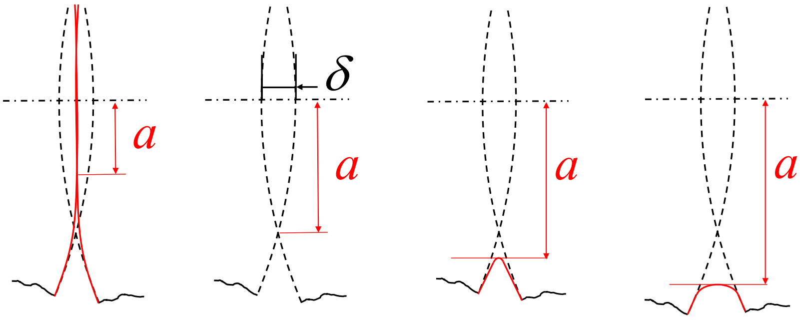

In this very brief overview of physically-based contact laws, we have omitted important interaction laws that are available in the literature, usually from analytical derivations on a pair of spherical particles. When capillarity is at play in unsaturated granular materials, the capillary force can be computed (although not in a fully analytical manner) [SCND09]. Electrostatic forces between charged particles can also be modeled [THJ06]. More generally, it should be reminded that thanks to the analytical derivations of many researchers, it is generally possible to implement in a DEM code a physically-based contact law, for which material parameters can be extracted directly from the material properties of the particles.

References

[Bar08] E. Barthel. Adhesive elastic contacts - JKR and more. *J. Phys. D: Appl. Phys.*, 41:163001, 2008.

[BM96] D. Bouvard and R. M. McMeeking. The deformation of interparticle necks by diffusion controlled creep. *J. Am. Ceram. Soc.*, 79:666–672, 1996.

[CMNN81] J. Christoffersen, M. M. Mehrabadi, and S. Nemat-Nasser. A micromechanical description of granular material behavior. *Journal of Applied Mechanics*, 48:339–344, 1981.

[CS79] P. A. Cundall and O. D. L. Strack. A discrete numerical model for granular assemblies. *Géotechnique*, 29:47–65, 1979.

[Dan68] P. Dantu. Etude statistique des forces intergranulaires dans un milieu pulvérulent. *Géotechnique*, 18:50–55, 1968.

[DMT75] B. V Derjaguin, V. M Muller, and Y. P. Toporov. Effect of contact deformations on adhesion of particles. *J. Colloid Interface Sci.*, 53:314–326, 1975.

[FC01] L. B Freund and E. Chason. Model for stress generated upon contact of neighboring islands on the surface of a substrate. *J. Appl. Phys.*, 89:4866–4873, 2001.

[FJMZ04] H. Fujita, G. Jefferson, R. M. McMeeking, and F. W. Zok. Mullite/alumina mixtures for use as porous matrices in oxide fiber composites. *J. Am. Ceram. Soc.*, 87:261–267, 2004.

[JHM02] G. Jefferson, G. K. Haritos, and R. M. McMeeking. The elastic response of a cohesive aggregate - a discrete element model with coupled particle interaction. *J. Mech. Phys. Solids*, 50:2539–2575, 2002.

[JKR71] K. L. Johnson, K. Kendall, and A. D. Roberts. Surface energy and the contact of elastic solids. *Proc. R. Soc. Lond. A*, A324:301–313, 1971.

[JMLB12] D. Jauffrès, C. L. Martin, A. Lichtner, and R. K. Bordia. Simulation of the toughness of partially sintered ceramics with realistic microstructures. *Acta Mater.*, 60:4685–4694, 2012.

[KESR$^+$07] H. Kruggel-Emden, E. Simsek, S. Rickelt, S. Wirtz, and V. Scherer. Review and extension of normal force models for the Discrete Element Method. *Powder Technol.*, 171:157–173, 2007.

[Lud08] S. Luding. Cohesive, frictional powders: Contact models for tension. *Granular Matter*, 10(4):235–246, 2008.

[MB09] C. L. Martin and R. K. Bordia. The effect of a substrate on the sintering of constrained films. *Acta Mater.*, 57:549–558, 2009.

[Mis03] B. K. Mishra. A review of computer simulation of tumbling mills by the discrete element method: Part I-contact mechanics. *International Journal of Mineral Processing*, 71(1-4):73–93, 2003.

[MJ00] S. D. Mesarovic and K. L. Johnson. Adhesive contact of elastic-plastic spheres. *J. Mech. Phys. Solids*, 48:2009–2033, 2000.

[ODVE13] M. Obermayr, K. Dressler, C. Vrettos, and P. Eberhard. A bonded-particle model for cemented sand. *Computers and Geotechnics*, 49:299–313, 2013.

[PC04] D. O. Potyondy and P. A. Cundall. A bonded-particle model for rock. *Int. J. Rock Mech. Min. Sci.*, 41:1329–1364, 2004.

[PLKY98] J. Pan, H. Le, S. Kucherenko, and J. A. Yeomans. A model for the sintering of spherical particles of different sizes by solid state diffusion. *Acta Mater.*, 46:4671–4690, 1998.

[RD11] F. Radjai and F. Dubois. *Discrete-element modeling of granular materials*. Wiley-Iste, 2011.

[SCND09] L. Scholtès, B. Chareyre, F. Nicot, and F. Darve. Micromechanics of granular materials with capillary effects. *International Journal of Engineering Science*, 47(1):64–75, jan 2009.

[SFM99] B. Storakers, N. A. Fleck, and R. M. McMeeking. The viscoplastic compaction of composite powders. *J. Mech. Phys. Solids*, 47:785–815, 1999.

[SML15] A. Singh, V. Magnanimo, and S. Luding. A contact model for sticking of adhesive mesoscopic particles. *arXiv:1503.03720v1*, 2015.

[THJ06] T. Tang, C-Y. Hui, and A. Jagota. Adhesive contact driven by electrostatic forces. *J. Appl. Phys.*, 99:54906, 2006.

[WSB$^+$15] A. Weuster, S. Strege, L. Brendel, H. Zetzener, D. E. Wolf, and A. Kwade. Shear flow of cohesive powders with contact crystallization: experiment, model and calibration. *Granular Matter*, 17(2):271–286, 2015.

[ZZYY08] H. P. Zhu, Z. Y. Zhou, R. Y. Yang, and A. B. Yu. Discrete particle simulation of particulate systems: A review of major applications and findings. *Chem. Eng. Sci.*, 62:5728–5770, 2008.

[LRW17] S. Luding, N. Rivas and T. Weinhart. From soft and hard particle simulations to continuum theory for granular flows. *ALERT geomaterials Doctoral School 2017, Aussois, France.*

Good practice for sample preparation – Construction of granular packings

G. Combe[1] **and J.-N. Roux**[2]

[1] Univ. Grenoble Alpes, Grenoble INP, CNRS, 3SR, F-38000 Grenoble, France*
[2] Laboratoire Navier, Univ. Paris-Est, 2 Allée Kepler, Cité Descartes, 77420 Champs-sur-Marne

This paper introduces several numerical recipes *to build equilibrated granular assemblies under static loadings with Discrete Element Methods (DEM). Each preparation technique has to be characterised in terms of internal variables apt to capture its specific influence on the equilibrium configuration obtained. The possible comparisons with laboratory assembling procedures for static granular samples under prescribed stresses will be evoked. All the assembling procedures proposed rely on mechanical models, and involve some implementation of a type of DEM enabling static equilibrium states with enduring intergranular contacts to be modelled, such as "molecular dynamics" like approaches (MD, see the paper of S. Luding et al. [LRW]) or "contact dynamics" (CD, F. Radjaï [Rad]).*
This article draws heavily from the chapter 6 of the book entitled "Discrete-element Modeling of Granular Materials", edited by F. Radjaï and F. Dubois [RD11].

1 Introduction

1.1 Motivation

Both in experiments and in simulations one needs a sample of the material in order to study its mechanical properties, or sometimes a specific configuration (a "structure", i.e., a granular specimen with a special shape and particular boundary conditions that one wishes to characterise under specific loadings). Laboratory assembling methods (such as air pluviation, layerwise deposition and dry or moist tamping...) are experimental recipes, sometimes described in official standards (*e.g.*, the ASTM recommen-

---

*Institute of Engineering Univ. Grenoble Alpes dation for “Soil Specimen Preparation for Laboratory Testing” [SM76]). The DEM practicioner is confronted with a very similar situation, with individual grains that need to be assembled. In addition, some delicate choices have to be made regarding geometric and micromechanical ingredients of the model. In view of the well-known influence of the initial state on the mechanical behaviour in quasi-static conditions, it is essential to have a good control of the first step of a discrete simulation study, which is the assembling stage.

1.2 Internal parameters for sample homogeneity checking

Objectives may differ for the study of intrinsic material properties and for specific configurations and structures. In the sequel, we shall focus on the first case, and discuss the ability of the assembling methods to form well controlled *homogeneous representative samples*. To check for the quality of a numerical equilibrated specimen, a number of internal variables are measured, which usually comprise the following list.

- Density, or solid fraction Φ, i.e., the proportion of the sample volume occupied by the solid grains;
- Coordination number z, i.e., the average number of force-carrying contacts per grain, or, more generally, the connectivity, which is the distribution of local coordination number values $(x_i)_{i=0,1,2\dots}$, or in other words the proportion of grains with i force-carrying contacts (in the absence of distributed forces such as gravity, a fraction x_0 of the grains are “rattlers” and carry no force at all);
- the stress tensor (static contribution only);
- the distribution of contact orientations (i.e., orientations of normal directions of contacts), characterised by *fabric tensors*;
- except for disks or spheres, the distribution of the orientations of the grains themselves.

Those state variables are determined by the assembling procedure and are known to influence the subsequent mechanical properties of the system in the quasi-static regime. The quality of the obtained sample should also be assessed in view of its homogeneity and of the accuracy with which equilibrium conditions are fulfilled. Homogeneity is particularly sensitive to the boundary conditions applied to the system as it is being prepared. In this article, we will discuss two types of boundary conditions: rigid walls (applying controlled stresses or strains to the system), and (possibly deformable) periodic cells (as described in [RD11]).

1.3 Equilibrium conditions

Regarding equilibrium conditions, several simple criteria might be used. Those criteria should be satisfied for the correct force-carrying contact network to be identified.

Typically, if the system is insufficiently equilibrated, some parts of the force-carrying network, those bearing small forces, will not be clearly determined, and contacts will keep opening and closing in the residual motion. We now draw up a list of simple equilibrium criteria, both geometric and mechanical.

(i) All force-carrying grains should have at least m contacts per grains. m depends on spatial dimension ($D = 2$ or 3), on the grain shapes, on the type of loading applied and on contact interactions (see below);

(ii) the kinetic energy (both its translation its rotation parts) of all objects moving with respect to the centre of mass of the system (which is usually immobile in simulation practice) should be negligible.

The value of m in criterion (i) (i.e. $x_1 = x_2 = ... = x_{m-1} = 0$) stems from the condition of stability applied to one grain, the rest of the assembly being fixed. Considering smooth, strictly convex objects (no sharp edges or corners), one frictional grain cannot be stable with less than two contacts ($m = 2$) in 2D. In 3D, a sphere with two contacts can be equilibrated but with one mechanism (see [RD11] for details). In the presence of gravity, spheres with only two contacts are no longer observed in practice. One may require $m \geq 3$. In the presence of resistance to rolling (and pivoting), it is possible to find equilibrated grains with $m = 1$. Frictionless assemblies with no rolling resistance require larger values of m (for strictly convex, smooth objects: $m = 3$ in 2D and $m = 4$ in 3D if there is no cohesion and no gravity). The rattler proportion x_0 should vanish in the presence of gravity or body forces. In the sequel, the study is restricted to disks (2D) or spheres (3D) with sliding friction but no resistance to rolling or pivoting in the contacts (see Luding, Alert 2017 [LRW]).

As to condition (ii) it might be stated in a more quantitative form as follows. Let e_c denote the average kinetic energy per grain, and d the average diameter under pressure P. Then, referring to the typical contact force Pd^{D-1} in dimension D, one may require $\dfrac{e_c}{Pd^D} < \epsilon_E$, with a sufficiently small number ϵ_E (one possible value, usually acceptable in practice, is $\epsilon_E = 10^{-8}$).

Conditions on the balance of forces and moments should be valid for each grain for the force-carrying structure to be correctly identified. Let us consider a particle i, subjected to external force $\vec{\gamma}_i$, and transmitting forces $\vec{f}_{ij}$ to each contacting neighbour j. We define the *absolute* error in force balance on i, as:

$$\delta_i = \| \sum_{j \neq i} \vec{f}_{ij} - \vec{\gamma}_i \|,$$

and the *relative error* in force balance on i, as

$$\Delta_i = \delta_i / \max_j (\| \vec{f}_{ij} \|).$$

Similar definitions are adopted for torque balance equations. Equilibrium requirements are then expressed as follows, introducing preset tolerance levels ε_A and ε_R:

(iii) for each grain i, $\delta_i < \varepsilon_A$;

(iv) for each grain i, $\Delta_i < \varepsilon_R$;

(v) similar conditions on moments.

Condition (iii) is necessary, but may not be sufficient to guarantee the quality of the equilibrium state. If some grains are only carrying small forces of the order of ε_A, one cannot tell whether they are in equilibrium and with which other grains they should be in contact. ε_A should be adapted to the typical average contact force F (of the order of Pd^{D-1} for grains of diameter d under pressure P). In practice, it is observed [AR07a, PR08] that $\varepsilon_A < 10^{-4}F$ usually allows to identify the force network unambiguously. But if one wishes to be sure that all contacts are exactly determined, one may also enforce (iv), a more demanding condition. Setting $\varepsilon_R \leq 10^{-3}$ is usually satisfactory, and ensures that the list of force-carrying contacts is correctly determined, and that the forces themselves are accurately evaluated. Of course, the larger the simulated system, the smaller the typical lowest contact forces at equilibrium, and it eventually becomes impossible to evaluate them all accurately. It is however feasible in samples of disks or spheres containing of the order of 10000 grains.

The present paper focusses on two frequent situations: *isotropic* granular assemblies (section 2), under constant isotropic stresses, and anisotropic packings obtained by deposition under gravity (Section 3), like in some laboratory procedures. In both situations we investigate the homogeneity of the obtained configurations, which are characterised with suitable state variables, and briefly discuss the influence of some control parameters.

2 Granular assemblies under isotropic loading

We now focus on techniques designed to assemble granular packings in a homogeneous, isotropic stress state (a hydrostatic pressure), in the absence of body forces (such as gravity). The sample shape is a rectangle in 2D or a rectangular parallelepiped in 3D. Such samples are prepared by applying the desired pressure through some manipulations of the boundary conditions, which might significantly affect the results. We therefore compare the samples obtained by periodic boundary conditions to the ones confined within rigid walls. As first step, one should define the initial configuration from which the DEM simulation starts.

2.1 The initial state before isotropic compression

Grain diameters should first be drawn according to the prescribed distribution (we restrict our attention here to circular or spherical particles, otherwise one should also pick up shape parameters), and then the grain centres are either positioned according to one of the geometric algorithms [RD11], or placed on the sites of some regular lattice, and then mixed, to produce a generically disordered configuration. This mixing stage involves some dynamical simulation method, in which trajectories are computed once the particles are attributed random initial velocities. Such calculations might in principle be carried out with any of the DEM approaches described in the present treatise, although deformable particle MD will usually prove less efficient than rigid particle methods (contact dynamics, or event-driven calculations), because of the cost of refining trajectories during collisions. One should therefore prefer CD or event-driven methods at this stage. The mixing effect will be optimized in the absence of dissipation, *i.e.*, with frictionless particles and a coefficient of restitution equal to 1 (like in [Com02] or in [AR07a], in which the original "molecular dynamics for hard spheres", the event-driven method introduced in the 50's by Alder and Wainwright for the conservative hard sphere fluid, is implemented). The effects of this agitation stage depend on the number of collisions per particle at a given solid fraction, and may also be assessed in terms of the distance travelled by particles (diffusion). Fig. 1 is an illustration of such a process for disks in 2D. Particles start on the sites of a square lattice, with spacing l_0, and then get agitated and mixed up until the average traveled distance reaches $5\ l_0$. One may also check for the isotropy of the final state, *e.g.*, computing a near neighbour fabric tensor defined via a radical tessellation. The computation cost of this agitation stage is negligible compared to that of the subsequent compression (of the order of one second of CPU time for the examples of Fig. 1).

2.2 Granular assemblies confined by rigid walls

One may distinguish two different methods to compress samples enclosed in rigid walls: either the walls move inwards, or the grains are inflated within a fixed cell. The calculations stop when an equilibrium configuration is reached with the prescribed pressure on the walls.

2.2.1 Mobile walls

- *Stress control*:

In the first approach one exerts forces on the walls, which corresponds to the prescribed pressure level within the granular sample. The wall is then regarded as a mobile rigid object, just like any grain, with mass m_p, velocity $\vec{v}_p$ and acceleration $\vec{a}_p$. To simulate isotropic compression, one usually forbids wall rotations. To reduce sources of inhomogeneities near the boundaries, it is better to use frictionless walls in the compression of the granular packing. Thus one needs only to consider the motion of a rigid wall along its normal direction (one degree of freedom). In order to fix the motion of the centre of mass in rectangular or rectangular parallelepipedic cells, the motions of opposite walls should not be independent. It is convenient either to fix one of them, or to require opposite walls to have opposite velocities $\pm\vec{v}_p$. In the latter case

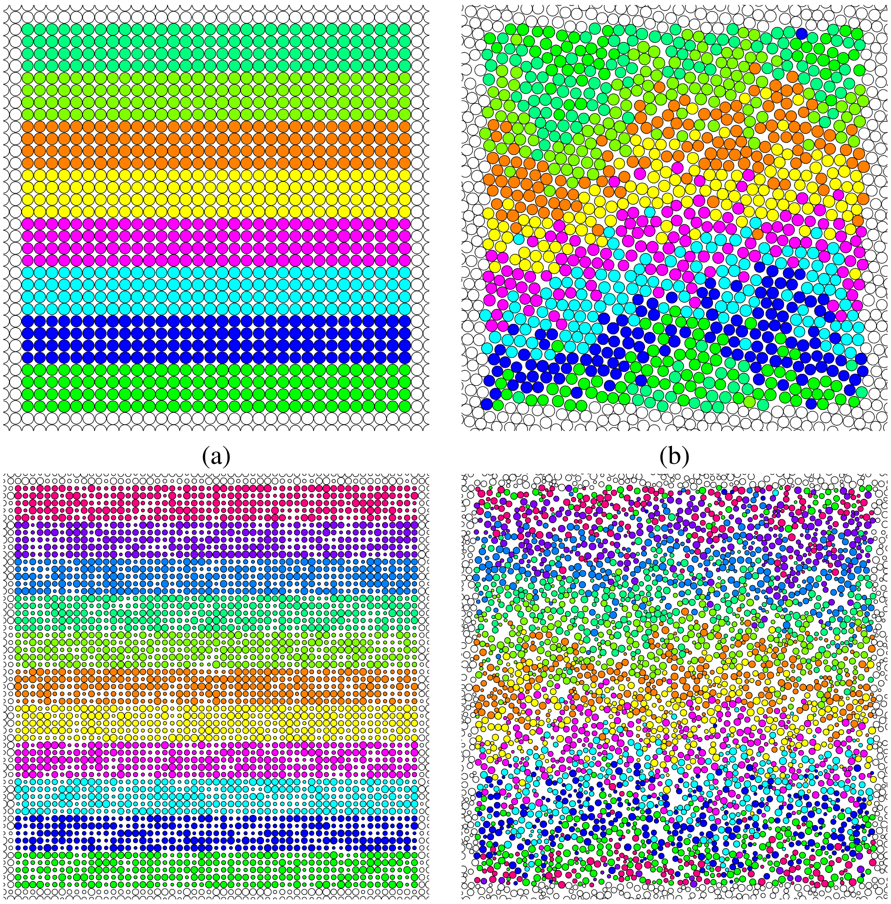

(a) (b)

(c) (d)

Figure 1: Illustration of agitation stage, simulated with Contact Dynamics in a periodic cell of fixed size. (a) Sample of 1024 slightly polydisperse disks ($\min(d) = 0.9 \cdot \max(d)$) initially placed on square lattice (spacing $= \max(d)$). (b) Sample (a) after 10300 time steps. Distance traveled by grains, $\mathcal{D}$: $\min(\mathcal{D}) = 0.7d$, $\max(\mathcal{D}) = 11.4d$, $\langle \mathcal{D}/d \rangle = 5$. (c) Sample of 3025 disks, with wider polydispersity ($\min(d) = 0.4 \cdot \max(d)$), initially on square lattice with spacing $\max(d)$. (d) Sample (c) after 4600 time steps. Distance traveled by grains: $\min(\mathcal{D}) = 0.2d$, $\max(\mathcal{D}) = 16.6d$, $\langle \mathcal{D}/d \rangle = 5$.

the external force conjugate $\vec{v}_p$ (counted positively for inward motion) can be identified (on writing down its power) as $2A_pP$ with P the prescribed pressure and A_p the wall area, and at equilibrium it should balance the sum of normal forces exerted by the grains on both opposite walls. In a simulation of an isotropic compression process with walls, one thus has (at most) 3 degrees of freedom for the 6 walls in 3D, and 2 for the 4 walls in 2D. The cell may also be requested to keep fixed aspect ratios: for instance, one may choose to compress a cubic cell by just reducing the edge length of the cube. In such a case, one does not control independently all three principal stresses along the 3 directions normal to the walls (only the average stress P might be controlled), and the sample may end up in a state with different principal stress values. This difference should dwindle and vanish, due to symmetry, as the system size increases.

Whenever stresses are controlled, the walls are dynamical objects, and their motion satisfies Newton's second law, involving normal forces $\vec{f}_{ip}$ exerted by grains onto the walls and external forces $\vec{F}_p$ applied to them:

$$\vec{a}_p = \frac{1}{m_p} \cdot \left[\vec{F}_p - \sum_{i \in \mathcal{P}} \vec{f}_{ip} \right] \quad ; \tag{1}$$

with $\mathcal{P}$ denoting the set of the indices of the grains contacting the wall.

The wall mass m_p might in principle be chosen arbitrarily. In practice a convenient choice, ensuring that the grains and the walls equilibrate on comparable time scales, consists in attributing to the wall a mass of the order of the sum of the masses of the grains that might come in contact with it. Thus in a square or cubic sample of N grains with average mass m one may choose $m_p = N^{1/D}m$.

The wall motion is computed by integration of (1). The importance of inertia and accelerations in the compression process might be evaluated using the inertial number I [CR03, RC05], which reads, for a wall of area A_p (a length in 2D), transmitting stress σ_0 to the sample, of thickness L_p in the direction normal to the wall,

$$I = \frac{||\vec{v}_p||}{L_p} \sqrt{\frac{m_p d}{\sigma_0 \, A_p}}. \tag{2}$$

In general the final state varies with the maximum values of I reached in the compression process, and a slow compression limit is approached as $I \to 0$. One may thus choose to enforce a condition on I, limiting the wall velocities, so that the final state will not be sensitive to the compression dynamics. Requesting $I \leq 10^{-4}$ is usually sufficient in that respect.

Fig. 2 illustrates the isotropic compression of a 2D system, initially a "granular gas" in which grains do not touch one another. Note that the condition on the velocity, limiting the inertial number to low values really becomes relevant in the final stage of such a process, when a contact network forms in the sample bulk, carrying stresses on the order of σ_0. In the beginning of the process, setting such an upper limit to the

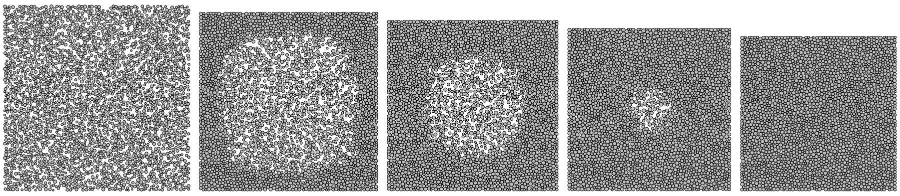

Figure 2: Illustration of an isotropic compression of a 2D ”granular gas” (3025 frictionless disks) by exerting forces on the walls. Contact Dynamics computational method.

compression rate might exceedingly slow down the simulation for loose arrangements with few contacts.

Let us also mention the possibility to drive the wall with overdamped dynamics, introducing a viscous force $-\zeta \vec{v}_p$ in (1), opposing the wall velocity $\vec{v}_p$, which might for large ζ dominate the inertial term, whence:

$$\vec{v}_p = \frac{1}{\zeta}\left[\vec{F}_p - \sum_{i \in \mathcal{P}} \vec{f}_{ip}\right]. \tag{3}$$

This was used in simulations of dense granular flows [dCEP$^+$05].

- *Control of displacements*:

Another approach consists in imposing the wall positions. As they are gradually modified, this amounts to imposing increments of displacements and strains in the system. An isotropic confinement with prescribed pressure might thus be obtained on progressively adjusting the positions of the walls so as to balance external force $\vec{F}_p$ with the forces exerted by the grains onto the wall:

$$\vec{F}_p = -\sum_{i \in \mathcal{P}} \vec{f}_{ip} \tag{4}$$

In Molecular Dynamics, the solution to Eq. (4) exploits the elasticity of the contacts between the grains and the wall. In practice, solving (4) might however involve some iterations due to the non-linearity of the contact law. No such approach seems to be available in Contact Dynamics because contacts are assumed to be perfectly rigid. This approach may be applied simultaneously to opposite walls, which may thus move independently in that case.

- *Remarks*:

As shown in Fig. 2, the isotropic compression process of a granular sample caused by inward displacements of the surrounding walls, propagates a compaction front within the sample. One should fear some lack of homogeneity of the final state, with differences between the centre and the periphery. Such inhomogeneities might be enhanced with frictional particles, apt to produce significant arching effects, potentially reducing stresses in the centre, and for which a greater sensitivity of the final configuration to the assembling process is generally observed. Moreover, the presence of the walls locally favours particle alignments and semi-ordered patterns.

Such wall effects were quantified in the 2D results of [Com02], shown in Fig. 3. Solid fraction Φ and average contact force $\langle f\rangle$ are measured in 2D assemblies of frictionless disks, with average diameter d, isotropically compressed within rigid walls, and averaged over several samples, showing some systematic dependence on the number of grains, N. As N increases, both quantities approach a finite limit, with a correction decreasing as $N^{-1/2}$. This is interpreted as the contribution of a peripheral zone (area $\propto N^{1/2}$) where the solid fraction is somewhat lower and the average contact force somewhat larger than their values in the uniform bulk (area $\propto N$ for large N). This interpretation is confirmed on measuring the average force in the sample core, $\langle f_{\setminus p}\rangle$, on excluding a peripheral zone of thickness $3d$. $\langle f_{\setminus p}\rangle$ (Fig. 3(b)) does not depend on N, and coincides, within statistical uncertainties, with the large system limit $\langle f\rangle\|_{N\to\infty}$.

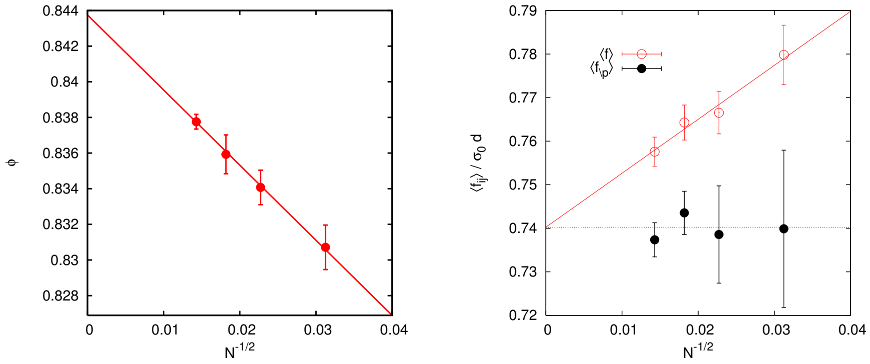

(a) (b)

Figure 3: Averages of (a) solid fraction Φ and (b) mean contact force $\langle f\rangle$ over samples with different numbers N of disks, isotropically compressed between mobile walls, plotted against $N^{-1/2}$. Error bars extend to one standard deviation on each side of the average. Plot (b) also shows the $\langle f_{\setminus p}\rangle$, the mean force evaluated away from the walls. Results from [Com02].

These data thus evidence a significant wall effect, which however disappears in the bulk, by excluding an outer zone (a few diameters wide).

One may also expect the walls to induce some specific anisotropy in the distribution of contact orientations (the *fabric* of the contact network), favouring contacts in the directions normal to the walls. Fig. 4(b) shows a polar histogram of contact orientations. Such histograms are symmetric about the vertical axis (because contacts are not oriented, angles θ and $\theta + 180°$ play the same role) and may thus be plotted on a half circle only. The left (dark grey) half of the circular plot and its right (light grey) half respectively correspond to the statistics of contact orientations in the central part of the sample, excluding a peripheral zone, and in the whole system. Respectively, the expected anisotropy is present near the walls and disappears in the bulk (3 diameters away from the walls), where the fabric is isotropic. The effects of the walls on the fabric are also confined to their immediate vicinity.

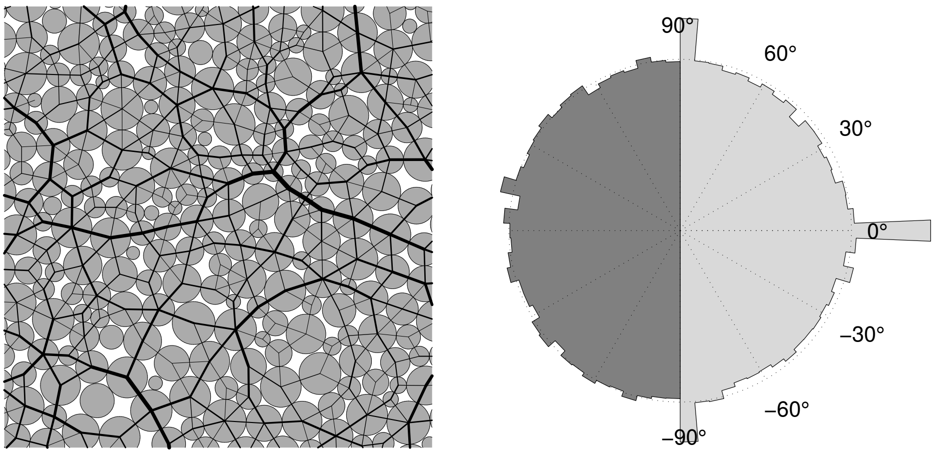

(a) (b)

Figure 4: (a) Detail of an isotropically confined 4900 disk sample, with the usual encoding of contact force intensity as stroke thickness. (b) Polar histograms of contact orientations, for all contacts (light grey, right), and excluding the periphery (dark grey, left). Statistics over 17 samples of 4900 grains each (about 150000 contacts). Results from [Com02].

To test for contact density and stress homogeneity, the system is split into a set of concentric, square "coronas" as shown in Fig. 5. Those coronas were chosen with constant surface area (and, consequently, varying thickness a). X_c (see Fig. 5) grows from inner to outer coronas, and for the outermost one approaches the half-width of the sample, $X_{\max}$. Fig. 6(a) shows the average number of contacts per unit area as a function of the position of the corona, evidencing wall effects, and homogeneity in the bulk. A similar analysis can be carried out for the solid fraction, confirming the interpretation of the results of Fig. 3(a). For solid fraction, and contact density (or coordination number) isotropically compressed samples enclosed in rigid walls are found homogeneous, apart from local wall effects, both with frictionless and frictional grains.

The average stress, $(\sigma_{xx} + \sigma_{yy})/2$, is also measured in each corona, and the results are shown in Fig. 6(b). Stress components are evaluated with the classical formula

[Lov44, Web66], suitable for equilibrated granular configurations, i.e.

$$\sigma_{\alpha\beta} = \frac{1}{\Omega} \sum_{N_{ij}} f_{ij}^{\alpha} l_{ij}^{\beta}, \tag{5}$$

in which

- Ω denotes the volume (or the area in 2D) of the subsystem in which the average stress is measured;
- N_{ij} is the number of contacts within Ω,
- f_{ij}^{α} denotes coordinate α ($\alpha = x, y$ in 2D, $\alpha = x, y, z$ in 3D) of the force between two grains i and j in contact,
- l_{ij}^{β} is coordinate β of the *branch vector* pointing from the center of grain i to the center of grain j [*].

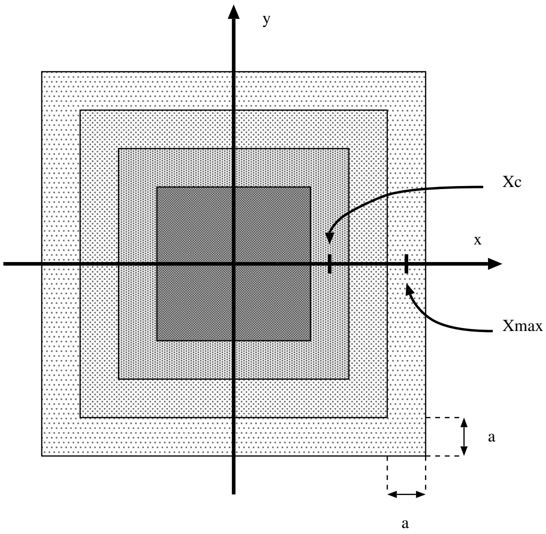

Figure 5: The square sample is split into equal area, varying thickness coronas, half diameter X_c growing from central to peripheral ones.

Fig. 6(b) shows that stresses decrease on approaching the sample centre. The effect is weak with frictionless grains, but it is quite important and cannot be neglected in the presence of intergranular friction. This is the main drawback of the process of isotropic compression through inward motion of rigid walls. One way to significantly improve the system homogeneity is to apply load cycles (e.g., in simple shear). This, however, also increases the density [FL95] and produces fabric anisotropy, with

---

[*] These “centres” might be chosen arbitrarily within each grain. One usually uses disk or sphere centres.

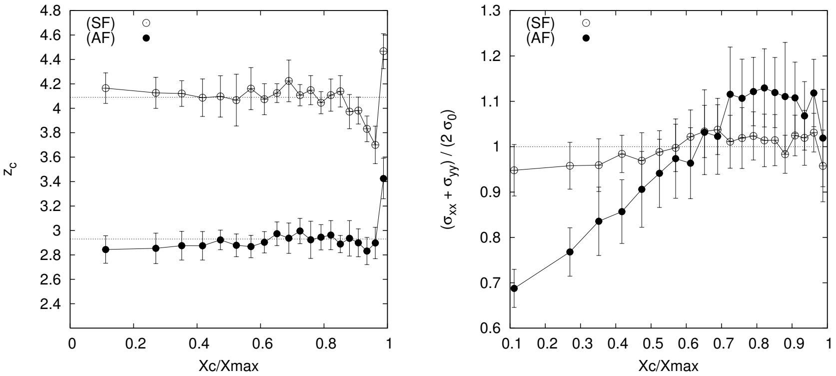

(a) (b)

Figure 6: Homogeneity test of (a) coordination number, and (b) average stress, $(\sigma_{xx} + \sigma_{yy})/2$ (normalized by σ_0, the applied macroscopic stress) in samples of 5041 disks, isotropically confined within rigid walls. Averages taken within concentric coronas, as shown in Fig. 5. Dotted lines indicate values averaged over the whole sample. Data shown for frictionless disks (SF) and frictional ones (AF, friction coefficient $\mu = 0.5$). Results averaged over 10 samples, error bars indicate sample-to-sample fluctuations. Contact stiffness parameter ([RD11]) $\kappa = 1000$.

favoured contact orientations along the direction of compression in the last cycle [Com02].

Another method to improve stress homogeneity within the sample consists in applying forces attracting grains toward the cell centre while the sample is being compressed, with intensities that decrease in time and vanish as the final equilibrium is approached. Although possibly efficient (see Fig. 7), this trick requires a delicate calibration of the time dependence of this additional force field, which must be present long enough for the inhomogeneity due to the compression process to be erased, but might lead to the opposite effect, larger stresses in the centre, if it does not vanish soon enough. Another drawback, apparent in Fig. 7, is the non-uniform density of contacts.

2.2.2 Fixed walls

With fixed walls, an isotropic compression is achieved on gradually increasing all particle diameters, the growth factor being adjusted according to the desired stress level. The rate with which diameters are increased might be chosen rather arbitrarily in initial, loose “granular gas” states. As the measured pressure p increases and becomes of the order of the prescribed value P, an adequate rule is to multiply, at a given time step, all diameters by some factor $1 + \alpha$, where the small number α is proportional to $(P/p) - 1$. The contact law will provide useful guidance for the choice of a suitable

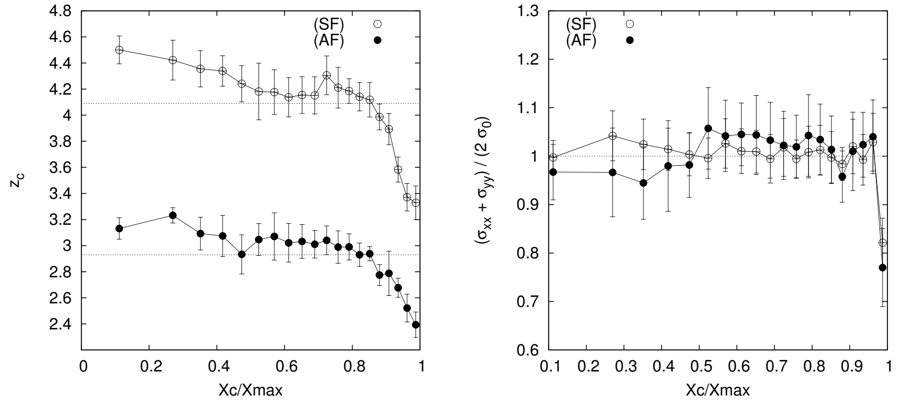

(a) (b)

Figure 7: With the same notations as in Fig. 6, average contact density (a) and average stress, normalized by σ_0 (b), in same sample series with friction coefficient $\mu = 0$ (SF) and $\mu = 0.5$ (AF), using the temporary centripetal force field trick.

factor, so that equilibrium under P might be approached at a reasonable rate, avoiding too large unbalanced forces. Stresses in the final equilibrium state, just like in the fixed cell aspect ratio version of the preparation method with moving boundaries, are not exactly isotropic in one sample, but isotropy is retrieved at the statistical level (either on averaging over many realizations of similar samples, or on approaching the limit of large sample size).

Before the mechanical behaviour of a given material is probed in quasi-static conditions, with a certain value of the friction coefficient μ in the contacts, it is possible to use a different coefficient of friction μ_0. One should however use $\mu_0 < \mu$, because reducing the friction coefficient destabilizes an equilibrated granular packing. A mechanical test with $\mu < \mu_0$ would start with a dynamical collapse of the initial contact network, and would not qualify as quasi-static. Some authors [CV05] defined the minimum and the maximum density states as those obtained, respectively, with $\mu_0 = \mu$ and $\mu_0 = 0$. That the maximum density (referred to as "random close packing" or RCP) state may be defined, as an equilibrium state of frictionless particles under isotropic stress [OSLN03, AR07a], if the compression is fast enough [AR07a, RCT07], is widely agreed upon. The definition of the loosest possible state, on the other hand, is more delicate, as it depends on the contact law (on the friction coefficient, in particular) and, possibly, on the assembling process.

Anyway, the compression procedure based on inflating the particles proves able to produce isotropic, homogeneous states (apart from local wall effects). As μ_0 grows from 0 to μ in the preparation stage, the material behaviour, under subsequent growing deviator stress, gradually changes from strongly dilatant to contractant (Fig. 8): the classical behaviour of granular materials with dense or loose initial configurations is

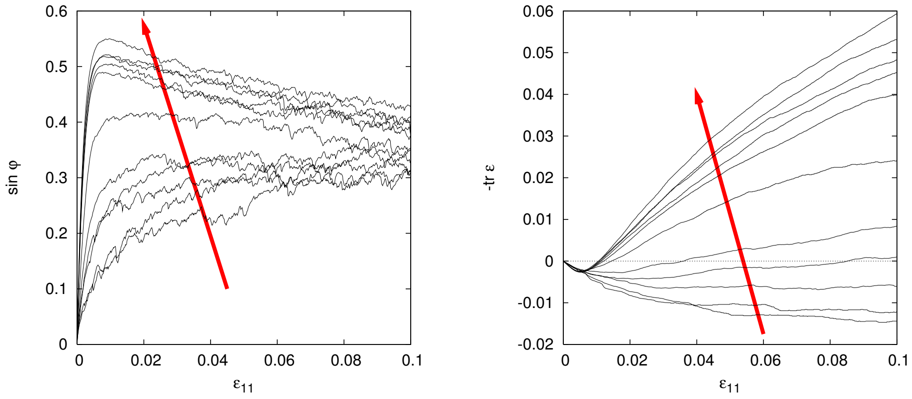

(a) (b)

Figure 8: Triaxial tests on polydisperse bead samples (5324 particles, $R_{\text{max}}/r_{\text{min}} = 2$, friction coefficient $\mu = 1$), initially assembled in states of different solid fraction (the arrows indicate how curves vary as Φ grows from 0.6 to 0.648) on varying the friction coefficient in the isotropic compression stage, carried out with inflatable particles. (a) $\sin\varphi$ with φ the mobilized internal friction angle, versus axial strain ϵ_{11}. (b) Volumetric strain versus ϵ_{11}. (Results by P. Villard, Laboratoire 3SR, Univ. Grenoble Alpes, France).

observed.

2.3 Confined granular assemblies and periodic boundary conditions

We now discuss the assembling process by isotropic compression with periodic boundary conditions (PBC), which allows one to obtain statistically homogeneous samples (no wall effects without walls!). Applying periodic boundary conditions to the simulation cell (a parallelogram in the example of Fig. 9) amounts to considering an infinite collection of copies of the cell, in correspondence with one another by a group of translations (like the pattern on some wallpapers). In a periodically repeated cell (Fig.9), any distinction between "central" and "peripheral" regions is meaningless: given one definition of the periodic cell, all of its images by an *arbitrary* translation are equally acceptable definitions. In 2D, one may also imagine that the cell is the surface of a torus (but the dynamics are not affected by any curvature effect). Confining granular assemblies with PBC is quite similar to the inflatable grain approach of Sec. 2.2.2, but instead of expanding grains within a fixed container one considers fixed-size grains within some homogeneously shrinking periodic space. The dynamics of a collection of grains within a deformable periodic cell are dealt with in detail in [RD11]. Only a few essential aspects are presented here. A linear operator $\mathbf{h}$ is defined, which maps

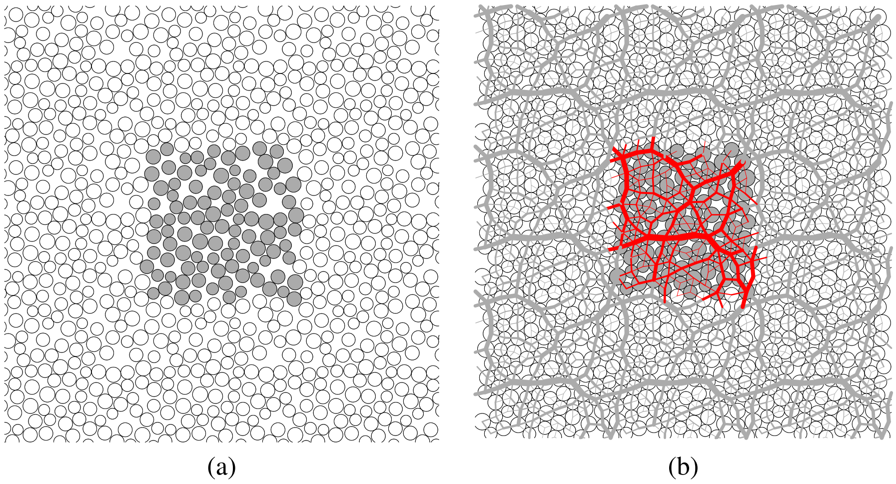

(a) (b)

Figure 9: Periodic boundary conditions: an example in 2D. Dark grey particles belong to the simulation cell, which is surrounded by infinitely many identical replicas in all directions. (a) “Granular gas” before isotropic compression. (b) Compressed state, in equilibrium under isotropic pressure. Force networks are periodic too, and particles in the simulation cell interact with one another and also with their copies within neighbouring copies of the cell.

vector $\vec{s}$, with coordinates s_α, $-1/2 \leq s_\alpha \leq 1/2$, $1 \leq \alpha \leq D$, within a unit cube (or square in 2D), onto vector $\vec{r}$, the actual position vector in the simulation cell. Thus in the example of Fig. 10, vectors $\vec{u}$ and $\vec{v}$ are the column vectors of the matrix of $\mathbf{h}$. Particle velocities $\dot{\vec{r}}$ comprise two contributions:

$$\dot{\vec{r}} = \dot{\mathbf{h}}\vec{s} + \mathbf{h}\dot{\vec{s}}, \tag{6}$$

the first one expressing the effect of the global shrinkage (or expansion) of physical space. In application to isotropic compression, one may use a diagonal matrix for $\mathbf{h}$ (i.e., the sample remains a rectangular parallelepiped). One may either control strains and impose, e.g., some shrinking or expansion rate to the cell, or directly write down dynamical equations for $\mathbf{h}$ (stress-controlled procedure). The aim we are pursuing here is to obtain well-equilibrated states under some prescribed stress level. The Cauchy stress tensor in a periodic system is to be evaluated with eq. (5)*, in which the sum runs over all interactions of the particles within the cell. Some of them involve some “copies” of those particles, belonging to adjacent cell replicas, and the branch vector involved in the formula should join the centres of objects that are actually in contact.

---

*The kinetic part of stresses, $\sum_{i=1}^{N} m_i \vec{v}_i \otimes \vec{v}_i$, which should be added to the contribution written in (5) [AR07a], vanishes in the quasi-static limit.

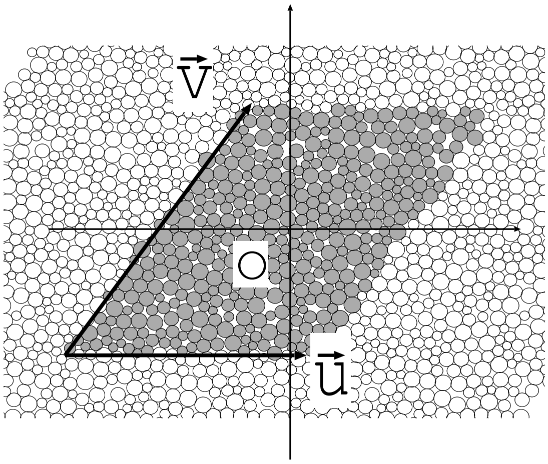

Figure 10: Vectors defining the basic cell, a parallelogram, in 2D sample with PBC.

In the stress-controlled isotropic compression procedure, the prescribed value of the stress is $\sigma_{\alpha\beta} = \sigma_0 \delta_{\alpha\beta}$ and the cell motion is driven by the difference between σ_0 and internal stress $\sigma_{\alpha\alpha}$, for each direction α. One writes

$$\frac{\ddot{h}_{\alpha\alpha}}{h_{\alpha\alpha}} = \frac{L^{D-2}}{M} \left[\sigma_{\alpha\alpha} - \sigma_0 \right], \tag{7}$$

in which M is a generalised mass associated to global strain parameters and L is a reference cell diameter (one may use $L = h_{\alpha\alpha}$). Eq. (7) should be integrated along with the equations of motion of the grains, until the system stabilizes in an equilibrium state with $\sigma_{\alpha\alpha} = \sigma_0$. Mass M should be of the order of the sum of all particle masses[†] for the characteristic frequency of oscillation of $h_{\alpha\alpha}$ to be similar to the one that would be observed in a subsystem of size L within a macroscopic granular medium. Such a choice for M leads in practice, as the final equilibrium is approached, to rather slow changes of cell dimensions compared to the equilibration times of grains within a fixed cell [AR07a]. As for confining procedures with rigid walls, one may choose to enforce an upper limit to strain rates $\dot{h}/h$, inertial effects being characterised by the inertial number I defined in eq. (2) (in which $\dot{h}/h$ should replace $||\vec{v}_P||/L_P$).

PBC's are observed to produce satisfactorily homogeneous and (for isotropic stresses) isotropic static equilibrium states. As with the method of inflatable grains, one may compress with a friction coefficient μ_0 smaller than the one used in the subsequent quasistatic testing of the assembled material. On setting μ_0 to zero, homogeneous RCP configurations are obtained, with Φ close to 0.64 in equal-sized bead assemblies. The coordination number on the force-carrying structure, or corrected coordination

---

[†] In practice, one can observe that when M is of the order of the mass of the biggest grain it works fine.

number, defined as

$$z^* = z/(1 - x_0), \tag{8}$$

is equal to 6 with spherical beads in the limit of rigid contacts (i.e., for large enough values of stiffness parameter κ defined in [RD11]). This is due to the generic isostaticity property of force-carrying networks in static equilibrium states of rigid, frictionless disks or spheres [Rou00, Com02, OSLN03, AR07a]. As μ_0 increases towards μ, looser, less coordinated states are obtained (z may decrease, typically, to about 4 and z^* to about 4.5 for moderate values of μ – for 3D spheres). More remarkably, it is also possible [AR07a] to produce very dense samples, with Φ approaching the maximum RCP value, but with quite low coordination numbers ($z^* \simeq 4.5$, $z \simeq 4$ – for 3D spheres and $z^* \simeq 3$ – for 2D discs). Such states are obtained on maintaining strongly agitated, granular gas states at very high densities, close to the maximum solid fraction, and then isotropically compressing with the final value μ of the friction coefficient. In practice, it is convenient to dilate RCP configurations so that all contacts open, then to mix the grains with some event-driven, energy-conserving procedure, before applying the confining pressure to the sample. The observation that very different coordination numbers can correspond to the same density in homogeneous, isotropic granular samples raises unsolved questions about which structures are obtained in laboratory experiments, and indicates that the internal states of a homogeneous sample of granular material under a given isotropic pressure should not be only characterised by their density (even with a perfectly isotropic fabric). Measuring elastic moduli, which are sensitive to coordination numbers [AR07b], could provide useful clues. Equally dense, but differently coordinated isotropic initial states, once subjected to a triaxial compression test, reach about the same maximum deviator stress, but the strain needed to mobilize internal friction is larger for poorly coordinated initial packings [RC05, ECC$^+$06]. An example of 2D DM simple shear tests on 9801 discs giving quite same conclusions is shown on figure 11.

3 Granular samples under gravity

3.1 Homogeneity

Granular packings subjected to their weight are necessarily anisotropic, as the vertical direction plays a special role. Denoting the vertical coordinate as z, one generally has, in the absence of any further cause of anisotropy, $\sigma_{xx} = \sigma_{yy} \neq \sigma_{zz}$. Stresses will also be inhomogeneous, with σ_{zz} increasing with depth in order to balance the weight of the material lying above altitude z. If the free surface is horizontal at altitude $z = H$, one should have, provided lateral walls do not exert any vertical force,

$$\sigma_{zz}(z) = \int_z^H \rho_m \Phi(u) g du, \tag{9}$$

in which $\Phi(u)$ denotes the solid fraction, varying with vertical coordinate u, and ρ_m is the mass density of the solid grains. On writing (9), it is implicitly assumed that Φ

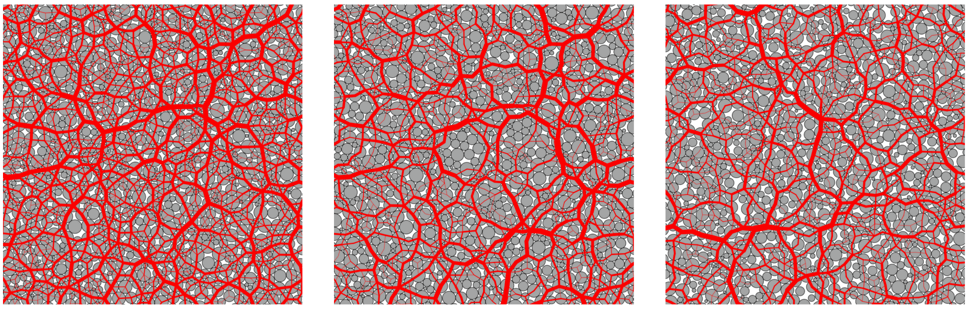

(a) Sample A (b) Sample A’ (c) Sample B

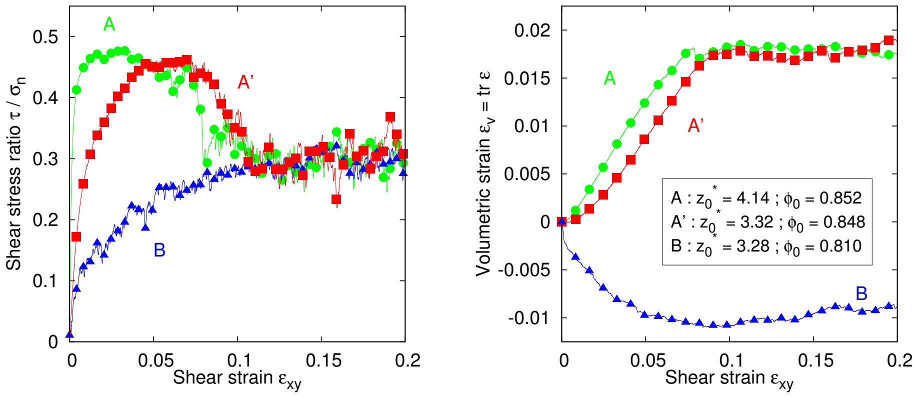

(d) (e)

Figure 11: Simple shear tests on packings of 9801 frictional polydisperse disks with periodic boundary conditions. 3 different samples are tested: sample A is initially very dense ($\phi_0 = 0.852$) with a high coordination number ($z_0^* = 4.14$); sample A’ is initially very dense ($\phi_0 = 0.848$) but with a small coordination number ($z_0^* = 3.32$); finally, sample B is initially loose ($\phi_0 = 0.810$) with a small coordination number ($z_0^* = 3.28$). (a), (b) and (c) are zooms of the force networks of samples A, A’ and B. (d) Gives the evolution of the shear strength along the shear strain for the 3 samples tested. (e) shows the volumetric (surface in 2D) evolution along the shear strain for the 3 samples tested.

is uniform in horizontal layers. We focus here on the numerical procedures suitable to prepare granular samples in equilibrium under their own weight, in well-controlled states with the least possible level of inhomogeneity. This aim can be characterised by the two criteria:

(a) transverse isotropy of internal state within horizontal planes;

(b) uniform values of all dimensionless state variables.

Those two conditions define an "ideal" sample under gravity, which is the most appropriate to investigate intrinsic material behaviours. Conditions (a) and (b) should be satisfied, at least approximatively, for numerical samples to be used as Representative Volume Elements (RVE).

Transverse isotropy (a) means that all horizontal directions play the same role. Condition (b) ensures that the solid fraction, the coordination number, the distribution of distances between neighbouring grains (normalized by the average diameter), the mobilization of friction or the fabric parameters should be uniform, i.e. their average values in a subsystem are independent of their positions inside the sample. By taking a constant Φ in (9), stress σ_{zz} will increase linearly with depth, like the hydrostatic pressure in an incompressible fluid. Lateral boundaries should not affect the internal state of the material for state variables to be uniform in horizontal planes. In practice frictional vertical walls will balance some part of the weight and perturb vertical stresses, possibly throughout the whole sample, especially for tall, elongated shapes. Thus, the so-called Janssen effect in silos [Spe06] entails that the vertical stress, instead of steadily increasing with depth, approaches a maximum, of the order of $\rho_m \Phi g L$, if L is the sample width. Moreover, the stresses in horizontal planes are not uniform, with σ_{zx}, σ_{zy} vanishing near the centre and reaching a maximum value at the container walls. Those effects are localized to small lateral regions close to the wall if $H \gg L$. In numerical simulations one should therefore choose frictionless walls, or laterally periodic boundary conditions, unless the Janssen effect is desired.

Condition (b) is quite stringent, and some small mitigations should be accepted in practice. First, near the bottom substrate, and near the free surface, different local states are usually observed. These are boundary effects, and one may check in practice that they do not affect the bulk material behavior. Condition (b) implies that the material should not be sensitive to stress intensity, thereby assuming that the limit of rigid contacts is approached ($\kappa \to \infty$). The elastic deflection of contacts necessarily increases with depth, but its influence on packing geometry should be negligible. If condition (b) is correctly satisfied, then one important result characterising the material state is the ratio of principal stresses (known as "the coefficient of earth pressure at rest" in a geotechnical context [Jak44]))

$$K_0 = \frac{\sigma_{xx}}{\sigma_{zz}} = \frac{\sigma_{yy}}{\sigma_{zz}}, \tag{10}$$

which should be uniform within the sample, except for possible corrections near the bottom or the free surface. If conditions (a) and (b) are satisfied with good approximation, then the material state might be analysed as if it were perfectly homogeneous, and transversely isotropic, apart from force intensities which increase linearly with depth. One remaining difference [ECC$^+$06] with samples assembled under uniform stresses, without gravity, but with the same ratio K_0, should be pointed out: samples under gravity do not contain any rattler, $m > D$ for each grain. However some of the grains are only subjected to their weight (plus, possibly part of the weight of one or a small number of grains relying on it). Those grains are analogous to rattlers in the absence of gravity, and their contacts should be ignored before referring to homogeneous granular structures without gravity. Thus one can define the corrected coordination number z^* as the value of the coordination number within the assembly once it is deprived of those grains and their contacts. This definition is the analog of relation (8) used in homogeneously confined systems.

In the sequel three procedures to assemble grains under gravity are discussed: grain by grain deposition, dumping and controlled pluviation.

3.2 Grain-wise deposition

On depositing grains one by one, and letting them stabilize under their own weight on the free surface of the sample, one obtains remarkably anisotropic structures. Thus Calvetti *et al.* [CCL97], in an experimental study of a model 2D assembly of parallel cylinders (the so-called "Schneebeli material" [Sch56]), assembled samples of about 1000 grains, each one placed manually after the other. Their model material was polydisperse, cylinder diameters ranging between 8 mm and 20 mm. The resulting fabric exhibited quite a strong anisotropy, peaking in orientations at $\pm 45^\circ$ with respect to the horizontal direction. Moreau [Mor00], in a numerical simulation by DEM of a grain-wise deposition procedure, observed similar results on fabric anisotropy, with polygonal particles.

The granular layer shown in Fig. 12, in equilibrium under its own weight, is the result of such a simulation of a grain-wise deposition process. The rough substrate is a monolayer of fixed grains, and the simulation cell is laterally periodic. The assembling rule implemented in that case requests each grain to have two contacts before a new one is deposited. The new grain is then placed on top of the free surface, with a velocity equal to zero. Given a randomly chosen value of its (horizontal) coordinate x, drawn with a uniform distribution within the cell, its coordinate in the vertical direction takes the lowest possible value allowed by the non-interpenetration condition, so that it touches one of the previously deposited grains.

Fig. 13(a) shows that a very strong fabric anisotropy is obtained with this assembling procedure. Favoured directions correspond to the contacts of a disk supported by two neighbours. The grain-wise deposition procedure produces samples of uniform solid fraction, apart from local bottom and free surface effects, as shown in Fig. 14(a). Beyond a thin superficial layer, local stresses σ_{yy} and σ_{xx} increase linearly with depth, as expected, see Sec. 3.1. The earth pressure coefficient, K_0, can be identified as the

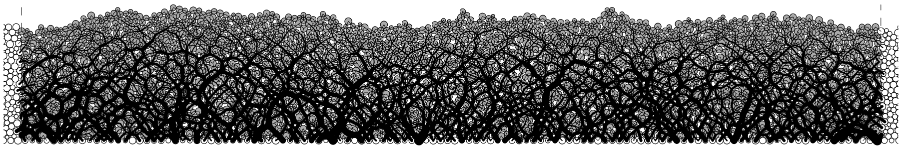

Figure 12: A horizontal layer of 3600 disks deposited one by one, in equilibrium under its weight, on a rough substrate. Force intensities are encoded, as usual, as line thicknesses.

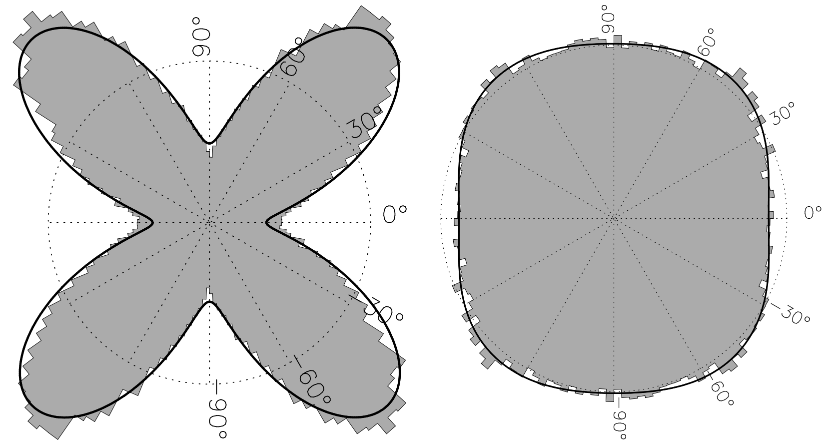

(a) (b)

Figure 13: Histogram of contact orientations in layers of frictional grains. Statistics obtained on 10 samples of 9801 grains. The dotted line corresponds to an isotropic fabric. Grains only supporting their own weight are excluded from the statistical analysis. (a) Grain-wise deposition, corrected coordination number $z^* = 3.53$. (b) Dumping, $z^* = 3.06$.

constant ratio of vertical stress gradients (one has $K_0 \simeq 0.5$ in the present case):

$$K_0 = \left[\frac{d\sigma_{yy}}{dy}\right]^{-1} \frac{d\sigma_{xx}}{dy}. \tag{11}$$

Stress ratio σ_{xx}/σ_{yy} approaches K_0 as depth increases.

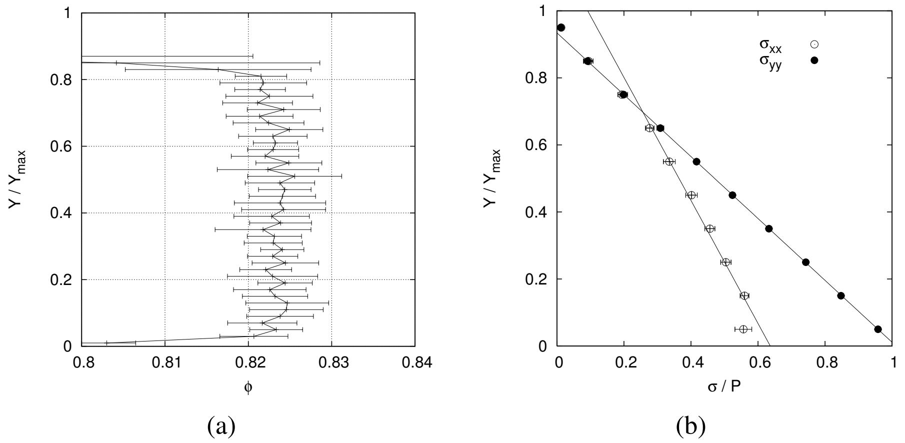

(a) (b)

Figure 14: Analysis of grain-wise deposited layers. Data measured in thin layers, averaged over 10 samples of 9801 grains ($\kappa = 1000$ at bottom, the pressure due to the self-weight of the sample being maximum at the bottom), plotted as functions of altitude Y above the substrate, normalized by layer thickness Y_{max}: (a) local solid fraction Φ; (b) horizontal (σ_{xx}) and vertical (σ_{yy}) stresses. P is the bottom vertical stress.

3.3 Dumping

This procedure (which could be termed "sedimentation" in the presence of a fluid) consists in suddenly "plugging in" gravity in a homogeneous granular gas sample. The final structure is characterised by a rather small level of fabric anisotropy (Fig. 13(b)). The dumping procedure is simple and its computational cost is much lower than that of the grain-wise deposition method. One major drawback is, however, the inhomogeneity of the final state, which does not meet the criteria of Sec. 3.1. The solid fraction is usually not constant. Fig. 15 shows a slight, but systematic increase of Φ away from the bottom (compare to Fig. 14(a)). In the dynamical phase following the application of gravity, the granular layer hits the fixed bottom wall of the container, whence an elastic wave travelling up the sample, which tends to decrease the density in the bottom region bouncing off the substrate. This effect depends on the initial density, on the velocity of grains hitting the ground, and, likely, on contact stiffness too. Fig. 15(b). evidences a nearly hydrostatic vertical stress field (the effect of the density gradient remaining small in that case), and a coefficient K_0 closer to 1 ($K_0 \simeq 0.9$) with respect to samples made by grain-wise deposition.

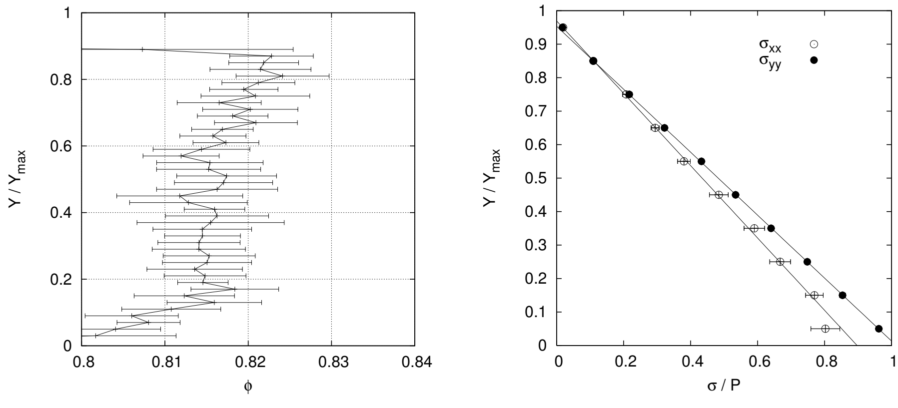

(a) (b)

Figure 15: Analog of Fig. 14, with 10 samples of 9801 grains each, assembled with the dumping method.

3.4 Controlled pluviation

Among the different procedures used in soil mechanics laboratories to prepare samples of granular materials, controlled pluviation, as schematised in Fig. 16, is known to produce samples with satisfactory homogeneity. This procedure was studied in detail, experimentally by Benahmed [Ben01] (see also [BCD04]), and numerically by Emam *et al.* [ECC$^+$06]. The method is designed to ensure a constant flux of grains falling onto the free surface of the growing sample, with a constant mass flow rate per unit area Q, and constant vertical velocity V_P. In practice, grains are subjected to a free fall from height H_P above the free surface, and relation $V_P = \sqrt{2gH_P}$ is assumed, neglecting the hydrodynamic drag in air (which is a good approximation in practice for H_P of the order of 10 cm and grain diameters above 0.1 mm). To maintain a constant H_P the upper reservoir has to move up with the same rate as the free surface. The final state is controlled by parameters Q and V_P, which are conveniently put into dimensionless form, for grains of diameter d, made of a material with mass density ρ, on defining a reduced rate $Q^* = Q/(\rho\sqrt{dg})$ and a reduced height of free fall $H_P^* = H_P/d = \dfrac{V_P^2}{4g^2 d}$. Q^* may be regarded as the ratio of a local rearrangement time for one grain on the surface, $\sqrt{d/g}$, to m/Qd^2, the characteristic time during which a grain belongs to the agitated layer, a few diameters thick, near the free surface,

The numerical implementation of the controlled pluviation procedure in discrete sim-

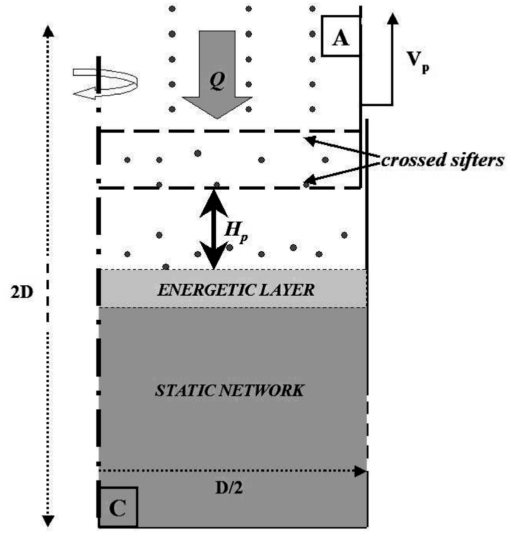

Figure 16: Schematic view of the experimental controlled pluviation apparatus. Holes in the bottom of the upper reservoir control the mass flow rate Q. Crossed sifters (grids) distribute the "raining" grains uniformly on the free surface. The free fall of the grains is assumed to start with zero velocity at the lower grid. The reservoir and the grids are moving up with controlled velocity, so that the height of free fall above the free surface of the sample is constant [ECC$^+$06].

ulation is quite simple: grains are placed onto the free surface at randomly chosen positions in the horizontal plane, with velocity V_P, with a frequency corresponding to the desired mass flow rate per unit area. For large flow rates, the procedure becomes rather ambiguously defined, especially for small H_P, because of the lack of a clear definition of the free surface, when its fluctuations are of the order of H_P. In the opposite limit of very small deposition rates, the choice of $H_P^* = 0$ corresponds to the grain-wise deposition procedure of Sec. 3.2.

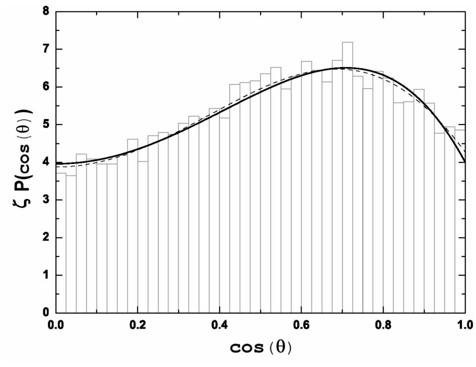

Figure 17: Numerical samples of glass beads of diameter d, assembled by controlled pluviation. Distribution of $|\cos\theta|$ (fabric anisotropy) in a numerical sample of 10000 beads assembled by controlled pluviation, normalised by the coordination number. Continuous line: its expansion in Legendre polynomials to order 4. Dotted line: its expansion to order 6. Results from [ECC$^+$06].

The fabric anisotropy, in transversely isotropic 3D pluviated samples, is conveniently expressed by the probability density $P(\cos\theta)$ of the cosine of the angle between the contact normal and the vertical direction. $P(\cos\theta)$ is an even function with an expansion by Legendre polynomials of even order

$$P(\cos\theta) = \sum_{k=0}^{+\infty} B_{2k} P_{2k}(\cos\theta). \tag{12}$$

In practice the three first terms ($k = 0$, 1 and 2) often suffice to parametrise the distribution with good accuracy, as shown in Fig. 17, and coefficients B_2 and B_4 can be obtained measuring moments $\mu_2 = \langle\cos^2\theta\rangle$ and $\mu_4 = \langle\cos^4\theta\rangle$. For isotropic fabrics, $P(\cos\theta)$ is constant in interval $[0, 1]$ (uniform distribution), and one has $\mu_2 = 1/3$ and $\mu_4 = 1/5$.

Simulation results show that controlled pluviation produces homogeneous samples satisfying the criteria of Sec. 3.1, with local corrections near the substrate and near

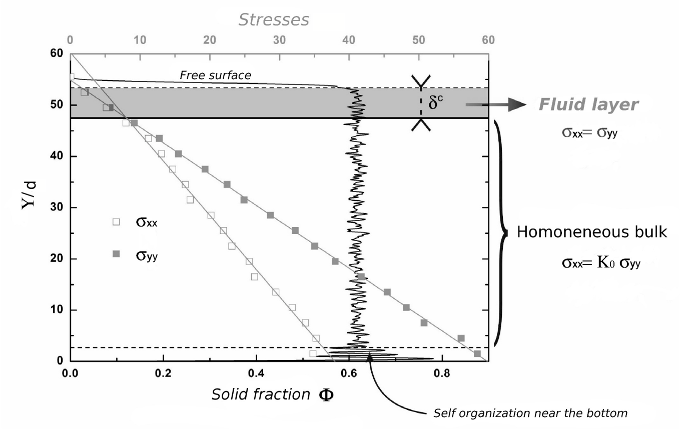

Figure 18: Numerical samples of glass beads of diameter d, assembled by controlled pluviation. Horizontal (σ_{xx}, grey open squares) and vertical (σ_{yy}, grey square dots) stress versus altitude y (in units of d). Solid, thick line: solid fraction Φ versus y/d. Results from [ECC$^+$06], similar to [IWML14].

the free surface. A constant density is obtained (Fig. 18). Likewise, the coordination number z is uniform within the sample. Beneath some surface layer (several diameters thick), horizontal and vertical stresses grow proportionally, evidencing a constant coefficient K_0 in the limit of large systems. Near the surface, ratios σ_{xx}/σ_{yy} closer to 1 reflect the history of the assembling process. The recently deposited material belongs first to an agitated fluid-like layer penetrating a few diameters below the free surface with a nearly isotropic stress tensor. Then, as it is buried at greater depth, a solid structure forms and supports anisotropic stresses. It may be checked that the buried material, if subjected to an oedometric test, responds with characteristic stress ratio K_0 [IWML14]. The stress anisotropy is observed to increase (i.e., coefficient K_0 decreases) as H_P increases, as does the solid fraction Φ. Ref. [ECC$^+$06] gives a functional form for the dependence of Φ on H_P/d for fixed reduced flow rate Q^*. Increasing Q^*, on the other hand, will reduce Φ, as grains have less time to rearrange into a more densely packed structure.

Samples numerically assembled on simulating controlled pluviation are very good, judging from the homogeneity criteria we have been emphasizing in the present article. Their properties, for given material characteristics and given control parameters H_P^* and Q^*, are reproducible. One drawback, though, at least for spherical beads, is the inability of the pluviation technique to produce loose samples (i.e., which would contract under shear). Experimental results with glass beads [ECC$^+$06] also indicate that only very dense to moderately dense samples are obtained by controlled pluviation in the laboratory; this is most likely due to a specific behaviour of spherical particles, as opposed to sand grains [Ben01]. Another issue is whether, or to what extent, laboratory samples and numerical ones, both prepared by controlled pluviation, with the same parameters H_P^* and Q^*, have the same internal state. One may check, at least, that the dependence of the final solid fraction Φ on Q^* and H_P^* is similar [ECC$^+$06]. In principle, provided contact laws are correctly calibrated, experimental and numerical results should coincide. It turns out, though, that, unlike the rheological behaviour of granular materials in quasi-static conditions or in dense flow, the properties of samples produced by pluviation depend sensitively on the viscous terms of the contact law which govern the dissipation in collisions (or, in other words, on the coefficients of restitution). As such dissipative ingredients of micromechanical laws implemented in simulations do not usually result from a physical identification approach, accurate quantitative comparisons between experiments and simulations are still difficult (for more details, see ALERT 2017, papers of Martin [Mar] and Luding [LRW]).

Results from controlled pluviation studies might contribute to explain the heterogeneities obtained with other procedures. In the dumping method, the grains near the bottom experience a free fall over from a lower altitude, and thus tend to assemble at lower density than those falling from the top part of the initial configuration, due to a smaller H_P. However, the accretion rate also increases because grains from the top accelerate more, hence one has a lower Q^* for the bottom grains, which would tend to induce a larger density. It seems that both effects do not compensate each other. The elastic wave mentioned in Sec. 3.3 introduces another phenomenon, though, which is not accounted for on referring to controlled pluviation. Another assembling procedure consists in pouring grains with a constant (dimensionless) flow rate Q^* from a fixed altitude H_V. Thus, the height of free fall $H_P^* = H_V^* - y/d$ decreases as the vertical coordinate of the free surface, y, increases. Such samples should exhibit a density gradient, and form looser structures at the top, especially if H_P^* decreases to low values. Fig. 19 shows that the numerical results abide by this prediction in quantitative form, as the local density conforms to the Φ dependence on H_P^*, applied locally with a gradually varying $H_P^* = H_V^* - y/d$.

4 Conclusions

In this article, we have been focussing on the numerical procedures suitable to prepare representative volume elements of material in homogeneous states, to be further tested like in [TLM]. Like in the bulk of the published numerical studies on static and quasistatic properties of granular materials, we did not attempt to reproduce laboratory assembling procedures quantitatively. How to design accurate numerical models of dynamical processes in which agitated, fluid-like materials jam and stabilize in history-dependent solid configurations is still quite an open issue, due to the influence in such situations of features of the models that are not identified in a physical approach at the contact scale (e.g., viscous dissipation. See also [Mar, LRW]). Among the wide variety of numerical recipes used in simulations to assemble samples in static equilibrium in a given state of stress, a few ones have been discussed, with emphasis

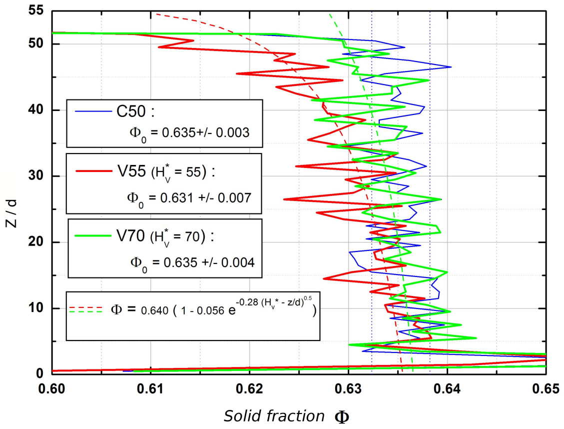

Figure 19: Vertical solid fraction profile in laterally periodic 3D samples assembled under gravity. Samples V55 and V70, obtained by pouring grains from constant altitude H_V (55 or 70 diameters) above the container bottom exhibit density profiles in agreement with the controlled pluviation results, applied locally (dotted lines), with varying pluviation height $H_v - z$. C50 is a constant density profile obtained with the controlled pluviation (constant $H_P^* = 50$) procedure.

on the homogeneity criteria that a sample should satisfy for the intrinsic constitutive laws of the material to be adequately investigated in relation to its microstructure and micromechanics. Possible sources of inhomogeneities, and systematic tendencies regarding the influence of control parameters governing the assembling process on the final internal state of equilibrated samples have been reported, in the hope that our study, although not exhaustive, will provide useful guidelines for new practitioners of discrete element simulations.

References

[AR07a] I. Agnolin and J.-N. Roux. Internal states of model isotropic granular packing. i. assembling process, geometry and contact networks. *Physical Review E*, 76(6):061302, 2007.

[AR07b] I. Agnolin and J.-N. Roux. Internal states of model isotropic granular packing. iii. elastic properties. *Physical Review E*, 76(6):061304, 2007.

[BCD04] N. Benahmed, J. Canou, and J.-C. Dupla. Structure initiale et propriétés de liquéfaction statique d'un sable. *Comptes-Rendus Académie des Sciences, Mécanique*, 332:887–894, 2004.

[Ben01] N. Benahmed. *Comportement mécanique d'un sable sous cisaillement monotone et cyclique : application aux phénomènes de liquéfaction et de mobilité cyclique*. PhD thesis, Ecole Nationale des Ponts et Chaussées, 2001.

[CCL97] F. Calvetti, G. Combe, and J. Lanier. Experimental micromechanical analysis of a 2d granular material: relation between structure evolution and loading path. *Mechanics of cohesive frictional materials*, 2(2):121–163, 1997.

[Com02] G. Combe. *Mécanique des matériaux granulaires et origines microscopiques de la déformation*. Sciences pour le génie civil SI 8, Etudes et Recherches des Laboratoires des Ponts et Chaussées. Laboratoire Central des Ponts et Chaussées, Paris, 2002.

[CR03] G. Combe and J.-N. Roux. Discrete numerical simulation, quasistatic deformation and the origins of strain in granular materials. *3ème Symposium International sur le Comportement des sols et des roches tendres. Deformation Characteristics of geomaterials.*, pages 1071–1078, 2003.

[CV05] B. Chareyre and P. Villard. Dynamic spar elements and discrete element methods in two dimensions for the modeling of soil-inclusion problems. *Journal of Engineering Mechanics*, 131:689–698, 2005.

[dCEP$^+$05] F. da Cruz, S. Emam, M. Prochnow, J-N. Roux, and F. Chevoir. Rheophysics of dense granular flows: Discrete simulation of plane shear flows. *Physical Review E*, 72:021309, 2005.

[ECC$^+$06] S. Emam, J. Canou, A. Corfdir, J.-C. Dupla, and J.-N. Roux. *Elaboration et comportement mécanique de matériaux granulaires solides modèles : expériences et simulations numériques*, pages 105–146. Sciences pour le génie civil SI 12, Etudes et Recherches des Laboratoires des Ponts et Chaussées. Laboratoire Central des Ponts et Chaussées, Paris, 2006.

[FL95] E. Flavigny and J. Lanier. Densification des sables: quelques remarques issues des essais de laboratoire. *Actes des Journées L. Ménard, CFMS, Paris*, pages 73–81, 1995.

[IWML14] O. I. Imole, M. Wojtkowski, V. Magnanimo, and S. Luding. Micro-macro correlations and anisotropy in granular assemblies under uniaxial loading and unloading. *Physical Review. E*, 89:042210, 2014.

[Jak44] J. Jaky. The coefficient of earth pressure at rest. in hungarian: A nyugalmi nyomás tényezöje. *J. Soc. Hung. Eng. Arch. (Magyar Mérnök- És Építész-Egylet Közlönye)*, 78(22):355–358, 1944.

[Lov44] A.E.H. Love. *A treatise on the mathematical theory of elasticity*. Dover Publication, 1944.

[LRW] S. Luding, N. Rivas, and T. Weinhart. From soft and hard particle simulations to continuum theory for granular flows. *ALERT geomaterials Doctoral School 2017, Aussois, France.*

[Mar] C.L. Martin. Advanced contact laws. *ALERT geomaterials Doctoral School 2017, Aussois, France.*

[Mor00] J.-J. Moreau. Réponse d'une couche granulaire à une action locale. In Ecole Nationale des Ponts et Chaussées, editor, *Colloque physique et mécanique des matériaux granulaires*, pages 193–198, Champs-sur-Marne, 2000. Presses du Laboratoire Central des Ponts et Chaussée.

[OSLN03] C. S. O'Hern, L. E. Silbert, A. J. Liu, and S. R. Nagel. Jamming at zero temperature and zero applied stress: The epitome of disorder. *Physical Review E*, 68:011306, 2003.

[PR08] P.-E. Peyneau and J.-N. Roux. Solidlike behavior and anisotropy in rigid frictionless beas assemblies. *Physical Review E*, 78:041307, 2008.

[Rad] F. Radjai. The contact dynamics (CD) method. *ALERT geomaterials Doctoral School 2017, Aussois, France.*

[RC05] J.-N. Roux and F. Chevoir. Discrete numerical simulation and the mechanical behaviour of granular materials. *Bulletin des Laboratoires des Ponts et Chaussées*, 254:109–138, 2005.

[RCT07] J.-N. Roux, F. Chevoir, and F. Toussaint. Close packing states for binary mixtures of spherical grains: a numerical simulation study. *Bulletin des Laboratoires des Ponts et Chaussées*, 268-269:141–152, 2007.

[RD11] F. Radjaï and F. Dubois, editors. *Discrete-element Modeling of Granular Materials*. Wiley-Iste, 2011.

[Rou00] J.-N. Roux. Geometric origin of mechanical properties of granular meterials. *Physical Review E*, 61(6):6802–6836, 2000.

[Sch56] G. Schneebeli. Une analogie mécanique pour les terres sans cohésion. *Comptes rendus de l'Académie des Sciences*, 243(1):125–126, 1956.

[SM76] D.A. Sangrey and R.J. Mitchell. *Soil specimen preparation for laboratory testing*. American Society for Testing and Materials (ASTM), 1976.

[Spe06] M. Sperl. Experiments on corn pressure in silo cells–translation and comment of Janssen's paper from 1895. *Granular Matter*, 8(2):59–65, 2006.

[TLM] K. Taghizadeh, S. Luding, and V. Magnanimo. DEM applied to soil mechanics. *ALERT geomaterials Doctoral School 2017, Aussois, France.*

[Web66] J. Weber. Recherches concernant les contraintes intergranulaires dans les milieux pulvérulents. *Bulletin de Liaison des Ponts et Chaussées*, 20:1–20, 1966.

DEM applied to soil mechanics

K. Taghizadeh, S. Luding, V. Magnanimo

*Multi-Scale Mechanics, Faculty of Engineering Technology (ET),
MESA+, University of Twente, Enschede, The Netherlands*

Dense granular materials, as soils, behave differently from classical solids. Soils thus can barely be described by the continuum theories developed for solids, with attempts in this direction leading to a wide class of empirical correction terms. In fact, the behavior of the material at the macro-scale, considering the continuum fields of density, strain and stress, is intimately related to particle-scale variables and kinetic processes that are typically not known. Already from its first appearance in the late seventies DEM was found to be a powerful tool for modeling the behavior of soils taking the particles and their micro-mechanics into account. DEM allows the simulation of fairly complex non-linear, bifurcation, stability and interaction problems in geotechnical engineering, and standard laboratory tests can be easily simulated.

In this chapter we address some well known geo-mechanical and -technical element tests, namely triaxial and shear tests, as well as wave propagation in soil samples, and show how to use DEM to correctly and effectively reproduce them. Non-linear hysteretic stress-strain and -volume responses of the material can be reproduced already by simple particle contact models. On the other hand, DEM offers the unique chance to "look inside" the soil samples such that microscopical information can be inferred in addition to the macroscopic field information that is also available from laboratory tests. Long-term goal is to use such insights to develop a new class of continuum models, based on the micro-scale mechanics, to describe large-scale industrial and technical applications.

1 Introduction

In our daily life we are surrounded by granular materials like soil, sand, coffee, nuts, food- or detergent-powders, pharmaceutical products like tablets, and many others. Granular materials constitute over 75% of raw materials feedstock to industry, including pharmaceutical, mining, agriculture, chemical, biotechnological, textile, etc. In spite of their ubiquity and apparent simplicity, their behavior is far from being fully understood. This leads to the loss of about 10% of the world's energy consumption in processing, storage and transport of granular materials, and to uncontrollable natural hazards, related to avalanches or landslides due to instability of slopes or foundations.

These materials behave differently from usual solids or fluids and show peculiar mechanical properties like dilatancy, history dependence, ratcheting and anisotropy. The behavior of granular materials is highly non-linear and involves irreversibility (plasticity), possibly already at very small strains, due to rearrangements of the elementary particles [Bar94, God90, SNDD09]. Furthermore, complex soil behavior also originates from the multi-phase nature of these materials that exhibits both elastic and plastic non-linearities due to solid-fluid coupling. Non-linear behavior can be characterized by rigidity and degree of non-linearity, which can be determined from measurements of soil stiffness, peak strength and failure strain [Atk00].

In analogy to "classical" solids, the behavior of granular materials depends on the amount of deformation the sample is subjected to. Roughly speaking, we can distinguish (i) an elastic regime at very small strain, (ii) a non-linear elasto-plastic regime that holds from small to intermediate strain, and (iii) a fully plastic regime at large strain, where the material flows (solid to fluid transition) at constant stress and volume – if sheared long enough. As special note on the elastic regime, soil behavior is considered to be truly elastic only in the range of extremely small strains. For slightly higher strain, soil already exhibits a non-linear stress-strain relationship, even though stress is almost fully recovered under unloading. For larger strain, the material deforms irreversibly and deformations are permanent (plastic). The elastic material stiffness is defined only for small strain and can be found from measurements of the (shear) wave velocity in situ or laboratory tests or by probing, i.e. incremental stress-strain tests. The peak strength of the material and its flow parameters can be measured in routine laboratory tests at larger strains, even though the initiation of shear bands must be carefully taken into account, see Fig. 1.

In this chapter, we explore the different strain regimes of soils with the aid of the Discrete Element Method (DEM), as introduced in the chapter by Luding [LRW], in the case of dry material; for alternative particle simulation approaches, see Refs. [LRW, TWT, Rad] and for the modeling of (partly) saturated samples, see Ref. [DAM$^+$]. We briefly explain the techniques used to experimentally characterize soils in each regime and then we show how to carry on these experiments numerically with DEM, see also Refs. [CR, DS]. DEM simulations of (element) tests in order to complement laboratory studies, require properly calibrated contact models [LRW, Mar] as well as a careful preparation of the samples [CR] before they can provide additional information on the particle-scale, which is usually not accessible experimentally. From such information/data, novel continuum constitutive models (based on micro-mechanical parameters like micro-structure, anisotropy or particle orientations, along with the traditional fields stress, strain and density) can be developed [LRW, TWT] to better predict the soil behavior in large scale applications.

The paper is organized as follows:

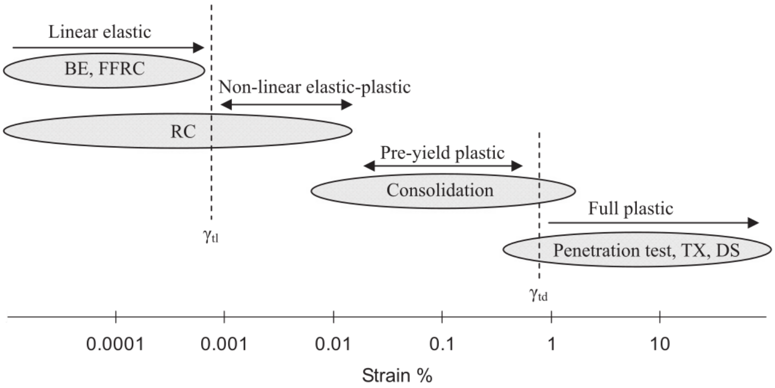

Figure 1: Strain regimes of soil and typical characterization tests. Notation: BE is a bender element; FFRC is a free-free resonant column test; RC is a resonant column test; TX is a triaxial test; DS is a direct shear test, where γ_{tl} is the linear elastic threshold strain; γ_{td} is the degradation threshold strain [Atk00, LSL14].

Section 2-Numerical background: Brief overview on the numerical modeling and parameters used for simulations.

Section 3-Sample preparation: Brief overview on the sample preparation for numerical element test simulations.

Section 4-Elasticity (very small strain stiffness) in geomaterials: Review of the most common used techniques to measure elastic stiffness of soils at very small strain and numerical simulation of both static and dynamic approaches.

Section 5-Element tests for small and intermediate strain: Several examples of typical element tests at small and intermediate strain, namely uniaxial compression test, triaxial and shear tests.

Section 6-Summary and conclusion.

2 Numerical background

The Discrete Element Method (DEM) [CS79, Lud08, LRW, Mar] investigates the response of soils to deformations/loads by looking at the constituent particles. At the basis of DEM are force laws [LRW, Mar] that relate the interaction force to the overlap and tangential displacement of two particle contact surfaces (Fig. 2). If all forces $\mathbf{f}_i$ acting on particle i are known, the problem is reduced to the integration of Newton's equations of motion for the translational and rotational degrees of freedom. Gravity is neglected in all simulations here, so that the applied deformations can be assumed isotropic.

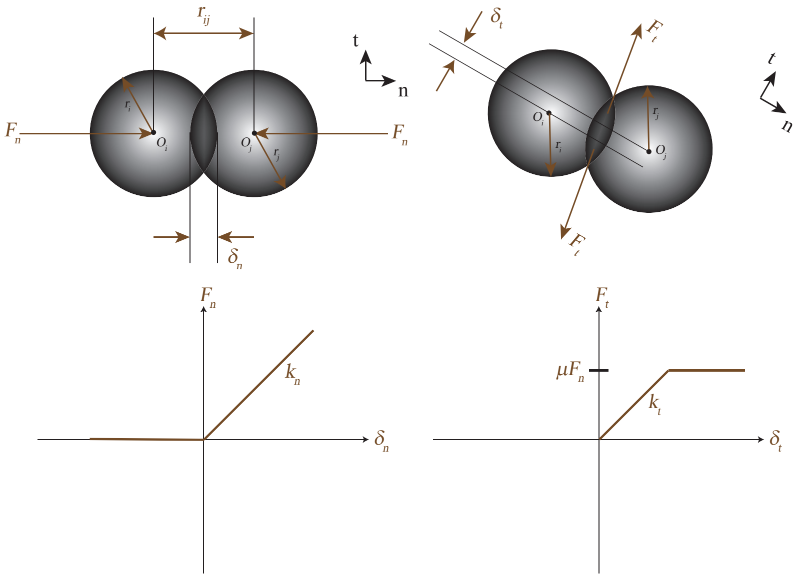

(a) (b)

Figure 2: (a) Normal contact model with the normal overlap distance δ_n. (b) Tangential contact model with the tangential displacement δ_t. Tangential force is coupled to the normal force via Coulomb's law, $f_t \leq \mu_s f_n$, where for the sliding case one has dynamic friction with $f_t = \mu_d f_n$.

The simplest normal contact force model, which takes into account excluded volume and dissipation, involving linear repulsive and linear dissipative forces, is given as $\mathbf{f}_n = f_n \hat{\mathbf{n}} = (k\delta_n + \gamma\dot{\delta})\hat{\mathbf{n}}$, where k is the spring stiffness, γ is the contact viscosity parameter, δ_n is the overlap and $\dot{\delta}$ is the relative velocity in the normal direction $\hat{\mathbf{n}}$. An artificial background dissipation force, $\mathbf{f}_b = -\gamma_b \mathbf{v}_i$, proportional to the velocity $\mathbf{v}_i$ of particle i is added, resembling the damping due to a background medium, as e.g. a fluid. For more realistic contact interactions in the normal direction, the Hertzian model must be considered [LRW, Mar, Lud98]. Note that the choice of contact model (linear or non-linear) affects the collisional behavior between two particles as well as the bulk behavior [JS06]. When the linear and Hertzian contact models are compared, a major difference is due to the initial contact stiffness, where the former presents a finite value, while the latter has stiffness proportional to deformation. However, the difference between the two models becomes smaller when the consolidation pressure is higher. We use linear contact model for examples in the following sections as it is simple and easier to implement.

DEM simulations are slow when large-scale phenomena and industrial applications of granular materials are taken into account. Even with the most advanced computational techniques available today, it is not possible to simulate realistic numbers of particles with complex geometries. Thus, continuum models are more desirable to describe granular materials where principles of continuum mechanics can be applied. In a classical continuum model, the mechanical behavior of the materials is based on the relation between stress and strain [GL13, LRW, TWT]. However, a comprehensive description of the granular behavior must not cancel out features at the microscale, that, in principle, govern the behavior at macroscale, such as geometrical arrangements of the particles and restructuring. In order to bridge this gap, we propose to use a micromechanical-based continuum description, where information at the microscale are transferred to larger-scale, via the so-called micro-macro transition [KLM14, LRW, TWT]. In the following, we describe the general procedure to average microscopic quantities to continuum tensorial variables.

2.1 Averaged macroscopic parameters

To describe and better understand the relationships between macroscopic quantities, tensors are split up into isotropic, deviatoric and antisymmetric parts. Any tensor $\boldsymbol{T}$ can be decomposed as:

$$\boldsymbol{T} = \frac{1}{2}(\boldsymbol{T} + \boldsymbol{T}^T) + \frac{1}{2}(\boldsymbol{T} - \boldsymbol{T}^T) = \boldsymbol{T}_{\text{sym}} + \boldsymbol{T}_{\text{skew}}, \tag{1}$$

where $\boldsymbol{T}_{\text{sym}}$ and $\boldsymbol{T}_{\text{skew}}$ are the symmetric and antisymmetric parts of the tensor and the superscript T stands for transpose. Since we will focus on the symmetric part, we drop the subscript and further decompose $\boldsymbol{T} := \boldsymbol{T}_{\text{sym}}$ uniquely into its spherical and deviatoric parts as

$$\boldsymbol{T} = T_{\text{v}}\boldsymbol{I} + \boldsymbol{T}_D \tag{2}$$

with $T_{\text{v}} = (1/3)\text{tr}(\boldsymbol{T})$ and the traceless deviator $\boldsymbol{T}_D = \boldsymbol{T} - T_{\text{v}}\boldsymbol{I}$. The latter contains information about the eigensystem of $\boldsymbol{T}$, that is identical to the eigensystem of $\boldsymbol{T}_D$ itself.

Any (deviatoric) tensor can be transformed using a transformation matrix $\boldsymbol{R}$ to obtain its diagonal form:

$$\boldsymbol{T}_{\text{D}}^{\text{eig}} = \begin{pmatrix} T_{\text{D}}^{(1)} & 0 & 0 \\ 0 & T_{\text{D}}^{(2)} & 0 \\ 0 & 0 & T_{\text{D}}^{(3)} \end{pmatrix} = \boldsymbol{R}^T \cdot \boldsymbol{T}_D \cdot \boldsymbol{R}, \tag{3}$$

$\boldsymbol{T}_D^{(i)} = T_i - T_{\text{v}}/3$, where T_i's are eigenvalues of $\boldsymbol{T}$. Also, $T_{\text{D}}^{(1)}$, $T_{\text{D}}^{(2)}$ and $T_{\text{D}}^{(3)}$ are the eigenvalues sorted such that, as convention, $T_{\text{D}}^{(1)} \geq T_{\text{D}}^{(2)} \geq T_{\text{D}}^{(3)}$. $\boldsymbol{R} = (\hat{\boldsymbol{n}}_1, \hat{\boldsymbol{n}}_2, \hat{\boldsymbol{n}}_3)$ is the orthogonal transformation matrix, composed of the corresponding eigenvectors, which transforms $\boldsymbol{T}_D$ to its eigensystem. According to linear algebra, Eq. (3) can also be expressed as:

$$\boldsymbol{T}_D \cdot \hat{\boldsymbol{n}}_\alpha = T_D^{(\alpha)} \hat{\boldsymbol{n}}_\alpha \tag{4}$$

with $T_D^{(\alpha)}$ and $\hat{\boldsymbol{n}}_\alpha$ the α-eigenvalue and eigenvector of $\boldsymbol{T}_D$, respectively. The symbol "$\cdot$" represents the inner product of the tensor $\boldsymbol{T}_D$ and the vector $\hat{\boldsymbol{n}}_\alpha$ which leads to a vector parallel to $\hat{\boldsymbol{n}}_\alpha$.

In the following, we provide a consistent decomposition for strain, stress and fabric tensors. We choose here to describe each tensor in terms of its isotropic part (first invariant of the tensor) and the second (J_2) and third (J_3) invariant of the deviatoric tensor:

$$J_2 = \frac{1}{2}\left[(T_{\mathrm{D}}^{(1)})^2 + (T_{\mathrm{D}}^{(2)})^2 + (T_{\mathrm{D}}^{(3)})^2\right] \tag{5}$$

$$J_3 = \det(\boldsymbol{T}_D) = T_{\mathrm{D}}^{(1)} T_{\mathrm{D}}^{(2)} T_{\mathrm{D}}^{(3)} \tag{6}$$

J_3 can further be written as $J_3 = T_{\mathrm{D}}^{(1)} T_{\mathrm{D}}^{(2)} (-T_{\mathrm{D}}^{(1)} - T_{\mathrm{D}}^{(2)})$, since we are dealing with deviators.

2.2 Strain

For any deformation, the isotropic part of the infinitesimal strain tensor ε_{v} (in contrast to the true strain ϵ_v) is defined as:

$$\varepsilon_{\mathrm{v}} = \dot{\varepsilon}_v \mathrm{dt} = \frac{\varepsilon_{xx} + \varepsilon_{yy} + \varepsilon_{zz}}{3} = \frac{1}{3}\mathrm{tr}(\mathbf{E}) = \frac{1}{3}\mathrm{tr}(\dot{\mathbf{E}})\mathrm{dt}, \tag{7}$$

where $\varepsilon_{\alpha\alpha}$= $\dot{\varepsilon}_{\alpha\alpha}\mathrm{dt}$ with $\alpha\alpha = xx,\ yy$ and zz as the diagonal elements of the strain tensor $\mathbf{E}$ in the Cartesian $x,\ y,\ z$ reference system. The integral of $3\varepsilon_v$ denoted by $\epsilon_{\mathrm{v}} = 3\int_{V_0}^{V} \varepsilon_{\mathrm{v}}$, is the true or logarithmic strain, i.e. the volume change of the system, relative to the initial reference volume, V_0 [GDL10].

Several definitions are available in literature [TZ06] to define the magnitude of the deviatoric strain. Here, we use the objective definition of the deviatoric strain in terms of its eigenvalues $\varepsilon_d^{(1)}$, $\varepsilon_d^{(2)}$ and $\varepsilon_d^{(3)}$ which is independent of the sign convention.

The deviatoric strain is then:

$$\varepsilon_{dev} = \sqrt{\frac{\left(\varepsilon_d^{(1)} - \varepsilon_d^{(2)}\right)^2 + \left(\varepsilon_d^{(2)} - \varepsilon_d^{(3)}\right)^2 + \left(\varepsilon_d^{(3)} - \varepsilon_d^{(1)}\right)^2}{2}}, \tag{8}$$

where $\varepsilon_{dev} \geq 0$ is the magnitude of the deviatoric strain.

2.3 Stress

From the simulations, one can determine the stress tensor (compressive stress is positive as convention) components:

$$\sigma_{\alpha\beta} = \frac{1}{V} \left(\sum_{p \in V} m^p v_\alpha^p v_\beta^p - \sum_{c \in V} f_\alpha^c l_\beta^c \right), \tag{9}$$

with particle p, mass m^p, velocity v^p, contact c, force f^c and branch vector l^c, while Greek letters represent components x, y, and z [Lud05, IKML13]. The first sum is the kinetic energy density tensor while the second involves the contact-force dyadic product with the branch vector. Averaging, smoothing or coarse graining [WTLB12, WHTL13] in the vicinity of the averaging volume, V, weighted according to the vicinity is not applied in this study, since averages are taken over the total volume.

The isotropic stress is denoted as hydrostatic pressure:

$$p = \sigma_\mathrm{v} = \frac{1}{3} \mathrm{tr}(\boldsymbol{\sigma}) \tag{10}$$

As already mentioned, we will focus on the eigenvalues of the deviatoric stress tensor $\lambda_i^s = \sigma_i^\mathrm{D} = \sigma_i - p$, with the principal directions being the same for $\boldsymbol{\sigma}$ and $\boldsymbol{\sigma}^D$.

The (scalar) deviatoric stress for our $3D$ simulations is:

$$\sigma_\mathrm{dev} = \sqrt{\frac{(\lambda_1^s - \lambda_2^s)^2 + (\lambda_1^s - \lambda_3^s)^2 + (\lambda_2^s - \lambda_3^s)^2}{2}}. \tag{11}$$

The deviatoric stress ratio, $s_\mathrm{dev} = \sigma_\mathrm{dev}/p$, quantifies the "stress anisotropy" - where $\sigma_\mathrm{dev} = \sqrt{3J_2^\sigma}$, with J_2^σ the second invariant of the deviatoric stress tensor and the third stress invariant is $J_3^\sigma = \lambda_1^s \lambda_2^s \lambda_3^s = \lambda_1^s \lambda_2^s (-\lambda_1^s - \lambda_2^s)$.

2.4 Structural (Fabric) Anisotropy

Besides the stress of a static packing of grains, an important microscopic quantity of interest is the fabric/structure tensor. For disordered media, the concept of a fabric tensor naturally occurs when the system consists of an elastic network or a packing of discrete particles. A possible expression for the components of the fabric tensor is provided in [Lud05, MTLL04]:

$$F_{\alpha\beta}^\nu = \langle F^p \rangle = \frac{1}{V} \sum_{p \in V} V^p \sum_{c=1}^{N} n_\alpha^c n_\beta^c , \tag{12}$$

where V^p is the particle volume of particle p which lies inside the averaging volume V, and n^c is the normal vector pointing from the center of particle p to contact c. $F^{\nu}_{\alpha\beta}$ are thus the components of a symmetric rank two 3×3 tensor. In a large volume with some distribution of particle radii, the relationship between the trace of fabric, volume fraction ν and the average coordination number C is given by $3{F_\mathrm{v}}^{\nu} := F^{\nu}_{\alpha\alpha} = g_3 \nu C$, as first reported in [Lud07] and also confirmed from our wider friction (μ) data. The coordination number C gives the average number of contacts per particels , $C = N_c/N_p$, while the term g_3 corrects for the fact that the coordination number for different sized particles is proportional to their surface area such that for a monodisperse packing $g_3 = 1$ and for a polydisperse packing $g_3 > 1$ [GDL10, MTLL04, SMLW12].

A different formulation for the fabric tensor considers simply the orientation of contacts normalized with the total number of contacts N_c, as follows [LRM12, Sat82, Oda72]:

$$F_{\alpha\beta} = \frac{1}{N_c} \sum_{c=1}^{N} n^c_\alpha n^c_\beta \,, \tag{13}$$

The relationship between Eq. (12) and Eq. (13) is:

$$F_{\alpha\beta} \cong \frac{F^{\nu}_{\alpha\beta}}{g_3 \nu C} = \frac{3F^{\nu}_{\alpha\beta}}{F_\mathrm{v}}, \tag{14}$$

with the equality holding in the case of monodisperse systems.

We can define the deviatoric tensor $\boldsymbol{F}^\mathrm{D}$ and calculate the eigenvalues $\lambda^f_i = F_i - F_\mathrm{v}/3$ with $F_\mathrm{v} = 1$, and F_i the eigenvalues of the deviatoric fabric based on Eq. (13).

We assume that the structural anisotropy in the system is quantified (completely) by the anisotropy of fabric, i.e. the deviatoric fabric, with scalar magnitude similar to Eqs. (8) and (11) as:

$$F_\mathrm{dev} = \sqrt{\frac{(\lambda^f_1 - \lambda^f_2)^2 + (\lambda^f_1 - \lambda^f_3)^2 + (\lambda^f_2 - \lambda^f_3)^2}{2}} \,, \tag{15}$$

proportional to the second invariant of $\boldsymbol{F}^\mathrm{D}$, $F_\mathrm{dev} = \sqrt{3J^F_2}$, where λ^f_1, λ^f_2 and λ^f_3 are the three eigenvalues of the deviatoric fabric tensor.

Like for strain and stress, the factor $1/2$ in the definition is somehow arbitrary. Since in soil mechanics, the axial-symmetric case is often the relevant one, the factor $1/2$ turns out to be convenient. In the simple case of axial symmetric deformations, the deviatoric strain, stress and fabric definitions take into account the difference between the eigenvalue of the main compressive (axial) direction and the average values in the isotropic plane as follows in the exemplary case of fabric:

$$F^*_\mathrm{dev} = \lambda^f_1 - \frac{\lambda^f_2 + \lambda^f_3}{2}. \tag{16}$$

In all cases, the elements of the tensor have been normalized by $F_{\mathrm{v}}/3$. Note that if $\lambda_2^f = \lambda_3^f$, Eqs. (15) and (16) coincide. Analogous to equations (15) and (16), F_{dev} and F_{dev}^* can also be defined using the definition of fabric presented in Eq. (12).

3 Sample preparation

The preparation procedure is an essential step in any physical/numerical experiment to obtain reproducible and reliable results, especially when friction is involved. In this chapter, the initial configuration is such that spherical particles are generated (randomly and/or systematically), with low volume fraction and rather large random velocities in a 3D box, such that they have sufficient space and time to exchange places and to randomize themselves. The packing is treated as a piece of a larger sample via periodic boundaries, i.e. if a particle exits the simulation volume at one side, it enters at the opposite side at a corresponding position with the same velocity; particles feel each other across the periodic boundaries.

The initial configurations are obtained by first homogeneously compressing a granular gas up to a volume fraction below the jamming volume fraction, i.e. where the transition from solid-like to liquid-like behavior occurs. The system is then relaxed to allow the particles to dissipate kinetic energy and achieve a zero-pressure static configuration [IKML13, KIML14, GDL10]. One possible criterion for a relaxed static state is the ratio of kinetic to potential energy. When this ratio becomes smaller than a given limit (10^{-7} in this study), the packing is said to be in a static state. This is followed by an isotropic compression-decompression cycle up to a desired maximum volume fraction $\nu_{\max} = 0.82$, as depicted into Fig. 3 [IKML13, GDL10, KSM$^+$17]. Preparation can be carried out with different deformation modes (strain or stress-control). For instance, the system boundaries (periodic walls) can be strain-controlled to follow a cosine-shape (to avoid shocks and inertia), as well as pressure control can be applied to the virtual walls [IWML14]. It was observed that moving the periodic walls causes inhomogeneity in the system. Therefore, this preparation is carried out with uniform strain field deformation, where at every time-step all particles are moved according to the momentary strain-rate tensor. Isotropic compression is defined by the strain-rate tensor

$$\dot{\mathbf{E}} = \dot{\varepsilon}_{\mathrm{v}} \begin{bmatrix} -1 & 0 & 0 \\ 0 & -1 & 0 \\ 0 & 0 & -1 \end{bmatrix}, \tag{17}$$

where $\dot{\varepsilon}_v$ is the strain-rate (compression > 0 and decompression < 0) amplitude applied until the target volume fractions is achieved. $\dot{\varepsilon}_v = 12.6$ [$\mu\mathrm{s}^{-1}$] is used in this part of the work.

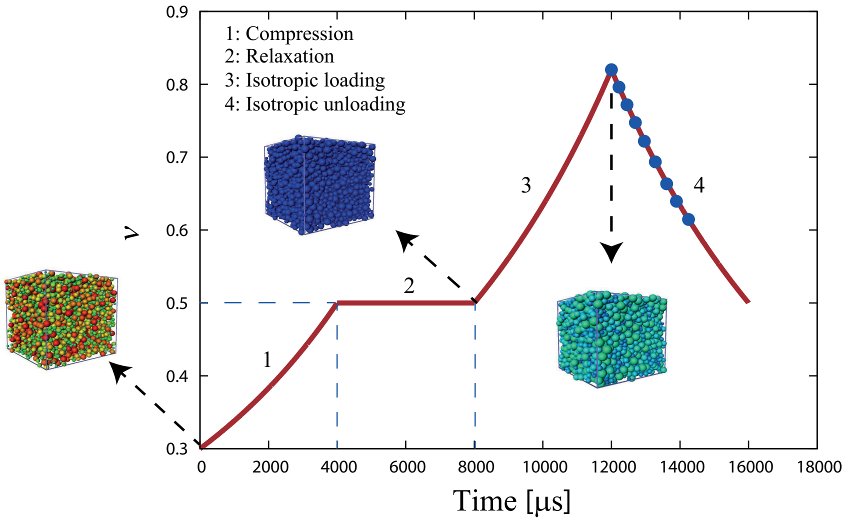

Figure 3: Evolution of volume fraction as a function of time during sample preparation: (1) A frictional granular gas is homogeneously compressed from $\nu = 0.3$ to $\nu = 0.5$; and (2) relaxed at $\nu = 0.5$; (3) the sample is compressed from $\nu = 0.5$ to $\nu = 0.82$; (4) finally, the sample is decompressed from $\nu = 0.82$ to $\nu = 0.5$. Blue bullets '•' represent the chosen configurations for further tests. The color of particles indicates their average overlap. Large (artificial) overlaps are present in the initial random gas (red particles), whereas in the relaxed packing (blue) particles practically do not touch.

A short summary of the values of the parameters used for our DEM simulations is shown in Table 1. Note that the units are artificial and can be consistently rescaled to quantitatively match the values obtained from the experiments. Several preparation protocols can be used to obtain equilibrated numerical samples in given stress/density/fabric states, see e.g. [MGJS04, MLRJ$^+$08, LRW, CR].

4 Elasticity (very small strain stiffness) in geomaterials

Many industrial and geotechnical applications that are crucial for our society involve granular systems at small strain levels. That is the case of structures designed to be far from failure (e.g. shallow foundations or underlying infrastructure), where strains in the soil are small and a sound knowledge of the bulk stiffness is essential for the realistic prediction of ground movements [Cla11].

An elastic response, in granular materials, is measured when small stress and strain increments about a prestressed, equilibrated configuration, are related in a reversible

Parameter	Symbol	Value	S.I. Units
Time Unit	t_u	1	1 μs
Length Unit	l_u	1	1 mm
Mass Unit	m_u	1	1 μg
Number of Particles	N	4096	[–]
Average radius	$\langle r \rangle$	1	1 mm
Polydispersity	$w = r_{\max}/r_{\min}$	3	[–]
Particle density	ρ_p	2000	2000 [kg/m^3]
Normal stiffness	k_n	10^5	10^8 [kg/s^2]
Tangential stiffness	k_t/k_n	0.2	[–]
Rolling friction	μ_r	0	[–]
Restitution coefficient	e	0.804	[–]
Normal Viscosity	γ_n	1000	1 [kg/s]
Friction Viscosity	γ_t/γ_n	0.2	[–]
Rolling Viscosity	γ_r/γ_n	0.2	[–]
Torsion Viscosity	γ_r/γ_n	0.2	[–]
Background viscosity	γ_b	100	0.1 [kg/s]

Table 1: Summary and numerical values of particle parameters used in the DEM simulations.

way, associated with an elastic potential energy. A stiffness degradation curve is normally used to explain the shear stiffness for a wide range of shear strain. Atkinson and Sallfors (1991) categorized the strain levels into three groups, analogue to those introduced in Sec. 1: the very small strain level, where the stiffness modulus is constant; the small strain level, where the stiffness modulus varies non-linearly with the strain; and the large strain level, where the soil is close to failure and the soil stiffness is relatively small. This explanation was illustrated using the normalized stiffness degradation curve by comparing with the ground response from geo-technical construction and the measurement accuracy from laboratory investigation [AS91, Mai93] as shown in Fig. 4.

An elastic response is only observed for very small strain (order of 10^{-6} or 10^{-5}) intervals, and should in fact be viewed as an approximation, as dissipation mechanisms are always present (in particular, particle friction) and preclude the general definition of an elastic energy. The relative amount of dissipation decreases as the size of the probed strain interval approaches zero. For that reason, the material behavior is best characterized as“quasielastic” in that limited range [Cla11, Bur89]. In such limited regime, elastic moduli may then be measured either statically, with adequate devices apt to capture very small strains, or deduced from propagation of sound wave veloci-

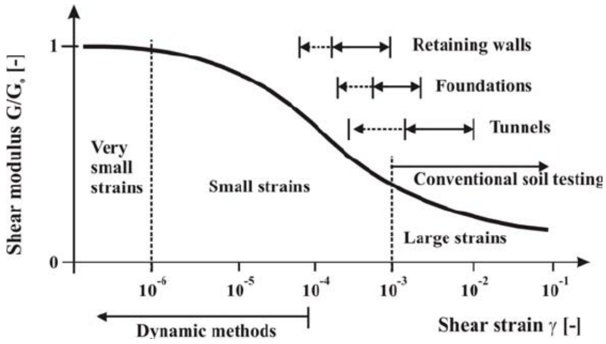

Figure 4: Typical representation of stiffness variation as a function of the shear strain amplitudes; comparison with the ranges for typical geo-technical problems and different tests [AS91, Mai93].

ties.

The aim of this section is to briefly introduce the most common experimental techniques used to measure the very small strain stiffness, and further explain how to study the granular stiffness via DEM simulations. Particular attention is devoted to the dependence of elastic moduli on the stress state, since this is an important controllable experimental parameter, and on fabric that can be inferred via DEM.

4.1 Experimental measurements of small-strain stiffness

Estimation of stiffness has traditionally been made in a triaxial apparatus using precise displacement transducers or resonant column devices. In recent years, several methods become commercially available to determine the stiffness of geomaterials both in the laboratory and in the field [Cla11, Bur89]. The laboratory tests are classified as dynamic or static, as described in Table 2. Dynamic testing occurs at a strain rate high enough to initialize an inertial effect within the specimen, whereas static testing occurs at a much lower repetition rate at which inertial effects are obsolete.

	Type of test	Strain (%)
Static	Triaxial (TX)	> 0.0001
Dynamic	Resonant column (RC)	0.00001 - 0.01
	Bender element (BE)	< 0.001
	Ultrasonic transducer (UT)	< 0.0001

Table 2: List of experiments classified as static or dynamic and their strain regimes.

4.1.1 Dynamic methods

Wave propagation

The use of wave propagation to describe the small strain stiffness of a granular material has been a well documented, widely-used technique, as evidenced in the literature. Velocity testing, which includes BE (Bender Elements) and UT (Ultrasonic Transducers) technology, has been gaining popularity due to its relative ease of implementation. The instrumentation consists of a pair of piezoelectric transducers, function generator, signal amplifier, voltage divider for the input signals and digital oscilloscope. Usually transducers are installed at the top and bottom of a triaxial or oedometric cell. This allows to probe the stiffness of the soil along a given stress path [Saw12]. Fig. 5 shows a schematic drawing of the setup and peripheral electronics [TSML17]. The transmitting transducer sends the input electric signal through the medium and the receiving transducer receives the propagated signal. An image of Bender Element is shown in Fig. 6. See Refs. [LS05, GYH13] for technical details on the transducers.

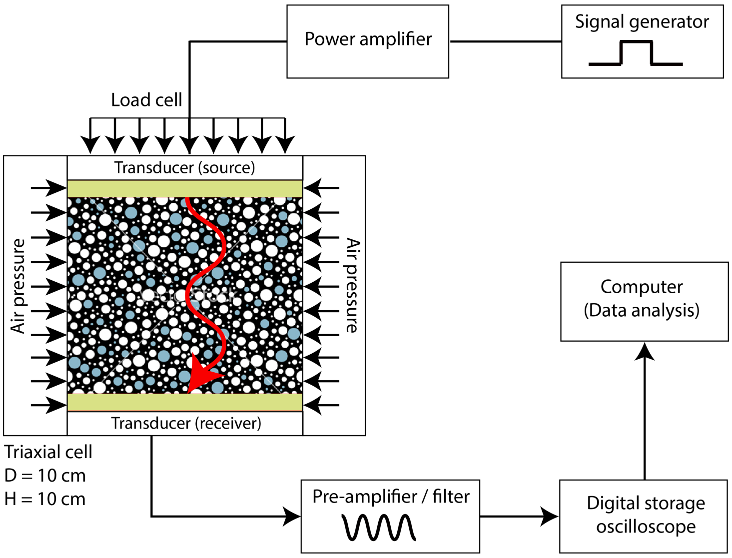

Figure 5: Schematic drawing of an experimental setup of wave propagation testing [TSML17].

Knowing the distance between the two elements, and observing the time required for the shear wave to propagate, a value of the shear wave velocity can be obtained. From this point only the specimen dimensions and soil bulk density are required to produce a stiffness estimate.

The signal-to-noise ratio is improved by repetitive averaging of sufficient number of detected signals using the digital oscilloscope and then sent to a computer for further processing. Concerning the travel time and distance, necessary to calculate the

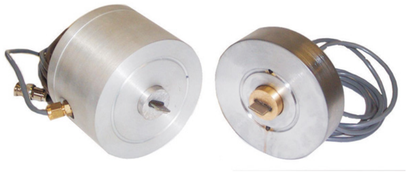

Figure 6: Bender elements used in the experimental tests.

wave velocity, the determination of travel distance (distance between transducers) is generally considered less problematic of the two [VA95, LS05, SL17a, SL17b].

The determination of the travel time, on the other hand, is more controversial. A typical signal gathered from an impulse input signal is presented in Fig. 7, with the amplitude normalized by the maximum amplitude recorded. Suggested criteria and recommendations vary depending on installation, application and input signal. The first arrival method calculates the time difference between the first peak in the transmitted signal (A) and the first deflection observed in the output signal (B). The peak-peak method takes the time between the first (A) peak in the input signal and the first (C) and/or second (D) in the received signal. The most common methodology is to interpret the received signal in the time domain, and to consider peak-peak time or the first arrival methods [LS05, JCV99].

By measuring the travel time (t) and the tip-to-tip distance between transmitting and receiving transducers (L), the wave velocity in the specimen (V) is obtained as:

$$V = \frac{L}{t} \tag{18}$$

The longitudinal velocity V_p and the shear velocity V_s can be measured by using P-wave or S-wave transducers respectively. In the long-wavelength limit, the longitudinal, P-wave modulus M is related to the P-wave velocity V_p in the medium by

$$M = \rho_{bulk} V_p^2, \tag{19}$$

where ρ_{bulk} is the bulk density of the sample, which is, in turn, related to volume fraction ν and particle density ρ_p as:

$$\rho_{bulk} = \nu \rho_p. \tag{20}$$

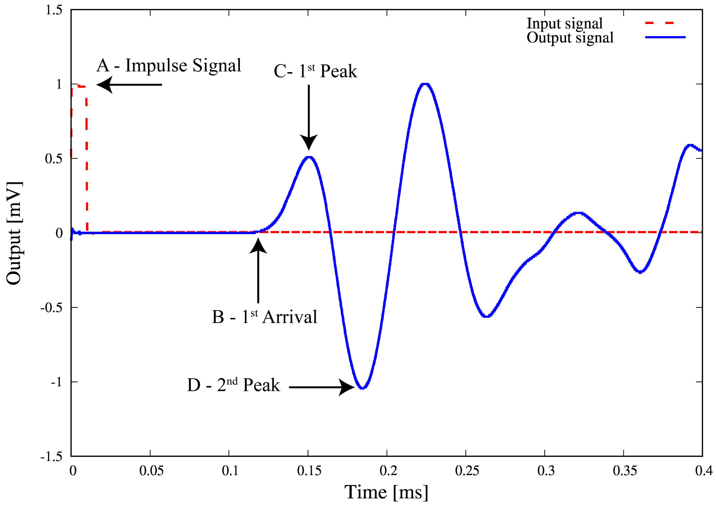

Figure 7: Typical input and output signals from the transmitting and receiving piezoelectric transducers.

Similarly, the small-strain shear modulus $G = G_{max}$ is determined from the measured S-wave velocity V_s as:

$$G \quad = \quad \rho_{bulk} V_s^2 . \tag{21}$$

Resonant column test

A typical fixed-free, torsional device is shown in Fig. 8. A cylindrical soil specimen is confined between two flat ends. The bottom end is often fixed and the top end is capable of exciting the specimen by torsional or longitudinal vibration. The vibration is applied using an electromagnetic drive system with variable frequency. One of the important advantages of RC testing is that measurements can be performed in the small strain range, similarly to the wave propagation tests, just as done in field seismic testing (see Table 2).

The test starts by vibrating the cylindrical soil specimen at the top end. The frequency of vibration is gradually increased until reaching the first-mode fundamental frequency of the sample. At this frequency, measurements are made of the resonance frequency, amplitude of vibration and damping. Knowing the geometry and the end constraints of the sample, the measured resonance frequency is then used to calculate the shear wave propagation velocity. The shear modulus is then obtained directly from the derived velocity and the density of the sample, Eq. (21). By applying the same procedure at different frequency levels, the strain-dependent modulus (degradation curve) can be obtained. In addition to the shear modulus, the RC test offers the possibility to measure the damping ratio that is (usually) not accessible via piezoelectric transducers.

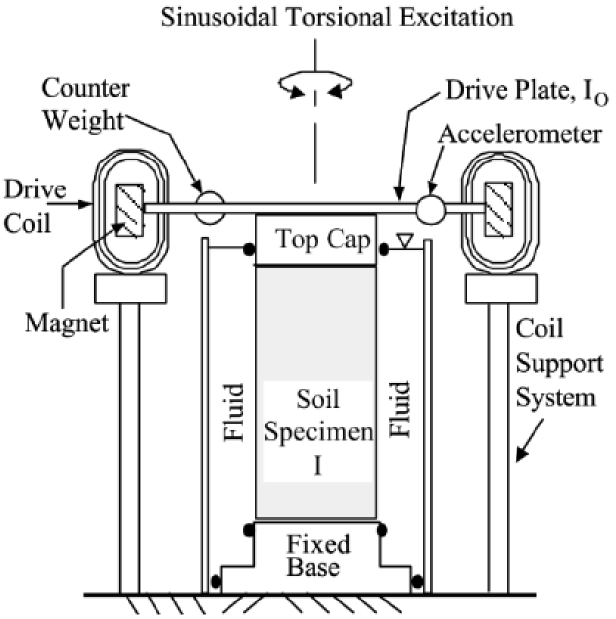

Figure 8: Simplified Diagram of a Fixed-Free, Torsional Resonant Column [SS⁺00]

4.1.2 Static methods

Though the use of wave propagation has become a prevalent technique, so-called static tests are still commonly used to estimate soil stiffness since they allow measurments of the moduli, while determining other paramters such as shear strength or friction angle. In this case, the stiffness is determined by measuring the stress and strain associated with deformations in conventional element tests apparatus. The most typical static measurements are made in triaxial cells [JJSW08, COO07].

The hardship faced with this method of obtaining stiffness parameters of soil is the need to mount on-specimen measurement devices that can monitor the deformations occurring without incurring deformations themselves. Devices include high-resolution miniature LVDT's (Linear Variable Differential Transformers), proximity sensors, and local deformation transducers. Such specimen measurement techniques are vital in order to remain in the small strain measurement region since off-specimen forms of measurements cannot reach nearly as high resolutions of less than 0.05% strain. Depending on the device (triaxial, true-triaxial, hollow cell) and the LVDT's adopted, several material moduli can be measured.

4.2 DEM simulation of small-strain stiffness

In this section, we show how to use DEM simulations to study the elastic behavior of granular materials. Both dynamic and static experiments, as described above, can be reproduced via DEM.

4.2.1 Dynamic method (wave propagation)

For the sake of simplicity, the dynamical wave propagation DEM experiment is illustrated for the case of a monodisperse, structured packing. This section is mainly reporting results from [MML06]. A Face Centered Cubic (FCC) square-layers in the x-y-plane are stacked on top of each other (in z-direction), such that each layer fits into the holes of the one below, and each second layer is just a z-shifted copy of the original. The distance between square layers is $l_0 = d/\sqrt{2}$ for a particle diameter d. Fig. 9 shows the regular packing where square layers in the x-y-plane (4 × 4) are stacked in the z-direction (200 layers). Based on a particle-centred square in the first layer, a unit-cell (cuboid) therefore has a volume $V_u = \sqrt{2}d^3$ and contains 2 particles with volume $2V_p = (\pi/3)d^3$ such that the volume fraction is $\nu = 2V_p/V_u = \pi/(3\sqrt{2}) \approx 0.74$. Each particle has four contacts inside each square-layer, and eight with particles in both neighbouring layers, corresponding to a coordination number $\mathcal{C} = 12$. This structure will not change in the simulations described below, i.e. the case of small amplitude perturbations is considered. Note that the packing is translationally invariant in the x- and y-directions, but different in the z-direction, hence it is an anisotropic system (see Fig. 9).

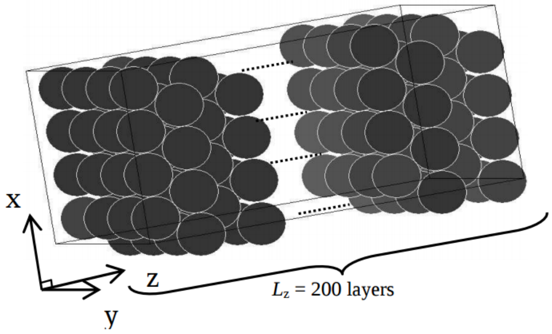

Figure 9: Snapshot of a typical face centred cuboid packing from [LM07].

The typical packing used is long in the z-direction ($200l_0$ with l_0 the distance between layers), which allows to study the wave for a long time and large distances. $l_x = l_y = 4d$ was used in x and y directions. Details of the numerical parameters used are given in [MML06, LM07].

While creating the regular structure, the position of particles is chosen such that the overlap is the same at all contacts in the system, hence allowing for an isotropic stress, $\sigma^0_{xx} = \sigma^0_{yy} = \sigma^0_{zz}$ despite the anisotropic structure. The contact overlaps are chosen much smaller than the particle diameter, $\delta/d \approx 10^{-3}$. Being the packing regular and homogeneous, the system is in a static equilibrium.

Waves are excited by applying a small perturbation at one side of the system, i.e. by shifting a layer of particles. Compressive (P) and shear (S) modes can be triggered by directing the perturbation parallel or perpendicular to the wave propagation direction, respectively. More specifically, a $x-y$-layer is shifted by $\Delta z/d = 10^{-4}$. This displacement amplitude, Δz, that excites the wave is still small as compared to the typical overlap $\Delta z/\delta = 10^{-1}$.

The traveling plane wave can be observed in various quantities like stress, displacement, kinetic energy, etc. Since the system is made of layers, it is possible to "record" the pulse at each layer as a function of time. As an example, Fig. 10 shows the output of a numerical experiment where a plane compressive P-wave is created and propagates in z-direction. The scaled normal stress is plotted versus time at different positions along $z-$direction. The figure resembles the travel of the wave as seen in experiments (Fig. 7). By looking at the behavior of stress over time in a given layer, it is possible to detect the arrival time with the methods described, e.g. first arrival, or peak-to-peak. Since the distance between the source layer and the arrival layer is known, the velocity can then be calculated by Eq. (18). With increasing distance from the excited "source" layer the particles experience an increase in stress (signal arrival) with a time delay and also with smaller amplitude and a slower rate of change [OOtW15].

It is important to note here that, as consequence of the use of periodic boundaries, two opposite ends of the system are connected, and a tensile wave would travel in the direction opposite to the compressive pulse. These waves will interfere after having travelled half of the system. In order to avoid this, and to maximize the distance that can be traveled by a pulse, two layers of particles at the opposite ends of the system are fixed, the other two directions remain periodic. This avoids the tensile pulse, but not boundary reflections that lead to an oscillating signal, traveling after the primary pulse, see Fig. 10.

4.2.2 Static method (infinitesimal strain)

In this section we use Discrete Element simulations to reproduce static experiments for the characterization of the elastic stiffness of granular packings. In order to investigate the elastic response, we perform so-called strain probing tests in several points along the isotropic preparation (pre-strain) path [KLM14] shown in Fig. 3 (red dotted points).

Since isotropic samples are considered, only two independent moduli are needed to characterize the bulk material. The elastic constants B (bulk modulus) and G (shear

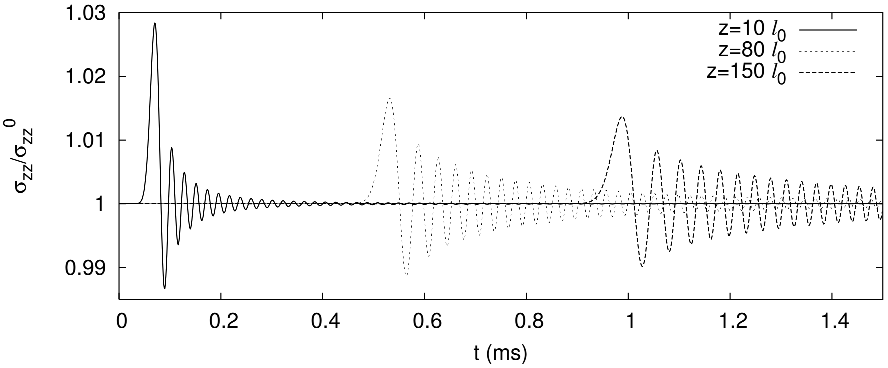

Figure 10: Normal stress (σ_{zz}) scaled by the equilibrium stress (σ^0_{zz}) as function of time at different positions $z/l_0 = 10$, 80, and 150, with the distance from the source, z, and the layer distance l_0 [MML06].

modulus) are chosen here. The other moduli can be obtained from these two via the classical solid mechanics relations.

After applying sufficient relaxation (see Sec. 3 and Ref. [CR]), incremental pure volumetric or pure deviatoric strains are applied to the samples, in order to obtain the bulk and shear moduli, respectively [MLRJ$^+$08, KLM14, CVT03, MGJS04]. Since we apply infinitesimal strain perturbations, we do not expect contact opening or closing to occur. However, the friction coefficient is set infinity ($\mu = \infty$) to prevent any sliding at contacts during probing. For each calculation, we verify that the applied strain is small enough to be in the linear response regime, i.e. the elastic moduli are constant with strain amplitude.

After probing the configurations, the effective scaled, non-dimensional elastic moduli of the granular assembly are obtained as the ratio between the measured increment in stress and the applied strain:

$$B^* = \delta P^* / 3\delta\varepsilon_{vol} \qquad \text{and} \qquad G^*_{xy} = \delta\left(\sigma^*_{xx} - \sigma^*_{yy}\right) / \delta\left(\varepsilon_{xx} - \varepsilon_{yy}\right) \tag{22}$$

where $P^* = Pd/k_n$ and $\boldsymbol{\sigma}^* = \boldsymbol{\sigma} d/k_n$ are the non-dimensional pressure and stress respectively.

We scan a wide range of inter-particle friction coefficients and volume fractions, in order to understand how the interplay of contact/particle properties and system preparation affect the microstructure and thus the elastic moduli. The same procedure is applied for samples created with different values of contact friction, $\mu = 0 - 10$. So that, packings at the same density achieve different pressure and microstructure.

As an example, the variation of the bulk and shear moduli with applied strain amplitude is shown in Fig. 11 for $\mu = 0.001$ for different volume fractions. The elastic moduli stay practically constant for small amplitudes ($3\delta\varepsilon_{vol}$ and $\delta\varepsilon_{dev} < 10^{-4}$ with very slow rate $\approx 10^{-5}$) and this can be considered as the elastic regime. By increasing the amplitudes of the perturbation, B^* and G^* start to increase and decrease non-linearly, respectively, i.e. packings are no longer in the elastic regime. The elastic regime becomes larger for higher volume fraction (see Fig. 11) and higher friction (data not shown here).

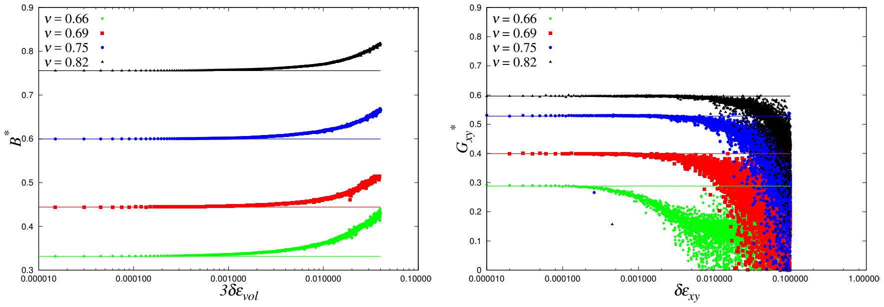

(a) (b)

Figure 11: Evolution of dimensionless (a) bulk modulus B^* and (b) shear modulus G^* with the respective applied isotropic $3\delta\varepsilon_{vol}$ and shear $\delta\varepsilon_{xy}$ strain amplitudes for different states at different volume fractions $\nu = 0.66, 0.69, 0.75$ and 0.82, for samples with friction coefficient of $\mu = 0.001$. Corresponding lines represents the small strain elastic limit values of B^* and G^*.

In Fig. 12, we plot the variation of the bulk B^* and shear G^* modulus, with volume fraction for packings with different coefficients of friction μ. As expected, the elastic moduli always increases with increasing density. However, the increase of the moduli is slower for packings with high friction. We can relate this behavior to a lower average number of contacts (i.e. lower fabric F_v) for samples prepared with strong friction at the same volume fraction. The value of the initial fabric is proportional to the number of contacts, and influences the subsequent evolution of the moduli.

When the elastic moduli are plotted against the isotropic fabric F_v in Fig. 13, the data for the bulk modulus approximately collapse in a unique scaling law, implying a general relation between bulk stiffness and isotropic micro-structure. On the other hand, no scaling is found for the shear modulus G^*_{xy}, even if data follow a similar trend with ν. Further investigations are needed. It is worth mentioning that the coefficient of friction has no direct influence on the elastic moduli but rather it effects B^* and G^* indirectly through the preparation that leads to a different state variable F_v. In fact, friction is set to infinity during the probing to prevent actual sliding of contacts. The tangential component of the force contributes to the overall shear stiffness G^* in a similar way for all samples as k_t is identical for all cases involving $\mu \neq 0$, while the Coulomb threshold, i.e. sliding, is never reached.

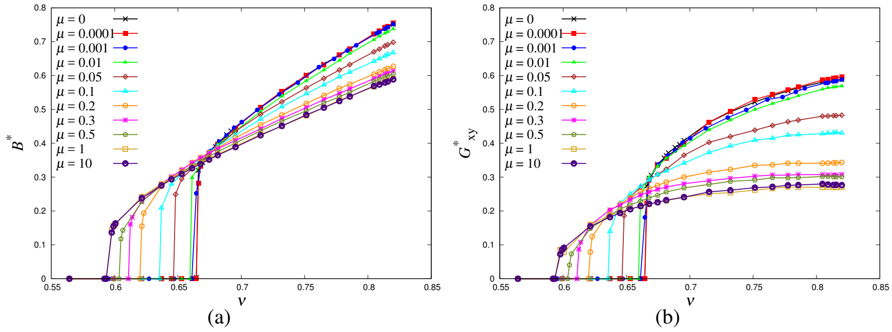

(a) (b)

Figure 12: Evolution of the normalized (a) bulk modulus B^* and (b) shear modulus G^*_{xy} with volume fraction ν for different coefficients of friction, μ, as shown in the legend.

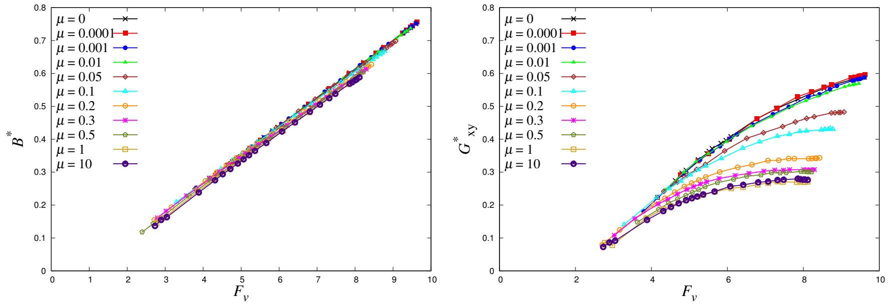

(a) (b)

Figure 13: Evolution of the normalized (a) bulk modulus B^* and (b) shear modulus G^*_{xy} with volume fraction ν for different coefficients of friction, μ, as shown in the legend.

4.2.3 Moduli via the stiffness matrix

For the sake of completeness, we want to mention here a method for the numerical characterization of elasticity in granular materials based on the instantaneous contact network. In simulations, an elastic model is considered for well-equilibrated configurations, in which the contact structure behaves just like a network of linear elastic springs. One may then build the stiffness matrix (also known as the "dynamical matrix") for this network, with stiffness parameters k_n and k_t as detailed in [AR07, ML17, KR01]. The elastic moduli are then obtained by solving an appropriate system of linear equations, for the small (linear and angular) displacements of all the grains associated with global strains and stresses. We refer to [KRP$^+$17a, AR07] and to the companion paper [KRP$^+$17b] for details about the stiffness matrix and its treatment.

5 Element tests for small and intermediate strain

Laboratory testing of soils is a fundamental element of geotechnical engineering. The complexity of testing required for a particular project may range from a simple moisture content determination to specialized strength testing. The purpose of laboratory testing is to reproduce in-situ soil loading under controlled boundary conditions. Soils existing at a depth below the ground surface are affected by the weight of the soil above. The influence of this weight, known generally as the overburden stress, causes a state of stress to exist which is unique at that depth for that soil. When a soil sample is removed from the ground, that state of stress is relieved as all confinement of the sample has been removed. In testing, it is important to reestablish the in-situ stress conditions and to study changes in soil properties when additional stresses representing the expected design loading are applied.

The soil loading test apparatus commonly used to determine strength and stiffness parameters for routine designs are oedometers, triaxial cells and direct shear testers. Each one of them applies stress and strain to the sample in different configurations. The essential features of soil behavior during loading and unloading can be seen in typical stress-strain curves. In the following section 5.1 the most common soil testing devices are shown and explained. In section 5.2 the same element tests are simulated and analyzed via DEM.

5.1 Experimental tests

5.1.1 Oedometer test

The oedometer test is classical in soil mechanics for obtaining parameters for calculation of consolidation settlements and for assessing the stress history of soils. The test specimen is in the form of a disc of soil, held inside a metal ring and lying between two porous stones. The upper porous stone, which can move inside the ring with a small clearance, is fixed below a metal loading cap through which pressure can be applied to the specimen. The whole assembly sits in an open cell of water to which the pore water in the specimen has free access. The confining ring imposes a condition of zero lateral strain on the specimen. The compression of the specimen under pressure is measured by means of a dial gauge or electronic displacement transducer operating on the loading cap [KC12]. The initial pressure applied depends on the type of soil. Following this, a sequence of pressure increments is applied to the specimen. Fig. 14 shows the schematic diagram of an oedometer cell.

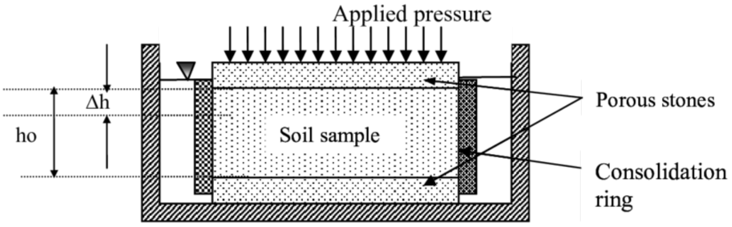

Figure 14: Schematic diagram of an oedometer cell.

5.1.2 Tri-axial test

Triaxial tests provide a reliable means to determine the friction angle of natural clays and silts, as well as reconstituted sands in drained or undrained conditions. The stiffness at intermediate to large strains can also be evaluated. This test is able to reproduce at the lab the initial effective stresses and stress changes, in a very realistic way [Bar97]. The triaxial test set-up is shown in Fig. 15. The sample is enclosed by a thin rubber membrane and placed inside a plastic cylindrical chamber that is usually filled with water or glycerine. The sample is subjected to a total confining pressure by the fluid in the chamber acting on the membrane. A back pressure is applied directly to the specimen through a port in the bottom pedestal. Thus, the sample is initially consolidated with an effective confining stress. To cause shear failure in the sample, axial stress is applied through a vertical loading ram. The axial load applied by the loading ram corresponding to a given axial deformation is measured by a proving ring or electronic load cell, the deflections of which are monitored by either indicators, LVDTs or DCDTs.

5.1.3 Direct shear test

The direct shear (DS) test is performed by placing a specimen into a cylindrical or square-shaped shear box which is split in the horizontal plane [WB13]. A vertical (normal) load is applied over the specimen that is allowed to consolidate. While either the upper or lower part of the box is held stationary, a horizontal load is exerted on the other part of the box in an effort to shear the specimen on a predefined horizontal plane. A diagram of the apparatus and the shearing action is demonstrated in Fig. 16. The DS is the oldest and simplest form of shear test arrangement. It is routinely used to calculate the yield locus (macroscopic friction and cohesion) of soils. It has several inherent shortcomings due to the forced plane of shearing:

- The failure plane is predefined and horizontal; this plane may not be the weakest, which would be more relevant for design.

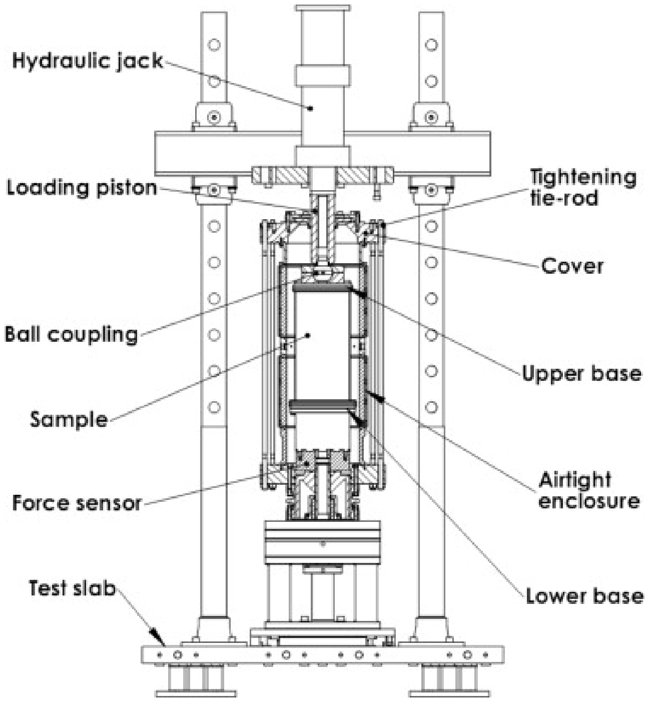

Figure 15: Schematic diagram of a triaxial test apparatus [TTC+12].

- Unlike in the triaxial test, there is little control over the drainage or saturation of the soil.
- The stress conditions across the soil sample are very complex. The distribution of normal stresses and shearing stresses over the sliding surface is not uniform; typically the edges experience more stress than the center. Due to this, there is progressive localized failure of the specimen, i.e. the entire strength of the soil is not mobilized simultaneously [WB13].

Despite of these shortcomings, the direct shear test is commonly used as it is simple and easy to perform in both soil mechanics and powder technology communities. The device uses much less soil than a standard triaxial device, therefore consolidation times are shorter. The DS provides reasonably reliable values for the effective strength parameters. Repeated cycles of shearing along the same direction provide an evaluation of the residual strength parameters.

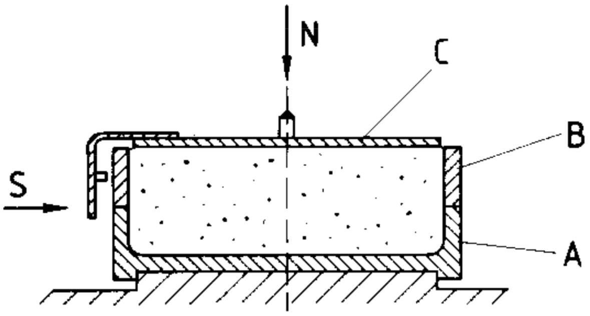

Figure 16: Schematic diagram of direct shear test.

5.2 Numerical tests

Element tests are (ideally homogeneous) macroscopic tests in which one can control the stress and/or strain path. Such macroscopic experiments are important to study the elasto-plastic (pre-failure) behavior of soils, for calibrating and developing constitutive relations, but they provide little information on the microscopic origin of the bulk strength and flow behavior. A complementary approach involves simulating these experiments via the Discrete Element Method (DEM), since it provides information about the micro-structure beyond what is experimentally accessible, see e.g. Refs. [TZ06, IKML13, Tho00, Tho10] among others. In the following, we will show examples of DEM simulations of simple element tests. Note that the numerical parameters as given in Table 1 are used here and samples prepared in Sec. 3 are used as initial configurations.

5.2.1 Uniaxial test (oedometer)

Results in this section are mainly taken by [IKML13]. One element test which can easily be realized (experimentally as well as numerically) is uniaxial compression (in a cylindrical or box geometry) involving an axial deformation of a bulk sample while the lateral boundaries of the system are fixed. Uniaxial compression is achieved by moving the particles in the z-direction according to a prescribed strain rate, with a diagonal strain-rate tensor

$$\dot{\mathbf{E}} = \dot{\varepsilon}_u \begin{pmatrix} 0 & 0 & 0 \\ 0 & 0 & 0 \\ 0 & 0 & -1 \end{pmatrix},$$

where $\dot{\varepsilon}_u$ is the strain-rate (compression > 0 and decompression/tension < 0) amplitude applied in the uniaxial mode. The negative sign (convention) of $\dot{E}_{zz}$ corresponds to a reduction of length, so that tensile deformation is positive. During loading (compression) the volume fraction increases from ν_0 to a maximum $\nu_{\max} = 0.820$. Even though the strain is imposed only on one mobile periodic wall with normal in the z-direction, which leads to an increase of compressive stress during compression, also the non-mobile x and y walls experience some stress increase as expected for "solid" materials with non-zero Poisson ratio. We next will discuss the influence of friction on the evolution of stress and structural anisotropy as functions of deviatoric strain during uniaxial loading. Under uniaxial compression, not only does stress builds up, but also the anisotropy of the contact and force networks develops, as it relates to the creation and destruction of new contacts [IKML13].

The deviatoric stress ratio, $s_{dev} = \sigma_{dev}/P = \sigma^*_{dev}/P^*$ is shown in Figs. 17(a) for a frictionless ($\mu = 0$) and several frictional (μ = 0.01, 0.02, 0.05, 0.1, 0.2, 0.3, 0.5 and 1.0) systems during uniaxial loading. As the deviatoric strain applied to the system is increased during uniaxial loading, the deviatoric stress ratio initially grows for all the friction coefficients shown. In some cases (for small μ), the maximal s_{dev} is reached before the maximum deviatoric strain applied ($\varepsilon_{\mathrm{dev}}^{\max}$ =0.1549) is reached. For some of the configurations studied, a *steady state* is observed in which further application of deviatoric strain does not lead to visible further increase/decrease in the deviatoric stress. At the maximum applied deviatoric strain, we observe that not all configurations (especially the highest friction coefficients) have reached steady state. For the systems with lower microscopic friction coefficients, a slight decrease of the deviatoric stress ratio for larger deviatoric strains is seen. The slope of the deviatoric stress ratio, which represents its growth rate shows a decreasing trend with increasing friction. We recall here that the initial packings are different since they are prepared with different friction coefficients at the same volume (packing fraction). Due to this, the pressure increases with increasing friction while the coordination number decreases with friction. The slope of the deviatoric stress ratio in Fig. 17(a), related to the initial scaled shear stiffness of the isotropic packing is at the same time dependent on these two quantities [MLRJ$^+$08, Wal87].

Along with the deviatoric stress ratio, for a characterization of the contact network of the particles, we plot the deviatoric fabric magnitudes F_{dev} of the systems discussed above as function of the deviatoric strain during uniaxial loading in Fig. 17(b). The deviatoric fabric magnitude builds up from different (random, but small) initial values and reaches different maxima within the same range of deviatoric strains ($\varepsilon_{\mathrm{dev}} \approx 4-6\%$). For larger strains, we observe a decrease in the structural anisotropy.

Interestingly, for systems with higher friction coefficients (μ = 0.3, 0.5 and 1.0), after the decrease in the structural anisotropy, further loading in the axial direction leads to a (small) second increase of the deviatoric fabric until, at maximum compression, the deviatoric fabric again reaches a local maximum. This indicates that more contacts are created in the axial compressive direction compared to the horizontal plane at the beginning of the loading cycle. At the first maximum ($\varepsilon_{\mathrm{dev}} \approx 0.06$), the material behavior changes such that the number of contacts created in the horizontal plane becomes higher with respect to the vertical plane. This trend reverses again as maximum compression is reached for systems with higher friction coefficients.

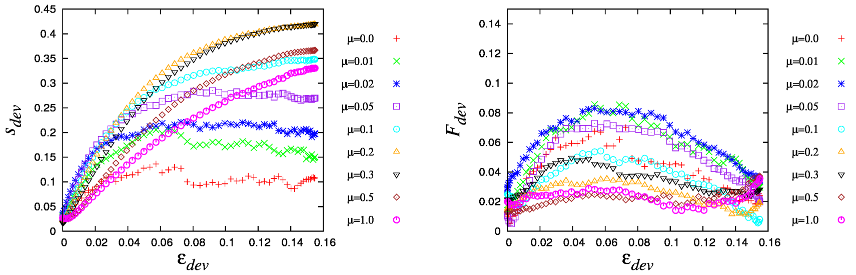

(a) (b)

Figure 17: (a) Deviatoric stress ratio plotted as function of deviatoric strain during uniaxial loading, (b) corresponding plots of the deviatoric fabric, for different microscopic friction coefficients [IWML14].

5.2.2 Triaxial test

Starting from frictionless and frictional samples ($\mu = 0, 0.1$ and 0.5) prepared in Sec. 3, configurations with identical pressure level $P^* = 0.004$ are taken and relaxed to dissipate their kinetic energy. Note that due to friction, the initial volume fractions of these configurations are different (decreasing with μ), even though the pressure is identical.

After relaxation, triaxial loading is initiated. This is achieved by moving the periodic wall in the axial z-direction according to a half-cosinusoidal strain path while maintaining constant pressure on the other two periodic walls. In addition to the three friction coefficients considered, the sample prepared with $\mu = 0$ is also compressed under triaxial load by using different finite friction coefficients, i.e. $\mu = 0.1$ or 0.5. This creates loose ($\mu \neq 0$ during preparation) and dense ($\mu = 0$ during preparation) initial samples (see also Ref. [CR]), where all the samples have same pressure $P^* = 0.004$.

We perform monotonic triaxial tests until the failure point is reached. This is identified as the maximum axial stress reached before stress reduction (or softening) begins. The evolution of volume fraction during the triaxial test for all cases is shown in Fig. 18(a). The symbols represent data where friction is *inactive* during the preparation stage (dense states) while the solid lines represent data where friction is *active* (loose states). Several observations can be made from the figure. First, the volume fraction appears to remain fairly constant at $\nu = 0.67$ for the frictionless ($\mu = 0$) data. Second, for initially dense samples (dotted lines), the volume fraction decreases during monotonic loading (dilatancy), whereas for initially loose samples, it increases (contractancy).

In Fig. 18(b), we plot the evolution of the scaled deviatoric stress σ_{dev} as function of the axial strain ε_1 for different preparation procedures. To further probe into the various configurations and obtain information about their microstructure, in Fig. 18(c), we also plot the corresponding evolution of the deviatoric fabric as function of the deviatoric strain. The first plot (Fig.18(a)) shows that DEM is nicely able to qualitatively capture the shear behavior of soils. The first samples first reach a peak and then soften toward a critical state, where the material can be further sheared at constant deviatoric stress and volume (Fig.18(a)) and (b)) while loose samples monotonically reach the critical state. For both loose and dense samples, higher interparticle friction means higher strength. When looking at the fabric (Fig. 18(c)), we observe a similar behavior as shear stress. However, peak and critical state are delayed (in strain) with respect to stress. This behavior suggests that contact forces adapt to shear strain faster than the contact network. See also Ref. [Tho00] for DEM simulations of triaxial tests of soils.

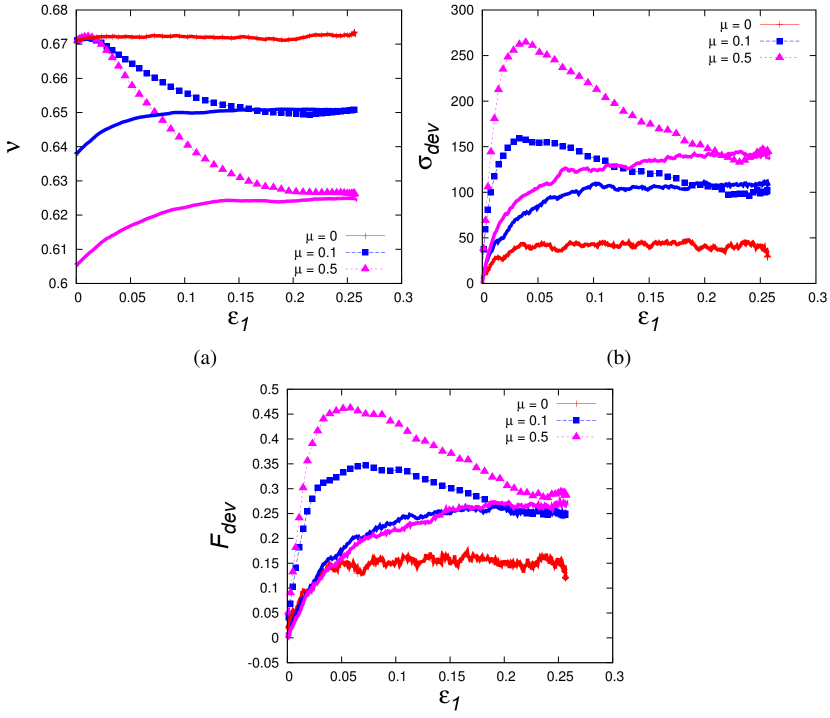

(a)

(b)

(c)

Figure 18: Evolution of (a) volume fraction (b) deviatoric stress and (c) deviatoric fabric with axial strain for different inter-particle friction. Symbols represent data where friction is off during preparation while the solid lines are for tests where friction is on during sample preparation.

5.2.3 Shear cell

After choosing the initial configurations from the loading branch of the preparation path (see Fig. 3 in Sec. 3), we perform pure shear and simple shear tests on each initial configuration. These two element tests are somehow different with respect to the shear cell test in Sec. 5.1.3. In fact, they are homogeneous tests in a periodic 3D box, and can be interpreted as material points in the middle of the direct shear cell experiment (where the shear band develops) [SPO⁺17].

Pure shear (volume conserving): We perform volume conserving pure shear by applying the following strain-rate tensor to our periodic sample:

$$\dot{\mathbf{E}} = \dot{\varepsilon}_D \begin{pmatrix} 1 & 0 & 0 \\ 0 & -1 & 0 \\ 0 & 0 & 0 \end{pmatrix},$$

where $\dot{\varepsilon}_D$ is the strain-rate (compression > 0) amplitude applied to the wall.

Simple shear: Simple shear is another test which can be performed using DEM. In this case the samples are in cuboid volume with periodic boundaries in x-z-directions and Lees-Edwards [LE72] periodic boundaries in y-direction, see Fig. 19(b). The particles are sheared along the x-direction and the stress is kept constant along the y-direction, σ_{yy} = constant.

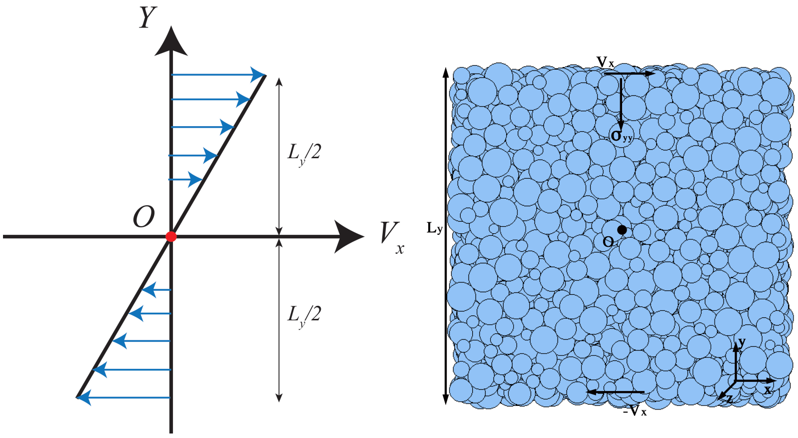

Figure 19: Simulation of a 3D system of polydisperse particles under y-normal stress controlled simple shear with Lees-Edwards periodic boundaries.

The shear movement of particles is achieved by moving the particles in the x-direction according to a prescribed constant shear strain-rate tensor:

$$\dot{\mathbf{E}} = \dot{\gamma} \begin{pmatrix} 0 & 1 & 0 \\ 1 & 0 & 0 \\ 0 & 0 & 0 \end{pmatrix},$$

where, the shear rate is $\dot{\gamma} = \partial V_x / 2\partial y$, and V_x is the shear velocity in the x-direction, kept constant. The vertical stress is adapted by the motion of all particles in order to increase or decrease the stress towards its desired value. The periodic boundaries are also adjusted at each time step.

We start by choosing two configurations, frictionless and frictional ($\mu = 0.5$), at the same confining pressure. It is clear that samples with different friction coefficients at the same confining pressure show different volume fraction. Volume fractions of frictionless and frictional samples are $\nu = 0.7$ and 0.65 respectively. We then apply simple shear deformation with a constant axial stress along the y-axis ($\sigma^*_{yy} = 0.02$). We continue shearing the samples until they reach the steady state. Volume fractions of the two samples are now $\nu = 0.7$ and $\nu = 0.63$ for the frictionless and frictional samples respectively. At this point, we pick up two new configurations from the frictionless and frictional preparation paths that have those volume fraction values. Finally, these two new samples are sheared under pure shear (constant volume) until they reach their steady state.

Now, we want to compare the behavior of the material under pure shear and simple shear deformation. The samples sheared before they have same volume fractions in the critical state. In Fig. 20, we plot the evolution of volume fraction ν, deviatoric stress σ^*_{dev} and fabric F_{dev} versus shear strain. As prescribed, both frictionless and frictional samples show the same volume fraction at steady state (Fig. 20(a)). However, by looking at Fig. 20(b) and 20(c), we can see differences between the frictionless and frictional cases. The deviatoric stress and fabric evolve differently between the two shear modes, as the rise is faster in the simple shear case than in the pure shear case. But, this pronounced difference is not observed in the frictionless samples where the behavior under two modes nicely coincides. This element test comparison reveals the importance of choosing the right input parameters for DEM and and the right preparation procedure/conditions [CR]. An interesting comparison between real experiments and simulations in a direct shear cell is reported in Ref. [TZ06].

5.2.4 Large strain and onset of flow

Finally in this section, we use data from simple shear numerical tests in the previous section to briefly introduce failure and flow. The shearing strength of a soil sample is generally defined as its maximum resistance to shearing forces. Plotting the peak and residual shear stress values versus applied normal stress (extracted from Fig. 20) for frictionless and frictional samples analyzed in section 5.2.3 under simple shear, results

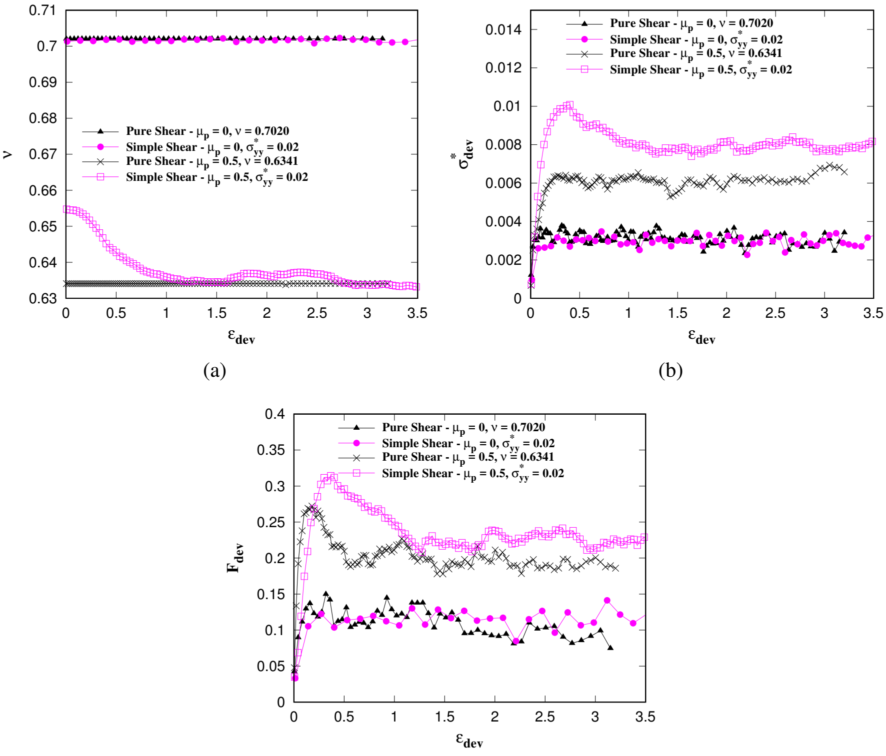

(a) (b)

(c)

Figure 20: (a) Volume fraction ν, (b) dimensionless shear stress $\sigma^*_{dev} = \sigma_{dev} d/k_1$ and (c) deviatoric fabric F_{dev}, plotted against deviatoric strain ε_{dev}. Two different values of shear control conditions are given in the legend. Different colors represent frictionless and frictional shearing as given in the inset.

in the four lines in Fig. 21. These lines define the Mohr-Coulomb yield (failure) loci for our granular material, as they give the maximum shear stress σ^*_{dev} that the material can sustain for each applied pressure P^*. For the sake of simplicity, these loci are often approximated with linear functions:

$$\sigma^*_{dev} = P^* \tan\phi + c \tag{23}$$

where c is the cohesive strength ($c \cong 0$ for cohesionless soils) and ϕ is the angle of internal friction. In the case of the residual strength, the cohesion c drops to zero and the angle of residual strength ϕ_r fully characterizes the material in this phase [ASC17]. When the yield surface is reached, the granular material fails and starts to flow. The flow behavior after failure belongs to the domain of granular rheology, see Ref. [LRW] for more details.

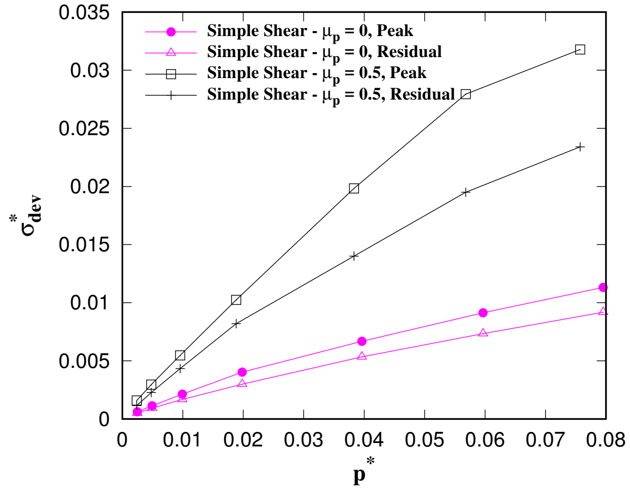

Figure 21: Peak and residual shear strength at different normal stresses obtained for frictionless and frictional (cohesionless $c = 0$) samples by a simple shear test.

6 Summary and conclusion

In this chapter, we have described how to use particle simulations [LRW, Rad] to reproduce laboratory tests, typically used in soil mechanics to infer stiffness and strength characteristics of soils, see also Refs. [CR, DS]. We have looked at different strain regimes, from elasticity at very small strains, via small and intermediate strains where non-linearity is predominant, up to shear failure at large strain.

Each section started by a brief review of different testing devices in geo-mechanics labs for soil characterization in a specific regime. Then, individual element tests were simulated using DEM and results were described and interpreted. Dynamic and static methods for the determination of the elastic moduli of a granular material were used in the very small strain regime, while oedometric (uni-axial) compression/tension, triaxial and direct shear tests were applied in the case of intermediate and large strains.

Results show that DEM is a powerful tool to investigate laboratory-scale models, able to complement the macroscopic informations available by physical testing with microscale insights, paving the way to new micro-mechanical based constitutive models for field scale applications in soil mechanics.

7 Acknowledgment

Helpful discussions with B. Soltanbeigi, R. K. Srivastava, H. Shi and O. I. Imole are gratefully acknowledged. The financial support of the European-Union Marie Curie Initial Training Network, T-MAPPP, funded by FP7 (ITN 607453), is appreciated, see http://www.t-mappp.eu/ for more information.

References

[AR07] I. Agnolin and J.-N. Roux. Internal states of model isotropic granular packings. iii. elastic properties. *Physical Review E*, 76(6):061304, 2007.

[AS91] J.H. Atkinson and G. Sallfors. Experimental determination of soil properties (stress-stiain-time). In *Proc. 10th Eur. Conf: Soil Mech., Florence 3. 915*, volume 958, 1991.

[ASC17] A. Altunbas, B. Soltanbeigi, and O. Cinicioglu. Determination of active failure surface geometry for cohesionless backfills. *Geomechanics and Engineering*, 12(6):965–981, 2017.

[Atk00] J.H. Atkinson. Non-linear soil stiffness in routine design. *Géotechnique*, 50(5):487–508, 2000.

[Bar94] J.-P. Bardet. Numerical simulations of the incremental responses of idealized granular materials. *International Journal of Plasticity*, 10(8):879–908, 1994.

[Bar97] J.-P. Bardet. *Experimental soil mechanics*. Prentice Hall, NJ, 1997.

[Bur89] J.B. Burland. Ninth laurits bjerrum memorial lecture:" small is beautiful"—the stiffness of soils at small strains. *Canadian geotechnical journal*, 26(4):499–516, 1989.

[Cla11] C.R.I. Clayton. Stiffness at small strain: research and practice. *Géotechnique*, 61(1):5–37, 2011.

[COO07] L. Cui, C. O'Sullivan, and S. O'Seill. An analysis of the triaxial apparatus using a mixed boundary three-dimensional discrete element model. *Geotechnique*, 57(10):831–844, 2007.

[CR] G. Combe and J.-N. Roux. Good practice and sample preparation - construction of granular packings. *ALERT geomaterials Doctoral School 2017, Aussois, France*.

[CS79] P.A. Cundall and Otto D.L. Strack. A discrete numerical model for granular assemblies. *Geotechnique*, 29(1):47–65, 1979.

[CVT03] F. Calvetti, G. Viggiani, and C. Tamagnini. A numerical investigation of the incremental behavior of granular soils. *Rivista italiana di geotecnica*, 37(3):11–29, 2003.

[DAM+] J.-Y. Delenne, L. Amarsid, P. Mutabaruka, V. Richefeu, and F. Radjai. Fluid-grain coupling using the Lattice Boltzmann method. *ALERT geomaterials Doctoral School 2017, Aussois, France*.

[DS] F.-V. Donzé and L. Scholtés. Predicting the strength of anisotropic shale rock: empirical nonlinear failure criterion vs. Discrete Element Method. *ALERT geomaterials Doctoral School 2017, Aussois, France*.

[GDL10] F. Göncü, O. Durán, and S. Luding. Constitutive relations for the isotropic deformation of frictionless packings of polydisperse spheres. *Comptes Rendus Mécanique*, 338(10-11):570–586, 2010.

[GL13] F. Göncü and S. Luding. Effect of particle friction and polydispersity on the macroscopic stress–strain relations of granular materials. *Acta geotechnica*, 8(6):629–643, 2013.

[God90] J.D. Goddard. Nonlinear elasticity and pressure-dependent wave speeds in granular media. *Proceedings of the Royal Society of London A: Mathematical, Physical and Engineering Sciences*, 430(1878):105–131, 1990.

[GYH13] X. Gu, J. Yang, and M. Huang. Laboratory measurements of small strain properties of dry sands by bender element. *Soils and Foundations*, 53(5):735–745, 2013.

[IKML13] O.I. Imole, N. Kumar, V. Magnanimo, and S. Luding. Hydrostatic and shear behavior of frictionless granular assemblies under different deformation conditions. *KONA Powder and Particle Journal*, 30:84–108, 2013.

[IWML14] O.I. Imole, M. Wojtkowski, V. Magnanimo, and S. Luding. Micro-macro correlations and anisotropy in granular assemblies under uniaxial loading and unloading. *Physical Review E*, 89(4):042210, 2014.

[JCV99] X. Jia, C. Caroli, and B. Velicky. Ultrasound propagation in externally stressed granular media. *Physical Review Letters*, 82(9):1863, 1999.

[JJSW08] F. Jafarzadeh, H. Javaheri, T. Sadek, and D.M. Wood. Simulation of anisotropic deviatoric response of hostun sand in true triaxial tests. *Computers and Geotechnics*, 35(5):703–718, 2008.

[JS06] S. Ji and H.H. Shen. Effect of contact force models on granular flow dynamics. *Journal of engineering mechanics*, 132(11):1252–1259, 2006.

[KC12] J.A. Knappett and R.F. Craig. *Craig's soil mechanics*. 2012.

[KIML14] N. Kumar, O.I. Imole, V. Magnanimo, and S. Luding. Effects of polydispersity on the micro–macro behavior of granular assemblies under different deformation paths. *Particuology*, 12:64–79, 2014.

[KLM14] N. Kumar, S. Luding, and V. Magnanimo. Macroscopic model with anisotropy based on micro–macro information. *Acta Mechanica*, 225(8):2319–2343, 2014.

[KR01] N.P. Kruyt and L. Rothenburg. Statistics of the elastic behaviour of granular materials. *International Journal of Solids and Structures*, 38(28):4879–4899, 2001.

[KRP$^+$17a] M.H. Khalili, J.-N. Roux, J.M. Pereira, S. Brisard, and M. Bornert. Numerical study of one-dimensional compression of granular materials. i. stress-strain behavior, microstructure, and irreversibility. *Physical Review E*, 95(3):032907, 2017.

[KRP$^+$17b] M.H. Khalili, J.-N. Roux, J.M. Pereira, S. Brisard, and M. Bornert. Numerical study of one-dimensional compression of granular materials. ii. elastic moduli, stresses, and microstructure. *Physical Review E*, 95(3):032908, 2017.

[KSM$^+$17] R. Kievitsbosch, H. Smit, V. Magnanimo, S. Luding, and K. Taghizadeh. Influence of dry cohesion on the micro- and macro-mechanical properties of dense polydisperse powders & grains. *EPJ Web Conf.*, 140:08016, 2017.

[LE72] A.W. Lees and S.F. Edwards. The computer study of transport processes under extreme conditions. *Journal of Physics C: Solid State Physics*, 5(15):1921, 1972.

[LM07] S. Luding and O. Mouraille. Mechanic waves in sand: effect of polydispersity. *Partec*, 2007.

[LRM12] L. La Ragione and V. Magnanimo. Contact anisotropy and coordination number for a granular assembly: A comparison of distinct-element-method simulations and theory. *Physical Review E*, 85(3):031304, 2012.

[LRW] S. Luding, N. Rivas, and T. Weinhart. From soft and hard particle simulations to continuum theory for granular flows. *ALERT geomaterials Doctoral School 2017, Aussois, France.*

[LS05] J.-S. Lee and J.C. Santamarina. Bender elements: performance and signal interpretation. *Journal of geotechnical and geoenvironmental engineering*, 131(9):1063–1070, 2005.

[LSL14] C. Lee, H. Shin, and J.-S. Lee. Behavior of sand–rubber particle mixtures: experimental observations and numerical simulations. *International Journal for Numerical and Analytical Methods in Geomechanics*, 38(16):1651–1663, 2014.

[Lud98] S. Luding. Collisions & contacts between two particles. *Physics of dry granular media*, pages 285–304, 1998.

[Lud05] S. Luding. Anisotropy in cohesive, frictional granular media. *Journal of Physics: Condensed Matter*, 17(24):S2623, 2005.

[Lud07] S. Luding. The effect of friction on wide shear bands. *Particulate Science and Technology*, 26(1):33–42, 2007.

[Lud08] S. Luding. Introduction to discrete element methods: basic of contact force models and how to perform the micro-macro transition to continuum theory. *European Journal of Environmental and Civil Engineering*, 12(7-8):785–826, 2008.

[Mai93] R.J. Mair. Developments in geotechnical engineering research: Application to tunnels and deep excavations. In *Proceedings of the Institution of Civil Engineers-Civil Engineering*, volume 97, pages 27–41. Thomas Telford-ICE Virtual Library, 1993.

[Mar] C.L. Martin. Advanced contact laws. *ALERT geomaterials Doctoral School 2017, Aussois, France*.

[MGJS04] H.A. Makse, N. Gland, D.L. Johnson, and L. Schwartz. Granular packings: Nonlinear elasticity, sound propagation, and collective relaxation dynamics. *Physical Review E*, 70(6):061302, 2004.

[ML17] A. Merkel and S. Luding. Enhanced micropolar model for wave propagation in ordered granular materials. *International journal of solids and structures*, 106:91–105, 2017.

[MLRJ$^+$08] V. Magnanimo, L. La Ragione, J.T. Jenkins, P. Wang, and H.A. Makse. Characterizing the shear and bulk moduli of an idealized granular material. *EPL (Europhysics Letters)*, 81(3):34006, 2008.

[MML06] O. Mouraille, W.A. Mulder, and S. Luding. Sound wave acceleration in granular materials. *Journal of Statistical Mechanics: Theory and Experiment*, 2006(07):P07023, 2006.

[MTLL04] M. Madadi, O. Tsoungui, M. Lätzel, and S. Luding. On the fabric tensor of polydisperse granular materials in 2D. *International Journal of Solids and Structures*, 41(9):2563–2580, 2004.

[Oda72] M. Oda. Initial fabrics and their relations to mechanical properties of granular material. *Soils and foundations*, 12(1):17–36, 1972.

[OOtW15] J. O'Donovan, C. O'Sullivan, G. the, and D.M. Wood. Anisotropic stress and shear wave velocity: (DEM) studies of a crystalline granular material. *Granular Matter*, (17):197–216, 2015.

[Rad] F. Radjai. The contact dynamics (CD) method. *ALERT geomaterials Doctoral School 2017, Aussois, France*.

[Sat82] M. Satake. Fabric tensor in granular materials. In *Proc., IUTAM Symp. on Deformation and Failure of Granular materials, Delft, The Netherlands*, 1982.

[Saw12] A. Sawangsuriya. *Wave Propagation Methods for Determining Stiffness of Geomaterials*. INTECH Open Access Publisher, 2012.

[SL17a] R.K. Shrivastava and S. Luding. Effect of disorder on bulk soundwave speed : A multiscale spectral analysis. *Nonlinear Processes in Geophysics Discussions*, 2017:1–37, 2017.

[SL17b] R.K. Shrivastava and S. Luding. Wave propagation of spectral energy content in a granular chain. *EPJ Web Conf.*, 140:02023, 2017.

[SMLW12] M.R. Shaebani, M. Madadi, S. Luding, and D.E. Wolf. Influence of polydispersity on micromechanics of granular materials. *Physical Review E*, 85(1):011301, 2012.

[SNDD09] L. Sibille, F. Nicot, F.-V. Donzé, and F. Darve. Analysis of failure occurrence from direct simulations. *European Journal of Environmental and Civil Engineering*, 13(2):187–201, 2009.

[SPO$^+$17] B. Soltanbeigi, A. Podlozhnyuk, J.Y. Ooi, C. Kloss, and S.-A. Papanicolopulos. Comparison of multi-sphere and superquadric particle represent ion for modelling shearing and flow characteristics of granular assemblies. *EPJ Web Conf.*, 140:06015, 2017.

[SS$^+$00] K.H. Stokoe, J.C. Santamarina, et al. Seismic-wave-based testing in geotechnical engineering. In *ISRM International Symposium*. International Society for Rock Mechanics, 2000.

[Tho00] C. Thornton. Numerical simulations of deviatoric shear deformation of granular media. *Géotechnique*, 50(1):43–53, 2000.

[Tho10] C. Thornton. Quasi-static simulations of compact polydisperse particle systems. *Particuology*, 8(2):119–126, 2010.

[TSML17] K. Taghizadeh, H. Steeb, V. Magnanimo, and S. Luding. Elastic waves in particulate glass-rubber mixture: experimental and numerical investigations/studies. *EPJ Web Conf.*, 140:12019, 2017.

[TTC$^+$12] V.N. Trinh, A.M. Tang, Y.-J. Cui, J.-C. Dupla, J. Canou, N. Calon, Lucie Lambert, A. R., and O. Schoen. Mechanical characterisation of the fouled ballast in ancient railway track substructure by large-scale triaxial tests. *Soils and foundations*, 52(3):511–523, 2012.

[TWT] D. Tunuguntla, T. Weinhart, and A. Thornton. Discrete particle simulations with MercuryDPM. *ALERT geomaterials Doctoral School 2017, Aussois, France*.

[TZ06] C. Thornton and L. Zhang. A numerical examination of shear banding and simple shear non-coaxial flow rules. *Philosophical Magazine*, 86(21-22):3425–3452, 2006.

[VA95] G. Viggiani and J.H. Atkinson. Interpretation of bender element tests. 8(32):373A, 1995.

[Wal87] K. Walton. The effective elastic moduli of a random packing of spheres. *Journal of the Mechanics and Physics of Solids*, 35(2):213–226, 1987.

[WB13] D.M. Wood and M. Budhu. The behaviour of Leighton Buzzard sand in cyclic simple shear tests. 2013.

[WHTL13] T. Weinhart, R. Hartkamp, A.R. Thornton, and S. Luding. Coarse-grained local and objective continuum description of three-dimensional granular flows down an inclined surface. *Physics of Fluids*, 25(7):070605, 2013.

[WTLB12] T. Weinhart, A.R. Thornton, S. Luding, and O. Bokhove. From discrete particles to continuum fields near a boundary. *Granular Matter*, 14(2):289–294, 2012.

Predicting the strength of anisotropic shale rock: Empirical nonlinear failure criterion vs. Discrete Element Method model

F.-V. Donzé[1] and L. Scholtès[2]

[1] *Université Grenoble Alpes, Laboratoire 3SR*
[2] *Université de Lorraine, CNRS, CREGU, Laboratoire GeoRessources*

Conventional triaxial tests performed on samples of Tournemire shale showed a strong nonlinearity of the plastic yield response. For this type of rock, the use of a conventional linear Mohr–Coulomb criterion to predict the evolution of the strength is of limited value and should be replaced by nonlinear failure criteria such as the one proposed by Singh, which is based on the critical stress introduced by Barton. Moreover, the experimental tests showed a strong dependency of the strength on the bedding orientation. Singh's empirical nonlinear failure criterion provides an improved prediction of strength, but it does not explain the associated failure mechanisms. To overcome this limitation, a Discrete Element Method (DEM) model has been used to simulate the triaxial tests performed on the Tournemire shale. The model confirms that (I) for a perpendicular orientation of the bedding with respect to the maximum principal stress direction, fracture occurs through the bedding plane leading to a maximum strength, (II) for a parallel orientation of the bedding, splitting along the bedding planes appears, leading to an intermediate strength and (III) for an orientation of 45°, the deformation always localizes along the bedding orientations, leading to a minimum strength. The DEM model, in its current formulation, fails to reproduce the saturation of the failure envelop in the present case.

1 Introduction

Strength prediction of caprocks is a basic requirement to assess their integrity [Jon03,Mil04,Dam06]. By integrity, we mean the ability of the rock to keep its mechanical properties below its plastic limit as well as maintaining its hydraulic conductivity low enough to prevent major fluid migration or irreversible damage, while the in-situ stress state or the fluid pressure can vary considerably. At the petroleum reservoir or underground nuclear waste storage scale, rocks cannot be considered as intact environments because fracture sets or faults are generally present, modifying significantly the strength and hydraulic properties of the medium [Hoo11].

Nonetheless, even though these discontinuities need to be considered above the meter scale, the intact rock properties still need to be thoroughly characterized before any further hydromechanical investigations. Focusing on the intact rock strength is a key point because in the upper crust conditions, rocks behave as dilatant materials when subject to plastic deformation and this increase of volume can induce dramatic changes in its hydraulic properties..

Caprocks or underground storage barrier rocks present very low permeability values, i.e. well below the milliDarcy level. In sedimentary rocks, this appears in clay rich rocks, which is the case for most of shale rocks [Hen2016].

A particular point is that the strength of these rock types varies in a nonlinear manner with the confining pressure and it is interesting to note that despite this unanimously observed behavior, the linear Mohr-Coulomb criterion is still widely used to predict the failure of shales [Bar13].

Ultimately, the analytical formulation of a complete non-linear failure criterion should be based on the mineralogy content of the rock. However, such formulation can become highly complex and requires large amounts of data (see Shen *et al.*, 2012 for example). In a first approach, due to the difficulty to perform exhaustive experimental testing, one could try to define a simple but nonetheless reliable formulation to predict the strength of shale rock. Non-linear empirical formulations, such as the ones proposed by Hoek and Brown [Hoe97] or Singh *et al.* [Sin11,Sin15], are valuable attempts.

A second point is that these rocks usually present an anisotropic structure, characterized by lamination, parallel layering or bedding features. These fabric properties induce a strong anisotropic behavior for both their elastic and plastic properties. It is thus crucial to take this mechanical and micro-structural anisotropy into account when formulating a strength model [Com17].

Empirical formulations are easy to use, but they poorly explain underlying mechanical processes. This is why, besides setting up simple analytical formulation, numerical model are very useful to help in understanding failure mechanisms. An interesting numerical tool to perform such analyses is the Discrete Element Method [Don95,Don09,Pot04,Lud17,Mar17]. Because DEM considers, at a certain level, the fabric properties of the material, it provides indications on how the microstructure of a material can drive the deformation.

In this paper, we propose to study the strength of the Tournemire shale rock and, based on experimental laboratory test results, compare the Mohr-Coulomb criterion to the one proposed by Singh et al. [Sin11,Sin15]. Finally, the Discrete Element Method will be used to discuss how the fabric can contribute to the non-linearity and the anisotropic nature of the mechanical response (see also Ref. [Lud17]).

2 Tournemire shale: triaxial tests and the Mohr-Coulomb failure criterion

Triaxial tests performed on Tournemire shale rock samples drilled along different orientations relative to the bedding ($\beta = 0^\circ, 45^\circ, 90^\circ$) were performed to characterize their respective strength [Bon17]. These tests were carried out at confining pressures ranging from 2.5 to 80 MPa, with a strain rate of $3 \times 10^{-7}\ \mathrm{s}^{-1}$. Plotting the peak stress values for different differential stresses vs. confining stresses provides the trends of the plastic yield envelop (Figure 1). As expected for rock-like materials, the failure envelop is nonlinear. Moreover, the orientation of the principal stress relative to the bedding greatly modifies the strength of the medium, with a minimum strength observed for loadings applied at 45° relative to the bedding and a maximum strength for 90°. Following Mohr-Coulomb theory, the apparent friction coefficient as well as the uniaxial compressive strength of the material can be calculated by fitting a least-squares line on the three plots (Figure 1). The conventional Mohr–Coulomb criterion for transversely isotropic rocks can be written as:

$$\sigma_1 = \sigma_{c\beta} + \frac{1+\sin\varphi_{\beta 0}}{1-\sin\varphi_{\beta 0}}\sigma_3 \tag{1}$$

where σ_1, σ_3 are the major and minor principal stresses at failure, with

$$\sigma_{c\beta} = \frac{2\sigma_{\beta 0}\cos\varphi_{\beta 0}}{1-\sin\varphi_{\beta 0}} \tag{2}$$

the unconfined compressive strength (UCS) of the material and β the angle defining the orientation of the bedding (isotropy plane) with respect to the major principal stress direction. In equation 2, $c_{\beta 0}$ and $\varphi_{\beta 0}$ are the Mohr–Coulomb cohesion and peak friction angle obtained from the triaxial tests performed at low confining pressure ($\sigma_3 \rightarrow 0$).

In its conventional linear form, the Mohr–Coulomb criterion may thus be written as:

$$\sigma_1 - \sigma_3 = \sigma_{c\beta} + \frac{2\sin\varphi_{\beta 0}}{1-\sin\varphi_{\beta 0}}\sigma_3 \tag{3}$$

Using equation 3, one can determine the respective UCS and friction coefficient for the three orientations β (Table 1).

Bedding orientation β [-]	Friction coefficient μ_β [-]	UCS $\sigma_{c\beta}$ [MPa]
90° (green line)	0.35	31.15
45° (red line)	0.20	23.32
0° (blue line)	0.20	44.99

Table 1: Tournemire rock strength parameters obtained from fitting the experimental data [Bon17] with the conventional linear Mohr–Coulomb criterion. The color code refers to Figure 1.

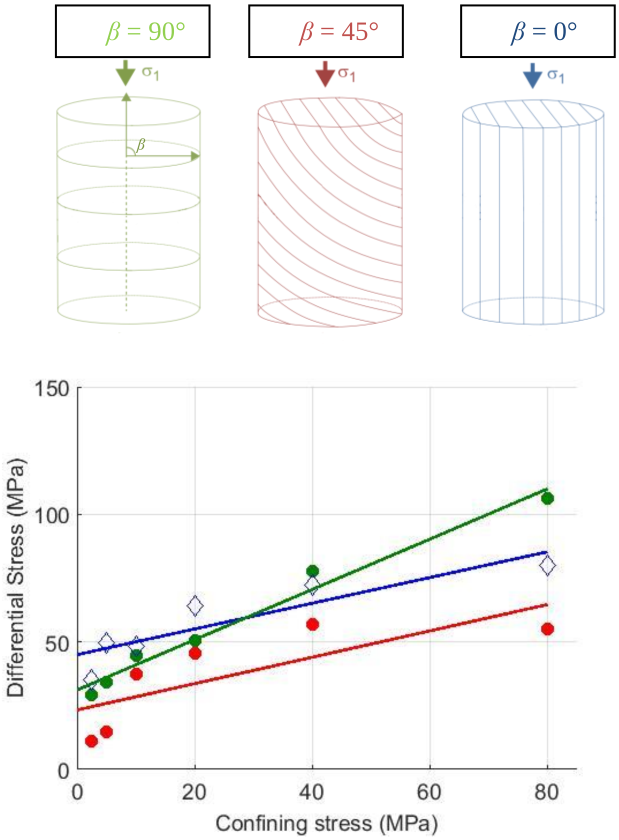

Figure 1: Top: Sample configurations for each bedding orientation. Bottom: Peak stresses in the differential stress (σ_1 - σ_3) vs. confining stress σ_3 plan with the associated Mohr-Coulomb failure envelops obtained using the least-square method (β = 90° in green, β = 45° in red and β = 0° in blue).

It can be seen that fitting the Mohr-Coulomb failure criterion to the experimental data is a hazardous strategy as it clearly overestimates the UCS but also the plastic yield at high confining stresses. Indeed, the failure of the material is highly nonlinear and cannot be approximated by a Mohr-Coulomb type criterion. One can also be puzzled by the representativity of the friction coefficient values at low and high confining stresses.

3 Nonlinear strength criterion

Recent studies based upon the results of hundreds of triaxial tests carried out on laminated rocks [Sin11,Sin15] showed that the linearity of the strength envelop is lost when $\sigma_3 = \sigma_{crt} \approx \sigma_c$ (UCS) for the majority of shale rocks [Bar13]. This critical confining stress σ_{crt} has been proposed [Bar76] to identify the limit value of the supported differential stress by the rock. In case of fully saturated rocks containing an important clay fraction, this critical stress is generally observed.

A possible approach to formulate such a non-linear rupture criterion is to add a second-degree term to the conventional linear Mohr–Coulomb criterion given in equation (3), to take into account the non-linearity in the strength criterion [Sin15]. Replacing the friction angle by the coefficient of friction, the resulting criterion can be written as,

$$\sigma_1 - \sigma_3 = \sigma_{c\beta} + \frac{2\mu_{\beta 0}}{\sqrt{1+\mu_{\beta 0}^2} - \mu_{\beta 0}}\sigma_3 - \frac{1}{\sigma_{crt}}\frac{\mu_{\beta 0}}{\sqrt{1+\mu_{\beta 0}^2} - \mu_{\beta 0}}\sigma_3^2 \quad \text{for } 0 \leq \sigma_3 \leq \sigma_{crt} \quad (4)$$

where $\mu_{\beta 0}$ is the coefficient of internal friction of the rock (i.e. $\mu_{\beta 0} = tan(\varphi_{\beta 0})$) with planes of anisotropy oriented at an angle β from the major principal stress direction. For confining pressures $\sigma_3 > \sigma_{crit}$, the criterion takes on a constant value such as,

$$\sigma_1 - \sigma_3 = \sigma_{c\beta} + \frac{\sin\varphi_{\beta 0}}{1-\sin\varphi_{\beta 0}}\sigma_{crt} \quad \text{for} \quad \sigma_3 > \sigma_{crt} \quad (5)$$

To apply the above criterion, the UCS $\sigma_{c\beta}$ of the rock at a given orientation β should be known, which is unfortunately not the case for the triaxial tests carried out in [Bon17]. Nonetheless, these UCS can be extrapolated from the low confinement peak stresses (see Figure 2). Using the apparent friction coefficients and the UCS for each bedding orientation as well as the critical stress value σ_{crt} given in Table 2, the Singh failure envelops fitting the data set provided by Bonnelye et al. [Bon17] can be obtained (Figure 2).

Bedding orientation β [-]	Friction coefficient μ_β [-]	UCS σ_c [MPa]	$\sigma_{crt} / max(\sigma_c)$ [-]
90° (green line)	0.7	27	1.25
45° (red line)	0.7	10	1.25
0° (blue line)	0. 8	20	1.25

Table 2: Tournemire rock strength parameters used to calibrate the Singh non-linear failure criterion.

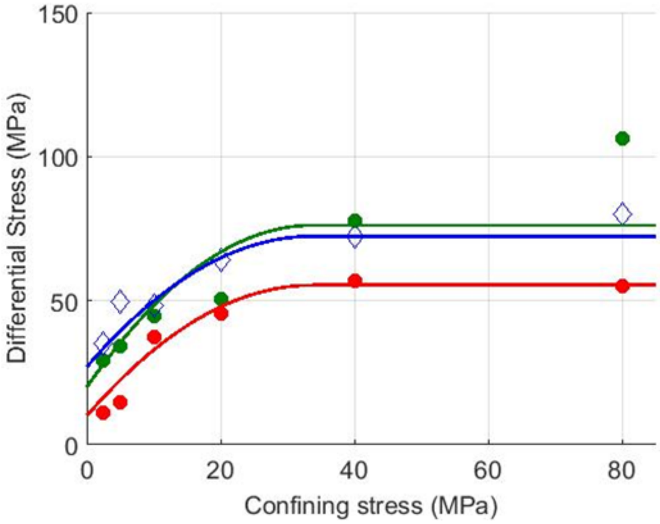

Figure 2. Singh [Sin15] failure criterion applied to Tournemire Shale rock fitting the experimental dataset [Bon16], (β = 90° in green, β = 45° in red and β = 0° in blue).

It can be seen that using a non-linear criterion, the complete spectrum of the peak friction coefficients are considered whatever the confining stress value is. Moreover, the UCS can be predicted in a more reasonable manner. Note that the only extra requirement needed to set up this nonlinear strength criterion is the value of the critical stress σ_{crt} which is estimated from the UCS.

4 Discrete Element modeling

In order to simulate the behavior of the Tournemire shale rock, we use the bonded particle model (BPM) proposed by [Sch13] implemented in the open source code YADE Open DEM [Koz08,Koz09,Šmi10]. The rock sample is represented by a dense polydisperse assembly of spherical discrete elements interacting through elastic-brittle constitutive laws. A linear force-displacement relationship is defined for both the normal and the tangential directions to the contacts. The contact forces can increase up to threshold values defined through a Mohr-Coulomb type failure criterion associated to a tensile cut off. Interparticle bonds can thus fail under either mode I (tensile) or mode II (shear) rupture. Explicit time domain integration is used to solve the dynamic problem involving Newton's second's law of motion. A non-viscous type damping is introduced to decrease the inertial response of the discrete elements and thus ease the convergence towards a quasi-static equilibrium.

Based on the approach proposed by [Dua15], fabric anisotropy is explicitly modeled by introducing preferentially oriented weakness planes in the discrete element packing (Figure 3). The weakness planes are defined at the inter-particle scale, by setting the contacts orientation accordingly to the direction of the bedding (or lamination) of the geomaterial. These weakness planes have mechanical properties that differ from the ones making up the rock matrix (e.g. without cohesion to mimic pre-existing microcracks). The procedure consists in finding every bond dipping sub-parallel to the beddings and reorienting them according to the bedding orientation (Figure 3). Obviously, the amount of weakness planes introduced in the medium directly affects its degree of anisotropy and has thus to be predefined accordingly. The weakness planes obey the joint contact logic introduced by Scholtès and Donzé [Sch12], which was inspired by the "smooth joint contact" logic initially proposed by Ivars *et al.* [Iva10].

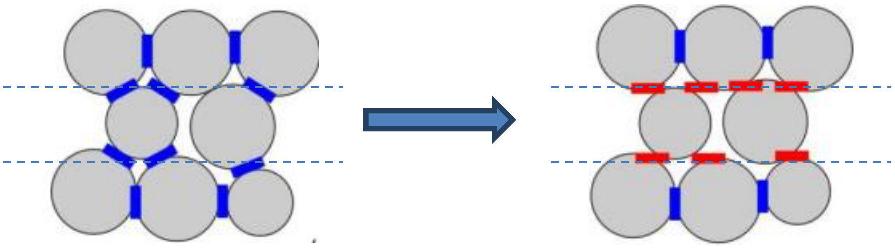

Figure 3. Introducing fabric and strength anisotropy in the DEM model: (left) detection of the bonds dipping sub-parallel to the bedding plane , (right) reorientation of the bonds according to the direction of the bedding (right)(adapted from Dinç and Scholtès [Din17]).

4.1 Reproducing the anisotropic response of the strength

The degree of anisotropy can be quantified by the 'anisotropy ratio' defined by Ramamurthy [Ram01] as the ratio between the maximum and the minimum compressive strength $\sigma_{c\beta}$ of the rock for a given confining pressure. If not known, three tests conducted at respective orientations $\beta = 0°, 90°$ and $45°$ can be used.

The DEM model is used here to simulate the Tournemire shale rock experiments introduced previously. Rather than a limited study of only three orientations, it is straightforward to consider several other orientations to obtain a more complete characterization of the strength dependence on rotation. The evolution of the UCS for different bedding orientations is presented in Figure 4. It can be seen that the numerical model can reasonably predict the UCS given by Singh's criterion from the extrapolation of the experimental data set. The anisotropy ratio obtained by Singh is 2.7 (from Table 2) compared to 2.23 for the numerical model (see Figure 4).

Based on these results, it can be examined in detailed how the stress loading along different bedding orientations leads to these different strength values. One has to mention that clay particles found in shale rocks are very small, of the order of the micrometer, and their shape depends on the type of clay (e.g. smectite, illite or kaolinite [Wil14]). The present numerical model does not intend to reproduce the rock medium of clay particle shapes and sizes, but rather is a discrete representation reproducing the localization of the deformation at the lamination scale. This localization is indeed strongly dependent on the orientation of the anisotropy as reported by Bonnelye *et al*. [Bon17] and presented in Figure 5.

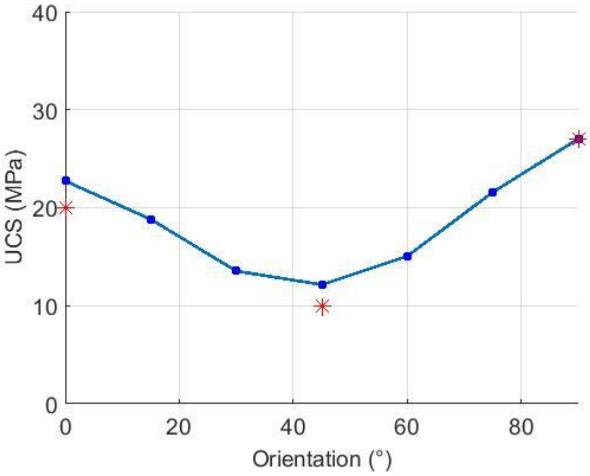

Figure 4. Variations of the UCS vs. the anisotropy angle. The red dots are the values predicted by Singh (Table 2) and the blue line corresponds to the values obtained numerically.

Different types of localization were observed in the post-mortem samples of Tournemire shale. The samples were soaked in epoxy in order to see at sample scale and microscale the evolution of strain localization. One observes formation of shear fractures crossing the laminations when they are perpendicularly oriented to the maximum stress direction (Figure 5, left). In this case, this is the peak friction coefficient of the intact matrix which is the driving parameter of the localization process, whereas for a 45° orientation of the bedding, the weak anisotropic planes are now mainly reactivated, leading to an overall sliding process along the lamination direction (Figure 5, center). This orientation corresponds to the weakest strength of the sample. Finally, for a 0° orientation of the bedding, there is a competition between a split process along the vertical weak planes and the formation of shear fractures occurring in the direction associated to the peak friction coefficient of the intact matrix (Figure 5, right). The resulting strength might be dependent on the density of the bedding planes. These different types of localization were also predicted by the DEM model (Figure 5, top). For the three different configurations, the deformation field has been represented in the 3D numerical sample: the zones colored in red indicate where a maximum deformation occurs. For an orientation of $\beta = 90°$, the fracture is always localized in a single fracture, for an orientation of $\beta = 45°$, the deformation is localized along the bedding orientation and for an orientation of $\beta = 0°$, both splitting and shearing processes are generated.

4.2 Reproducing the non-linearity of the failure envelop

The differential stresses versus the confining stress are presented in Figure 6. For comparison, the values obtained experimentally, Singh criterion and the DEM model ’s results are plotted on the same graph. The increase of the strength with the increase of the confining stress at low stress is reproduced by both Singh and the DEM model. However, the DEM model fails to reproduce the strong curvature and saturation of the failure envelop. As the confining stress increases, the strength of the numerical model increases linearly, exceeding dramatically the values obtained experimentally. Even selecting a low friction angle value at the level of the bonds when these break, the apparent shear strength is overestimated in the present case. It seems that an important key property of the material is not considered in the numerical model. It could be related to changes in the fabric itself. It has been observed experimentally that on the fracture plane, the grains are reoriented in a very thin layer, producing a smooth fracture [Bon17]. Added to the fact that the shale rocks contain water which cannot escape during the deformation due to the low permeability, the resulting effective stress along the fracture planes tends to decrease. These features thus must be taken into account in the DEM model.

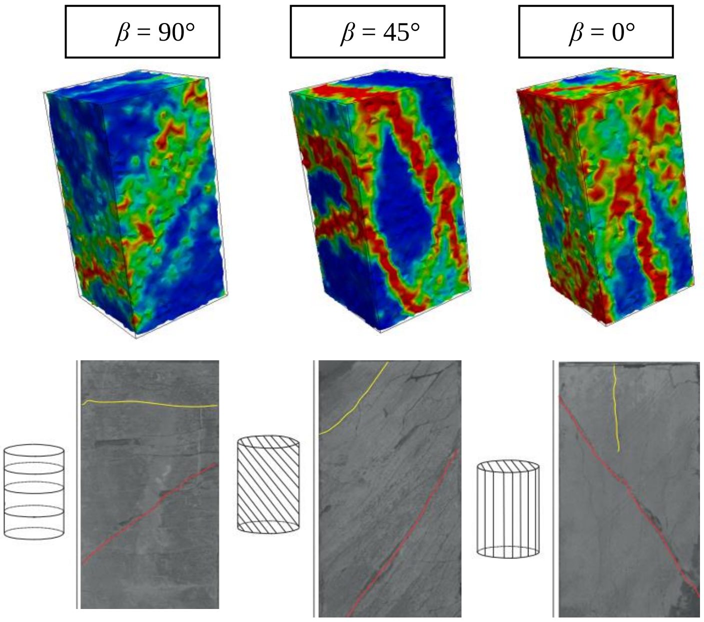

Figure 5. On top, the localization of the deformation predicted by the DEM model for different bedding β orientations. The zones colored in red correspond to the high shear strain values. Bottom, for the corresponding orientations β, post mortem images of fractured samples from Bonnelye et al., [Bon17]. The bedding orientation is highlighted as yellow lines, whereas the fractures are red lines.

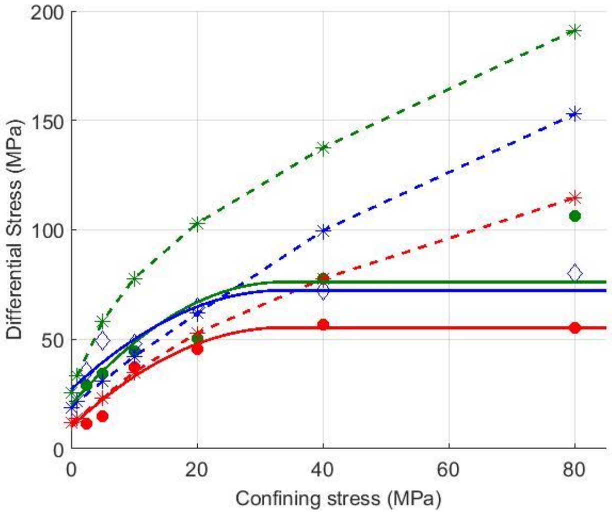

Figure 6. Differential stress as a function of confining stress: the values obtained experimentally, the Singh's criterion (plain curves) and the DEM model prediction (dashed lines with stars) are plotted for β = 90° in green, β = 45° in red and β = 0° in blue.

5 Conclusions

Experimental triaxial tests carried out on Tournemire shale rock have shown that the bedding orientation has a strong impact on peak stress, with the orientation β = 45° the weakest and β = 90° the strongest. A nonlinear failure envelope with saturation has also been observed. As strength criterion based on the critical stress concept is more relevant to express a realistic plastic yield envelop rather than just considering a conventional linear Mohr–Coulomb criterion, which provides unreasonable values of both friction coefficient and UCS. Note that back analysis of thousands of triaxial tests, indicates that for the application of the Singh criterion, the critical confining pressure for inherently anisotropic rocks may be taken nearly equal to 1.25 of the maximum UCS value. In the present study, it has been shown that this value also provided a good prediction of the experimental results.

Since Mohr–Coulomb and Singh criteria do not provide any description on how the failure develops in the sample, we used a discrete element model. From the experimental tests, post-mortem sample analysis showed that the way fracture develops in the sample depends on the bedding orientation. For an orientation β = 90°, a fracture occurs through the bedding plane at all confining pressures. For an orientation β = 0°, the fracture propagates along the bedding planes at low confining pressures and through the bedding planes when the confining pressure increases. Finally, for an orientation β = 45°, deformation localizes along the bedding plane as it is aligned with the maximum shear stress. The numerical simulations show exactly the same trends, supporting the assumption that in this type of material, at the first order, the lamination scale anisotropy and heterogeneity cannot be ignored. However, the model fails to reproduce the limited shear strength for the higher confining values: the model needs to be improved to also reproduce the inner properties of the clay fraction and interplay with pore water.

Acknowledgments

The experimental tests providing the data set were funded by TOTAL and it is part of the “Fluids and Faults” project.

References

[Bar76] N. Barton. The shear strength of rock and rock joints, *International Journal of Rock Mechanics and Mining Sciences and Geomechanics Abstracts, 13(9): 255–279, 1976.*

[Bar13] N. Barton. Shear strength criteria for rock, rock joints, rockfill and rock masses: Problems and some solutions. *Journal of Rock Mechanics and Geotechnical Engineering, 5(4): 249-261,* 2013

[Bon17] A. Bonnelye, A. Schubnel, C. David, P. Henry, Y. Guglielmi, C., Gout, A-L Fauchille & P. Dick, Strength anisotropy of shales deformed under uppermost crustal conditions. *Journal of Geophysical Research: Solid Earth, 122(1):110-129, 2017.*

[Com17] G. Combe & J.N. Roux. Good practice and sample preparation - Construction of granular packings. *ALERT geomaterials Doctoral School 2017, Aussois, France*.

[Dam06] K. Damen, A. Faaij & W. Turkenburg. Health, safety and environmental risks of underground CO 2 storage–overview of mechanisms and current knowledge. *Climatic Change, 74(1): 289-318, 2006*.

[Din17] Ö. Dinç & L. Scholtès. Discrete analysis of damage and shear banding in argillaceous rocks, *submitted to rock mechanics and rock engineering, 2017.*

[Don95] F.-V. Donzé & S. A. Magnier. Formulation of a 3-D numerical model of brittle behaviour. *Geophysical Journal International, 122(3): 790-802, 1995.*

[Don09] F.-V. Donzé, V. Richefeu, & S. A. Magnier. Advances in discrete element method applied to soil, rock and concrete mechanics. *Electron J Geotech Eng, 8, 1-44, 2009.*

Dua15] K. Duan, C.Y. Kwok & M. Pierce. Discrete element method modeling of inherently anisotropic rocks under uniaxial compression loading. *International Journal for Numerical and Analytical Methods in Geomechanics. 2015.*

[Hen16] P. Henry, Y. Guglielmi, A. Morereau, S. Seguy, R. Castilla, C. Nussbaum, P. Dick, J. Durand, D. Jaeggi, F.V. Donze & A. Tsompela. Permeability – Fluid Pressure – Stress Relationship in Fault Zones in Shales. *In AGU December Fall Meeting Abstracts, 2016.*

[Hoe97] E. Hoek & Brown. Practical estimates of rock mass strength, *International Journal of Rock Mechanics and Mining Sciences, 34(8):1165-1186, 1997.*

[Hook] J.N. Hooker, P. Eichhubl, G. Xu, H. Ahn, A. Fall, P. Hargrove, S. Laubach & E. Ukar. Effects of fracture reactivation and diagenesis on fracture network evolution: Cambrian Eriboll Formation, NW Scotland. *In AGU December Fall Meeting Abstracts (Vol. 1, p. 1097), 2011.*

[Iva11] D. M. Ivars, M.E. Pierce, C. Darcel, J. Reyes-Montes, D.O. Potyondy, R.P. Young, & P.A. Cundall. The synthetic rock mass approach for jointed rock mass modelling. *International Journal of Rock Mechanics and Mining Sciences, 48(2): 219-244, 2011*

[Jon03] R.M. Jones & R. R. Hillis. An integrated, quantitative approach to assessing fault-seal risk. *AAPG bulletin, 87(3): 507-524, 2003.*

[Koz08] J. Kozicki, & F.-V. Donzé. A new open-source software developed for numerical simulations using discrete modeling methods. *Computer Methods in Applied Mechanics and Engineering, 197(49), 4429-4443, 2008.*

[Koz09] J. Kozicki, & F.-V. Donzé. Yade-open dem: an open-source software using a discrete element method to simulate granular material. *Engineering Computations, 26(7): 786-805, 2009.*

[Lud17] S. Luding, N. Rivas & T. Weinhart. From soft and hard particle simulations to continuum theory for granular flows. *ALERT geomaterials Doctoral School 2017, Aussois, France.*

[Mar17] C.L. Martin. Advanced contact laws. *ALERT geomaterials Doctoral School 2017, Aussois, France.*

[Mil04] S.D. Mildren, R.R., Hillis, T., Kivior & J.G. Kaldi, Integrated seal assessment and geologic risk with application to the Skua Field, Timor Sea, Australia. In Timor Sea Petroleum Geoscience, *Proceedings of the Timor Sea Symposium, Darwin, Northern Territory, 19-20, 2003*.

[Pot04] D.O. Potyondy & P.A. Cundall, A bonded-particle model for rock. International journal of rock mechanics and mining sciences, 41(8), 1329-1364, 2004.

[Ram01] T. Ramamurthy. Shear strength response of some geological materials in triaxial compression. *International Journal of Rock Mechanics and Mining Sciences, 38(5): 683-697, 2001*

[Sch12] L. Scholtès & F.-V. Donzé. Modelling progressive failure in fractured rock masses using a 3D discrete element method. *International Journal of Rock Mechanics and Mining Sciences, 52, 18-30, 2012*

[Sch13] L. Scholtès & F.-V.Donzé, A DEM model for soft and hard rocks: role of grain interlocking on strength. *Journal of the Mechanics and Physics of Solids, 61(2): 352-369, 2013*

[She12] W.Q. Shen, J.F. Shao, D. Kondo & B. Gatmiri, A micro–macro model for clayey rocks with a plastic compressible porous matrix. *International Journal of Plasticity, 36: 64-85, 2012.*

[Sin11] M. Singh, A. Raj, & B. Singh. Modified Mohr–Coulomb criterion for non-linear triaxial and polyaxial strength of intact rocks. *International Journal of Rock Mechanics and Mining Sciences, 48(4): 546-555, 2011*

[Sin15] M. Singh, N. K. Samadhiya, A. Kumar, A.V. Kumar& B. Singh. A non-linear criterion for triaxial strength of inherently anisotropic rocks. *Rock Mechanics and Rock Engineering, 48(4): 1387-1405, 2015.*

[Šmi10] V. Šmilauer, E. Catalano, B. Chareyre , S. Dorofeenko, J. Duriez, A. Gladky, J. Kozicki, C. Modenese, L. Scholtès, L. Sibille, J. Stránský, K. Thoeni. Yade reference documentation. Yade Documentation, 474, 1-531, 2010.

[Wil14] M. J. Wilson, L. Wilson & I. Patey. The influence of individual clay minerals on formation damage of reservoir sandstones: a critical review with some new insights. Clay Minerals, 49(2), 147-164, 2014.

Discrete particle simulations with MercuryDPM

D. Tunuguntla, T. Weinhart, A. Thornton

University of Twente, The Netherlands
MercuryLab BV, The Netherlands

In this paper we give a brief introduction to the open-source particle simulation code MercuryDPM, available at `http://MercuryDPM.org`. The focus is on practically using the code, with detailed installation and running instructions given. A large section is dedicated to coarse-graining, an advanced method for mapping discrete (particle) data to continuum data. MercuryDPM includes a coarse-graining tool, MercuryCG, and the chapter ends with exercises to both demonstrate MercuryDPM and MercuryCG.

Preface

The information contained in this chapter is taken from the book 'The Fundamentals of Discrete Particle Simulations' March 2017 edition. MercuryLab BV holds the copyright of the aforementioned book. All copyright material reproduced in this chapter is done with the written permission of MercuryLab BV.

1 About MercuryDPM

MercuryDPM is a code for efficiently performing fully *three-dimensional* discrete particle simulations [Tea13, TKF$^+$13, Wea17]. The method is referred to as discrete element method (DEM), as introduced in [LRW], or discrete particle method (DPM) in other literature. It is a very versatile, object-orientated C++ code, which is easily understandable. It has been tested for several `Linux` distributions, `Mac OS` and `Windows 10.1`. The users specify the particulars of their simulation (initial positions, inflow, outflow, walls, interaction parameters) in a single driver file, which calls the kernel to do the simulations. All kernel functions are documented here, and there are several driver samples available. To avoid breaking already existing code, a suite of self-tests has been developed testing pre-existing features of the code.

Since it was first started, MercuryDPM has evolved and gained many novel features. The main features include:

- The hierarchical grid: This neighbourhood search algorithm effectively computes interaction forces, even for highly poly-dispersed particles distributions.
- Statistics: MercuryDPM has an in-built advanced statistics package, MercuryCG, to extract continuum fields such as density, velocity, structure and stress tensors, either during the computation or as a post-processing step. It can also be applied to extract drags and partial stresses in polydispersed flows.
- Access to continuum fields in real time: The code can be run in live statistics mode, which means it can respond to its current macroscopic state. An illustrative example of using this would be a pressure-release wall, i.e., a wall whose motion is determined by the macroscopic pressure created by particle collisions and moves such that its pressure (not position) is controlled.
- Contact laws for granular materials: many granular contact force models are implemented, including elastic (linear or Hertzian), plastic, cohesive (dry or wet), temperature, pressure, and time-dependent force laws (sintering), and frictional forces (sliding/rolling/torsion).
- Simple C++ implementation: MercuryDPM consists of a series of C++ classes that are flexible, but easy to use. This allows the user to generate advanced applications with only a few lines of code.
- Handlers: The code has handlers for particles, walls and boundaries. Thus, each object type has a common interface, even though individual objects can have completely different properties. This also makes it easier for the user to create new objects.
- Complex walls: The code not only supports simple flat walls, but also axial-symmetric, polyhedral and helical screw walls are available. Additionally, due to the handler interface, it is easy for more advanced users to define new types of walls themselves.
- Specialised classes: Many specialised classes exist that reduce the amount of code required by the user to develop standard geometries and applications. Examples include chute flows, vertically vibrated walls and rotating drums.
- Species: Particles and walls each have a unique species, which is hidden for basic use of the code; however, this feature can be enabled by a single function call. Different particle properties for each species and different interaction forces for each pair of species can then be defined, allowing the simulation of mixtures.
- Self-test suite and demos: MercuryDPM comes with a large (over 100) number

of self-tests and demo codes. These serve two purposes: 1) they allow us to constantly test both new and old features so we can keep bugs to a minimum; 2) they serve as tutorials, for new users, of how to do different tasks.

- Simple restarting: every time a code is run (and at intervals during the computation) restart files are generated. Codes can be restarted without recompilation simply by calling the executable again with the restart file name as an argument. Also the restart files are complete in the sense that they contain all the information about the problem. In this way, small changes can be made (for example with the individual particle density or the coefficient of restitution) and the simulation can be rerun without the need for recompilation of the code.
- Interface to other particle simulation codes: The restarting interface is further used to provide an interface to load external data (including experimental data, other particle codes such as EDEM, and molecular dynamics) into MercuryDPM for post-processing with MercuryCG.
- Visualisation: The particles output can be visualised easily using the free packages VMD and Paraview.

2 Installation Instructions

2.1 Windows versions older than 10.1

Since MercuryDPM was originally designed for use with Unix systems, Windows users must first install a linux emulator software to allow compatibility. We recommend the program Cygwin (Click here).

This is not necessary for Windows 10.1; please see MercuryDPM website for Windows 10 instructions.

2.1.1 Installation of Cygwin

After downloading and opening the relevant executable (most likely `setup-x86.exe`), follow the default instructions until you see a screen resembling the one below asking you to select packages:

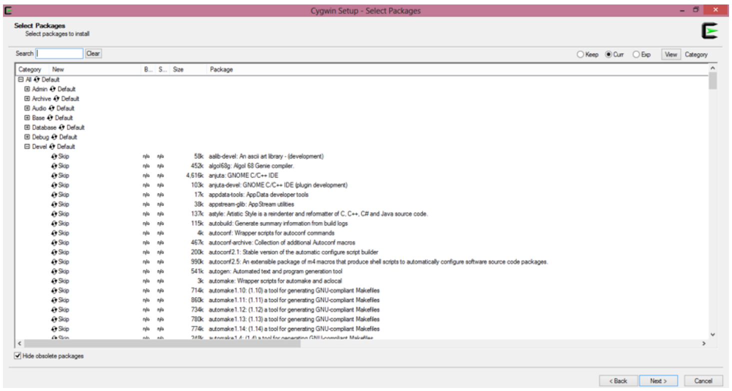

Cygwin Setup - Select Packages

Select Packages
Select packages to install

Search

○ Keep ● Curr ○ Exp Category

Category	New	B...	S...	Size	Package
⊟ All Default					
⊞ Admin Default					
⊞ Archive Default					
⊞ Audio Default					
⊞ Base Default					
⊞ Database Default					
⊞ Debug Default					
⊟ Devel Default					
	Skip	n/a	n/a	58k	aalib-devel: An ascii art library - (development)
	Skip	n/a	n/a	452k	algol68g: Algol 68 Genie compiler.
	Skip	n/a	n/a	4,616k	anjuta: GNOME C/C++ IDE
	Skip	n/a	n/a	103k	anjuta-devel: GNOME C/C++ IDE (plugin development)
	Skip	n/a	n/a	17k	appdata-tools: AppData developer tools
	Skip	n/a	n/a	38k	appstream-glib: AppStream utilities
	Skip	n/a	n/a	137k	astyle: Artistic Style is a reindenter and reformatter of C, C++, C# and Java source code.
	Skip	n/a	n/a	115k	autobuild: Generate summary information from build logs
	Skip	n/a	n/a	4k	autoconf: Wrapper scripts for autoconf commands
	Skip	n/a	n/a	467k	autoconf-archive: Collection of additional Autoconf macros
	Skip	n/a	n/a	200k	autoconf2.1: Stable version of the automatic configure script builder
	Skip	n/a	n/a	990k	autoconf2.5: An extensible package of m4 macros that produce shell scripts to automatically configure software source code packages.
	Skip	n/a	n/a	541k	autogen: Automated text and program generation tool
	Skip	n/a	n/a	3k	automake: Wrapper scripts for automake and aclocal
	Skip	n/a	n/a	714k	automake1.10: (1.10) a tool for generating GNU-compliant Makefiles
	Skip	n/a	n/a	860k	automake1.11: (1.11) a tool for generating GNU-compliant Makefiles
	Skip	n/a	n/a	734k	automake1.12: (1.12) a tool for generating GNU-compliant Makefiles
	Skip	n/a	n/a	780k	automake1.13: (1.13) a tool for generating GNU-compliant Makefiles
	Skip	n/a	n/a	774k	automake1.14: (1.14) a tool for generating GNU-compliant Makefiles

☑ Hide obsolete packages

At this point, the packages listed below should be included by clicking on the '+' icon of the relevant heading and then clicking the name of the relevant package until a version number is displayed.

The majority of the relevant packages may be found under the *'Devel'* heading which can be seen in the above image, although it may be easier to simply find the relevant packages using the search bar at the top-left of the window. It is not necessary at this point to fully understand the function of each package; for now, they simply need to be installed.

The necessary packages are:

1. The complete X11 package
2. cmake and cmake-gui: A cross-platform makefile generation system. (*Note:* cmake-gui is **not available** in the 32-bit version of Cygwin. For 32-bit machines 'ccmake', which is included with cmake, may instead be used).
3. make: the GNU version of the 'make' utility
4. If you do not already have a C++ compiler installed, you should also install the 'gcc-g++ C++ compiler' package, which is also under the *'Devel'* heading.
5. *Optional:* You may additionally wish to install 'gnuplot' and 'gnuplot-x11' which will allow you to easily and quickly visualise results produced using MercuryDPM.

Note, it is highly advisable to keep your Cygwin updated to the latest version.

2.1.2 Installation of SVN

In addition to Cygwin, the installation of MercuryDPM will require an SVN client such as 'TortoiseSVN' (`http://tortoisesvn.net`). Once downloaded, Tortoise SVN may simply be installed using the default setup.

Once this process is complete, we are ready to download MercuryDPM itself! This can be achieved by following the simple steps below:

1. Open Windows explorer.
2. Choose a folder into which you want to copy the MercuryDPM source code, for example 'C:/cygwin/home/username/MercuryDPM'
3. Right click and select: *'SVN Checkout'*. You will then see the screen shown below:

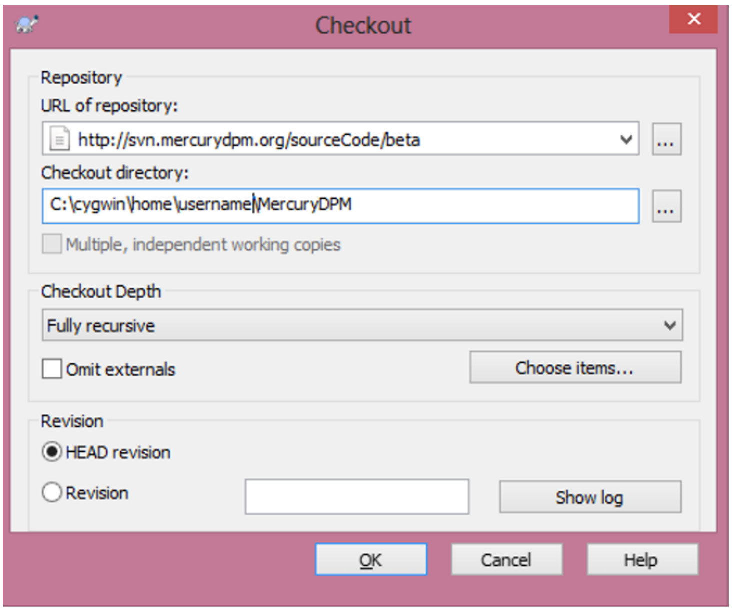

Checkout

Repository

URL of repository: http://svn.mercurydpm.org/sourceCode/beta

Checkout directory: C:\cygwin\home\username\MercuryDPM

☐ Multiple, independent working copies

Checkout Depth: Fully recursive

☐ Omit externals

Revision

● HEAD revision

○ Revision

4. Enter 'http://svn.mercurydpm.org/SourceCode/Beta' as URL. Note, if you want to download the 'release' version of Mercury, simply replace *'Beta'* in the above path with *'Release/[RELEASE NUMBER]'*. The number of the current release can be found on the MercuryDPM website (`http://mercurydpm.org`).
5. Click 'ok' and wait for the checkout to finish. Click 'ok'

2.1.3 Final steps

Now open the 'XWin Server' tool (under Start Menu -> Cygwin). You should now get a terminal similar to that used on Mac and Linux machines. Note that the 'XWin Server' is ***not*** the same as the main Cygwin terminal. Press the 'Windows' key and type 'XWin Server' to open it.

You are now ready to follow the instructions listed below in Installation of MercuryDPM. If `cmake-gui` is not installed use `ccmake` instead.

2.2 Linux and MacOS users

Before installing MercuryDPM, you have to make sure the following packages are installed:

1. Compiler with c++11 features, for instance clang 3.4 or higher.
2. SVN ('subversion') version 1.7 or above (Click here).
3. CMake version 2.8 or higher (Click here)
4. *Optional:* Doxygen, which may be used to create documentation while building your own source code (Click here).
5. For **Mac users**: the latest version of Xcode is recommended (Click here).
6. For **Mac users**: If you want to visualise your results, XQuartz may be installed as an alternative to X11 (Click here).

Once the above procedures have been followed and the relevant packages installed, we are ready to begin installing Mercury!

2.2.1 Installation of MercuryDPM

1. Open the terminal or shell. Create a directory called 'MercuryDPM', at a location of your choice, by typing

```
mkdir MercuryDPM
```

2. To get into the folder MercuryDPM, type

```
cd MercuryDPM/
```

3. Once in the folder MercuryDPM, download or check out the beta version of the DPM source by typing

```
svn checkout https://svn.MercuryDPM.org/SourceCode/Beta
    ↪ MercurySource
```

The above command downloads the DPM source code into the folder named 'MercurySource'. Please note that the symbol '↪' in the above box indicates a space delimiter, i.e. when typing the above command in the terminal the arrow is to be replaced with a space.

4. In the current folder, i.e. MercuryDPM, create another directory called 'MercuryBuild'

```
mkdir MercuryBuild
```

5. Get into the folder ’MercuryBuild’ by typing

```
cd MercuryBuild
```

Installation with CMake GUI:

1. Assuming CMake is successfully installed, go to the newly created ’MercuryBuild’ directory. From here, you can create the executables from the Mercury source code by typing:

```
cmake-gui ../MercurySource/
```

A GUI pops up on your screen as in the picture shown below

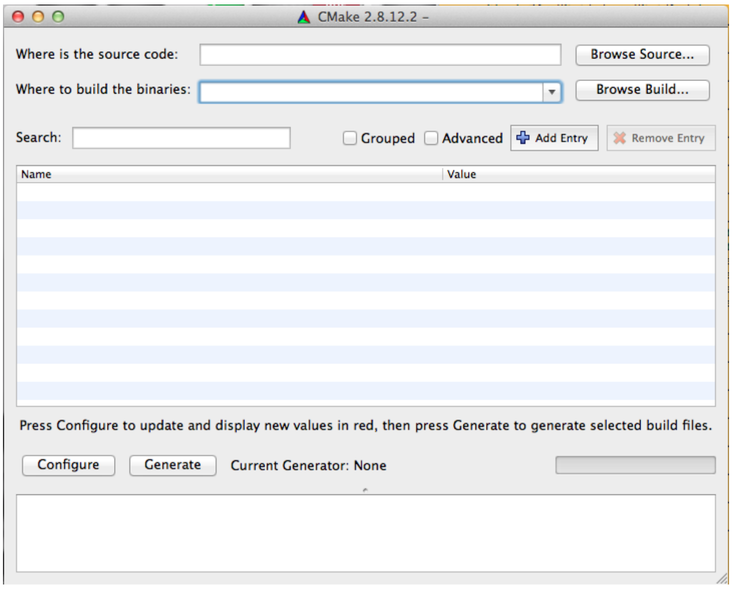

Press Configure to update and display new values in red, then press Generate to generate selected build files.

Current Generator: None

   (a) Click on ’Browse Source’ and locate the ’MercurySource’ directory.
   (b) Click on ’Browse Build’ and locate the ’MercuryBuild’ directory.
   (c) Make sure option ’Grouped’ is selected and ’Advanced’ is deselected.
   (d) Click ’Configure’

2. After clicking on ’Configure’, the following window appears on your screen:

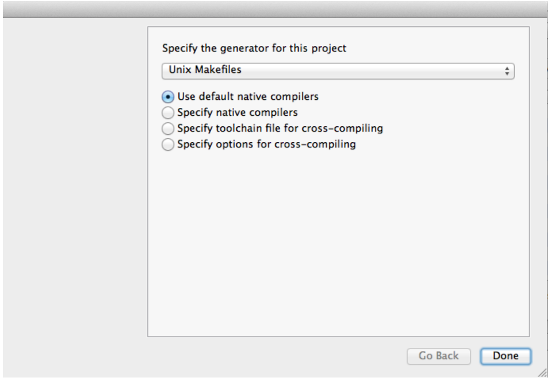

Specify the generator for this project

Unix Makefiles

● Use default native compilers
○ Specify native compilers
○ Specify toolchain file for cross–compiling
○ Specify options for cross–compiling

(a) Select 'Unix makefiles' under specify the generator for this code

(b) Choose 'use default native compilers'

(c) Click on 'Done'

3. Clicking on 'Done', builds all the files in the directory 'mercuryDPMSource' and creates the executables.

4. The building/installation progress is visible in the bottom panel of your CMake window, as seen in the screenshot below.

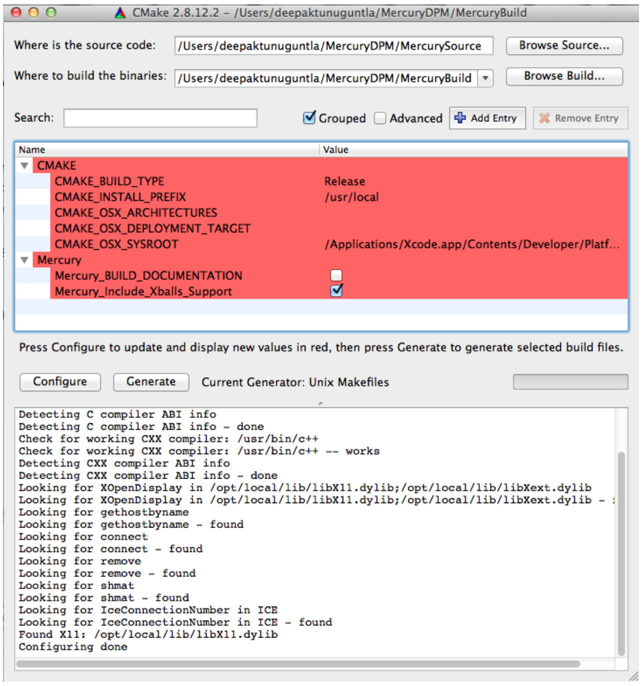

CMake 2.8.12.2 – /Users/deepaktunuguntla/MercuryDPM/MercuryBuild

Where is the source code: /Users/deepaktunuguntla/MercuryDPM/MercurySource

Where to build the binaries: /Users/deepaktunuguntla/MercuryDPM/MercuryBuild

Search:

☑ Grouped ☐ Advanced

Name	Value
CMAKE	
CMAKE_BUILD_TYPE	Release
CMAKE_INSTALL_PREFIX	/usr/local
CMAKE_OSX_ARCHITECTURES	
CMAKE_OSX_DEPLOYMENT_TARGET	
CMAKE_OSX_SYSROOT	/Applications/Xcode.app/Contents/Developer/Platf...
Mercury	
Mercury_BUILD_DOCUMENTATION	☐
Mercury_Include_Xballs_Support	☑

Press Configure to update and display new values in red, then press Generate to generate selected build files.

Current Generator: Unix Makefiles

```
Detecting C compiler ABI info
Detecting C compiler ABI info - done
Check for working CXX compiler: /usr/bin/c++
Check for working CXX compiler: /usr/bin/c++ -- works
Detecting CXX compiler ABI info
Detecting CXX compiler ABI info - done
Looking for XOpenDisplay in /opt/local/lib/libX11.dylib;/opt/local/lib/libXext.dylib
Looking for XOpenDisplay in /opt/local/lib/libX11.dylib;/opt/local/lib/libXext.dylib -
Looking for gethostbyname
Looking for gethostbyname - found
Looking for connect
Looking for connect - found
Looking for remove
Looking for remove - found
Looking for shmat
Looking for shmat - found
Looking for IceConnectionNumber in ICE
Looking for IceConnectionNumber in ICE - found
Found X11: /opt/local/lib/libX11.dylib
Configuring done
```

(a) Any red line in the bottom panel, indicates that some package is missing or needs to be installed to have a successful 'configure'. In that case, click on the 'Advanced' option to see exactly where the issue is or contact any of the MercuryDPM team of developers. Among the more frequent error messages are:

- `X11_XRES_INCLUDE_PATH` or `X11_XRES_LIB` not found

  You are missing the `X11_XRes` library; in Ubuntu, you can install them by opening a terminal and type

  ```
  sudo apt-get install libxres-dev
  ```

- `X11_XRT_INCLUDE_PATH` or `X11_XT_LIB` not found

  You are missing the `X11_Xt` library; in Ubuntu, you can install them by opening a terminal and type

  ```
  sudo apt-get install libxt-dev
  ```

- Some more solutions for common problems are mentioned here: `http://mercurydpm.org/downloads/trouble-shooting`.

(b) Once configured for the first time, under the group named 'CMAKE' type 'Release' at `CMAKE_BUILD_TYPE`. See the picture above.

5. Optional: for documentation tick the box `make_BUILD_DOCUMENTATION`, in the picture as shown below, before you click on 'Configure'.

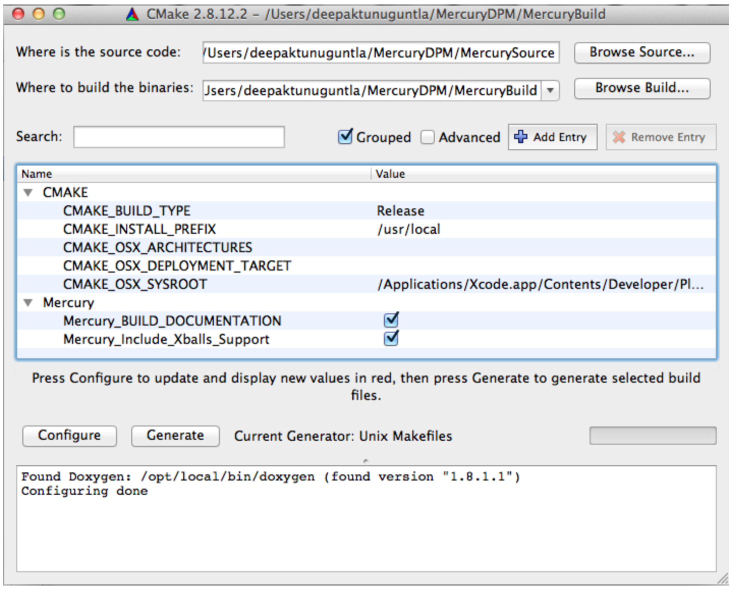

CMake 2.8.12.2 – /Users/deepaktunuguntla/MercuryDPM/MercuryBuild

Where is the source code: /Users/deepaktunuguntla/MercuryDPM/MercurySource

Where to build the binaries: Jsers/deepaktunuguntla/MercuryDPM/MercuryBuild

Search:

☑ Grouped ☐ Advanced

Name	Value
CMAKE	
CMAKE_BUILD_TYPE	Release
CMAKE_INSTALL_PREFIX	/usr/local
CMAKE_OSX_ARCHITECTURES	
CMAKE_OSX_DEPLOYMENT_TARGET	
CMAKE_OSX_SYSROOT	/Applications/Xcode.app/Contents/Developer/Pl...
Mercury	
Mercury_BUILD_DOCUMENTATION	☑
Mercury_Include_Xballs_Support	☑

Press Configure to update and display new values in red, then press Generate to generate selected build files.

Current Generator: Unix Makefiles

```
Found Doxygen: /opt/local/bin/doxygen (found version "1.8.1.1")
Configuring done
```

6. Once you entered all options and configured, click on 'Generate'.

7. To check if successfully installed, go to your build directory 'MercuryBuild' using the terminal and type

```
make fullTest
```

8. If all the tests have passed, MercuryDPM is successfully installed on your machine.

Without CMake GUI

1. For users without the GUI, cmake does include an alternative curses-based interface called 'ccmake'.
2. At the terminal, in directory MercuryBuild type

```
ccmake ../MercurySource/
```

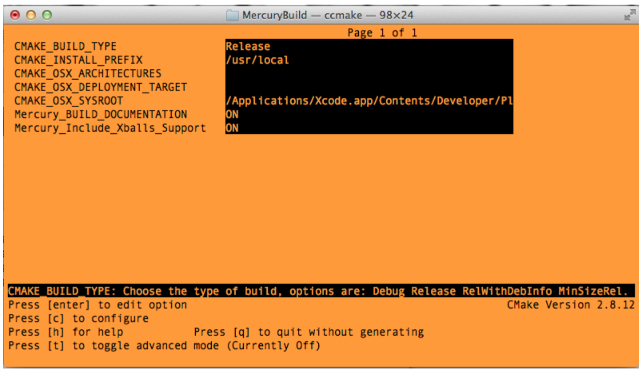

```
                                           Page 1 of 1
 CMAKE_BUILD_TYPE                 Release
 CMAKE_INSTALL_PREFIX             /usr/local
 CMAKE_OSX_ARCHITECTURES
 CMAKE_OSX_DEPLOYMENT_TARGET
 CMAKE_OSX_SYSROOT                /Applications/Xcode.app/Contents/Developer/Pl
 Mercury_BUILD_DOCUMENTATION      ON
 Mercury_Include_Xballs_Support   ON










CMAKE_BUILD_TYPE: Choose the type of build, options are: Debug Release RelWithDebInfo MinSizeRel.
Press [enter] to edit option                                                   CMake Version 2.8.12
Press [c] to configure
Press [h] for help           Press [q] to quit without generating
Press [t] to toggle advanced mode (Currently Off)
```

   (a) As seen in the above picture, pressing the key 'c' configures or builds the object files or executables from the source directory (MercurySource).

   (b) Moreover, before configuring, 'BUILD_DOCUMENTATION' or/and 'Xballs_Support' can be enabled or disabled.

   (c) Cmake experts can toggle to advanced mode by pressing the key 't' to have more options and choices.

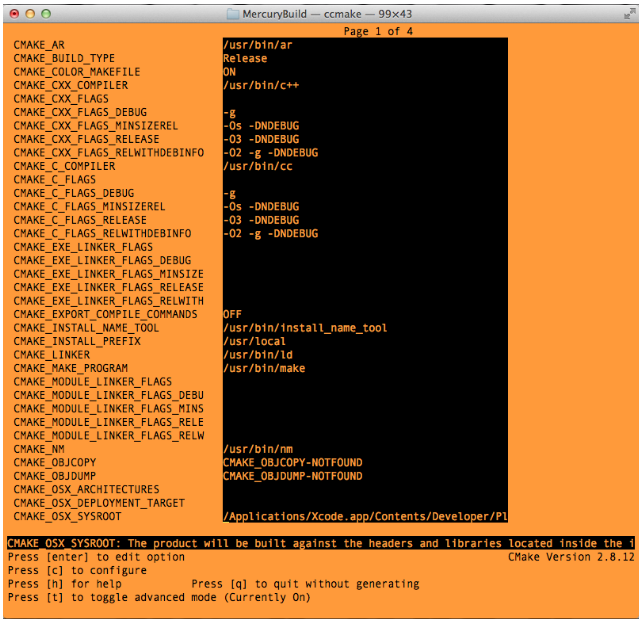

```
                                        Page 1 of 4
 CMAKE_AR                        /usr/bin/ar
 CMAKE_BUILD_TYPE                Release
 CMAKE_COLOR_MAKEFILE            ON
 CMAKE_CXX_COMPILER              /usr/bin/c++
 CMAKE_CXX_FLAGS
 CMAKE_CXX_FLAGS_DEBUG           -g
 CMAKE_CXX_FLAGS_MINSIZEREL      -Os -DNDEBUG
 CMAKE_CXX_FLAGS_RELEASE         -O3 -DNDEBUG
 CMAKE_CXX_FLAGS_RELWITHDEBINFO  -O2 -g -DNDEBUG
 CMAKE_C_COMPILER                /usr/bin/cc
 CMAKE_C_FLAGS
 CMAKE_C_FLAGS_DEBUG             -g
 CMAKE_C_FLAGS_MINSIZEREL        -Os -DNDEBUG
 CMAKE_C_FLAGS_RELEASE           -O3 -DNDEBUG
 CMAKE_C_FLAGS_RELWITHDEBINFO    -O2 -g -DNDEBUG
 CMAKE_EXE_LINKER_FLAGS
 CMAKE_EXE_LINKER_FLAGS_DEBUG
 CMAKE_EXE_LINKER_FLAGS_MINSIZE
 CMAKE_EXE_LINKER_FLAGS_RELEASE
 CMAKE_EXE_LINKER_FLAGS_RELWITH
 CMAKE_EXPORT_COMPILE_COMMANDS   OFF
 CMAKE_INSTALL_NAME_TOOL         /usr/bin/install_name_tool
 CMAKE_INSTALL_PREFIX            /usr/local
 CMAKE_LINKER                    /usr/bin/ld
 CMAKE_MAKE_PROGRAM              /usr/bin/make
 CMAKE_MODULE_LINKER_FLAGS
 CMAKE_MODULE_LINKER_FLAGS_DEBU
 CMAKE_MODULE_LINKER_FLAGS_MINS
 CMAKE_MODULE_LINKER_FLAGS_RELE
 CMAKE_MODULE_LINKER_FLAGS_RELW
 CMAKE_NM                        /usr/bin/nm
 CMAKE_OBJCOPY                   CMAKE_OBJCOPY-NOTFOUND
 CMAKE_OBJDUMP                   CMAKE_OBJDUMP-NOTFOUND
 CMAKE_OSX_ARCHITECTURES
 CMAKE_OSX_DEPLOYMENT_TARGET
 CMAKE_OSX_SYSROOT               /Applications/Xcode.app/Contents/Developer/Pl

CMAKE_OSX_SYSROOT: The product will be built against the headers and libraries located inside the i
Press [enter] to edit option                                                   CMake Version 2.8.12
Press [c] to configure
Press [h] for help           Press [q] to quit without generating
Press [t] to toggle advanced mode (Currently On)
```

(d) Once configured, press the key ’g’ to generate the executables.

3. To check if successfully installed, go to your build directory ’MercuryBuild’ using the terminal and type

```
make fullTest
```

4. If all the tests have passed, MercuryDPM is successfully installed on your machine.

2.3 MercuryDPM mailing list

Please now follow the instructions to sign up for the mailing list at `http://mercurydpm.org/support/mailing-list` in order to receive updates about the code.

3 Output files

Having explained in the previous section how to run a Mercury driver code, we next explain the form of the file output, and describe how relevant information may be extracted from these files. Mercury produces data regarding a wide range of system parameters and, as such, there exist a variety of manners in which this data may be obtained and processed.

Running a Mercury executable produces three main output files in which we are interested. Each of the files produced will carry the name of the code used followed by one of the extensions *.data*, *.fstat* and *.ene*.

For instance, building and running a file named *example.cpp* will produce *example.data*, *example.fstat* and *example.ene* (in addition to several other files which will be discussed in later sections).

3.1 The .ene file

The simplest of the three file types is the '.ene' file, which allows us to interpret the time evolution of the various forms of energy possessed by the system. Data is written at predefined time steps, with the system's gravitational energy (`ene_gra`), elastic potential (`ene_ela`) and translational (`ene_kin`) and rotational (`ene_rot`) kinetic energies being shown alongside the systems centre of mass position in the *x*, *y* and *z* directions (`X_COM`, `Y_COM` and `Z_COM`, respectively). They are computed as follows:

$$\mathrm{Ene}_{\mathrm{gra}} = \sum_{i=1}^{N_p} -m_i \vec{r}_i \cdot \vec{g}_i, \quad \mathrm{Ene}_{\mathrm{ela}} = \sum_{i=1}^{N_p} \frac{1}{2} k^n {\delta_i^n}^2 \text{ (for linear spring-damper force)},$$

$$\mathrm{Ene}_{\mathrm{kin}} = \sum_{i=1}^{N_p} \frac{1}{2} m_i v_i^2, \quad \mathrm{Ene}_{\mathrm{rot}} = \sum_{i=1}^{N_p} \frac{1}{2} I_i \omega_i^2, \quad (\mathrm{X}, \mathrm{Y}, \mathrm{Z})_{\mathrm{COM}} = \frac{\sum_{i=1}^{N_p} m_i \vec{r}_i}{\sum_{i=1}^{N_p} m_i}.$$

If no other potential forces are present, the sum of the three forces equals the total energy in the system, and thus can be used to track energy conservation:

$$\mathrm{Ene}_{\mathrm{tot}} = \mathrm{Ene}_{\mathrm{gra}} + \mathrm{Ene}_{\mathrm{kin}} + \mathrm{Ene}_{\mathrm{rot}} + \mathrm{Ene}_{\mathrm{ela}}.$$

A typical .ene file looks like this:

```
t      ene_gra   ene_kin    ene_rot  ene_ela    X_COM    Y_COM   Z_COM
0      1.40e-05        0          0        0     0.01     0.01 0.01400
0.01   1.35e-05    5e-07          0        0     0.01     0.01 0.01350
0.02   1.20e-05    2e-06          0        0     0.01     0.01 0.01200
0.03   9.50e-06 4.50e-06          0        0     0.01     0.01 0.00950
0.04   6.00e-06 8.00e-06          0        0     0.01     0.01 0.00600
0.05   1.70e-06 5.10e-09          0 1.11e-05     0.01     0.01 0.00170
0.06   5.55e-06 6.16e-06          0        0     0.01     0.01 0.00555
0.07   8.56e-06 3.15e-06          0        0     0.01     0.01 0.00856
0.08   1.05e-05 1.14e-06          0        0     0.01     0.01 0.01058
0.09   1.15e-05 1.30e-07          0        0     0.01     0.01 0.01159
0.095  1.17e-05 7.40e-12          0        0     0.01     0.01 0.01172
```

This data is taken from a simulation of a single particle ($r = 2\mathrm{cm}$, $m = 0.1\,\mathrm{g}$) bumping onto a horizontal plate at $z = 0$ due to gravity ($g = 10\,\mathrm{m/s^2}$). You can see the particle losing gravitational energy before the impact, then gaining it again. At the same time, the kinetic energy increases, has a peak at the beginning and end of the collision, then decreases again. During the impact, the kinetic energy decreases sharply and increases again, while the elastic energy increases and decreases in a similar manner.

We can use gnuplot to show how the energy is conserved until the collision happens:

```
MercuryBuild/Drivers/MercurySimpleDemos$ ./FreeFallSelfTest
MercuryBuild/Drivers/MercurySimpleDemos$ gnuplot
gnuplot> p ’FreeFallSelfTest.ene’ u 1:2 w l title ’Ene_grav’, \
’’ u 1:3 w l title ’Ene_kin’, ’’ u 1:5 w l title ’Ene_ela’, \
’’ u 1:($2+$3+$5) w l title ’Ene_tot’
```

The result is shown in Figure 1.

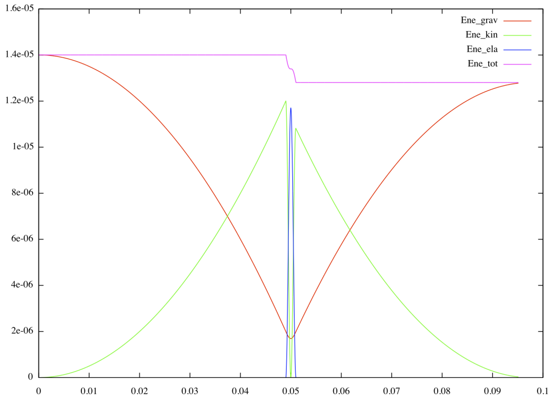

Figure 1: Energy over time for the free fall demo code.

3.2 The .data file

The next file type we will discuss ’ .data ’ although slightly more complicated, is perhaps the most useful and versatile of the three, as it provides full information regarding the positions and velocities of all particles within the system at each given time step.

The files are formatted as follows: at *each time step*, a single line stating the number of particles in the system (`N`), the time corresponding to the current step (`time`) and the maximal and minimal spatial boundaries defining the computational volume used in the simulations (`xmin, ymin, zmin, xmax, ymax, zmax`) is first output. This first line is structured as below:

`N, time, xmin, ymin, zmin, xmax, ymax, zmax`

```
1 0 0 0 0 0.01 0.01 0.01
0.01 0.01 0.014005 0 0 0 0.002 0 0 0 0 0 0 0
1 0.02 0 0 0 0.01 0.01 0.01
0.01 0.01 0.012005 0 0 -0.2 0.002 0 0 0 0 0 0 0
1 0.04 0 0 0 0.01 0.01 0.01
0.01 0.01 0.006005 0 0 -0.4 0.002 0 0 0 0 0 0 0
1 0.06 0 0 0 0.01 0.01 0.01
0.01 0.01 0.005773344765077 0 0 0.375052804297 0.002 0 0 0 0 0 0 0
1 0.08 0 0 0 0.01 0.01 0.01
0.01 0.01 0.01127440085102 0 0 0.175052804297 0.002 0 0 0 0 0 0 0
1 0.09512499999999 0 0 0 0.01 0.01 0.01
0.01 0.01 0.01277824639101 0 0 0.023802804297 0.002 0 0 0 0 0 0 0
```

This output is then followed by a series of `N` subsequent lines, each providing information for one of the `N` particles within the system at the current point in time. For each particle, we are given information regarding its current position in three dimensions (`x, y, z`), the magnitudes of the three components of its instantaneous velocity (`vx, vy, vz`), the radius of the particle (`rad`), its `angular` position in three dimensions (`qx, qy, qz`) and the three components of its instantaneous angular velocity (`omex, omey, omez`). The term `xi` represents an additional variable which can be specified by the user, as described in the documentation of `DPMBase::setInfo()`. By default, `xi` represents the *species index*, which stores information regarding the particle's material properties.

These parameters are output in the following order:

```
x, y, z, vx, vy, vz, rad, qx, qy, qz, omex, omey, omez, xi
```

The sequence of output lines described above is then repeated for each time step.

It should be noted that the above is the standard output required for three-dimensional data; for two-dimensional data, only five items of information are given in the initial line of each time step:

```
N, time, xmin, zmin, xmax, zmax
```

and eight in the subsequent `N` lines:

```
x, z, vx, vz, rad, qz, omez, xi
```

Finally, we discuss the .fstat file, which is predominantly used to calculate stresses.

The .fstat output files follow a similar structure to the .data files; for each time step, three lines are initially output, each preceded by a 'hash' symbol (#). These lines are designated as follows:

```
  # time, info
  # info
  # info
```

where `time` is the current time step, and the values provided in the spaces denoted 'info' ensure backward compatibility with earlier versions of Mercury.

This initial information is followed by a series of N_C lines corresponding to each of the N_C **particle *contacts*** (as opposed to **particles**) within the system at the current instant in time.

Each of these lines is structured as follows:

```
time, i, j, x, y, z, delta, deltat, fn, ft, nx, ny, nz, tx, ty, tz
```

Here, `i` indicates the number used to identify a given particle and `j` similarly identifies its contact partner. The symbols `x`, `y` and `z` provide the spatial position of the point of contact between the two particles `i` and `j`, while `delta` represents the overlap between the two and `deltat` the length of the *tangential spring*. The parameters `fn` and `ft` represent, respectively, the absolute normal and tangential forces acting on the particles, with the relevant direction provided by the unit vectors defined by `nx, ny, nz` for the normal component and `tx, ty, tz` for the tangential component.

4 Post processing using coarse graining

To formulate accurate continuum models one constantly needs to calibrate and validate them with the available experimental or numerical data, which are discrete in nature. Hence to perform this mapping in an efficient manner, accurate micro-macro transition methods are required to obtain continuum fields (such as density, momentum, stress, etc.) from discrete data of individual elements (positions, velocities, orientations, interaction forces, etc.). This is the focus of this chapter: *How to perform the micro-macro transitional step?*

Many different techniques have been developed to perform the micro-macro transition, from discrete data, including Irving & Kirkwood's approach [IK50] or the method of planes [TED95]; we refer the interested reader to [WTLB12a, LAM11] and references therein. Here, we use an accurate micro-macro transitional procedure called *coarse-graining*, as described in, e.g., [Bab97, WTLB12b, TTW16, LRW]. When compared with other simpler methods of performing the micro-macro transitions, the coarse-graining method has the following advantages: (i) the resulting macroscopic fields exactly satisfy the equations of continuum mechanics, even near the boundaries, see [WTLB12b]; (ii) the elements are neither assumed to be spherical or rigid; (iii) the resulting fields are even valid for a single element and a single time step, hence *no ensemble-averaging* is required, *i.e.* no averaging over several time steps or stamps. However, the coarse-graining method does assume that (i) each pair of elements has a single contact; *i.e.* elements are assumed to be convex in shape; (ii) the contact area can be replaced by a single contact point, implying that the overlaps are not too large; (iii) the collisions are enduring (*i.e.* not instantaneous). Often, micro-macro methods employ ensemble- or bulk-averaging to obtain accurate results; therefore, the methods are only valid for homogeneous, steady situations. The coarse-graining method overcomes these challenges by applying a local smoothing kernel, *coarse-graining function*, with a well-defined smoothing length, i.e. *coarse-graining scale*, that automatically generates fields satisfying the continuum equations. As an example, one could consider a *Gaussian* as a coarse-graining function with its standard deviation as a coarse-graining scale.

The coarse-graining method is very flexible and can be used with discrete data from any source, *e.g.* molecular dynamics, smoothed particle hydrodynamics, discrete particle simulations, experimental data [BDR$^+$13], etc. Coarse-graining has been successfully extended to allow its application to bulk flows near the boundaries or discontinuities [WTLB12b] and to analyse multi-component granular flows [TWT16]. Thus, the following section briefly lays out the idea and expressions of coarse graining.

4.1 Nomenclature

Given we have different types of constituents: (bulk) type-ν and boundary, whose interstitial pore-space is filled with a zero-density passive fluid. Each particle $i \in \mathcal{F}$, where $\mathcal{F} := \sum_\nu \mathcal{F}^\nu \cup \mathcal{F}^b$, will have a radius a_i, whose centre of mass is located at $\vec{r}_i$ with mass m_i and velocity $\vec{v}_i$. The total force $\vec{f}_i$ (1), acting on a particle $i \in \mathcal{F}$ is computed by summing the forces $\vec{f}_{ij}$ due to interactions with the particles of the same type $j \in \mathcal{F}^\nu$ and other type, $j \in \mathcal{F}/\mathcal{F}^\nu$, and body forces $\mathbf{b}_i$, *e.g.*, gravitational forces ($m_i\mathbf{g}$).

$$\vec{f}_i = \sum_{\substack{j \in \mathcal{F}^\nu \\ j \neq i}} \vec{f}_{ij} + \sum_{j \in \mathcal{F}/\mathcal{F}^\nu} \vec{f}_{ij} + \vec{b}_i, \text{ for all } i \in \mathcal{F} \qquad (1)$$

$$\text{and } \nu = 1, 2, 3, ..., boundary.$$

For each constituent pair, i and j, we define a contact vector $\vec{r}_{ij} = \vec{r}_i - \vec{r}_j$, an overlap δ_{ij} = max($a_i + a_j - \vec{r}_{ij} \cdot \vec{n}_{ij}$,0), where $\vec{n}_{ij}$ is a unit vector pointing from j to i, $\vec{n}_{ij} = \vec{r}_{ij}/|\vec{r}_{ij}|$. Furthermore, we define a contact point $\vec{c}_{ij} = \vec{r}_i + (a_i - \delta_{ij}/2)\vec{n}_{ij}$ and a branch vector $\vec{b}_{ij} = \vec{r}_i - \vec{c}_{ij}$, see Fig. 2. Irrespective of the size of constituent i and j, for simplicity, we place the contact point, $\vec{c}_{ij}$, in the centre of the contact area formed by an overlap, δ_{ij}, which for small overlaps has a negligible effect on particle dynamics.

In the following sections, we first present the idea of coarse-graining (CG) and then list the CG expressions for the *partial* and *bulk* quantities, using the above nomenclature.

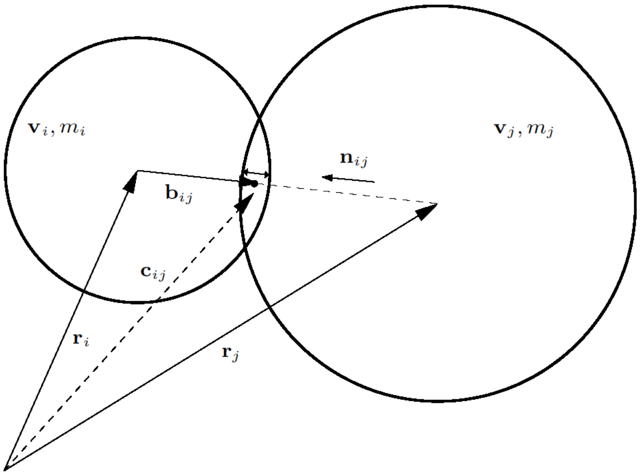

Figure 2: An illustration of two interacting constituents i and j, where the interaction is quantified by a certain amount of overlap δ_{ij}. If $\vec{r}_i$ and $\vec{r}_j$ denote the particles' centre of mass then we define the contact vector $\vec{r}_{ij} = \vec{r}_i - \vec{r}_j$, the contact point $\vec{c}_{ij} = \vec{r}_i + (a_i - \delta_{ij}/2)\vec{n}_{ij}$ and a branch vector $\vec{b}_{ij} = \vec{r}_i - \vec{c}_{ij}$.

4.2 Idea behind coarse-graining

To illustrate the idea, we consider the *partial* microscopic (point) mass density for a system (in a zero-density passive fluid) at point $\vec{r}$ and time t. From statistical mechanics, it is given as

$$\rho^{\nu,mic}(\vec{r},t) = \sum_{i\in\mathcal{F}^\nu} m_i \delta(\vec{r} - \vec{r}_i(t)), \tag{2}$$

where $\delta(\vec{r})$ is the Dirac delta function in $\mathbb{R}^3$. This definition complies with the basic requirement that the integral of the mass density over a volume in space equals the mass of all the particles in this volume.

To extract the *partial* macroscopic mass density field, $\rho^\nu(\vec{r},t)$, the *partial* microscopic mass density (2) is convolved with a spatial coarse-graining function $\psi(\vec{r})$, e.g. a Heaviside, Gaussian or a class of Lucy polynomials[1]. Thus, leading to

$$\begin{aligned} \rho^\nu(\vec{r},t) &:= \int_{\mathbb{R}^3} \rho^{\nu,mic}\psi(\vec{r} - \vec{r}')d\vec{r}', \\ &:= \sum_{i\in\mathcal{F}^\nu} m_i\psi(\vec{r} - \vec{r}_i(t)) = \sum_{i\in\mathcal{F}^\nu} m_i\psi_i. \end{aligned} \tag{3}$$

---

[1] For more details regarding the coarse-graining functions see *Tunuguntla et al.* [TTW16].

The result is equivalent to replacing the delta-function with a spatial *coarse-graining function* (that is positive semi-definite, integrable, and has finite support), $\psi(\boldsymbol{r})$, also known as a *smoothing function*. For simplicity, seen later, we define $\psi_i = \psi(\vec{r}-\vec{r}_i(t))$.

5 Coarse-graining expressions: novel micro-macro map

Using the same idea as explained in the previous section, expressions for partial quantities corresponding to constituent type-ν are

$$
\begin{array}{ll}
\text{Density:} & \rho^\nu = \sum_{i\in\mathcal{F}^\nu} m_i \psi_i, \\
\text{Momentum:} & \vec{P}^\nu = \sum_{i\in\mathcal{F}^\nu} m_i \vec{v}_i \psi_i, \\
\text{Velocity:} & \vec{u}^\nu = \vec{P}^\nu/\rho^\nu, \\
\text{Total partial stress:} & \vec{\sigma}^\nu = \vec{\sigma}^{kin,\nu} + \vec{\sigma}^{con,\nu}, \\
\text{Kinetic stress:} & \vec{\sigma}^{kin,\nu} = \sum_{i\in\mathcal{F}^\nu} m_i \vec{v}_i' \vec{v}_i' \psi_i, \\
\text{Contact stress:} & \vec{\sigma}^{con,\nu} = \sum_{i\in\mathcal{F}^\nu} \sum_{\substack{j\in\mathcal{F}^\nu \\ j\neq i}} \vec{f}_{ij}\, \vec{b}_{ij} \Psi_{ij} + + \sum_{i\in\mathcal{F}^\nu} \sum_{j\in\mathcal{F}/\mathcal{F}^\nu} \vec{f}_{ij}\, \vec{b}_{ij} \Psi_{ij},
\end{array}
\tag{4}
$$

where in the kinetic stress expression, $\vec{v}_i'$ is the fluctuation velocity of particle i, defined as $\vec{v}_i'(\vec{r},t) = \vec{u}(\vec{r},t) - \vec{v}_i(t)$. Furthermore, in the contact stress expression, $\vec{b}_{ij}$ is the, particle centre to contact point, branch vector as illustrated in Fig. 2. Ψ_{ij} denotes a line integral along the branch vector $\vec{b}_{ij}$, $\Psi_{ij} = \int_0^1 \psi(\vec{r} - \vec{r}_i + s\vec{b}_{ij})ds$, which ensures the distribution of the force, see (1), between two constituents i and j to the *partial* stresses to be proportional to the length of the branch vectors. In other words, the stresses are distributed proportionally, based on the fraction of the branch vectors contained within each constituent. Thus, for contacts between a small and a large constituent, the larger-sized constituent receives a larger share of the stress. All the above partial quantities are derived such that both the mass and momentum balance laws are exactly satisfied. For more details, see *Tunuguntla et al* [TTW16].

More importantly, all the above CG expressions, stated in Sec. 5, are implemented in MercuryDPM. Thereby allowing to extract the continuum fields from, both, the transient and steady particle data.

6 Exercises

6.1 Running simulations

After successfully installing MercuryDPM using the earlier stated installation instructions, the following exercises can be run as follows.

Exercise 1

To run the first exercise problem, which is the `Tutorial9.cpp`, please go to the `Tutorials` directory by typing the following

```
cd PathToMercuryFolder/MercuryBuild/Drivers/Tutorials
```

Please note that the `PathToMercuryFolder` is to be typed in by the user and can be different on different computers. Once in the `Tutorials` directory, `Tutorial9.cpp` can be executed by typing

```
./Tutorial9
```

After successfully running the `Tutorial9`, the main aim of the exercise is to implement the below listed changes in the source code `Tutorial9.cpp`. This is found in the following directory

```
cd PathToMercuryFolder/MercurySource/Drivers/Tutorials
```

In the source directory of the Tutorials, open the `Tutorial9.cpp` via any text editor, e.g. vi (terminal based) or Sublime text editor (GUI based). Once opened, please perform the below requested changes step by step.

- Gradually increase the inclination θ. When does the particle start to roll?
- Set sliding/rolling friction so particle only rolls at 25 degree inclination or more. Report your values.
- What happens if you set $\mu_s < \mu_{ro}$?
- Set $\mu_{ro} = 0$; how does the speed of the particle at time t_{max} depend on μ_s? Can you explain it?

At each step, rerun `Tutorial9.cpp` by following the same steps that were stated earlier. However, before running `./Tutorial9` make sure that you have recompiled and rebuilt the `Tutorial9.cpp` executable, in order to account for the changes you have made. This is done by typing

```
make Tutorial9
```

Note that the above command is to be typed in the terminal in the directory

```
PathToMercuryFolder/MercuryBuild/Drivers/Tutorials
```

Besides compiling, building and running the Tutorial9, one can also view their result by executing the following in

```
./Tutorial9.xballs
```

Note that the above executable is found in the same directory where `./Tutorial9` was also executed.

Exercise 2

After successfully finishing Exercise 1, run `HourGlass2D.cpp` and view the `xballs` output. The executable for HourGlass2D example can be found in the directory

```
PathToMercuryFolder/MercuryBuild/Drivers/MercurySimpleDemos
```

Similarly, the source code HourGlass2D.cpp is found in

```
PathToMercuryFolder/MercurySource/Drivers/MercurySimpleDemos
```

However, on running and executing the HourGlass2D exercise, for the first second you should see particles relaxing in the top half of the hourglass, which has a wall inserted at the neck to prevent the particles from falling through. At $t = 0.9s$, that wall is released, but instead of flowing into the lower part of the hourglass, the particles form an arch at the neck of the hourglass that prevents outflow.

(i) Run three more cases:

- (a) Lower each friction coefficient μ, $\mu_{rolling}$, $\mu_{torsion}$ by a factor of 2.
- (a) Lower each friction coefficient μ, $\mu_{rolling}$, $\mu_{torsion}$ by a factor of 4.
- (b) Set all friction coefficients μ, $\mu_{rolling}$, $\mu_{torsion}$ to 0.

Report what happens. For which cases do particles flow out? How long does it take them to flow out? Is friction a factor that influences the flow in an hourglass?

(ii) Now go back to the original, frictional case and modify the neck diameter. How large a neck do you need for the particles to flow?

Exercise 3

Run `FreeFallSelfTest.cpp`. Note that the executable is found in the directory

```
PathToMercuryFolder/MercuryBuild/Drivers/MercurySimpleDemos
```

Similarly, the source code FreeFallSelfTest.cpp is found in

```
PathToMercuryFolder/MercurySource/Drivers/MercurySimpleDemos
```

After running, use the resulting file `FreeFallSelfTest.ene` to plot the sum of kinetic and potential energy as a function of time (the total energy is the sum of the 2nd, 3rd, 4th and 5th column). Energy should be conserved.

1. Calculate the collision time t_c. Be aware that the code is in 2D, so mass $m_i = \rho\pi r_i^2$.
2. Gradually increase the timestep dt. When does energy conservation break down?
3. Plot the energy at time t_{max} as a function of dt/t_c. What ratio of time step over collision time is safe to use? What time step do you recommend?
4. Modify the dissipation coefficient such that the restitution coefficient for particle-wall collisions is 0.5, and run it. Plot the total kinetic energy. By how much does the energy drop after each collision? Does this drop in energy agree with the expected restitution coefficient?
5. Does the particle come to rest in a finite time? If so, when and why?

Exercise 4

Run `FreeCoolingDemo.cpp`, whose executable is also found in the

```
MercurySimpleDemos
```

directory. On a side note, we hope that by now it is clear that the executables and date files are found in the build directory whereas the source files are found in the source directory.

The FreeCoolingDemo code is used to measure the dissipation in a granular gas (such as sand dunes, shaken powders). However, the simulated volume is much too small to be realistic. To avoid wall effects, the wall should ideally be replaced by periodic walls, thus modelling a representative volume of a much larger system. However, there are some traps when introducing periodic walls:

Modify `FreeCoolingDemo.cpp` such that only 100 particles are produced and set $t_{max} = 10$ (or more).

- Run the code and plot the kinetic energy over time in log-log scale. You should see a power law decay.
- Now remove the four walls and replace them by periodic boundary conditions in both x and y-direction. Describe what happens with the kinetic energy over time.

- Give the particles random x- and y-velocities (with zero mean velocity) while keeping the kinetic energy, $E_{kin} = \frac{1}{2}\sum_{i=1}^{N} m_i|\vec{v}_i|^2$, approximately the same. Now you should see a similar behaviour as in the original case. Plot kinetic energy over time for both cases in one plot and describe the differences.
- Compare the mean velocity, $\vec{V} = \frac{1}{N}\sum_{i=1}^{N} \vec{v}_i$, of the initial state with the mean velocity of the final state. Do the same for the original case with fixed walls. Describe the differences and give an explanation for this behaviour.

6.2 Analysing data

Exercise 5

Five particles. To get accustomed to coarse-graining, we start with a very simple example: Five particles positioned on a irregular base made from five fixed particles, see Figure 3a. The system is nondimensionalised such that particle diameter $d = 1$, particle mass $m = 1$ and gravity $g = 1$.

Note, this case is chosen only to illustrate the ideas behind coarse-graining. A continuum description of granular media only makes sense if you average over a representative dataset, which is not the case here.

1. Compile and run the driver named `FiveParticles`, which is located in the `MercurySimpleDemos` directory. Use `xballs` to view the content of `FiveParticles.data`.

```
cd $MERCURY_BUILD/Drivers/MercurySimpleDemos
make FiveParticles
./FiveParticles
./FiveParticles.xballs
```

2. Compile `fstatistics` (in the `MercuryCG` folder). Now use `fstatistics` to create continuum fields for the very last time step (option `-tmin 20 -tmax 20.1`). Create fields varying in the x and y direction (option `-stattype XZ`), with a cg-width of $w = d/10$ (option `-w 0.1` or `-w_over_rmax 0.4`). Evaluate at points distributed over the whole domain with mesh size of $h_x = h_z = w/2$ (option `-h 0.05` or `-hx 0.05 -hz 0.05`). Thus the full command is like this:

```
make -C ../MercuryCG/fstatistics
../MercuryCG/fstatistics FiveParticles -stattype XZ
-w 0.1 -h 0.05 -tmin 20 -tmax 20.1
```

3. Now view the output in `Matlab` or `octave`. Usually, you have to write your own matlab script to view the output, but here we have provided you with a sample: run the script `FiveParticles.m` to load the content of `FiveParticles.stat` and produces a plot of the bulk density similar to Figure 3b.

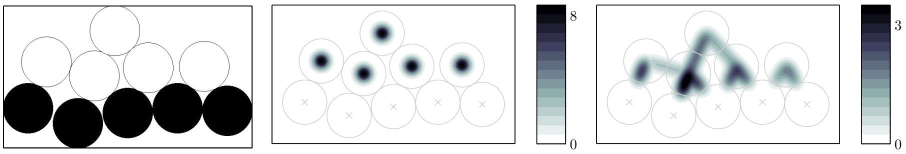

Figure 3: Snapshot of the final state of the `FiveParticles` simulation *(left)*. Coarse-graining is applied to obtain the bulk density ρ *(centre)* and pressure p *(right)*.

```
matlab
>> edit FiveParticles.m %run in Matlab to open the file in
    ↪ the editor
>> FiveParticles %run the file in Matlab
```

4. Modify the script `FiveParticles.m` to plot the pressure, and thus reproduce Figure 3c.

Exercise 6

Lees-Edwards shear cell. Now we study a more complex situation, in which a continuum formulation makes sense: granular media sheared at a constant rate $\dot{\gamma}$. For simplicity, we only consider a 2-dimensional granular medium. To simulate this, Lees-Edwards boundary conditions are used: two periodic boundaries are defined in x and y-direction, with particles crossing upward/downward through the y-boundary experiencing a velocity increase/decrease of $\Delta v = \dot{\gamma} W \vec{x}$. After a while, the flow will reach a steady-state with a uniform shear rate in the xz-plane, $\frac{\partial v_x}{\partial y} = \dot{\gamma}$.

1. Compile and run the driver named `LeesEdwards`, which is located in the `MercurySimpleDemos` directory. Use `xballs` to view the content of `LeesEdwardsSelfTest.data`.

```
cd $MERCURY_BUILD/Drivers/MercurySimpleDemos
make LeesEdwardsSelfTest
./LeesEdwardsSelfTest
./LeesEdwardsSelfTest.xballs
```

2. First we need to find out when the simulation becomes steady: To do this, plot the kinetic and potential energy in the whole system over time and check when it becomes steady. You can find time, translational kinetic and potential energy in columns 1, 3, and 5 of the file `LeesEdwardsSelfTest.ene`. Use a program like `gnuplot` to view the data.

```
gnuplot
>> plot 'LeesEdwardsSelfTest.ene' u 1:3
```

```
>> plot 'LeesEdwardsSelfTest.ene' u 1:5
```

3. The flow becomes steady very quickly, at about $t = 2$. To get good statistics, we need to run for a longer time: Open `LeesEdwardsSelfTest.cpp` and set the `timeMax` to 50 to get more data; then recompile and run the modified code.

   Use `fstatistics` to create continuum fields for the time interval $t > 2$. Create fields varying in the x and y direction, with a cg-width of $w = d/4$ and a mesh size of $h = d/4$. Then repeat the process to create fields varying only in the y direction, with a cg-width of $w = d/4$ and a mesh size of $h = d/10$. Thus the full command is:

```
../MercuryCG/fstatistics LeesEdwardsSelfTest -stattype XY
-w 0.25 -h 0.25 -tmin 2
../MercuryCG/fstatistics LeesEdwardsSelfTest -stattype Y
-w 0.25 -h 0.1 -tmin 2 -o LeesEdwardsSelfTest.Y.stat
```

4. Now view the output in `Matlab` or `octave`. Usually, you have to write your own matlab script to view the output, but here we have provided you with a sample: run the script `LeesEdwardsSelfTest.m` to load the content of `LeesEdwardsSelfTest.stat` and produce a plot of the velocity.

```
matlab
>> edit LeesEdwardsSelfTest.m
%run in Matlab to open the file in the editor
>> LeesEdwardsSelfTest
%run the file in Matlab
```

Exercise 7

A basic example of a 2D chute: In order to understand coarse-graining, it is useful to look at a simple example.

1. First checkout the following folder
   `svn checkout https://svn.mercurydpm.org/Training/CG/Chute2D`

   In the folder you have just checkout you find some data, fstat and restart files, in the subdirectory Data and some script files in the directory XBalls. Also these is a empty directory Exe that we will use in minutes.

2. Go to your MercuryBuild tree and the subdriectory XBalls and type

```
make xballs
```

   This will create an executable file `xballs`. Copy this file to Exe directory in Chute2D you have just checkout.

3. Go into the directory XBalls and use the two scripts to see the contains of the two data files. You will see two short 2D chute simulations; the first is stopping and the second is flowing an a steady-rate.

4. Go to your MercuryBuild tree and the subdirectory/Drivers/MercuryCG and type `make fstatistics` Again copy the file fstatistics to you Exe directory.

5. Go to Data directory and type

   ```
   ../Exe/fstatistics Chute2DStatic -stattype XZ -tmin 15
   -tmax 16 -n 200 -w 0.1+
   ```

   This will create a new file caled Chute2DStatic.stat

6. Go into the Matlab directory and run plotCG1.m. Here, we used a very small CG width what do we see in the static case?

7. Go back to the Data directory and type

   ```
   ../Exe/fstatistics Chute2DStatic -stattype XZ -tmin 15
   -tmax 16 -n 100 -x 5 10 -z 0 5 -w 0.1 -o Chute2DStatic.
       ↪ zoom.stat
   ```

   This create a new file Chute2DStatic.zoom.stat which is a (zoomed) more detailed look at a some region of the data.

8. Make a small change to plotCG1.m to plot the zoomed output. Hint look at line 3.

9. Now run the following commands

   ```
   ../Exe/fstatistics Chute2D -stattype XZ -tmin 100 -n 100 -w
       ↪  0.5 -o Chute2D.average.stat
   ```

   and

   ```
   ../Exe/fstatistics Chute2D -stattype XZ -tmin 100 -tmax 101
       ↪  -n 100
   -w 0.5 -o Chute2D.instant.stat
   ```

10. Use the Matlab file plotCG2 to compare when you see in time-averaged and a data snapshot

Exercise 8

1. If you check out

```
svn checkout https://svn.mercurydpm.org/Training/CG/
    ↪ Contraction
```

you will find 3D data on the granular flow through a contradiction. Use fstatistics to coarse-grain this data and see what structures you can find.

Exercise 9

Coarse graining can also be applied to experiment data. In this example we show you how this is possible. Figure 6.2 shows an images from a rotating drum experiment.

1. Firstly checkout

   ```
   svn checkout https://svn.mercurydpm.org/Training/CG/
       ↪ Experimental
   ```

   Note, this directory contains a lot of data and it may take a while to check out. Maybe type this before a coffee break.

2. First go into the Matlab directory and run the code TrackTheBeads.m This will display a few windows that demonstrates the steps this code takes.

   1. The first task of the script is to find the sizes of the images that have to be read. This is done in order to enable the script to read images with resolutions that are different from the resolution that is used for this particular experiment. When this is done, the script creates two annular shaped masks (stored in the Configuration directory), with the second being slightly smaller than the first. The larger mask is used to remove distractions such as the inner and outer parts of the drum from the images because those parts would cause false positives during the tracking part of the script if left unmasked. The smaller mask is used to check whether particles that are found during the tracking step are within the masked area or at the edges of the mask. This is necessary because the masking creates artefacts during the blurring that has to happen later on in the script. These artefacts cause false positives during the tracking step.

   2. The images are now ready to be inverted, this is done in order to make the black particles that are intended to be tracked show up as bright spots on a darker background. This is necessary because the scripts from The result of a blurring filter on a masked image. Artefacts at the edges of the mask is clearly visible. the Matlab Particle Tracing Code Repository are only able to track bright or fluorescent spots on darker backgrounds.

   3. After the images are masked and inverted, they are ready to be blurred and then tracked. The blurring and tracking parts of the script are done by the Matlab Particle Tracking Code Repository The blurring is done

by a function called bpass(), this function blurs the images so the edges of beads are less bright than the centres of the beads. This is done so the centres of the particles can be found by looking for the brightest pixel in a blob. It is important to note that this causes a possible weakness in this tracking method, because this method assumes that the bright spot of a particle does not move on a frame by frame basis. This assumption is safe in this case because the beads are so small, but for larger beads different methods of tracking should be studied. According to the documentation in the script, bpass() performs a bandpass by producing a lowpassed image by combining the original image with a Gaussian. A second image is then produced by combining the original image with a boxcar function. The boxcar version is then subtracted from the Gaussian version to produce a highpassed version of the original image.

4. After the image is blurred, the pkfnd() searches for bright spots in the image by stepping through the image pixel-by-pixel and checking whether a pixel is brighter than all of its neighbours. If a pixel is indeed brighter than all of its neighbours, its coordinates are stored in a matrix.

5. This matrix is one of the inputs of the cntrd() function, which looks for the centres of bright spots with sub-pixel accuracy. By stepping through the list of coordinates that was created by pkfnd() and calculating the weighted average x- and y-locations of the bright spots. When the locations of the bright spots have been found, the previously mentioned smaller mask is applied to the list of locations in order to filter out the false positives that were found on the edge of the masks. All bright spots that are found within the smaller mask are tagged with the current timestep and appended to a matrix that stores these coordinates.

6. After the program has looped through all the images it was told to read, this matrix is ready to be run through the function called track(). This is the function that tries to connect found bright spots in consecutive frames by using the minimal total squared displacement method. If a particle is ‘lost’ between two frames, a new track will be created when the particle is ‘found’ again.

7. Now that tracking is complete, the velocity components in the x- and y-direction are calculated using a 5 point stencil. The function that is used is
$$f = \frac{f(x+2h) + 8f(x+h) - 8f(x-h) + f(x-2h)}{12h} \tag{5}$$

8. The coordinates and velocities of particles are then formatted in the appropriate format for MercuryDPM (The leading lines are in 3D data format and the following lines are in format 14) This data is stored as a .data file. Now we can coarse-grain this data as if it had been created by MercuryDPM.

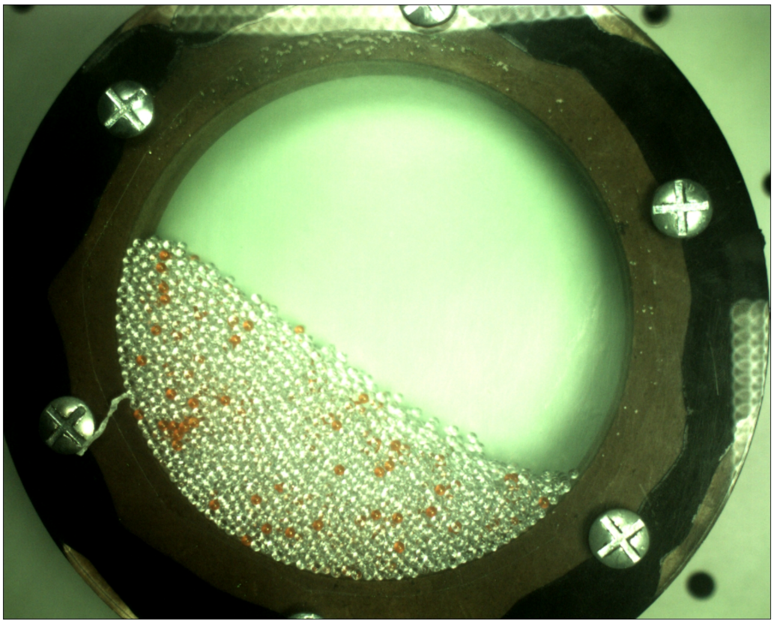

Figure 4: Snapshot of a rotating drum experiment

3. Now change line 14 to `plot_to_check_finding = 0;` and rerun the code. This will suppress the output and analyse all 1500 frame. Note, this will take a few minutes to run. This will create a file called TestData.data in the Output directory.

4. Use your coarse-graining script with the flags `-stattype XY -n 100 -w 1` to create a .stat file from this .data file.

5. Run AnalysisTestData.m to generate a coarse-grained velocity and density plot of experimental data.

References

[Bab97] M. Babic. Average balance equations for granular materials. *Intl. J. Eng. Sci.*, 35(5):523–548, 1997.

[BDR$^+$13] R. P. Behringer, J. Dijksman, J. Ren, J. Zhang, T. Majmudar, B. Chakraborty, D. Bi, and A. Tordesillas. Jamming and shear for granular materials. In *POWDERS AND GRAINS 2013: Proc. 7th Int. Conf.*

Micromechanics of Granular Media, volume 1542, pages 12–19. AIP Publishing, 2013.

[IK50] J. H. Irving and J. G. Kirkwood. The statistical mechanical theory of transport processes. iv. the equations of hydrodynamics. *J. Chem. Phys.*, 18:817–829, 1950.

[LAM11] S. Luding and F. Alonso-Marroquín. The critical-state yield stress (termination locus) of adhesive powders from a single numerical experiment. *Granul. Matt.*, 13(2):109–119, 2011.

[LRW] S. Luding, N. Rivas, and T. Weinhart. From soft and hard particle simulations to continuum theory for granular flows. *ALERT geomaterials Doctoral School 2017, Aussois, France*.

[Tea13] A. R. Thornton and et al. A review of recent work on the discrete particle method at the University of Twente : An introduction to the open-source package MercuryDPM. In *DEM 6: 6^{th} International Conference on Discrete Element Methods and Related Techniques*, pages 393–399, 2013.

[TED95] B. D. Todd, D. J. Evans, and P. J. Daivis. Pressure tensor for inhomogeneous fluids. *Phys. Rev. E*, 52(2):1627–1638, 1995.

[TKF$^+$13] A. R. Thornton, D. Krijgsman, R. Fransen, S. Gonzalez, D. Tunuguntla, A. te Voortwis, S. Luding, O. Bokhove, and T. Weinhart. Mercury-dpm: Fast particles simulations in complex geometries. *Newsletter EnginSoft*, 10(1):48–53, 2013.

[TTW16] D. R. Tunuguntla, A. R. Thornton, and T. Weinhart. From discrete elements to continuum fields: Extension to bidisperse systems. *Comput. Part. Mech.*, 3(3):349–365, 2016.

[TWT16] D. R. Tunuguntla, T. Weinhart, and A. R. Thornton. Comparing and contrasting size-based particle segregation models. *Comput. Part. Mech., DOI: 10.1007/s40571-016-0136-1*, 2016.

[Wea17] T. Weinhart and et al. *MercuryDPM: A Fast and Flexible Particle Solver Part A: Technical Advances*, pages 1353–1360. Springer Singapore, Singapore, 2017.

[WTLB12a] T. Weinhart, A. R. Thornton, S. Luding, and O. Bokhove. Closure relations for shallow granular flows from particle simulations. *Granul. Matt.*, 14(4):531–552, 2012.

[WTLB12b] T. Weinhart, A.R. Thornton, S. Luding, and O. Bokhove. From discrete particles to continuum fields near a boundary. *Granular Matter*, 14(2):289–294, 2012.

INPG – 3SR
46 avenue Félix Viallet
BP 53
38041 GRENOBLE CEDEX 9
FRANCE

ISBN 978-2-9542517-9-0

Fon: +33 (0) 456 528 621
Fax: +33 (0) 476 827 043
president@alertgeomaterials.eu
http://alertgeomaterials.eu

ALERT Doctoral School 2017
Discrete Element Modeling

Editors: K. Taghizadeh, G. Combe, S. Luding

S. Luding, N. Rivas, T. Weinhart
From soft and hard particle simulations to continuum theory for granular flows

F. Radjai
The contact dynamics (CD) method

J.-Y. Delenne, L. Amarsid, P. Mutabaruka, V. Richefeu, F. Radjai
Fluid-grain coupling using the Lattice Boltzmann method

C.L. Martin
Advanced contact laws

G. Combe, J-N. Roux
Good practice for sample preparation – Construction of granular packings

K. Taghizadeh, S. Luding, V. Magnanimo
DEM applied to soil mechanics

F.-V. Donzé, L. Scholtès
Predicting the strength of anisotropic shale rock: Empirical nonlinear failure criterion vs. Discrete Element Method model

D. Tunuguntla, T. Weinhart, A. Thornton
Discrete particle simulations with MercuryDPM

ISBN 978-2-9542517-9-0